PEM FUEL CELL CATALYST DEGRATION MECHANISM AND MATHEMATICAL MODELING

A Dissertation
Presented to
The Academic Faculty

by

Wu Bi

In Partial Fulfillment
of the Requirements for the Degree
Ph.D. in the
School of Chemical and Biomolecular Engineering

Georgia Institute of Technology
August 2008

PEM FUEL CELL CATALYST DEGRATION MECHANISM AND MATHEMATICAL MODELING

Approved by:

Dr. Thomas Fuller, Advisor
School of Chemical and Biomolecular Engineering
Georgia Institute of Technology

Dr. Yulin Deng, Co-Advisor
School of Chemical and Biomolecular Engineering
Georgia Institute of Technology

Dr. Martha Gallivan
School of Chemical and Biomolecular Engineering
Georgia Institute of Technology

Dr. Paul Kohl
School of Chemical and Biomolecular Engineering
Georgia Institute of Technology

Dr. Preet Singh
School of Material Science and Engineering
Georgia Institute of Technology

Date Approved: June 13, 2008

ACKNOWLEDGEMENTS

First and foremost, I would like to thank my research advisor, Dr. Thomas Fuller, for his consistent support and guidance through years of research on this dissertation work. I am especially happy to advance my mathematical simulation skills through this research work. Dr. Fuller is also a good mentor who gave students opportunities to participate proposal writing and invited journal articles review. I would also like to acknowledge my co-advisor Dr. Yulin Deng for his valuable advice on my research work. And I am grateful to Dr. Deng who provided the great opportunities for me to teach in his class. During my study at Georgia Tech, I took two very helpful electrochemistry classes taught by Dr. Paul Kohl and Dr. Preet Singh. I would like to thank both of them and Dr. Martha Gallivan who all served as my research committee members.

During this research work, I received several important assistance and support across the Georgia Tech campus. Dr. Martial Taillefert's lab from the School of Earth & Atmospheric Sciences provided the ICP/MS instrument for the Pt concentration tests. I have to give my special acknowledgement to his graduate student Melanie Beazley for a large number of ICP/MS sample tests. I would like to acknowledge Dr. Gary Gray at Georgia Tech Research Institute (GTRI) for the gas chromatography (GC) tests to determine gas permeation rates in membrane. Also I have to thank Dr. Chuck Compson from Dr. Meilin Liu's group and Dr. Yolande Berta from the Center for Nanostructure Characterization and Fabrication for the training of SEM/EDS sample preparation and

tests, Dr. Mike Haluska and Dr. Jungli Hong for the training and assistance of X-ray diffraction tests.

I am very grateful to all the research group members who shared the learning and research experiences on a daily basis. Specifically, I want to acknowledge Mr. Cheng Chen for the fluorine emission ion chromatography testing, Ms. Rajeswari Chandrasekaran for the cooperative work on statistical experimental design and analysis of catalyst degradation simulation results, Mr. Kevin Gallagher and Mr. David Wong for the MEA preparation at GTRI, and my supervised undergraduate student Ms. Yungchi (Gigi) Fan for the Pt oxidation and dissolution simulation work using MatLAB.

Also I have to thank the GTRI at Georgia Tech and the Toyota Motor Engineering and Manufacturing North America Inc. for the gracious financial supports on parts of this research work. I would like to acknowledge Toyota visiting engineer Norimitsu Takeuchi and his colleagues for the discussion of catalyst degradation modeling work.

Special thanks should be given to the graduate student Pavel Blagov at the Emory University providing the assistance for large cases of model computation. He is also a good friend whom I can learn and motivate from each other. I would like to thank him for the invited cooperative work in social sciences utilizing my simulation skills beyond chemical engineering.

Finally, I would like to thank my family's constant support and love from China. Without them, I would have no chance to accomplish this.

TABLE OF CONTENTS

LIST OF TABLES

LIST OF FIGURES

LIST OF ABBREVIATIONS

ADT	Accelerated degradation test
CCM	Catalyst coated membrane
CV	Cyclic voltammetry
D.I.	De-ionized
DOE	Department of Energy
ECA	Electrochemically active surface area
ECA_{AD}	Hydrogen adsorption electrochemically active surface area
ECA_{DE}	Hydrogen desorption electrochemically active surface area
GC	Gas chromatography
GDL	Gas diffusion layer
HOR	Hydrogen oxidation reaction
ICP	Inductively coupled plasma
ICP/MS	Inductively coupled plasma mass spectroscopy
MEA	Membrane electrode assembly
NHE	Normal hydrogen electrode
OCV	Open circuit voltage
ORR	Oxygen reduction reaction
PEM	Polymer electrolyte membrane
PFSA	Perfluorosulfonic acid
ppb	Parts per billion
ppm	Parts per million
ppt	Parts per trillion

PSD	Particle size distribution
PTFE	Polytetrafluoroethylene
RH	Relative humidity
RHE	Reference hydrogen electrode
RRDE	Rotating ring-disk electrode
sccm	Standard cubic centimeters per minute
SEM-EDS	Scanning electron microscopy/energy dispersive spectroscopy
SHE	Standard hydrogen electrode
TEM	Transition electron microscopy
UHP	Ultra high pure
XRD	X-ray diffraction

LIST OF SYMBOLS

Chapter 1

E_1	Reaction 1.1 thermodynamic potential (V)
E_2	Reaction 1.2 thermodynamic potential (V)
E_4	Reaction 1.4 thermodynamic potential (V)
E_5	Reaction 1.5 thermodynamic potential (V)

Chapter 2

E	Thermodynamic potential (V)
F	Faraday's constant (96485 C/equiv)
M_{Pt}	Pt molecular weight (0.1951 kg/mol)
r	Radius of spherical Pt nanoparticle (m)
R	Universal gas constant (8.314 J/mol/K)
T	Temperature (K)
U	Adjusted thermodynamic Pt electrochemical dissolution potential (V)
U^{θ}	Standard thermodynamic Pt electrochemical dissolution potential (1.188 V)
ρ_{Pt}	Pt metal density (21090 kg/m^3)
σ_{Pt}	Surface tension (J/mol)

Chapter 4

$c^0_{H_2}$	H_2 concentration at membrane/anode interface (mol/m^3)
$c^0_{O_2}$	O_2 concentration at membrane/cathode interface (mol/m^3)
D_{H_2}	Diffusivity of H_2 in membrane (m^2/s)

D_{O_2}	Diffusivity of O_2 in membrane (m^2/s)
H_{H_2}	Henry's constant of H_2 in Nafion® membrane ($mol/m^3/Pa$)
H_{O_2}	Henry's constant of O_2 in Nafion® membrane ($mol/m^3/Pa$)
L	Membrane thickness (m)
N_{H_2}	Hydrogen crossover flux during fuel cell potential cycling ($mol/m^2/s$)
N_{O_2}	Oxygen crossover flux during fuel cell potential cycling ($mol/m^2/s$)
N'_{H2}	Hydrogen crossover flux in crossover test ($mol/m^2/s$)
N'_{O2}	Oxygen in air crossover flux in crossover test ($mol/m^2/s$)
$p^0_{H_2}$	H_2 gas pressure in bulk (Pa)
$p^0_{O_2}$	O_2 gas pressure in bulk (Pa)
x	Dimensionless distance of Pt "band" from cathode
α	Ratio of hydrogen and oxygen permeability

Chapter 5

CL	Pt loading in the cathode (12.5 mg or 0.0125 g)
D	Pt particle diameter (nm)
D_0	Initial Pt particle diameter (nm)
D_f	Pt particle diameter after degradation (nm)
Ea	Activation energy (kJ/mol)
F	Faraday's constant (96485 C/equiv)
k_D^0	Fitted dissolution rate constant (g/cm^2 Pt/cycle)

M	Pt molecular weight (0.1951 kg/mol)
m_C^0	Initial Pt mass in the cathode (g)
m_C^f	Pt mass in the cathode after degradation (g)
m_{Pt}	Pt mass in the cathode during potential cycling(g)
N	Number of potential cycles
R	Universal gas constant (8.314 J/mol/K)
S_0	Initial cathode ECA (m^2/gPt)
S_{min}	Assumed minimum cathode ECA (m^2/gPt)
$S(N)$	Cathode ECA during potential cycling (m^2/gPt)
S_{XRD}	Calculated Pt surface area based on particle size measured by XRD (m^2/gPt)
T	Temperature (K)
ΔV	Voltage loss during potential cycling (mV)
ρ	Density of platinum (21.45 g/cm^3 or 21450 kg/m^3)
σ	Surface tension of Pt nanoparticle (2.37 J/mol)

Chapter 6

CL	Pt loading in the cathode (7.5 mg or 0.0075 g)
$D(N)$	Pt particle diameter (nm)
k'	Fitted Pt mass loss rate constant, g/cm^2 Pt/cycle
m_{Pt}	Pt mass in the cathode during potential cycling (g)
M	Pt molecular weight (0.1951 kg/mol)
N	Number of potential cycles
R	Universal gas constant (8.314 J/mol/K)
$S(N)$	Cathode ECA during potential cycling (m^2/gPt)

T	Temperature (K)
x	X-ray vertical penetration distances into cathode (micron)
ρ	Cathode or membrane (Nafion® 1100) density (g/cm^3)
ρ_{Pt}	Density of platinum (21.45 g/cm^3 or 21450 kg/m^3)
σ	Surface tension of Pt nanoparticle (2.37 J/mol)
μ/ρ	Cathode or membrane (Nafion® 1100) mass attenuation coefficients (cm^2/g)

Chapter 7

c_H	Proton concentration (M)
E	External applied voltage (V)
E_A	Pt electrochemical oxidation reaction anodic term activation energy (J/mol)
E_C	Pt electrochemical oxidation reaction cathodic term activation energy (J/mol)
F	Faraday's constant (96485 C/equiv)
k	Pt electrochemical oxidation rate constant (mol/m^2/s)
k_A	Pt electrochemical oxidation reaction anodic term rate constant (mol/m^2/s)
k_C	Pt electrochemical oxidation reaction cathodic term rate constant (mol/m^2/s)
M_{Pt}	Pt molecular weight (0.1951 kg/mol)
M_{PtO}	PtO molecular weight (0.2110 kg/mol)
n	Number of electrons transferred in Pt electrochemical oxidation (2 equiv/mol)
R	Universal gas constant (8.314 J/mol/K)
$RH\%$	Relative humidity
RR	Pt metal core radius (m)
t	Time (s)
T	Temperature (K)
U^o	Standard thermodynamic Pt oxidation potential (0.980 V)

U	Adjusted thermodynamic Pt oxidation potential (V)
α_a	Pt electrochemical oxidation anodic transfer coefficient
α_c	Pt electrochemical oxidation cathodic transfer coefficient
Γ_{max}	Maximum Pt oxide coverage per surface area (2.18e-5 mol/m^2)
$\Delta\mu_{Pt}^0$	Fitted chemical potential shift for PtO (J/mol)
θ	Pt surface oxide coverage
ρ_{Pt}	Pt metal density (21090 kg/m^3)
ρ_{PtO}	PtO density (14100 kg/m^3)
σ_{Pt}	Surface tension of Pt nanoparticles (J/mol)
σ_{PtO}	Surface tension of PtO nanoparticles (J/mol)
ω	Pt-O dipole-dipole interaction coefficient (J/mol)

Chapter 9

A	MEA in-plane area (25 cm^2=2.5E-3 m^2)
A_S	Specific surface areas of small Pt particles (m^2/m^3)
A_L	Specific surface areas of large Pt particles (m^2/m^3)
C	Pt ion concentration (mol/m^3)
CH	Relative proton activity (1 M/1 M=1)
C_{Ref}	Concentration reference value (1M=1000 mol/m^3)
D	Pt ions diffusion coefficient in electrolyte (m^2/s)
E	External applied voltage at cathode (V)
E_{SIMU}	Relative simulation error of initial cathode degradation rate
F	Faraday's constant (96485 C/equiv)
k, or k_1	Pt dissolution reaction rate constant (mol/m^2/s)
k_2	Pt oxidation reaction rate constant (mol/m^2/s)

M	Total Pt mass in cathode (kg)
M_{Pt}	Pt molecular weight (0.1951 kg/mol)
M_{PtO}	PtO molecular weight (0.2110 kg/mol)
n_1	Number of electrons transferred in Pt electrochemical dissolution (2 equiv/mol)
n_2	Number of electrons transferred in Pt electrochemical oxidation (2 equiv/mol)
N_S	Number of small Pt particles in each cathode mesh
N_L	Number of large Pt particles in each cathode mesh
N_{OUT}	Pt ion diffusion flux at the cathode/membrane interface (mol/m^2/s)
R	Universal gas constant (8.314 J/mol/K)
r_{1S}	Pt dissolution rate on small particles (mol/m^2/s)
r_{1L}	Pt dissolution rate on large particles (mol/m^2/s)
r_{2S}	Pt oxidation rate on small particles (mol/m^2/s)
r_{2L}	Pt oxidation rate on large particles (mol/m^2/s)
$RH\%$	Relative humidity
$RR_{x,S}$	Radius of small Pt particles at a specific location (x) in cathode (m)
$RR_{x,L}$	Radius of large Pt particles at a specific location (x) in cathode (m)
RR_O	Volume-average Pt particle radius in cathode (m)
RR_S	Volume-average small Pt particle radius in cathode (m)
RR_L	Volume-average large Pt particle radius in cathode (m)
S	Total Pt surface area in cathode (m^2)
t	Time (s)
T	Fuel cell temperature (K)
U_1^0	Standard thermodynamic potential of Pt dissolution (1.188V)
U_2^0	Standard thermodynamic potential of Pt oxidation (0.980V)
U_{1S}	Adjusted thermodynamic dissolution potential for small Pt particles (V)

U_{1L}	Adjusted thermodynamic dissolution potential for large Pt particles (V)
U_{2S}	Adjusted thermodynamic oxidation potential for small Pt particles (V)
U_{2L}	Adjusted thermodynamic oxidation potential for large Pt particles (V)
V	Volume of each cathode mesh (m^3)
V_i^{lab}	Variance of experimental data of catalyst mass, surface area, and radius
x	Distance away from the GDL/cathode interface into cathode or membrane (m)
X_i^{simu}	Simulated data of catalyst mass, surface area, and radius
X_i^{lab}	Experimental data of catalyst mass, surface area, and radius
α_{1a}	Anodic transfer coefficient of Pt dissolution reaction
α_{1c}	Cathodic transfer coefficient of Pt dissolution reaction
α_{2a}	Anodic transfer coefficient of Pt oxidation reaction
α_{2c}	Cathodic transfer coefficient of Pt oxidation reaction
ε_C	Nafion polymer or ionomer volume fraction in cathode
ε_M	Nafion polymer or ionomer volume fraction in membrane
Γ_{max}	Maximum Pt oxide coverage per surface area (2.18e-5 mol/m^2)
$\Delta\mu_{Pt}^{0}$	Fitted chemical potential shift for PtO (J/mol)
θ_S	Total surface oxide coverage at small Pt particles
θ_L	Total surface oxide coverage at large Pt particles
θ_{max}	Maximum surface oxide coverage at the top monolayer (=1)
θ_S^V	Pt oxide vacancy at the top surface monolayer of small Pt particles
θ_L^V	Pt oxide vacancy at the top surface monolayer of large Pt particles
ρ_{Pt}	Pt metal density (21090 kg/m^3)
ρ_{PtO}	PtO density (14100 kg/m^3)
σ_{Pt}	Surface tension of Pt nanoparticles (J/mol)
σ_{PtO}	Surface tension of PtO nanoparticles (J/mol)

ω	Pt-O dipole-dipole interaction coefficient (J/mol)

SUMMARY

The durability of carbon-supported platinum oxygen reduction electrocatalysts is one of the limiting factors for their commercial applications in PEM fuel cell cathodes. In this work, we applied both experimental and numerical tools to study Pt/C catalyst degradation mechanisms. An accelerated catalyst degradation protocol through cycling the cathode potential in a square-wave profile was applied to study cell performances, Pt/C catalyst ORR activity, and active surface area losses. Post-mortem analyses of cathode Pt particle size were conducted by X-ray diffraction. Changes of platinum distributions in CCMs were studied by SEM/EDS analyses with surface coated Au as the reference element.

The mechanisms of platinum deposition in membrane were investigated. It was confirmed by the SEM/EDS Pt distribution analyses that the deposited Pt atoms originated from the cathode. It was hypothesized that dissolved Pt ions from the cathode diffused into the membrane and were reduced by the permeated hydrogen from the anode. These deposited Pt atoms catalyzed the combustion of permeated oxygen and hydrogen. Pt band was predicted and experimentally confirmed at the location where the permeated hydrogen and oxygen completely reacted with each other.

An active research thrust for PEM fuel cells is the development of membranes for high temperature (above 80 °C) and low humidity operations. However a large tradeoff the benefits running fuel cell at relatively high temperatures was observed due to the

accelerated cathode degradation processes. And at low humidity conditions, the cathode degradation rate decreased due to the slow transport of soluble platinum ions in possible narrowed/limited water (or ionic) channel networks in polymer electrolytes.

From the Pt dissolution experiments in 0.5 M $HClO_4$ solution, large positive effects of holding potentials on dissolution rates and soluble Pt concentrations were observed. Without an external holding potential, Pt dissolution rate was orders of magnitude higher under the air condition than in a non-reacting nitrogen environment. However, the difference was less than 100% between the nitrogen and air environments at a holding potential of 0.8 V (vs. RHE). Hence we believed that at an open-circuit condition, platinum was oxidized by oxygen molecule and further dissolved in acidic electrolyte. While at closed-circuit conditions, both chemical and electrochemical oxidation and dissolution might be involved.

Platinum electrochemical oxidation kinetics was studied and simulated by cyclic voltammetry. In a simplified cathode degradation model, overall Pt particle growth by Pt mass exchange between small and large particles was clearly demonstrated through a favored Pt dissolution from small particles and Pt ion deposition onto large particles due to the particle size effect. The model also predicted the cycling upper potential and cycle frequency as the major positive effects on catalyst degradation, in an agreement with other literature results. We recommended further study of catalyst degradation especially on dissolution processes, and more durable electrode materials and an effective management of cell potentials will be needed to prolong cathode lifetime.

CHAPTER 1

INTRODUCTION

Fuel-cell technology was first demonstrated in 1839 by Sir William Robert Grove who converted hydrogen and oxygen into electricity using platinum electrodes and dilute sulfuric acid as the electrolyte [1]. More than a century later, fuel-cell technology attracts more and more attentions from chemistry to engineering, due to the fast growing global energy usage and environmental concerns. The first Polymer Electrolyte Membrane (PEM) fuel cell was developed by General Electric for a NASA space vehicle (Gemini program) in the 1960s.

Today hydrogen-air PEM fuel cells are considered as one of the most promising technologies for transportation applications, offering the high energy-conversion efficiency without greenhouse gas emission. Figure 1.1 shows an exploded view of a cell sandwich within a fuel-cell stack.

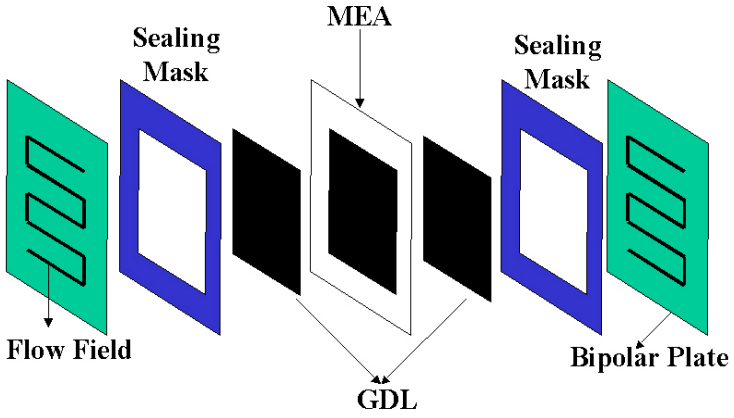

Figure 1.1: Illustration of PEM fuel-cell stack

The membrane electrode assembly (MEA) or catalyst coated membrane (CCM) consists of a thin film (25-175 μm) of proton-conductive membrane electrolyte covered with a catalyst layer (5-50 μm) on each side, serving as the anode and the cathode. One of the PEM fuel-cell technology breakthroughs [2] was the development of today's most common perfluorosulfonic-acid (PFSA) membrane Nafion®. The polymer molecule consists of a polytetrafluoroethylene (PTFE) backbone providing the chemical corrosion resistance, with perfluorinated-vinyl-polyether side chains terminated by sulfonate groups giving high proton conductivity. Another breakthrough technology [2] is the MEA preparation technique developed by Los Alamos National Laboratory [3]. In the so-called thin-film decal method, carbon-supported platinum catalyst ink is mixed with recast ionomers before being pressed onto the membrane. The recast ionomer network in the composite catalyst layer binds the catalyst particles together and forms a continuous pore-volume network for better proton transfer, which greatly reduces platinum loadings (from 5 mg/cm^2 to below 0.5 mg/cm^2).

Porous gas diffusion layers (GDL) cover both sides of MEA. The GDLs collect current and provide more uniform gas access to both catalyst layers. Hydrogen and oxygen (or air) gases are fed through flow channels in each bipolar plate. Electrochemical reactions take place on both the anodic and cathodic catalyst layer, producing electricity and water with protons transported through the membrane from the anode to the cathode. A series of such single cells can be connected to provide the required voltage, with the

bipolar plates shared by anodic hydrogen feeding one side and cathodic oxygen (or air) feeding the other side.

To commercialize the hydrogen PEM fuel-cell technology, the major technical gaps [4, 5] identified include material durability, cost and cell performance (efficiency, power density etc.). Many research efforts were diverted to improve fuel-cell performance and reduce cost, while durability issues have been reported much less frequently [6-9]. Just recently, more studies [10-15] and simulation [16, 17] work on fuel-cell degradation are being published.

In PEM fuel-cells, performance loss occurs principally through ionomer/membrane degradation, carbon-supported platinum catalyst degradation, and carbon support corrosion. During fuel-cell operation, the MEA is exposed to humid and chemically oxidizing & reducing environments. Membrane materials, especially the recast ionomers, are attacked by intermediate free radicals. This is partly confirmed by observing fluoride (F^-) and sulfate (SO_4^{2-}) ions in outlet water [12]. Severe chemical attack results in pin-hole formation [18] in membrane, greater cross-over of reactants and cell failure.

Carbon corrosion [19, 20] is accelerated by high potentials and can happen when the hydrogen fuel supply is insufficient (fuel starvation [21]) at anode, or partial hydrogen coverage [22, 23] during fuel cell start-up, shutdown or in case of water blockage. Other aggressive fuel-cell operating conditions, such as low humidity of

reactants [14] and thermal cycles [24], will accelerate one or more of the above degradation processes.

Catalysts are needed for efficient oxygen reduction and hydrogen oxidation. Carbon-supported platinum or Pt alloy nanoparticles are the most common catalysts for hydrogen PEM fuel cells. Platinum is one of the best oxygen reduction reaction (ORR) catalysts that are stable in acid. However, there is a small corrosion region of Pt in strong acidic media. A re-plot of the Pt^{2+} corrosion region in Figure 1.2, based on the thermodynamic equilibriums of Pt species [25] (reaction 1.1 to reaction 1.5) , shows the effects of electrochemical potential and pH at 25 °C in water. The shaded area in Figure 1.2 is the region of the Pt ions concentration higher than 10^{-6} mol/L. Decreasing pH will increase Pt ion concentration, whereas a medium potential range, for example around 1.0 V at pH of zero, gives the highest the Pt solubility. Low potentials limit the Pt dissolution reaction, and very high potentials also decrease the Pt ion concentration due to the formation of surface Pt oxide.

$$Pt + H_2O = PtO + 2H^+ + 2e^- \qquad \text{(Reaction 1.1)}$$

$$E_1 = 0.980 - 0.0591pH$$

$$PtO + H_2O = PtO_2 + 2H^+ + 2e^- \qquad \text{(Reaction 1.2)}$$

$$E_2 = 1.045 - 0.0591pH$$

$$Pt^{2+} + H_2O = PtO + 2H^+ \qquad \text{(Reaction 1.3)}$$

$$\log[Pt^{2+}] = -7.06 - 2\,pH$$

$$Pt = Pt^{2+} + 2e^- \qquad \text{(Reaction 1.4)}$$

$$E_4 = 1.188 + 0.0295 \log[Pt^{2+}]$$

$$Pt^{2+} + 2H_2O = PtO_2 + 4H^+ + 2e^- \qquad \text{(Reaction 1.5)}$$

$$E_5 = 0.837 - 0.1182\,pH - 0.0295 \log[Pt^{2+}]$$

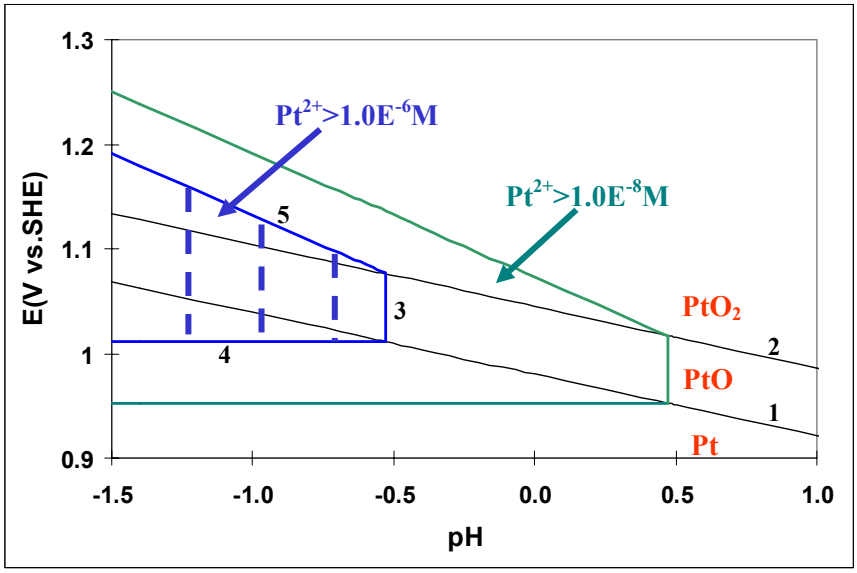

Figure 1.2: Pt corrosion region in pure water at 25° C

In fuel-cell vehicle driving conditions, cell potentials (or cathode potentials) change with the fuel cell power density output change. At a high open circuit voltage (OCV) under a vehicle idle condition, Pt dissolution rate is fast until accumulated Pt

surface oxides slowing down or blocking the dissolution process. At the reduced cathode potentials under the vehicle acceleration or high power demand conditions, surface oxides will be reduced and soluble Pt ions can be reduced back on Pt or carbon particles. So in such high-low potential cycles, catalyst degradation is accelerated with surface oxide reduced at the low potential phase and Pt dissolution taken place at the next high potential stage. It is generally believed that platinum nanoparticles are reconstructed through Pt dissolution and transport of ions of the soluble Pt in electrolyte. Also surface diffusion of Pt atoms was suspected to contribute to the Pt catalyst morphological changes. The catalyst degradation resulted in decreased cell performance and the loss of electrochemically active surface area (ECA) [6, 12, 13, 15, 26, 27].

This dissertation is focused on the carbon-supported platinum catalyst degradation mechanisms. The process of platinum deposition in Nafion® membrane is found to be related to hydrogen and air gas crossover in the membrane. Effects of temperature, relative humidity and oxygen partial pressures on Pt catalyst degradation are investigated. Detailed platinum dissolution mechanisms are preliminary investigated due to the complexity of possible multiple reactions involved and lack of effective analytical tools. Electrochemical reaction of platinum oxidation is experimentally studied and mathematical simulated. A mathematical model of Pt dissolution and soluble Pt ions transport in MEA is built to assist the understanding of catalyst degradation processes. In the next chapter, some important published studies are reviewed to further introduce and understand ORR platinum catalyst degradation processes.

CHAPTER 2

LITERATURE REVIEW

2.1 Platinum degradation experimental studies

2.1.1 Pt dissolution in a liquid electrolyte cell

The ionomer in the PEM fuel-cell electrode is strongly acidic with a proton concentration of around 1 M, depending on the number of side chains terminated with the sulfonate groups. For half-cell studies, an aqueous acid solution, such as sulfuric acid, is often used as the electrolyte to study platinum electrode dissolution. In these studies, the Pt electrodes were Pt wire, Pt foil, or carbon-supported Pt nanoparticles.

The equilibrium concentrations of platinum ions [Pourbaix diagram [25] platinum foil as electrode] were calculated from the Nernst equation ($E = E^0 + \frac{RT}{2F}\ln[Pt^{2+}]$: equation 2.1), with a standard potential (E^0) value of 1.188 V (vs. NHE) and a slope of 0.0295 V/decade at 25 °C. Bindra [28] studied Pt foil dissolution in 96 % phosphoric acid using a three-electrode liquid cell. The working electrode and the counter electrode were located in different compartments to prevent dissolved platinum ions from depositing on the counter electrode. Recently, Ferreira [29] studied the Pt nanoparticles solubility at different electrochemical potentials (0.9-1.1 V vs. NHE) in 0.5 M H_2SO_4 solution at 80 °C. The platinum ion concentration was determined by inductively coupled plasma mass spectroscopy (ICP/MS) method with a detection limit of 10 ng/g (ppb) Pt ion. According

to their report, the platinum ion concentration reached a pseudo steady level in 50-100 h. All of the studies showed a positive relationship between Pt ion equilibrium concentration and potential. The slope of Pt ion equilibrium concentration plot against potential in Bindra's study was very close to the predicted values (RT/2F) by the Nernst equation, whereas the slope in Ferreira's study was ten-fold smaller than that of predicted by the Nernst equation. The Pt ion concentrations that Ferreira *et al.* measured were higher than the interpolated data based on Pourbaix and Bindra's data when potentials were lower than 0.95 V. It was argued that: 1) carbon supported Pt nanoparticles were used instead of the polycrystalline platinum foils in Pourbaix [25] and Bindra's [28] experiments; 2) some Pt oxide may be soluble in the solution. In a similar study by Wang [30], both Pt wires and high-surface area 10 wt.% Pt/C on Teflonized carbon cloth (E-TEK, 0.5 mg_{Pt}/cm^2) gave the same equilibrium Pt ion concentration (about 1.0×10^{-8} M) in perchloric acid ($HClO_4$) at a potential of 0.9 V (vs. SHE) and 23 °C, which was nearly two orders of magnitude higher than the value predicted by the Nernst equation. For Pt wire, the concentration of Pt ions increased with potential from 0.65 V to 1.1 V, then started to decrease with further increasing potential. The above results are compared in Figure 2.1.

When the potential is higher than 1.0 V, Wang [30] explained that a significant fraction of surface Pt atoms are oxidized, thus blocking the electrochemical dissolution of platinum. Platinum oxide could go through chemical dissolution to generate Pt ions, but this reaction was believed to be extremely slow by Darling and Meyers [16]. So reaching the true equilibrium between platinum metal and its soluble ion was retarded by the

formation of platinum oxide on the metal surface and the slow rate of chemical dissolution of Pt oxide. At this point, there are no clear explanations of the above phenomena.

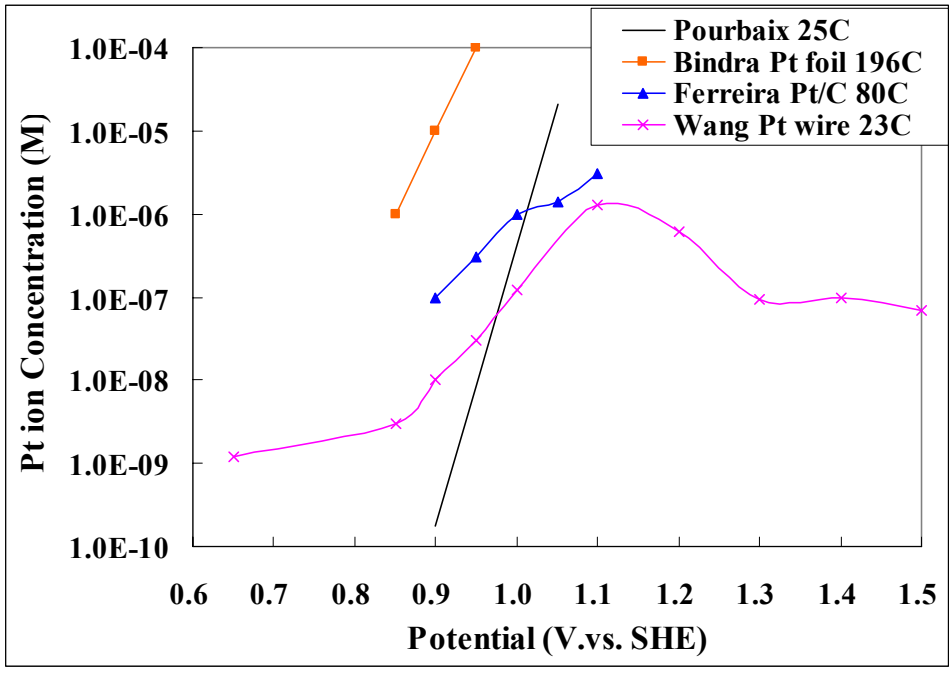

Figure 2.1: Re-plot of Pt ion equilibrium concentrations with potential in literature

In addition to the study of platinum dissolution at constant potential, Pt dissolution under potential cycling was investigated on wires and smooth sheets of Pt. The rate of Pt dissolution [31, 32] and the Pt electrode surface area loss [33] were reported. Later, Kinoshita [27] compared three different kinds of electrodes: Pt sheet electrode, unsupported Pt black electrode (25 m^2/g Pt), and 5 wt.% Pt electrode (93 m^2/g Pt) supported on graphitized carbon. A three-chambered cell was used with the working electrode (in 1 M H_2SO_4 at 23 °C) and the counter electrode separated by a porous glass frit. The concentration of Pt ion was determined colorimetrically. Both square and

triangular wave forms (1 cycle/min) were applied, with a lower potential of 0.05, 0.4 or 0.5 V and an upper potential of 1.0, 1.2 or 1.4 V (vs. NHE). Kinoshita's results [27] showed that the Pt ion concentration increased with the number of potential cycles, but with a reduced rate of Pt dissolution. The Pt sheet electrode yielded the highest Pt ion concentration (μg/geometric area), while the carbon supported Pt electrode gave the lowest value (only about 1% of the former). This was explained by the high chance of recapture of soluble Pt ions for reduction (replating) in the porous structure of carbon-supported Pt electrode. The square wave potential cycling yielded a more than 50 % lower Pt ion concentration compared to the triangular wave cycling, which was explained due to the fast Pt ions replating in the square wave cycling with the lower reduction potential than the average reduction potential in the triangular wave.

2.1.2 Pt catalyst degradation in PEM fuel cell electrode

Most studies support two degradation routes causing the catalyst metal-cluster agglomeration/growth (coarsening): Pt dissolution/replating process [10, 12, 13, 15], and possible Pt atom surface diffusion [12, 13]. The platinum nanoparticles coarsening caused by surface diffusion may not be significant under the typical low-temperature condition of PEM fuel cells (<100 °C), especially supported on relative "sticky" carbon.

Yu [15] studied the Pt/C catalyst stability under potential cycling in PEM fuel-cell electrode at 65 °C, 100% relative humidity (RH), and atmospheric gas pressure of hydrogen (anode) and nitrogen (cathode). Potential cycling was applied using a square wave between 0.87 V and 1.2 V vs. Reference Hydrogen Electrode (RHE) with a time

step of 30 seconds at each potential level. The measured potentials at 0.1 A/cm^2 of the fuel cell flowed with pure hydrogen (500 sccm) and oxygen (1000 sccm) decreased linearly with the number of potential cycles. At the same time, ECA values decreased rapidly from an initial value of 67 m^2/g_{Pt} during the first 400 cycles and then nearly leveled out at 33 m^2/g_{Pt} after 2800 potential cycles. Post test analysis showed a "band" of Pt metal in the membrane near the cathode, which clearly showed soluble Pt ions transported into membrane phase, mainly by diffusion. These Pt atoms are no longer electronically connected and thus not available for hydrogen oxidation reaction (HOR) and oxygen reduction reaction (ORR) reactions. The Pt mass loss from the cathode was permanent.

In another study by Xie [13], a long-time (1000 h) constant-current (1.07 A/cm^2) experiment was conducted at 80 °C, 100 %RH and 2.8 atm absolute gas pressure (hydrogen and air), using the lab-made MEAs with a Pt/C anode and a Pt_3Cr/C cathode. It was found that the Pt_3Cr particles and agglomerates were transported towards membrane phase reaching the cathode edge. But no Pt or Cr particles were observed in the membrane near the cathode side. The anode Pt/C nanoparticles showed the similar coarsening behaviors with Pt/C particles migrating towards the middle of the membrane forming a Pt rich zone (about 200 nm width) with rectangular large Pt crystals (20 nm) in the anode near the membrane phase. Interestingly, Pt particles were observed and confirmed by energy-dispersive X-ray spectroscopy in the membrane phase up to 3 μm from the anodic electrode after 1000 h of testing. The exact mechanism of anode Pt migration into membrane was not clear. The authors argued that the Pt nanoparticles have

much different physical and chemical properties from the bulk materials. So Pt redox potential could have a shift of –1.0 V (without the detailed explanation), with the resulted the thermodynamic equilibrium potential for Pt nanoparticles only around 0.03 V (vs. SHE). But Darling and Meyers [16] estimated that the potential shifts only by 0.038 V from the Kelvin equation (equation 2.2). The latter estimation seems more likely since the simulated Pt oxidation and Pt oxide reduction peak potential-location was validated by the measured cyclic voltammetry (CV) curve.

$$U = U^{\theta} - \frac{\Delta\mu_{Pt}}{2F} = U^{\theta} - \frac{1}{2F} \times \frac{\sigma_{Pt} M_{Pt}}{r \rho_{Pt}} \qquad \text{(Equation 2.2)}$$

Where, U^{θ}: thermodynamic equilibrium potential of bulk Pt (1.188 V)

σ_{Pt}: surface tension 2.37 J/m^2 (authors' personal communication with J. Bett)

M_{Pt}: molecular weight of Pt (195 g/mol)

r: radius of spherical Pt nanoparticle (3 nm)

ρ_{Pt}: density of Pt (2100 kg/m^3)

In another investigation by Ferreira [29], lifetime test at both OCV (open circuit voltage) and a constant-current (0.2 A/cm^2) for 2000 h were conducted on commercial MEAs with two 15-cell short stacks (800 cm^2 active area) at 80 °C, 100 % RH and 150 kPa$_{abs}$ gas of H_2 and air at the anode and the cathode. Both stacks experienced a rate of decay of 20 μV/h and 25 μV/h for OCV and 0.2 A/cm^2 lifetime tests, respectively. The ECA loss at the cathode in the OCV test was much faster than in the constant-current test

due to the faster Pt dissolution at the higher potential in the author's opinion. A "Pt band" was observed by SEM-EDS near the cathode/membrane interface in a MEA cross-section specimen after 2000 h of OCV testing. Once again, this confirmed Pt transportation from catalyst electrode into membrane phase at H_2/Air operation, similar to the H_2/N_2 potential cycling conditions in Yu's study [15]. Unfortunately, the detailed Pt deposition in the membrane and catalysts coarsening under these lifetime tests were not fully investigated.

In the same study by Ferreira [29], the accelerated degradation test (ADT) by 10,000 potential cycles between 0.6 and 1.0 V (vs. RHE) with a sweep rate of 20 mV/s was conducted using 100 % RH H_2/N_2 at 80 °C. The cathode active surface area (ECA) decreased with more potential cycling, from 63 to 23 m^2/g_{Pt} (almost leveled out). X-Ray diffraction with a small incidence angle allowed the separate analysis of Pt nanoparticles in the anode and the cathode. A volume-average Pt crystal size of 2.3 nm was calculated using the Scherrer equation for the fresh Pt catalyst powder. For the cycled MEA, the averaged particle size (diameter) increased to 3.9 nm and 10.5 nm in the anode and the cathode, respectively. The difference between the anode and the cathode was expected due to the higher Pt dissolution rate in the cathode with the higher potential.

The Pt particle size distributions were determined by TEM image analyses (not counting the non-spherical particles on carbon) at four different locations: 1 μm, 4 μm, 7 μm and 10 μm depth inside the cathode layer (towards the middle of the membrane). It was found that nearly all particles were supported on carbon at the location of 1μm away from the cathode surface. The particles with sizes larger than 10 nm were those deposited

in ionomer. The integrated area under the simulated Gaussian distribution (for Pt particles smaller than 10 nm) represented the Pt particle weight on carbon. The weight ratios of Pt on carbon decreased from 100 %, to 67 %, 60 % and 36 % at 1 μm, 4 μm, 7 μm and 10 μm locations, respectively. The Pt mass loss into the ionomer was proposed due to the micrometer-scale processes of Pt dissolution/replating and hydrogen reduction platinum ions. Besides the Pt loss into the ionomer, additional ECA loss was ascribed to Ostwald ripening which represents the diffusion process of Pt atoms on carbon support from one Pt particle to another. It was found that Ostwald ripening and dissolution/replating process equally contributed to the overall cathode averaged surface losses. Certainly this estimation depends on accuracy of TEM image analysis, which is limited by the areas (or the number of particles) analyzed.

The most recent study of Pt catalyst by Yasuda [34] investigated the Pt dissolution and deposition in PEM fuel cell by potential cycling. The TEM images revealed that Pt deposited at the cathode/membrane interface after 500 potential cycles under H_2/N_2 (anode/cathode) gas conditions. But no Pt band was observed in the membrane, which was different from Yu's study [15]. The author explained that it was due to the extremely low Pt ion concentration, and the higher tendency for soluble Pt to be replated on previously deposited Pt atoms for continuous Pt particle growth instead of Pt nucleation process forming new unstable Pt clusters. At the anode side, no deposition of Pt in the ionomer or the membrane phase was observed.

To study hydrogen and oxygen effects on Pt deposition, different gas combinations (N_2/N_2, H_2/air and H_2/N_2) were investigated. For N_2/N_2 case, the MEAs (Nafion® 117 as the membrane) had no Pt in the anodic carbon electrode and a standard hydrogen electrode was used as the reference electrode to regulate the cathode potential cycling. So the anode potential in nitrogen was not regulated and rose to a higher level than the other cases in hydrogen. The potential cycling range in N_2/N_2 case was 0.15-1.2 V (instead of 0.0-1.2 V to prevent hydrogen generation), while for the other two cases potential cycling ranges were both 0.65-1.2 V. It was found that Pt deposition occurred only in the anode (no Pt deposition in the cathode and the membrane) for the N_2/N_2 potential cycling test. The observed Pt in the anode confirmed the Pt ions transportation through the membrane and the electrochemical reduction of Pt ions in the anode. This also partially supported the Pt deposition by hydrogen reduction in a way of chemical reaction in the cases of flowing H_2 at the anodes. In fact, after the H_2/Air potential cycling, the deposited Pt atoms were found in the membrane 20-25 μm away from the cathode, instead of at the cathode/membrane interface. This suggested that a high concentration of oxygen suppressed the Pt deposition location away from the cathode/membrane interface. The detailed mechanisms, however, were not fully explained.

Dissolved Pt ions were detected in the cathode effluent flow during the constant current lifetime tests by Xie [12]. But in another Pt/Co/C liquid cell study by Yu [15] in 0.1 M $HClO_4$ solution, Pt ions were not detected by inductively coupled plasma (ICP) after 3200 potential cycles. This might be caused by the concentration of Pt ions below

the ICP detection limit due to the enhanced stability of Pt/Co alloy catalysts. The above studies suggest that Pt dissolution/replating processes is major contributor of catalyst degradation under the potential cycling conditions, whereas the catalyst coarsening by surface diffusion process could be also involved in the constant-current lifetime tests.

2.2 Mathematical modeling of platinum catalyst degradation

Darling and Meyers [16] simulated Pt dissolution and oxidation in a PEM fuel-cell with a supported Pt cathode. The model was a spatially lumped system with ionomeric solution filled in the porous Pt electrode. Neither mass transport nor a distribution of reaction-rate was included. The model allowed the spherical Pt particle growth and/or shrinkage with the involved reactions including Pt electrochemical dissolution, Pt electrochemical oxidation with water, and PtO chemical dissolution with proton. The Pt oxidation was the dominant reaction with a cathodic term of Butler-Volmer equation included to describe Pt oxide reduction, in addition to the anodic oxidation term only in the previous simulation work of Pt oxide growth [35-37]. The chemical dissolution rate of PtO was set to be extremely low (neglected). Since the Pt catalyst are carbon supported nanoparticles, a surface tension adjustment was applied on the thermodynamically equilibrium potentials by the Kelvin equation (Equation. 2.2) for Pt electrochemical dissolution. A similar adjustment for Pt Oxidation potential was also made. General mass balances were applied for Pt^{2+}, Pt, and PtO.

The Pt oxidation reaction rate constants were obtained by fitting parameter for the simulation to a cyclic voltammetry (CV) experiment. When the potential reaches 1.1 V, the surface was covered with a monolayer of platinum oxide, which agreed with Wang's study [38]. The equilibrium Pt ion concentration was determined by the steady state of Pt electrochemical dissolution before the complete monolayer oxide coverage blocking Pt electrochemical dissolution, while the steady state of both Pt oxidation and PtO chemical dissolution reactions determined the Pt equilibrium concentration beyond a monolayer oxide coverage. The simulated Pt ion equilibrium concentration kept increasing up to 1.1 V, then decreased sharply and nearly leveled out at 1.2 V. These features were similar to those observed in Wang's study [38], although the maximum Pt ion concentrations and peak locations were not same due to the differences in the two systems.

Recently Darling and Meyers [17] built a 1-D transient isothermal Pt degradation model with the features of Pt dissolution/oxidation and transport of the Pt ions in regions of the cell: anode GDL, anode catalyst layer, membrane, cathode catalyst layer, and cathode GDL. Porous electrode theory was used to model the anode/cathode catalyst layers. Water flow in membrane was neglected and a uniformly saturated membrane phase was assumed. General fuel/oxidant and Pt species (Pt, Pt^{2+}, PtO) mass balances were included with Pt ion transport by diffusion and migration. A simplified particle size distribution (PSD) was applied in the model. Only two different sizes (radii) of particles with the fixed ratio of small and large particle numbers were assumed. Both particle radii were allowed to change and the number density of each type particle was constant in this model. Total surface area and total Pt mass were kept constant, giving an estimate of the

average particle radius normalized to a uniform particle size distribution. The ECA was calculated from the average particle size and the Pt number density.

The simulated results showed that the Pt nanoparticles had the uniform size decrease across the cathode layer, while there was a particle size increase at the anode/membrane interface due to the interface deposition of Platinum transported from the cathode. The 400 h potentiostatic holds at 1.05 V yielded about 30 % ECA loss, and the loss rate slightly increased with time due to the faster platinum dissolution rate at smaller catalyst particles at the cathode, but this concavity was not observed in experiments. It was thought due to the neglected catalyst sintering in the model. Another possible explanation is that the potential offset modeled with the Kelvin equation was not correct. The model predicted the ECA loss rate of 1.11 m^2Pt/g/h at 2 seconds of potential cycling period, which was the double of the loss rate at the period of 60 seconds (0.55 m^2Pt/g/h). But the model over-predicted the rate by a factor of two to three, compared to the measured ECA loss rates.

More importantly, in PEM fuel cells the Pt depositions were located at the cathode/membrane interface or in the membrane depending on the gas at the cathode [13, 15, 29, 34]. The modeled Pt deposition location in anode [17] was more closely representing the degradation process in a phosphoric acid fuel cell. Also a more reasonable particle size distribution (PSD) may be applied instead of a simplified bimodal PSD.

CHAPTER 3

EXPERIMENTAL PROCEDURES AND ANALYTICAL TECHNIQUES

In this chapter, all testing instruments including the fuel cell test station and Pt dissolution liquid cell will be described. Detailed fuel cell testing procedures including the protocol for Pt catalyst degradation will be provided. Both in-situ and ex-situ catalyst characterization techniques are also discussed.

3.1 Fuel cell test station

All fuel cell tests were conducted on the 890CL Teledyne Energy System fuel cell test station. Cylinder nitrogen (Ultra High Pure grade from the Airgas Inc., Atlanta) was used as the purge or nonreacting gas on both the cathode and the anode sides. Hydrogen fuel (Ultra High Pure grade from Air Products and Chemical, Inc.) was continuously supplied from the hydrogen storage facility located in the Bunger-Henry research building. The fuel cell test station and the test article (fuel cell assembly) were located under a gas ventilation hood designed specifically for hydrogen operation. One hydrogen sensor is located in the hood exhaust, and two others are outside the hood in the research lab for safety purposes. Cylinder air (ultra zero grade from Airgas Inc., Atlanta) or cylinder pure oxygen or 50 % O_2 in N_2 (Ultra High Pure grade from Airgas Inc., Atlanta) was used as oxidant on the cathode side. Other special gases including 4 % H_2 in N_2 were also purchased from Airgas (Atlanta) with the highest grade of purity.

Flow rates of dry gases were controlled with mass flow controllers. The maximum flow rates of the controllers were 2000 sccm for hydrogen and 5000 sccm for air or oxygen. Anode and cathode gases can be fully humidified by passing through two separately controlled gas bubblers as shown in Figure 3.1. The gas connecting lines between humidifiers and fuel cell assembly were kept as short as possible, and the line temperatures on both anode and cathode sides were set 5 °C higher than the humidifier temperatures to prevent water condensation. Anode and/or cathode gases can also bypass the humidifiers to supply the fuel cell with dry gases (not shown in Figure 3.1). The fuel-cell assembly is temperature controlled, and relative humidity (RH %) of gas established by the humidifier temperature and the cell temperature. The gas pressure on each side can be raised up to 200 kPa above atmospheric pressure by adjusting a back pressure regulator. Fuel cell tests were normally conducted at atmospheric conditions unless noted with the backpressure levels. The Fuel cell test station was controlled and testing data were collected by software FuelCell v3.6 from the Scribner Associates, Inc.

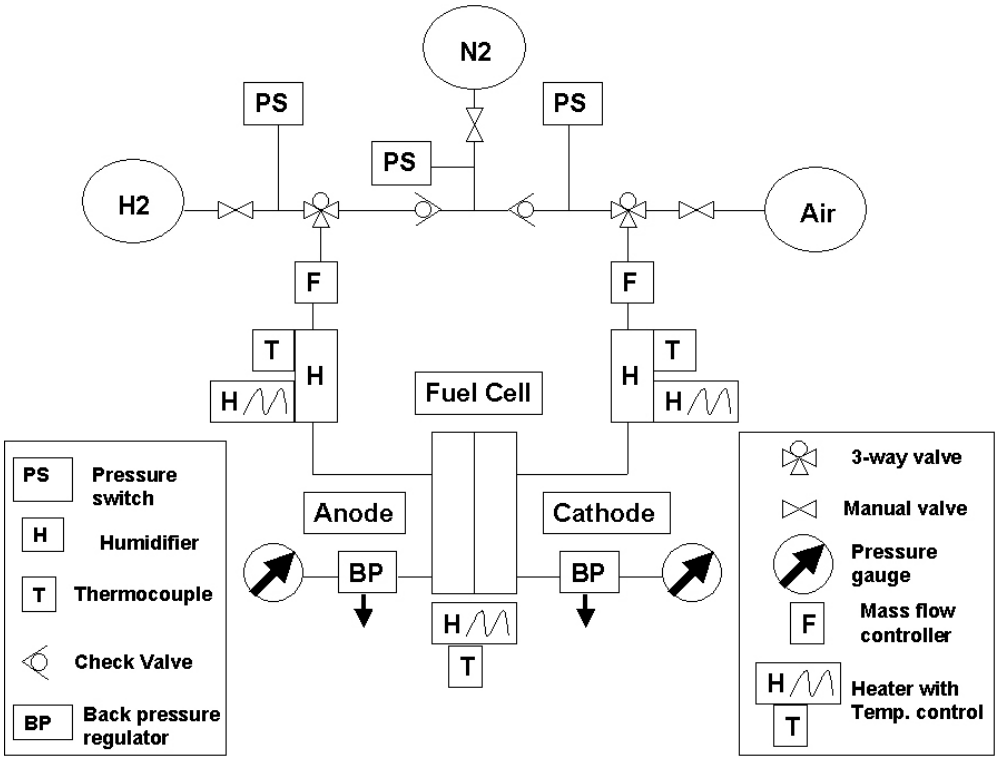

Figure 3.1: Fuel cell test station (890CL Teledyne Energy System) control loop

3.2 Single PEM fuel cell stack assemble

Commercial catalyst coated membranes (CCMs: 5×5 cm catalyst areas) were used in this dissertation work with Pt catalyst loadings: 0.3(anode)/0.5(cathode) mgPt/cm^2 in Nafion® 111 CCMs from DuPont or 0.3(anode)/0.3(cathode) mgPt/cm^2 in Nafion® 117 CCMs from the Fuel Cell Store, Inc. Both sides of a CCM were covered with gas diffusion layers (GDLs) from E-TEK. The three pieces were aligned between two graphite cellblocks with parallel flow channels for gas distribution. The Fuel Cell hardware (Figure 3.2) was purchased from the Fuel Cell Technology, Inc. PTFE coated fiberglass gaskets (from the Saint-Gobain Performance Plastics) were placed around a

membrane electrode assembly (MEA) for the sealing purpose. A torque of 5.65 N.m (50 lb.in) was applied to tighten the assembling bolts and keep uniform compression over the assembly.

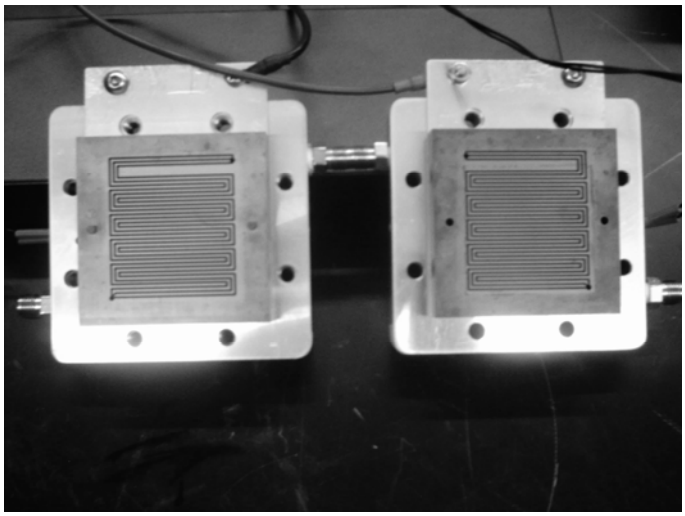

Figure 3.2: Fuel cell hardware from Fuel Cell Technology, Inc.

3.3 Accelerated catalyst degradation test protocol

Potential cycling tests were used to accelerate catalyst degradation. The approach was to separate catalyst degradation from membrane and other components degradation processes. Currently there is no standard accelerated degradation test (ADT) for PEM fuel cells. US Fuel Cell Council released a protocol on fuel-cell component testing in 2004 [39]. And General Motor proposed a 600 h catalyst square-wave potential cycling between 0.7-0.9 V (IR free) with a time step of 30 seconds for the Department of Energy (DOE) funded projects in 2006. Maximally following these guides and considering our

lab equipments, we designed an accelerated catalyst degradation test by potential cycling for this dissertation study.

Each fuel cell test started with wet-up and conditioning procedures that were slightly different for each of two kinds of CCMs with very different performances (Appendix A). Following CCM conditioning, the cell potential was cycled using a Potentiostat/Galvanostat (EG&G Princeton Applied Research 273A). Typically a square-wave that alternated between a high and a low potential level (such as between 0.87 and 1.2 V vs. reference hydrogen electrode (RHE)) was used. The anode served as both reference and counter electrodes. The cell temperature was typically in the range of 40-80 ºC with fully or partially humidified gases on both anode and cathode side. Gas humidity was controlled by setting the water temperature in each humidifier. Testing conditions are listed in Appendix B for all CCMs. Potentiostat control and data acquisition was accomplished with Corrware Software 2.8d1 (Scribner Associates Inc.). Non-destructive diagnostic tests (such as polarization curves, electrochemically active surface area (ECA) measurement, and the rate of hydrogen permeation) were conducted during the degradation test. Destructive post-mortem tests after degradation test (such as SEM, XRD, etc.) were used to characterize material structure changes. In some tests, waste water from the anode and cathode was collected to measure levels of soluble Pt and F ion by inductively coupled plasma mass spectroscopy (ICP/MS) and ion chromatography, respectively. All tests procedures and methods were detailed in chapter 3.5.

3.4 Liquid electrolyte electrochemical cell and dissolution experiment

A three-electrode, two-compartment H-cell similar to that described in the literature [28, 29, 38] was built to study Pt electrode dissolution in aqueous acidic solutions. The reference and counter electrodes were separated from the working electrode compartment by a glass frit. The working electrode was Pt gauze purchased from Sigma-Aldrich (100 mesh, 99.9 % pure). A mercury-mercurous sulfate (Hg/Hg_2SO_4 with saturated K_2SO_4) electrode (from Radiometer Analytical) was used as the reference electrode with a gold wire (Sigma-Aldrich, 99.99 % pure) counter electrode. Diluted $HClO_4$ solutions (0.5 M) were prepared from trace-metal pure 70 % acid (Fisher Scientific) with high purity 18 MΩ Millipore de-ionized water. The concentrations of Pt ions were very low (typically 10 pg/g to hundreds of ng/g level), and therefore the induced liquid junction potential is small.

Before the dissolution experiments, the Pt mesh electrode was electrochemically cleaned in 0.5 M $HClO_4$ repeatedly by 10 cycling potential cycles between -0.65 V and 0.4 V (vs. Hg/Hg_2SO_4 reference electrode) with a scan rate of 50 mV/s under the UHP nitrogen protection at room temperature (around 23 °C). Then the Pt electrode was removed and soaked in high purity 18 MΩ de-ionized (D.I.) water for 10 minutes with water exchanged several times. Next, the electrode was rinsed again with D.I. water and placed in another clean H-cell for the dissolution experiments. The electrolyte was stirred with a Teflon stir bar, and either nitrogen (UHP grade from Airgas, Atlanta) or air (ultra zero grade from Airgas, Atlanta) bubbled in the working-electrode chamber solution. Samples before and during the dissolution tests (either electrochemical dissolution or chemical dissolution) were collected and subjected to ICP/MS testing for Pt

concentration determination. The total acid solution was replenished by adding fresh solution during the dissolution tests.

3.5 Analytical techniques

3.5.1 Polarization curve and cell resistance

Fuel cell performance curves were measured in a constant current density (galvanic) mode. The cell temperature was 80 ºC, and fuel and oxidant gases were fully humidified. Anode and cathode line temperatures were set at 85 ºC. Hydrogen and air flow rates were 950 sccm and 3640 sccm, respectively. A fuel-cell polarization curve is obtained from the following procedure.

(a) With the load disconnected, purge the cell with N_2 for 15 minutes. Then switch to the fuel and oxidant gas flows, and apply a load (200 mA/cm^2). Run the cell for 15 minutes.

(b) Remove load only, wait 15 minutes for the system to stabilize. The average cell potential is recorded as the Open Circuit Voltage during the last 5 minutes testing.

(c) Then increase the current density, measure the cell potentials (and iR drop potentials) typically at 20, 30, 50, 100, 200, 500, 800, 1000 (mA/cm^2) values of current density. Normally, the test is stopped when the potential falls below 0.3 V. Similarly, report the average cell potential in the last 5 minutes during each 15 minutes testing.

The ohmic polarization (iR drop) was measured by the current-interrupt technique using software FuelCell for Windows™ V3.6 (the Scribner Associates, Inc.). Cell

resistances (ohm cm^2) were calculated in the range of the current densities between 0 and 100 mA/cm^2.

3.5.2 Gas crossover rate

The rate of hydrogen permeation (colloquially referred to as crossover) was determined by measuring a limiting current. During the test, hydrogen and nitrogen flowed at the anode and the cathode, respectively. Using a potentialstat, the potential of the cathode (working electrode) was slowly scanned from OCV (around 0.1 V vs. RHE) to 0.4V (vs. RHE) and held at 0.4 V (vs. RHE) to measure the pseudo-steady limiting oxidation current (mA/cm^2), which was used to calculate the rate of H_2 crossover ($mol/cm^2/h$). For the crossover tests in Chapter 4 to study Pt deposition location in membrane, the gas flow rates were 0.1 dm^3/min for hydrogen and 0.3 dm^3/min for nitrogen at the cell conditions of 65 ºC and 100 % RH. For all other tests in this dissertation on the purposes of monitoring membrane degradation and correcting the current density of catalyst activity at 0.9 V, the gas flow rates were 0.38 dm^3/min for hydrogen and 0.91 dm^3/min for nitrogen at 80 ºC and 100 % RH.

The permeation rate of oxygen molecule (in air) was measured by SRI-8610C gas chromatography (GC) with dry N_2 (0.1 dm^3/min) at the anode and 100 % RH air (0.3 dm^3/min) at the cathode. Both gases were at atmospheric pressure, and the cell temperature was 65 °C. The oxygen background in pure nitrogen was also tested. Both oxygen and nitrogen calibration curves at proper gas concentration ranges were prepared. Nitrogen effluents at the anode were sampled with a 1 cm^3 syringe for GC tests. The

oxygen volume percentages in N_2 effluents were determined, which were multiplied by the nitrogen flow rate (0.1 dm^3/min) and divided by CCM area (25 cm^2) to calculate the oxygen crossover rates (mol/cm^2/min) using the ideal gas law. Both hydrogen and oxygen crossover tests were repeated three times.

3.5.3 Electrochemically active surface area measurement

Electrochemically active surface areas (ECAs) of the cathode and/or the anode were measured by cyclic voltammetry (CV) at a sweep rate of 10 to 50 mV/s. Fully humidified 4 % H_2 in N_2 was supplied to the fuel cell anode, which served as the reference and the counter electrode. The gas channels of the working electrode were filled with D.I. water. The measured current in a CV curve was adjusted by the charging or de-charging current in the potential range of 0.4-0.5 V (vs. 4 % H_2 RHE). ECA (m^2/g_{Pt}) values were calculated by integrating the hydrogen adsorption charge on platinum, which was divided by a value of 210 μC/cm^2 (assuming hydrogen monolayer adsorption on the Pt surface) and further divided by catalyst loading (mg_{Pt}/cm^2). The cell temperature was typically at room temperature (around 23 ºC).

Instead of applying pure hydrogen, 4 % H_2 in N_2 was used to minimize the hydrogen crossover current. There was always small amount of dissolved oxygen in the deionized water, which resulted in a small negative oxygen reduction current at low potential region. But this negative current was eliminated when removing charging/de-charging current, since it does not change with potentials in the hydrogen adsorption region. Fully humidified pure nitrogen instead of deionized water could also be used in

the working electrode side, but resulted in less peak resolution in the hydrogen adsorption region of the CV curves. In this dissertation work, we preferred to apply 4 % H_2 and deionized water to measure electrode surface areas.

The electrochemically active surface areas (ECAs) of the Pt mesh electrode for dissolution tests were calculated by the last cyclic voltammetry curve in the electrochemical cleaning procedure before each dissolution test. Since the hydrogen adsorption and evolution peaks were not resolved well, an average ECA value was calculated from both hydrogen desorption and adsorption (down to -0.6 V vs. Hg/Hg_2SO_4 reference electrode) regions with charging/de-charging currents removed.

3.5.4 Catalyst activity

To characterize Pt/C catalyst activity, the current density at a cell potential of 0.9 V was measured for 15 minutes. Current densities measured in last three minutes were averaged as the reported values. The cell temperature was 80 ºC, and pure hydrogen and oxygen were fully humidified with flow rates of 1.0 dm^3/min and 2.0 dm^3/min, respectively. The measured current density was corrected by a hydrogen crossover limiting current density. Catalyst mass activity (A/gPt) was calculated by dividing the corrected current density (A/cm^2) by catalyst loading (gPt/cm^2). Specific activity (A/m^2Pt) was calculated by dividing mass activity (A/gPt) by the electrode electrochemically active surface area (m^2/gPt).

3.5.5 Inductively coupled plasma mass spectroscopy

Inductively coupled plasma mass spectroscopy (ICP/MS) was used to study Pt ion concentration in anode/cathode exhaust water streams or in acidic solution for the study of Pt dissolution in an electrochemical cell. For any water sample, 2.928 ml of sample was mixed with 0.060 ml of concentrated nitric acid (trace-metal grade from Fisher Scientific) and 0.012 ml 40 pg/g (ppt) multiple internal standard 2 % HNO_3 solution (including Bi, Ho, In, Sc, Tb and Y). For any $HClO_4$ solution sample, 0.030 ml of sample was mixed with 2.958 ml 2 % nitric acid (prepared from the concentrated trace-metal grade nitric acid from Fisher Scientific) and 0.012 ml 40 ppt multiple internal standard solution. Element Bi^{209} was selected as the internal standard. Varied Pt concentration solutions were prepared from a standard 1000 mg/L Pt in 10 % HCl solution (from SPEX CertiPrep Ltd) for calibration purposes in each group of tests. All samples were subjected to two runs of tests with the averaged values of counts per second (cps) reported. The Pt ion detecting limit of the instrument is about 1 parts per trillion (ppt).

3.5.6 F ion concentration by ion chromatography

Concentration of fluoride ions in the effluent water from the anode and the cathode were measured using ICS-2000 Ion Chromatography System (Dionex Corporation) to calculate F ion emission rates ($\mu g/h/cm^2$) and the cumulative F loss ($\mu g/cm^2$). Various F ion concentration solutions were prepared from a standard fluoride solution (from Ricca Chemical) for the calibration purposes.

3.5.7 SEM sample preparation and elemental analysis

Cross-sections of CCMs or MEAs were set vertically in metal mounting clips and set in epoxy resin (from Ted Pella, Inc.) for about 24 hours at 80 ºC as shown in Figure 3.3. The specimen was polished by four grades of silicon carbide polishing papers (from Struers, Inc.) in an order of #120 grade, #500 grade, #1200 grade and #4000 grade. Then its surface was coated with a uniform thin layer of gold by a gold sputter coater (International Scientific Instruments).

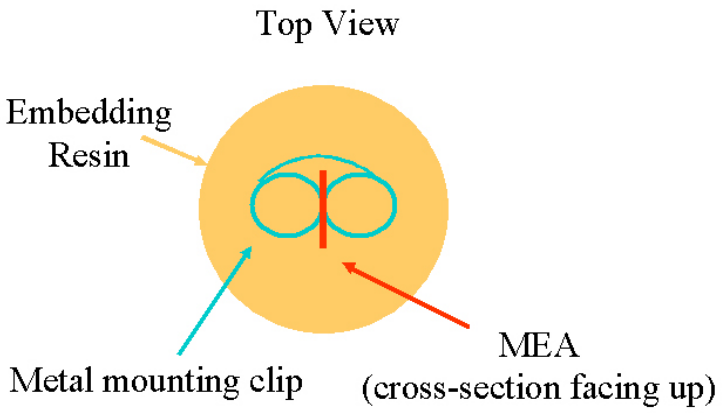

Figure 3.3: MEA cross-section specimen in resin

To estimate the quantity of Pt atoms deposited in the membrane after potential cycling, SEM-EDS Pt element quantification analyses were conducted at the anode, the cathode and the formed Pt "band" regions of the CCM cross-section samples. Since the deposited gold film on sample surfaces were very uniform at least at a micrometer level, the mass ratios of Pt to Au were used to estimate the Pt mass percentage distributions in the anode, cathode and Pt "band" regions with the reference metal of Au. Both La lines of Pt and Au were applied to determine the elements (La=9.44 keV for Pt and 9.71 keV for Au). The overlapping of Pt and Au peaks is not severe as shown in Figure 3.4 as one

example. A Hitachi S-800 FE SEM equipped with a Kevex Energy Dispersive Spectroscopy (EDS) detector was used to examine the Pt distribution across these specimens with an acceleration voltage of 15 KeV. For each region (anode, cathode and Pt "band"), its width (10 tests) and Pt/Au atomic ratio (5-10 tests) were measured. Overall Pt atom percentages distributed in different regions were estimated by the Pt/Au atomic ratios weighted by the width of the region.

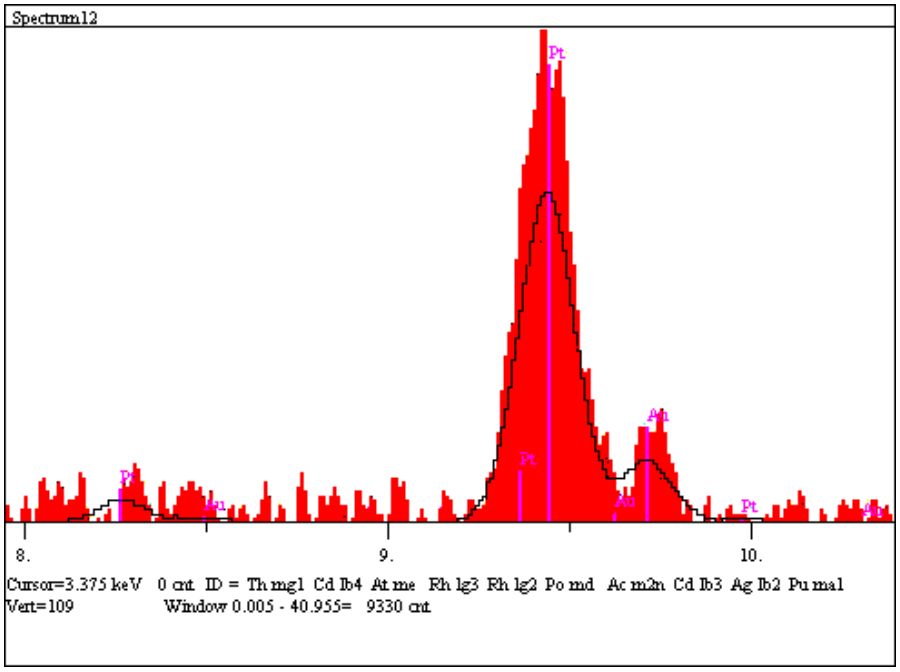

Figure 3.4: Pt and Au La peaks in SEM-EDS experiments

3.5.8 X-ray diffraction

To characterize thin cathode catalyst layer (around 10 microns) in CCMs, grazing angle mode X-ray diffraction (K_α Cu anode) with 1° or 2º angle of incidence was typically applied allowing no significant X-ray penetration into membrane separator. To

detect deposited Pt at the cathode/membrane interface or inside the membrane, X-ray incidence angle was increased up to 20 degrees. A un-mounted quartz sample holder (32mm diameter from Gem Dugout) with a CMC sample were secured on PANalytical X'Pert PRO MRD diffractometer. A continuous scan typically from 35º to 90º of 2θ with a scan rate of 1.8º per minute was generally applied. The volume-averaged Pt crystal sizes in samples were estimated by fitting Pt {111}, {220}, {220} and {311} peaks in Jade 7.5 (Material Data, Inc.).

CHAPTER 4

PT DEPOSITION AND PT "BAND" FORMATION IN NAFION® MEMBRANE

Given the high potential and oxidizing environment at the cathode, platinum has a small but finite solubility [25] in the acidic Nafion® ionomer matrix. This solubility leads to one of the Pt catalyst degradation processes. Specifically, under accelerated degradation tests that include potential cycling dissolution was identified [27, 31, 32] and subsequently simulated [16, 17]. Soluble Pt ions that are formed at the cathode can be transported to other regions of the fuel cell, such as the Nafion® membrane, by diffusion and migration. Ferreira [29] observed that Pt migrated into the membrane and formed a Pt "band" after 2000 h of open-circuit operation on H_2(anode gas)/air(cathode gas). Yasuda [34] further studied Pt dissolution and deposition in membrane under different potential cycling conditions. Following N_2/N_2 potential cycling, in the absence of hydrogen, Pt ions were transported through membrane and plated on the negative carbon electrode. Yasuda also found a Pt "band" in the membrane after 500 H_2/air potential cycles; however, Pt only deposited at the membrane-cathode interface in the H_2/N_2 case. But in another study by Yu [15], a Pt "band" was observed in the membrane (about 5 μm away from the cathode) after 2400 H_2/N_2 potential cycles. In our study, the Pt deposition process was investigated under H_2/N_2 and H_2/O_2 (varied oxygen partial pressure in N_2) under potential cycling conditions. Hydrogen and air crossover rates through Nafion® membrane were measured. A simplified model describing the Pt deposition process and the effects of hydrogen and air permeability is proposed. The model predicts the Pt "bands" locations in the membrane. For the first time, the quantity of Pt metal removed

from the cathode and transported into the membrane was estimated by SEM-EDS analyses.

4.1 Gas crossover

The rate of hydrogen crossover was determined with H_2 at the anode and nitrogen at the cathode under the same fuel cell conditions as those used during potential cycling. A positive potential sweep up to 0.4 V vs. RHE was conducted at the cathode with a sweep rate of 1 mV/s. At the end of the sweep, the potential was held constant for 60 seconds and the limiting oxidation current (mA/cm^2) was measured to calculate the H_2 crossover rate ($mol/cm^2/h$). The average limiting current was 3.10 ± 0.05 mA/cm^2. From this, the hydrogen crossover rate was calculated to be $1.61\pm0.03\times10^{-8}$ $mol/cm^2/s$, which is the same order of magnitude as found in Endoh's study with a Flemion SH50 membrane (50 μm thickness) [40].

Due to the difficulty of connection a separate reference electrode to fuel cell system, the rate of oxygen crossover in air was measured by gas chromatography (GC) instead of the electrochemical method. The test was at the cell temperature of 65 °C and atmospheric pressure condition. Both oxygen and nitrogen calibration curves at proper gas concentration ranges were prepared. Gas exited from the anode (nitrogen with small amount of oxygen) was sampled with a 1 cm^3 syringe for the GC tests. The volume percentages of oxygen in N_2 were determined, which were then multiplied by the nitrogen flow rate (0.1 dm^3/min) and divided by CCM area (25 cm^2) to calculate the

oxygen crossover rates (mol/cm^2/min) using the ideal gas law. Three GC tests for oxygen (in air) permeability gave an average crossover rate of $1.3\pm0.2\times10^{-9}$ mol/cm^2/s.

4.2 Pt deposition and Pt band formation

Fuel cell tests are described previously with the detailed testing procedures listed in Table 4.1. In brief, all 5×5 cm catalyst coated membrane (CCMs) and gas diffusion layers (GDLs) were assembled in the 25 cm^2 fuel cell testing hardware (Fuel Cell Technologies, Inc.). All CCMs were wet up and conditioned followed by degradation procedures. For tests on CCM #1-3, a square-wave that alternated between 0.87 and 1.2 V vs. reference hydrogen electrode (RHE) with a time step of 15 s at each potential was used. The anode served as both the reference and the counter electrodes. Pure H_2 was supplied to the anode and gas with varying partial pressures of oxygen (including N_2, air, 50 % O_2 or pure O_2) was supplied to the cathode. Degradation tests on CCM #4-6 included two steps of potential cycling (the same potential profile as in CCM #1-3) and/or constant current, flowing different cathode gases (pure oxygen or air). For CCM #6, both hydrogen and pure oxygen flow rates were set at ten times of required stoichiometry during the 25 hours constant current holding.

Table 4.1: Cathode gas and potential cycle numbers for CCMs degradation tests

CCM (membrane)	#1 (111)	#2 (111)	#3 (117)	#4 (111)	#5 (111)	#6 (111)
Testing Conditions	3000 cycles H_2/N_2	3000 cycles H_2/air	3000 cycles H_2/50 % O_2	3000 cycles H_2/O_2, then 3000 cycles H_2/air	3000 cycles H_2/air, then 3000 cycles H_2/O_2	3000 cycles H_2/air, then 25 hours 0.8A/cm^2 H_2/O_2

4.2.1 Pt band location and Pt deposition processes

Figure 4.1 shows the Pt distributions, determined by SEM-EDS, of a fresh CCM (with a Nafion® 111 membrane) and CCM #1-3 after potential cycling. There was no significant Pt found in the membrane for either the fresh CCM or the H_2/N_2 cycled CCM #1, whereas a clear Pt "band" formed in the membrane for the H_2/air cycled CCM #2 and the H_2/50 % O_2 cycled CCM #3. These Pt dissolution and deposition behaviors were similar to those found in Yasuda's study [34]. The regions near the cathode-membrane interface were not examined in this study. Platinum was expected to deposit at the cathode/membrane interface due to the Pt ion reduction by hydrogen from the anode for the H_2/N_2 potential cycling case.

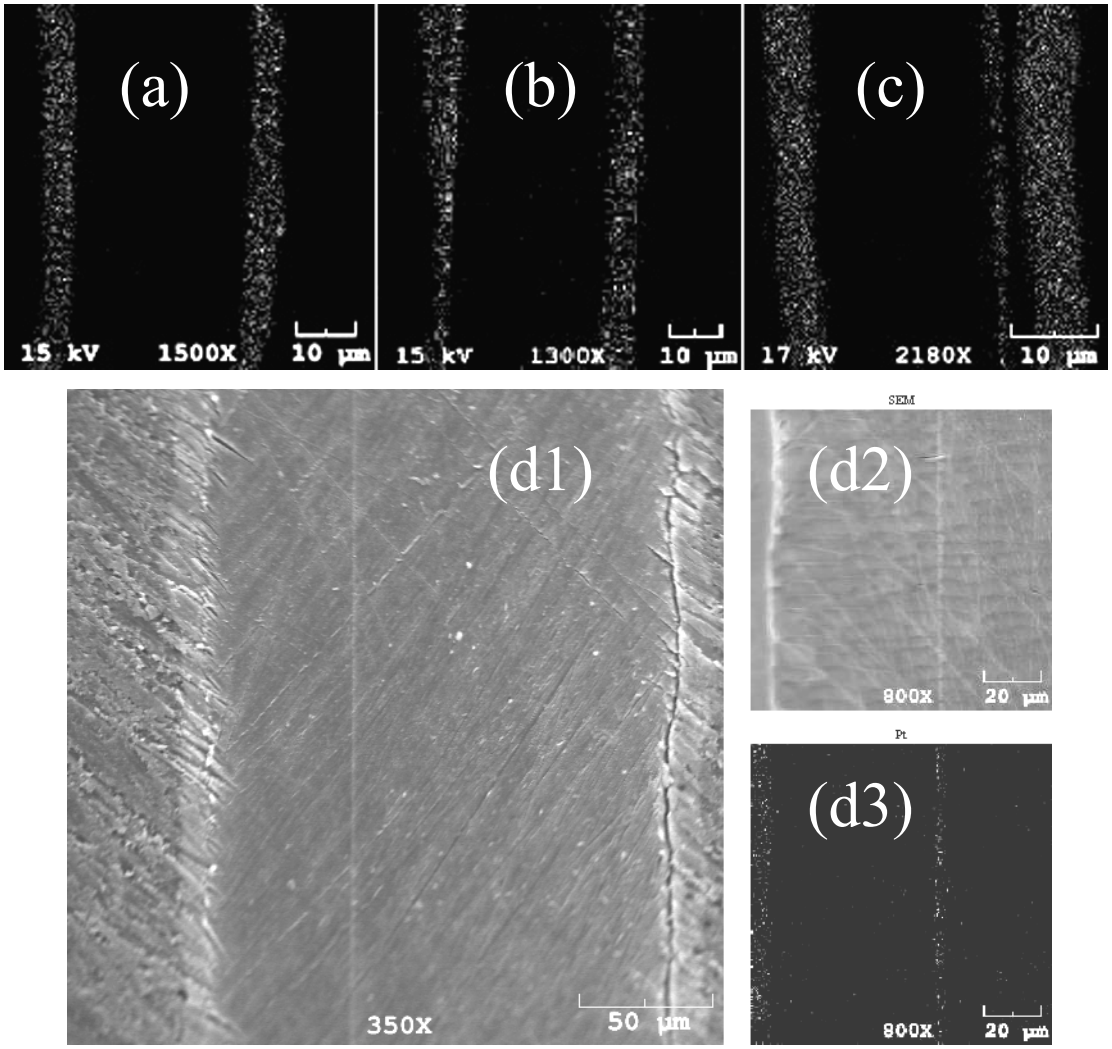

Figure 4.1: Pt distribution maps in the CCMs (left: anode; right: cathode): (a) Fresh, and cycled (b) CCM #1, (c) CCM #2, and (d1-d3) CCM #3

Since there was no element with a constant composition across CCM for reference, the coated Au layers not only provided a better electronic conduction but also functioned as a reference element to quantify the Pt composition in the CCM. The gold layers were assumed perfectly uniform in the micrometer scale (the SEM-EDS detector resolution range). The average Pt/Au atomic ratios and the widths of the anode, the cathode and the Pt "band" for the fresh CCM and the potential cycled CCM #1-2 are

listed in Table 4.2. CCM #3 has the different catalyst loadings, so the Pt distribution was not measured. Following potential cycling, the percentages of the total CCM platinum in the anode (39 %) remained very close to the values of the fresh CCM (40 %) and to the manufacturer's data (37.5 %), suggesting insignificant Pt loss from the anode.

Table 4.2: Average Pt/Au ratios and widths of anode, cathode and Pt "band" and calculate overall Pt% in CCMs

CCMs (Nafion® 111)	Fresh CCM		Cycled CCM #1		Cycled CCM #2		
	Anode	Cathode	Anode	Cathode	Anode	Cathode	Pt band
Pt/Au ratio	4.0±0.5	4.3±0.3	5.5±0.3	6.1±0.5	4.8±0.2	5.0±0.3	5.1±1.2
Width (μm)	5.2±1.2	7.2±1.1	5.1±1.6	7.1±1.0	5.3±0.8	7.0±1.1	1.0±0.1
CCM Pt%	40 %	60 %	39 %	61 %	39 %	53 %	8 %

It was found that about 8 %/(8 %+53 %)≈13 % Pt (originally in the cathode) were deposited in the membrane of CCM2 after 3000 H_2/air potential cycles. Since the width of the Pt band was only about 1.0 μm and the spatial resolution of the SEM-EDS is about 1-2 μm, the measured Pt/Au ratios in Pt "band" might not be very accurate as is evident by the relatively large standard deviation in Table 4.2. But when a Pt "band" is formed in the membrane, this method is still valuable as a quick and easy estimate of the average cathode Pt loss rate. The Pt loss rate (3.6×10^{-12} mol/cm^2/s or 2.5×10^{-3} mg/cm^2/h) during the total of 3000 potential cycles was about 10 times higher than the dissolution rate of Pt sheet during triangular-wave potential cycling between 0.05 and 1.4 V (vs. NHE) at 23 °C in 1 M H_2SO_4 [27].

Before potential cycling and Pt dissolution, the presumed H_2 and O_2 gas pressure profiles are sketched in Figure 4.2(a), assuming linear profiles and zero gas pressures at

membrane edges due to complete oxygen reduction at the anode and hydrogen oxidation at the cathode. Figure 4.1 (c, d1-3) shows that the Pt atoms were deposited in a single thin Pt "band" region instead of being uniformly deposited over a region between the edge of the band and the cathode. We believe that a hydrogen front in membrane (to reduce and deposit Pt ion: reaction 4.1) moved from the cathode to the Pt "band" location during the potential cycling. This is explained as follows: since the average rate of Pt deposition (or average Pt ion flux) in the membrane was three orders of magnitude lower than the H_2 crossover rate, we propose that hydrogen is consumed predominantly by reaction with oxygen at the deposited Pt, which functions as a catalyst (reaction 4.2). Without a catalyst, hydrogen and oxygen will not react with each other at 65 °C (much lower than the ignition temperature). However, it was reported that hydrogen catalytic combustion reaction [41] can take place at the Pt single crystal even at temperatures as low as 120 K. And H_2 combustion was continuous with water desorption from catalyst surface if temperature was higher than 170 K [42]. This catalytic combustion of hydrogen and water production in membrane has previously been applied to design a self-humidifying PEM fuel cell [43-45]. When H_2/air potential cycling starts, some dissolved Pt ions from the cathode diffuse into the membrane and are deposited by hydrogen reduction at locations very close to the cathode. Since oxygen dominated at these locations, hydrogen that diffuses through the membrane would be completely consumed by the catalytic combustion with the deposited Pt catalyst. This permits Pt ions to move further towards the anode in the membrane until they are reduced by the hydrogen diffusing from the anode. Such processes continue with Pt deposition and the hydrogen front moving away from the cathode. When the hydrogen front reaches a position where both hydrogen and

oxygen are completely reacted, Pt ions cannot move further towards the anode, and a pseudo-steady-state of Pt deposition and H_2/O_2 catalytic combustion is achieved. At this location, the mixed potential of dissolved H_2/O_2 dramatically decreases from above 0.8 V to below 0.1 V (vs. NHE) due to the transition from an oxygen-rich condition to a hydrogen-rich condition, and the deposited Pt should be stable. A simple linear gas profile in membrane is sketched in Figure 4.2(b) showing this state. Finally, as more Pt ions deposit at this location, a Pt "band" forms. We expect that the band width increases slightly as more Pt is deposited and also due to possible small fluctuation of gas partial pressures.

$$H_2 + Pt^{2+} \rightarrow Pt(membrane) + 2H^+ \qquad \text{(Reaction 4.1)}$$

$$H_2 + O_2 \xrightarrow{Pt(membrane)} 2H_2O \qquad \text{(Reaction 4.2)}$$

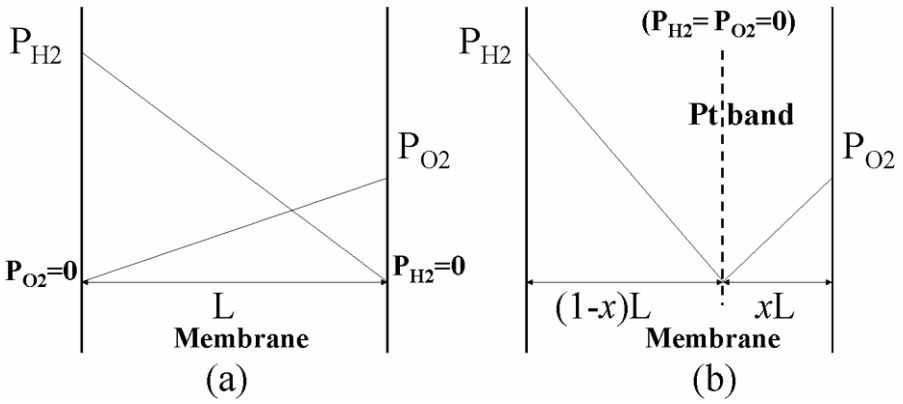

Figure 4.2: Simplified gas partial pressures profiles of the crossovered H_2 and O_2 in membrane: (a) before Pt deposition, (b) when Pt deposited at Pt "band" location

Based on the above straightforward Pt ion deposition processes, the Pt band location in the membrane can be predicted in terms of the rates of gas permeation. At a

steady state and assuming the gas profiles in Figure 4.2(b), the hydrogen and oxygen fluxes are related,

$$N_{H_2} = -2N_{O_2}. \qquad \text{(Equation 4.1)}$$

Assuming Fick's law,

$$\frac{D_{H_2} c^0_{H_2}}{1-x} = \frac{2D_{O_2} c^0_{O_2}}{x}. \qquad \text{(Equation 4.2)}$$

x is the dimensionless distance from the cathode-membrane interface to the center of Pt "band", D_{H_2} and D_{O_2} are effective diffusivities of H_2 and O_2 in membrane, and $c^0_{H_2}$ and $c^0_{O_2}$ are H_2 and O_2 concentrations at the membrane edge. Based on Henry's law,

$$c^0_{H_2} = H_{H_2} p^0_{H_2}, \qquad \text{(Equation 4.3)}$$

$$\text{and } c^0_{O_2} = H_{O_2} p^0_{O_2}. \qquad \text{(Equation 4.4)}$$

H_{H_2} and H_{O_2} are Henry's constants for H_2 and O_2 in Nafion® membrane. $p^0_{H_2}$ and $p^0_{O_2}$ are H_2 and O_2 partial pressures at membrane edges. Combining equations 4.2-4.4, we have

$$\frac{1}{x} = 1 + \frac{1}{2\alpha} \times \frac{p^0_{H_2}}{p^0_{O_2}}, \qquad \text{(Equation 4.5)}$$

where

$$\alpha = \frac{D_{O_2} H_{O_2}}{D_{H_2} H_{H_2}}. \qquad \text{(Equation 4.6)}$$

Therefore, the position of Pt "band" ($1/x$) should vary linearly with the ratio of hydrogen and oxygen partial pressures. The coefficient (α) was evaluated by hydrogen and oxygen in air permeability tests in terms of the crossover rates (N'_{H2} and N'_{O2}) as following:

$$\frac{N'_{H_2}}{N'_{O_2}} = \frac{D_{H_2} H_{H_2} p^0_{H_2} / L}{D_{O_2} H_{O_2} p^0_{O_2} / L} = \frac{1}{\alpha} \frac{p^0_{H_2}}{p^0_{O_2}} . \qquad \text{(Equation 4.7)}$$

α was calculated to be 0.38±0.05. The predicted Pt band locations are compared to the observed values for the tests on CCM #2-6 and also literature data shown in Figure 4.3. We can see that the predicted Pt band locations are close to the observed positions in our tests. The details of Pt deposition and bands formation in CCM #4-6 will be discussed in the section 4.2.2. Yasuda's study [34] (x ≈0.13) using a Nafion® 117 membrane and Ferreira's study [29] (x ≈0.14) using a Gore 5510 MEA were very close to the predicted data. The Pt band position in both Patterson's [46] (Gore MEA) and Ohma's [47] (Nafion® NRE212) studies under H_2/air cases were relatively closer to the anodes than the predicted locations. Ohma's data (110 h of open circuit tests) showed relatively poor agreement with the predicted results. In the case of flowing air at the cathode, only small amount of Pt particles were observed in TEM and no Pt band was formed due to the slow degradation rate at open circuit conditions. It is possible that the Pt band locations were not correctly reported due to the uncompleted Pt band formation. For H_2/N_2 potential cycling (hydrogen/oxygen pressure $\rightarrow$ infinity), the deposition of Pt was expected at the cathode-membrane interface ($1/x \rightarrow$ infinity) since there was no oxygen to suppress hydrogen crossover front. All Pt band relative locations observed in this dissertation work were listed in Table 4.3, which were close to the predicted positions. Membrane thickness will not change the relative location of Pt deposition. Cell temperature and gas relative

humidity will directly affect the gas partial pressures and may slightly affect the gas permeability ratio (α). For example, in tests of CCM #7-9 with cell temperature varied from 40 to 80 °C at fully humidified conditions, both hydrogen and oxygen partial pressure changed. However, the gas partial pressure ratio between hydrogen and oxygen remained constant, so the predicted Pt band relative locations (by equation 4.5) were the same, and confirmed by the observed data in Table 4.3. Gas humidity has an effect similar to the temperature variable as shown in the tests of CCM #12-13 as one example.

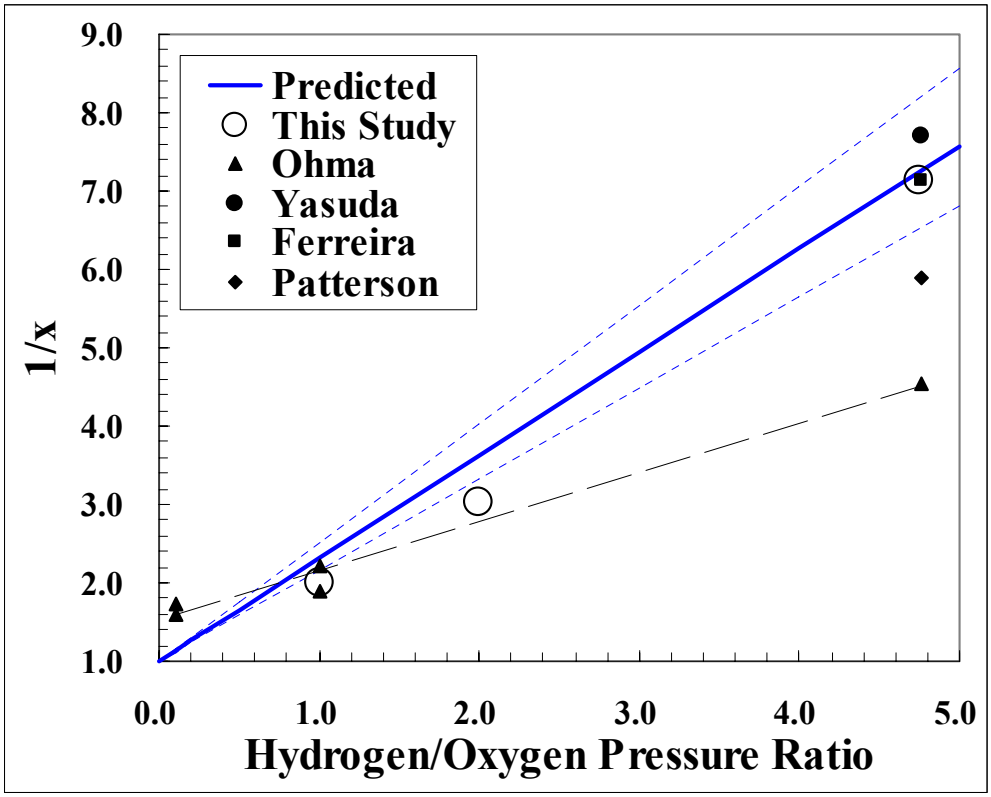

Figure 4.3: Comparisons of predicted Pt "band" locations with experimental data

Table 4.3: Summary of observed and predicted Pt band locations in all fuel cell tests

CCM#	Membrane	T(°C)	%RH	P_{H2}(bar)	P_{O2}(bar)	Predicted x	Observed x
1	111	65	100	0.75	0.000	0.00	0.00
2	111	65	100	0.75	0.158	0.14	0.14
3	117	65	100	0.75	0.375	0.28	0.33
4	111	65	100	0.75	0.158	0.14	0.15
4	111	65	100	0.75	0.750	0.43	0.49
5	111	65	100	0.75	0.158	0.14	0.17
5	111	65	100	0.75	0.750	0.43	0.50
6	111	65	100	0.75	0.158	0.14	0.16
7	111	80	100	0.54	0.113	0.14	0.16
8	111	40	100	0.94	0.197	0.14	0.18
9	111	60	100	0.81	0.171	0.14	0.18
10	117	60	100	0.81	0.000	0.00	0.00
11	117	60	50	0.91	0.000	0.00	0.00
12	117	60	100	0.81	0.171	0.14	0.18
13	117	60	50	0.91	0.192	0.14	0.15
14	117	60	100	0.81	0.810	0.43	0.53
15	117	60	50	0.91	0.910	0.43	0.48
16	117	60	100	0.81	0.171	0.14	0.18
17	117	60	100	0.81	0.171	0.14	0.18
18	117	60	100	0.81	0.171	0.14	0.18

In summary, deposition of platinum in the membrane was not observed under H_2/N_2 potential cycling. In contrast, for the case of H_2/pure O_2 or its mixture with N_2 as cathode gas potential cycling, the deposited Pt formed a "band" in the membrane due to the suppressed hydrogen crossover by H_2/O_2 catalytic combustion reaction on Pt that was deposited in the membrane. The Pt "band" position was well predicted by a simple model in terms of the rates of hydrogen and oxygen crossover in the membrane separator.

4.2.2 Multiple Pt bands formation and deposited Pt atom stability

In either this study or Ohma's study [47], Pt metal was not observed between the Pt "band" and the cathode. One possibility was that the Pt atomic concentrations were too

low to be detected in SEM and TEM images. Yasuda [34] believed that nucleation of Pt was not easy under oxygen-rich conditions with a high mixed potential of dissolved hydrogen and oxygen. But Ohma [47] explained that any deposited Pt atoms re-dissolve at high mixed potential location and the Pt ions move further towards the anode. To further understand Pt band formation processes, we investigated Pt ions deposition and re-dissolution possibility of the deposited Pt atoms in Nafion® membrane under varied oxygen partial pressures (CCM #4-6 tests).

Based on the calculated mixed potentials of the crossovered hydrogen and oxygen in membranes [47, 48], the Pt band formed in CCM #4 during the H_2/O_2 potential cycling was located in the low mixed potential region or the H_2 dominant environment during the following H_2/air potential cycling. So H_2/O_2 Pt band in CCM #4 should be stable and remain after the H_2/air potential cycling. As expected, both H_2/O_2 Pt band and H_2/air Pt band were observed in SEM-EDS Pt distribution map of the cross-section of CCM #4 (Figure 4.4). The relative distances (x) of H_2/air Pt band and H_2/O_2 Pt band away from the cathode in the membrane were 0.15 and 0.49, which were very close to the predicted values 0.14 and 0.43. The Pt content in each Pt band was estimated to be 6 % of total Pt in CCM #4 as shown in Table 4.4. The Pt content in the anode remained to be around 40 %, the same value as that in the fresh CCM.

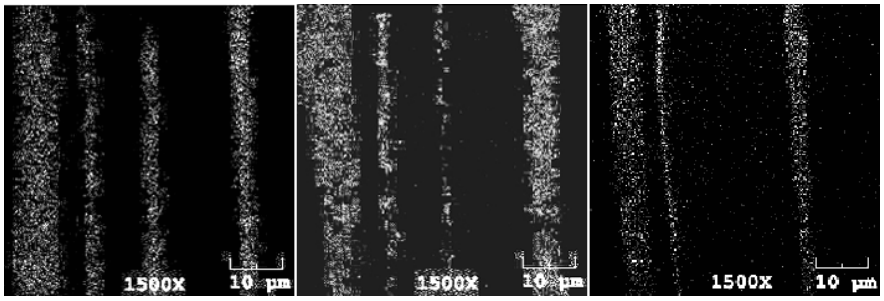

Figure 4.4: Pt distribution in the cross-section of CCMs with the cathode at left side (left: CC #4; middle: CCM #5; right: CCM #6)

Table 4.4: Average Pt/Au ratios and widths of the anode, the cathode and the Pt "bands" and the calculated overall Pt% in CCMs

CCMs/Regions		Pt/Au ratio	Width (μm)	Estimated CCM Pt%
CCM #4	Cathode	0.44±0.04	8.4±1.4	48
	H_2/air Pt band	0.31±0.09	1.5±0.2	6
	H_2/O_2 Pt band	0.32±0.05	1.4±0.2	6
	Anode	0.61±0.05	5.1±1.6	40
CCM #5	Cathode	1.0±0.1	8.4±2.0	45
	H_2/air Pt band	1.1±0.2	2.0±0.6	12
	H_2/O_2 Pt band	0.5±0.2	1.3±0.3	3
	Anode	1.4±0.1	5.3±2.2	40
CCM #6	Cathode	1.0±0.1	7.6±1.4	50
	H_2/air Pt band	1.6±0.2	0.8±0.1	8
	Anode	1.4±0.2	4.6±1.7	42

For CCM #5, it was firstly potential-cycled under the H_2/air environment followed by the H_2/O_2 potential cycling. Therefore, the Pt band formed under H_2/air would be located in the oxygen dominant region or the high mixed potential region during the H_2/O_2 potential cycling period (calculated to be 0.8-1.2V [47, 48] vs. RHE). Schematic profiles of gas concentration in CCM #5 before and after switching to the H_2/O_2 potential cycling are shown in Figure 4.5. After switching to the H_2/O_2 potential

cycling, hydrogen that permeated from the anode is expected to be completely consumed by the H_2-O_2 catalytic combustion reaction at the H_2/air Pt band. In contrast, only part of O_2 permeated through membrane would be consumed with the rest diffusing until to the anode. If the Pt atoms in H_2/air Pt band re-dissolve, the H_2/air Pt band would start to diminish after switching to the H_2/O_2 potential cycling. Besides Pt re-dissolution from Pt band (reaction 4.3), the crossovered hydrogen could be oxidized (reaction 4.4) and the crossovered oxygen could be reduced (reaction 4.5) at the Pt particles in the Pt band as a catalyst. The Pt re-dissolution reaction rate at a mixed potential of 0.8-1.2 V vs. RHE should not be higher than the cathode Pt dissolution rate under the H_2/air potential cycling condition, which was previously found to be two or three orders of magnitude lower than the measured rates of gas crossover (or the H_2-O_2 catalytic combustion reaction rate) [48].

$$Pt(\text{membrane}) \rightarrow Pt^{2+} + 2e^- \qquad \text{(Reaction 4.3)}$$

$$H_2(\text{crossovered}) \xrightarrow{\text{Pt membrane}} 2H^+ + 2e^- \qquad \text{(Reaction 4.4)}$$

$$O_2(\text{crossovered}) + 4H^+ + 4e^- \xrightarrow{\text{Pt membrane}} 2H_2O \qquad \text{(Reaction 4.5)}$$

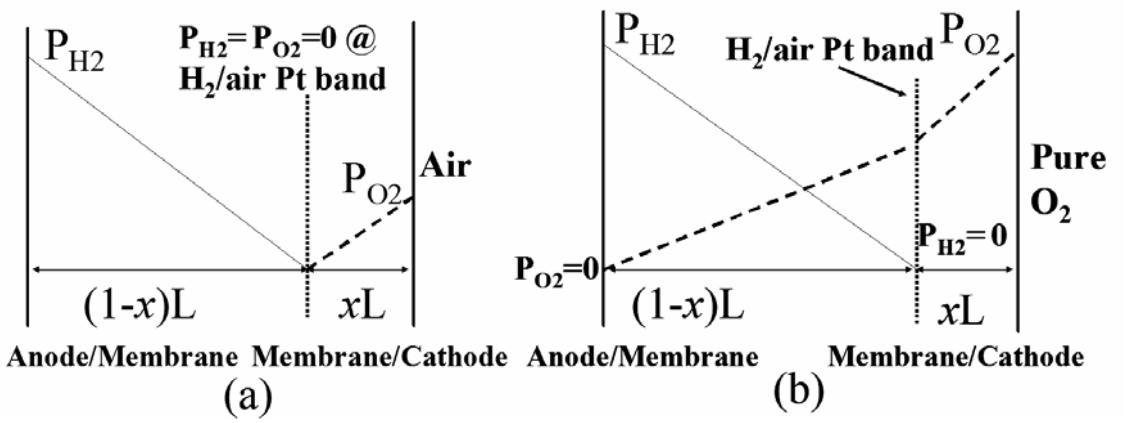

Figure 4.5: Simplified linear gas partial pressures profiles of the crossovered hydrogen and oxygen in the membrane: (a) before, (b) after switching to H_2/O_2 condition

Contrary to our expectations, H_2/air Pt band in CCM #5 remained and was denser and thicker than the H_2/O_2 Pt band as shown in Figure 4.4. The Pt band locations of the relative distances (*x*) away from the cathode were 0.17 and 0.50, also close to the predicted values. Analyses of Pt contents (Table 4.4) confirmed that about 12 % of total CCM Pt was in H_2/air Pt band, which was significantly higher than the 3 % in CCM #5 H_2/O_2 Pt band and 6 % in each of the two CCM #4 Pt bands. Compared to CCM #4, Pt remained in CCM #5 cathode was slightly lower after total 6000 potential cycles. This difference might be caused by the different cathode dissolution rates depending on the cathode electrochemically active surface areas and Pt oxide surface coverage on catalyst. Increased oxygen partial pressures resulted in increased Pt oxide surface coverage and slower dissolution rates of Pt [49]. Unfortunately, it is impossible to distinguish whether the CCM #5 H_2/O_2 Pt band resulted from the continuous dissolution of the cathode or from re-dissolution of Pt atoms in H_2/air Pt band or the combination of both processes.

A few possibilities could cause further growth of the H_2/air Pt band in CCM #5 instead of its diminishing. During the second phase of the H_2/O_2 potential cycling, a significant amount of Pt ions was continuously generated through the cathode Pt dissolution and was expected to diffuse to the final location of H_2/O_2 Pt band through the previously formed H_2/air Pt band. Pt ions could prefer to deposit on the Pt particles in the H_2/air Pt band by H_2 reduction, instead of passing through the H_2/air Pt band and being nucleated at a place closer to the final H_2/O_2 Pt band location due to the large surface tension of small Pt particles. A second possibility could be Pt ion diffusion channels in membrane became partially blocked when more and more Pt atoms deposited in the H_2/air Pt band. This could further increase the chance of Pt ions deposition in H_2/air Pt band, resulting in a denser H_2/air Pt band. As shown in Table 4.4, the ratio of the Pt/Au atomic ratio in the H_2/air Pt band to that in the anode was $1.1/1.4 \approx 0.79$ for CCM #5, which was higher than the ratio $0.31/0.61 \approx 0.51$ in CCM #4.

To minimize the amount of Pt ion dissolved from the cathode during the second H_2/O_2 potential cycling step, CCM #6 was subjected to a constant current at high current density (800 mA/cm^2) under the H_2/O_2 conditions for 25 hours. The cell voltage decreased slightly from an initial value of 0.731 V to 0.719 V at the end of the constant current procedure. The equilibrium Pt ion concentration of the cathode at such potentials would be several orders of magnitude lower than that at a potential of 1.2 V [30]. Figure 4.4 clearly shows only the H_2/air Pt band in CCM #6, located at the same relative distance of 0.16 away from the cathode as in CCM #4. The Pt band had a denser Pt content (ratio of Pt density in the band to in the anode: $1.6/1.4 \approx 1.14$) with a smaller Pt

band width than those in CCM #4 and CCM #5. The estimated Pt content was 8 % in CCM #3 H_2/air Pt band, which was slightly higher than 6 % in CCM #4, but significantly lower than 12 % in CCM #5. Previously CCM #2 with only 3000 H_2/air potential cycles yielded a similar denser ($5.1/4.8 \approx 1.06$) and narrower (1.0 ± 0.1 μm) H_2/air Pt band with a total 8 % Pt in Pt band. It is possible that more uniform gas crossover rates could result in a narrower and more dense Pt band. The similar Pt contents in the Pt band suggested that the Pt dissolution from the cathode was largely eliminated during the H_2/O_2 constant current holding. A H_2/O_2 Pt band was not formed in CCM #6 by re-dissolution of Pt atoms in H_2/air Pt band, which suggested such deposited Pt re-dissolution in membrane was not feasible.

More recently, Li [50] studied Pt particles deposited in Nafion® 211 membrane after H_2/air potential cycling by transmission electron microscopy (TEM). It was found the largest particle (an average size of 140 nm) in the Pt band (at 5 μm away from the cathode) and smaller particles on both sides of the Pt band (2-11 μm away from the cathode). And Yusuda [51] also found in TEM images that Pt particles deposited in Nafion® 117 up to 40 μm away from the cathode with an average particle size of 40 nm and even smaller particles deposited up to 85 μm away from the cathode, after 193 h of CCM potential holding at 1 V vs. RHE under H_2/air conditions. It is possible that those smaller Pt particles dislocated outside of the Pt band center on both sides were caused by the fluctuation of the hydrogen and/or oxygen crossover rates. Those Pt particles between the cathode and the Pt band could also come from the initial Pt deposition by hydrogen reduction before the Pt band formation. The later process was previously described in

section 4.2.1 and it was suggested that these Pt particles could function as a catalyst for H_2-O_2 catalytic combustion (reaction 4.2) and gradually suppress the hydrogen front away from the cathode until reaching a stable location (Pt band) where the crossovered H_2 and O_2 have a complete reaction with each other (or the mixed potential of the crossovered H_2 and O_2 decreases dramatically towards the H_2 dominant region near the anode). However, the crossovered gas pressure profile should be most likely as what it displayed in Figure 4.5 (a) with some fluctuation from time to time resulting in a concentrated Pt deposition region (Pt band). So those Pt particles between the cathode and the Pt band were located in the oxygen (air) dominant region (or a high mixed potential region) most often, for the possible re-dissolution. But, these small Pt particles remained in the oxygen dominant region. These observations agreed with our experimental results and supported the idea that Pt re-dissolution at a high mixed potential of the crossovered hydrogen and oxygen was not a feasible process.

Since we have not clearly understood the gas transport mechanism and the morphologies of the deposited Pt particles in Nafion® membrane, other involved processes affecting Pt re-dissolution might not be identified yet. The above results also indicate the difficulty of in-situ moving or recovering the lost Pt atoms in the membrane, although the deposited Pt atoms can be recovered through recycling the CCM. To improve the Pt catalyst lifetime on fuel cell applications, Pt dissolution should be minimized though designing more stable catalyst structures or alloying with other transitional metals.

CHAPTER 5

TEMPERATURE EFFECTS OF PT/C DEGRADATION UNDER POTENTIAL CYCLING

An active research thrust for PEM fuel cells is the development of high-temperature membranes to allow operation at temperatures above 80 °C. Increasing operating temperatures to 120 or 150 °C will improve electrochemical kinetics [52-54] and allow the anode to have better CO tolerance [55]. Most importantly, higher temperatures allow for smaller cooling systems, similar in size to those used in present vehicles, and simpler fuel cell stack design. However, the degradation processes are expected to be accelerated [5], and thus further limit the lifetime of PEM fuel cells at higher temperatures. So we investigated degradation of the carbon-supported Pt catalyst in CCMs under an accelerated degradation protocol by potential cycling at varied cell temperatures of 40, 60 and 80 °C. It was found that Pt/C catalyst degradation rates dramatically increased with temperature. This temperature effect would also be expected at temperatures beyond 100 °C.

5.1 Potential Cycling Degradation Test

The commercial CCMs (#7-9): 5×5 cm constructed from Nafion® 111 membrane and Pt/C catalyst layers with Pt loadings of 0.3 and 0.5 mg_{Pt} cm^{-2} in the anode and cathode respectively were used. All three CCMs were wet-up and conditioned as previously described (Appendix B). Following conditioning, the potential of the cell was cycled with a square-wave between 0.87 and 1.2 V vs. reference hydrogen electrode

(RHE) and a time step 30 s at each potential, using a Potentiostat/Galvanostat (EG&G Princeton Applied Research 273A). Pure hydrogen (0.38 dm^3/min) was supplied to the anode, which was served as both the reference and the counter electrodes. Air (0.91 dm^3/min) was fed to the cathode as the working electrode. During potential cycling, cell temperatures were 40 °C (CCM #7), 60 °C (CCM #8), and 80 °C (CCM #9), and both hydrogen and oxygen were fully humidified at the cell temperatures.

5.2 Results and Discussions

5.2.1 Membrane Fluorine Loss and Hydrogen Crossover Rate

Nafion® membrane degradation is accelerated at low humidity conditions [40], although the detailed degradation mechanisms are still under investigations. In this study of Pt/C catalyst degradation, the anode and cathode gases were fully humidified to minimize membrane/ionomer degradations. Both cathode and anode water effluents during the 7000 potential cycles were collected, and the fluorine ion concentrations in all samples were below 1.0 μg/g. Fluorine emission rates from both the anode and the cathode were relatively steady with some fluctuations at different stages of the degradation tests. Combined cumulative F losses (μg/cm^2) from both the anode and the cathode effluents are plotted in Figure 5.1. It is clear that the higher degradation temperature resulted in more F loss from membrane/ionomer. Nevertheless, even at the degradation temperature of 80 °C, there was only about 0.15 % total F loss with an average F ion emission rate of 0.56 μg/cm^2/h from CCM #9 membrane/ionomer during the degradation test (about 110 hours). These rates of fluorine loss were one to three

orders of magnitude lower than those observed during typical accelerated membrane degradation testing [56, 57]. Hydrogen crossover limiting currents were almost constant (1.5-2.1 mA/cm^2) during the potential cycling, indicating no significant membrane degradation occurred. The minimal membrane degradation during our testing protocol by square-wave potential cycling simplified the interpretation of results presented below.

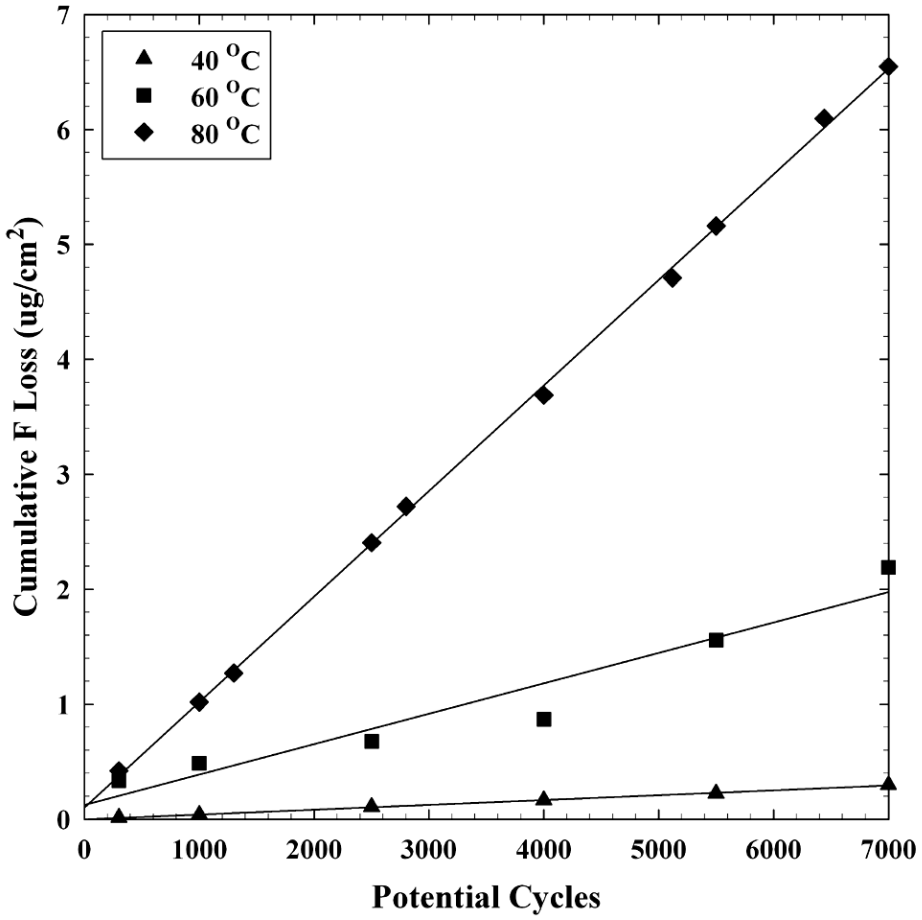

Figure 5.1: Cumulative fluorine loss (µg/cm^2) during potential cycling for CCM #7 (40 °C), CCM #8 (60 °C) and CCM #9 (80 °C)

5.2.2 Catalyst ECAs

The initial Cathode electrochemically active surface areas (ECAs) after cell conditioning were 64.0, 71.9 and 63.2 m^2/gPt for CCM #7, CCM #8 and CCM #9 cathodes, respectively. ECAs of all cathodes decreased with potential cycling. After 7000 potential cycles, CCM #7 lost 54.0 % of the initial ECA, while CCM #8 and CCM #9 had 70.7 % and 75.9 % losses respectively. The ECA of CCM #9 appeared to level out after 5500 potential cycles. And the initial ECA loss rates increased as the degradation temperature increased. A first order kinetic rate model [58],

$$\frac{dS(N)}{dN} = -kS(N), \qquad \text{(Equation 5.1)}$$

fits our surface area *S(N)* data quite well, where *N* is the potential cycle number and *k* is the first order reaction rate constant. It appears that there is a minimum surface area S_{min} (assume 20% of the initial surface area S_0) subjecting potential cycling for all three CCMs here. So an integrated form of the above equation,

$$\ln\left[\frac{S(N) - S_{\min}}{S_o - S_{\min}}\right] = -kN \qquad \text{(Equation 5.2)}$$

yielded the calculated reaction rate constants *k*, as shown in Figure 5.2. The reaction rate constants at these three different temperatures yielded an activation energy of 25.4 kJ/mol, close to the value 22.6±3.6 kJ/mol in a temperature range of 65-90 °C in Debe *et al.*'s study [58]. A similar decrease in surface area (with time rather than potential cycles) is observed in phosphoric acid fuel cells [13].

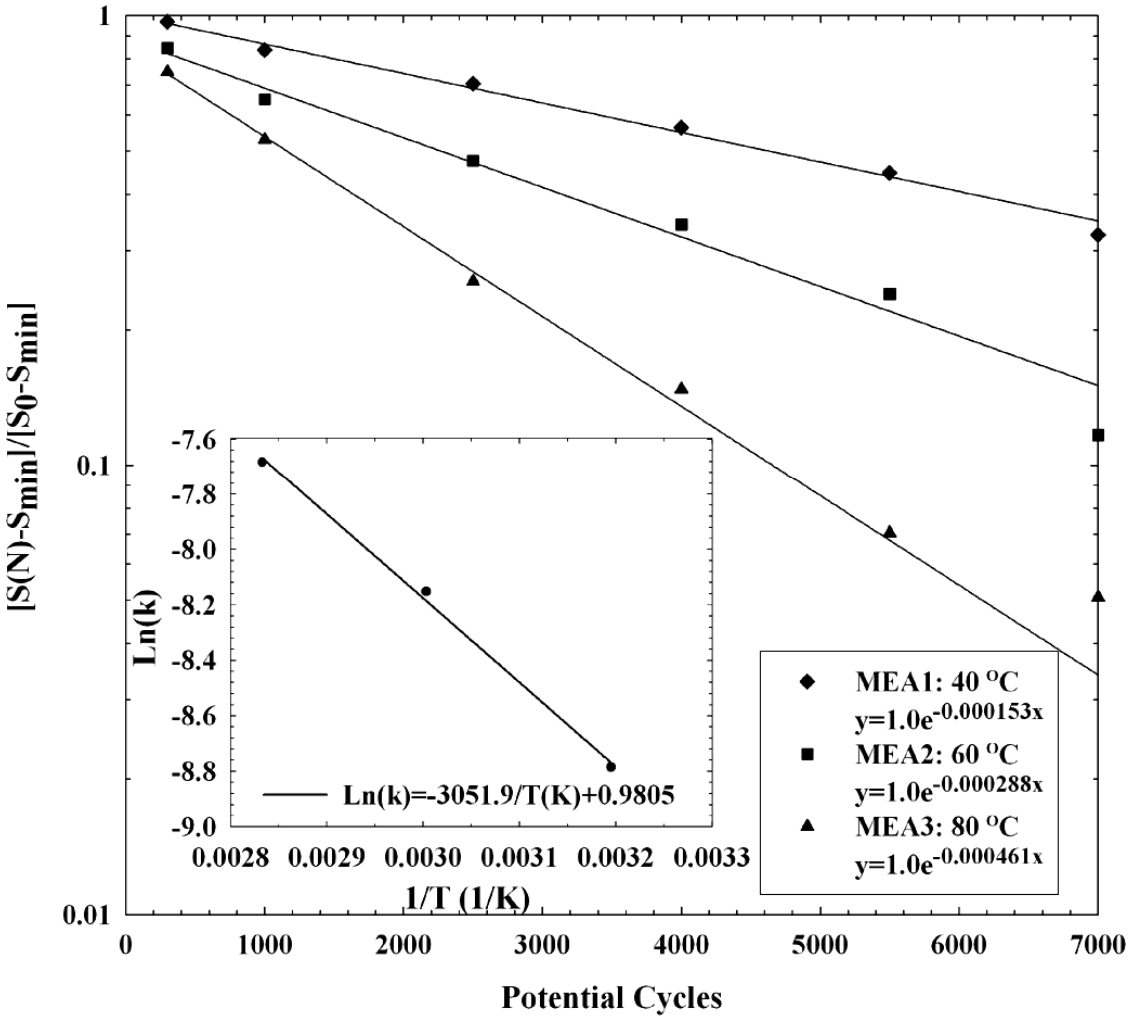

Figure 5.2: First order rate reaction of electrochemically active surface area losses under potential cycling

5.2.3 Polarization Curves and Cell Resistances

At intervals of about 1500 potential cycles, the degradation testing was interrupted, and the cell polarization measured. Figure 5.3 shows these polarizations over the course of the degradation tests. At the degradation temperature of 40 °C, the change in polarization of this cell (CCM #7) was small, about 40 mV, and the resistance appears

constant. In contrast, severe losses for the cell tested at 80 °C (CCM #9) were observed. Cell potentials at the current densities of 100 and 500 mA/cm^2 are plotted in Figure 5.4, which shows cell voltages decreased with the increased temperatures. The potential decay rates were 4.0 and 14.7 μV/cycle at 0.5 A/cm^2 for CCM #7 and CCM #8, which were essentially constant during the degradation tests at 40 and 60 °C, respectively. Yu *et al*. [15] observed a higher potential loss rate of about 30 μV/cycle at 0.5 A/cm^2 during the same square-wave potential cycling at 65 °C. The difference of the loss rates was probably caused by the different cell temperatures and/or differently prepared cathode catalysts. For CCM #9 degraded at 80 °C, cell potential loss rate was accelerated with the average potential loss rates of 29.5 μV/cycle for the first 2500 cycles and 126 μV/cycle for the last 3000 cycles at the current density of 0.1 A/cm^2.

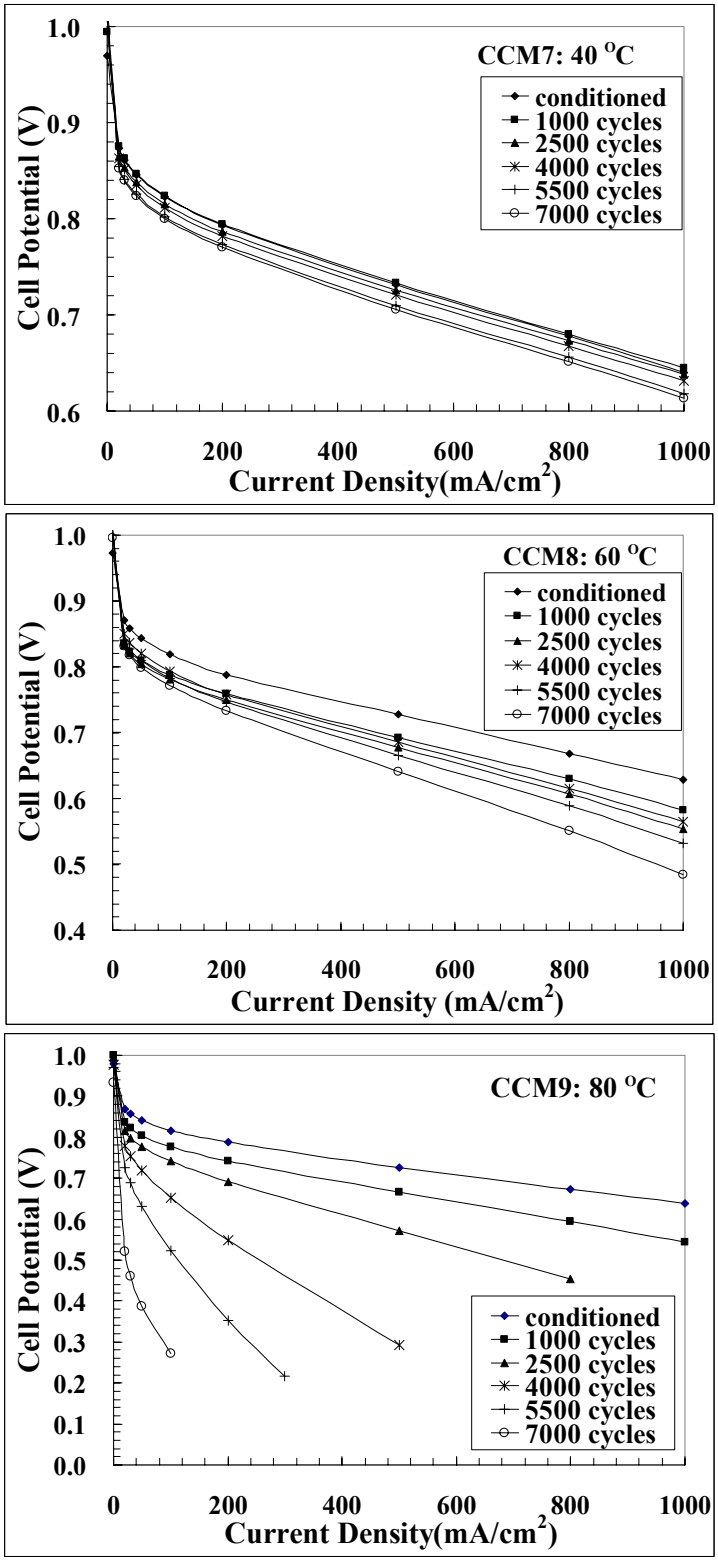

Figure 5.3: Cell potentials under potential cycling at 40 °C (CCM #7), 60 °C (CCM #8) and 80 °C (CCM #9)

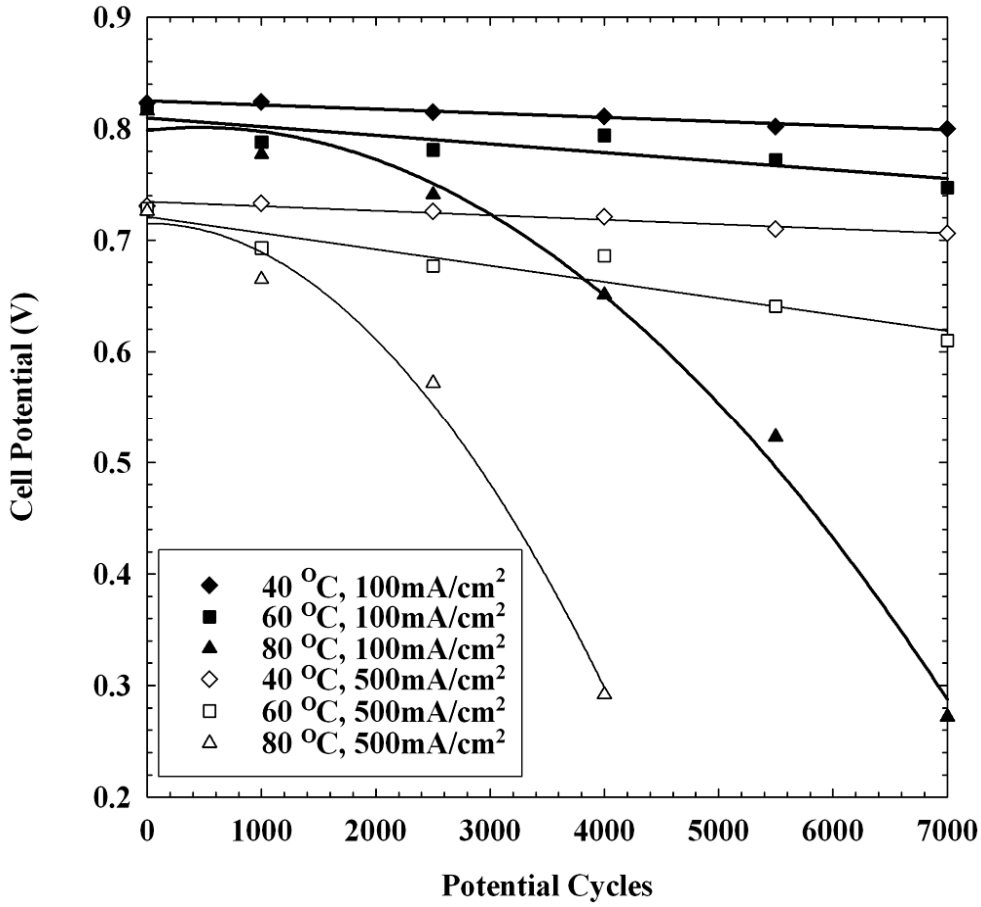

Figure 5.4: Cell voltages at current densities of 100 and 500 mA/cm^2 during potential cycling at 40 °C (CCM #7), 60 °C (CCM #8) and 80 °C (CCM #9)

Tafel slopes (mV per decade) calculated from iR compensated cell potentials between 20 and 50 mA/cm^2 are plotted together with cell resistance (ohm cm^2) in Figure 5.5. The Tafel slope of CCM #7 was constant near 66 mV per decade during the potential cycling at 40 °C, close to the calculated value (Ln(10)*RT/F) 70 mV per decade at 80 °C [59]. The Tafel slope of CCM #8 degraded at 60 °C increased slightly from 65 to 76 mV per decade, while CCM #9 degraded at 80 °C had a sharp increase starting at 2500

potential cycles with a value of 86 mV per decade to 322 mV per decade after 7000 potential cycles. The cell voltage losses,

$$\Delta V(\mathrm{mV}) = 70 \times \log\left[\frac{S(N)}{S_o}\right], \qquad \text{(Equation 5.3)}$$

calculated in terms of the electrochemically active surface area loss [15, 60] are plotted in Figure 5.6, assuming a 70 mV per decade Tafel slope. The measured cell voltage loses at the degradation temperature of 40 °C fit the predicted values closely. The large increase in the apparent Tafel slopes at the higher degradation temperatures caused the large deviations for the measured cell voltage losses, especially during the later half of the potential cycling on CCM #9.

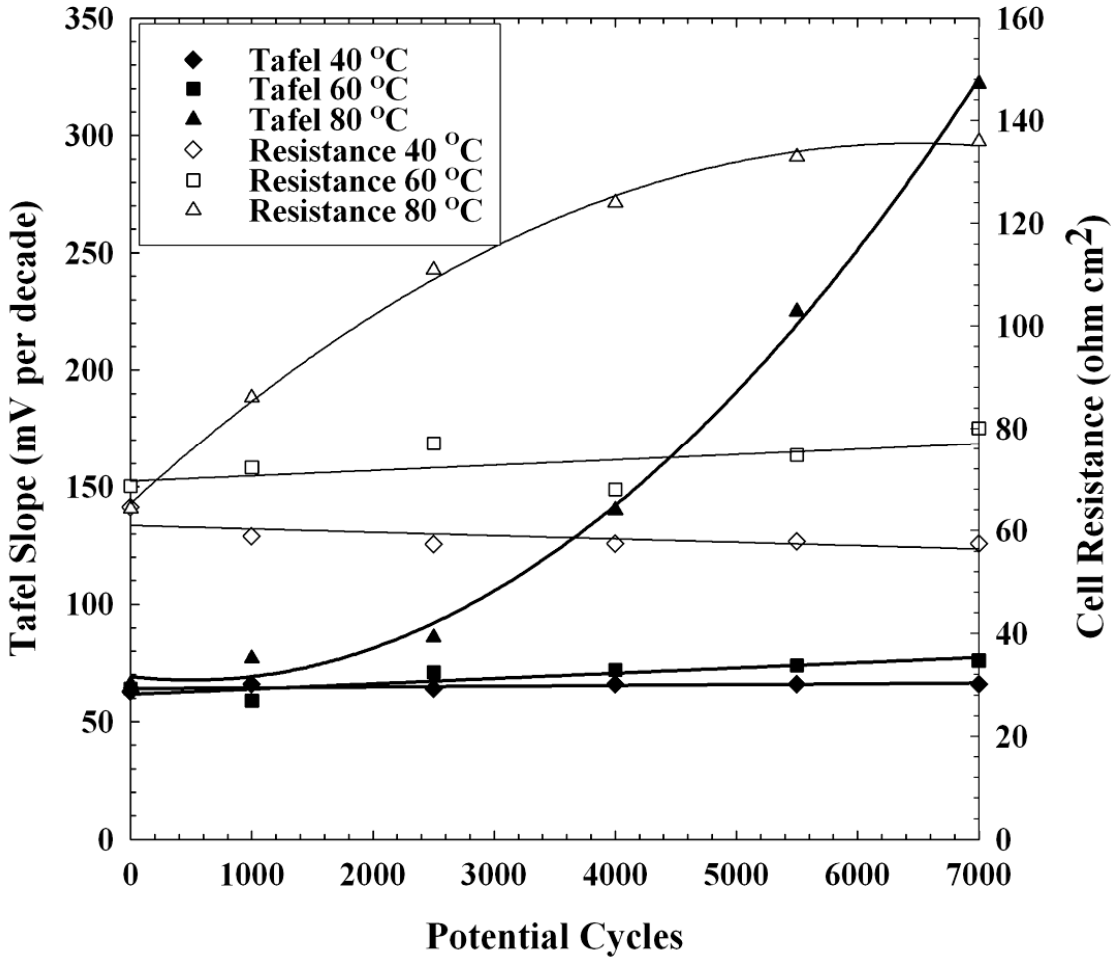

Figure 5.5: Tafel slope (mV per decade) and cell resistances (ohm.cm^2) during potential cycling for CCM #7 (40 °C), CCM #8 (60 °C) and CCM #9 (80 °C)

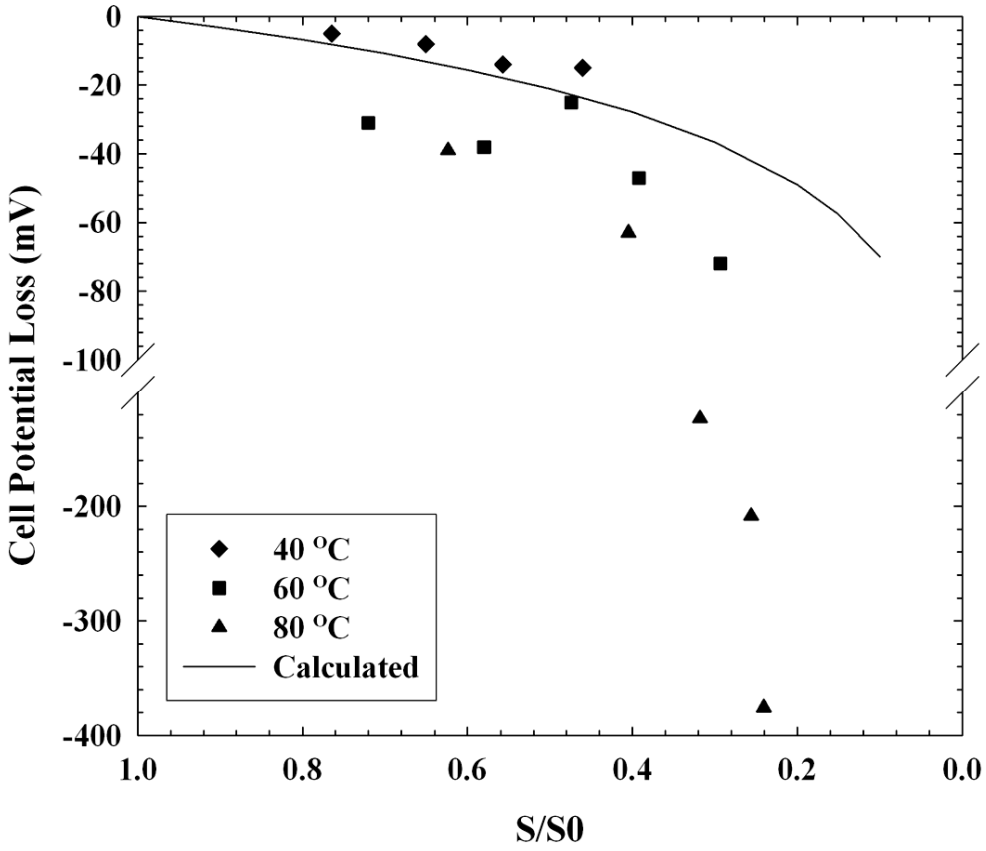

Figure 5.6: Measured and predicted cell voltage losses in terms of ECA losses for CCM #7 (40 °C), CCM #8 (60 °C) and CCM #9 (80 °C)

The initial cell resistances were between 0.064 and 0.069 ohm cm^2, close to the observed value (0.065 ohm cm^2) by Xu et al. [55]. During potential cycling, there were only minor changes of cell resistances on CCM #7 and CCM #8. In contrast, the cell resistance of CCM #9 doubled. Since the membrane degradation was negligible, we could assume the membrane conductivity was constant. The increase in cell resistance is ascribed to an increase in the electronic resistance in the cathode of CCM #9. The severe

carbon corrosion likely explains the accelerated cell performance decay at the later stage of potential cycling on CCM #9 (shown in the SEM image, and be discussed later).

5.2.4 Catalyst Activity

Catalyst mass activity (A/gPt) and specific activity (A/m^2Pt) of CCM #8 during degradation at 60 °C are plotted in Figure 5.7. The initial mass activity and specific activity were relatively low comparing to the other literature values [15, 59], probably due to the differently prepared cathode catalysts. Mass activity decreased from 50 to 15 A/gPt, by contrast the specific activity slightly increased after 4000 potential cycles. This increase of specific activity was also observed in Kinoshita [61] and Yu's [15] studies, possibly due to the increased Pt catalyst particle sizes with degradation. It should be noted that the mass activity is based on the original platinum loading. The data in figure 5.7 don't account for platinum that dissolves and diffuses away from the cathode and ultimately is deposited in the membrane. Unfortunately, catalyst activity data were collected only during CCM #8 degradation test, and no comparisons were made for the different degradation temperatures.

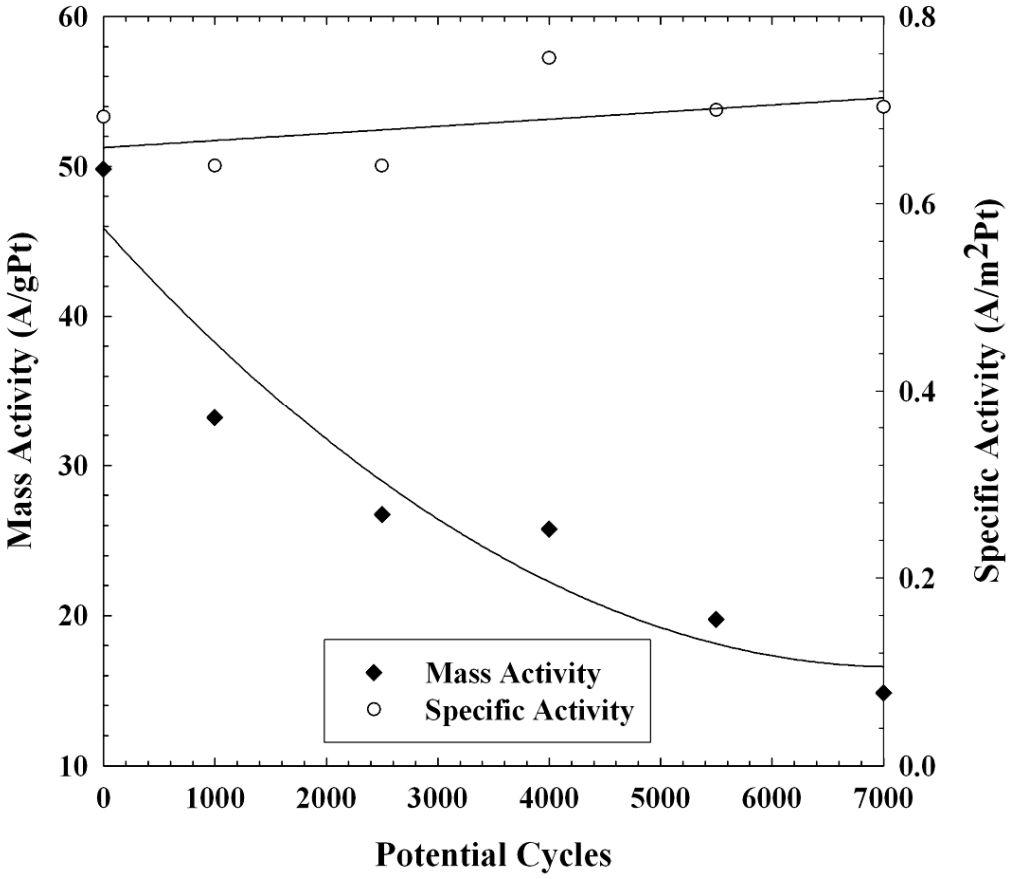

Figure 5.7: Measured catalyst mass activity and specific activity at 0.9 V cell voltage with pure oxygen at cathode for CCM #8 degraded at 60 °C

5.2.5 Pt Particle Sizes

Fresh and degraded CCM cathodes were examined by x-ray diffraction with a small grazing incident angle of 1 degree. The observed diffraction patterns in Figure 5.8 show the same Pt peak locations [15, 29] indicating a similar lattice parameter of 3.92 nm. The degraded cathodes yielded sharper Pt peaks compared to those from the fresh one due to the increased Pt particle average sizes. The calculated Pt particle average size increased with the increase of the degradation temperature as shown in Table 5.1. Such a

temperature effect on Pt particle size during potential cycling was also observed by Borup *et al*. recently [62]. Assuming a spherical shape of the Pt particles, the Pt catalyst surface area is given by,

$$S_{XRD}\left(\mathrm{m^2 g^{-1} Pt}\right) = \frac{6}{D} \times \frac{1000}{\rho}. \qquad \text{(Equation 5.4)}$$

D is estimated from the XRD data. These areas are compared with measured ECAs after 7000 potential cycles in Table 5.2. These data suggest that around 80 % of Pt surface area was electrochemically active for a typical fresh CCM used in this work. For the degraded three CCMs, the surface areas percentages remained in the cathodes were calculated from XRD and SEM-EDS analysis data, which will be discussed in the next section.

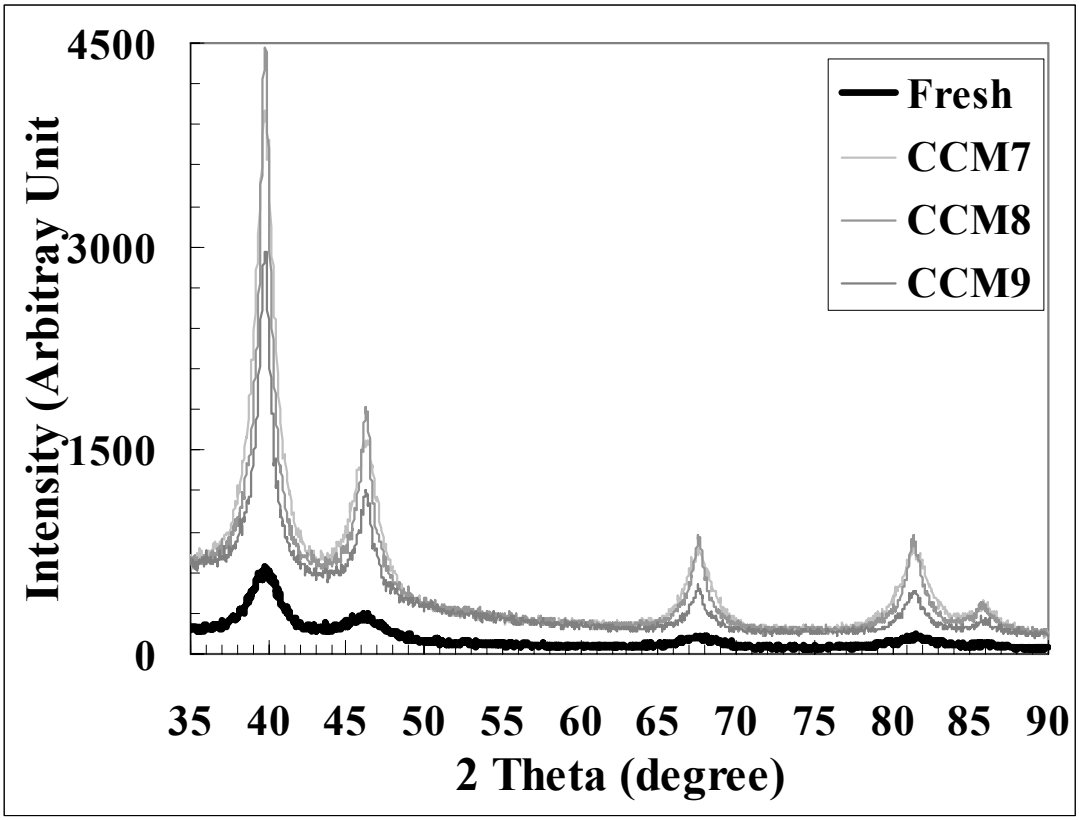

Figure 5.8: X-ray diffraction patterns of fresh cathode and degraded ones

Table 5.1: Pt particle sizes (nm) in fresh and degraded CCMs

CCMs	Pt {111}	Pt {200}	Pt {220}	Pt {311}	Average
Fresh	3.8	2.9	3.6	2.9	3.3
CCM #7	5.5	4.5	4.8	4.6	4.9
CCM #8	8.0	6.6	8.8	7.0	7.6
CCM #9	8.7	7.4	9.7	7.0	8.2

Table 5.2: Comparisons of the remained ECAs percentages with the estimated Pt surface areas percentages by XRD and SEM-EDS

CCM	D (nm)	S_{XRD} ($m^2 g^{-1}Pt$)	Rem. S_{XRD} %	ECAs ($m^2 g^{-1}Pt$)	Rem. ECAs %	Rem. Pt mass %	Estimated Rem. Surface %
Fresh	3.3	85	-	64-72	-		
CCM #7	4.9	57	69 %	29.4 (ini. 64.0)	46 %	73 %	50 %
CCM #8	7.6	37	45 %	21.1 (ini. 71.9)	29 %	61 %	27 %
CCM #9	8.2	34	41 %	15.2 (ini. 63.2)	24 %	52 %	21 %

5.2.6 Pt Distribution at CCM Cross-Sections

The cross-sections of degraded three CCMs were observed by SEM. Figure 5.9 shows the porous structures of the degraded CCM #9 cathode in SEM images. Such porous electrode structures were not observed in either the anodes or the cathodes of CCM #7 and CCM #8. This suggested that the significant carbon support corrosion at the high degradation temperature resulted in the accelerated cell performance loss. Since carbon corrosion is accelerated by high temperatures and high potentials, Pt catalyst and carbon support degradation were not separable applying this accelerated catalyst degradation protocol where the potential cycles between 0.87 V and 1.2 V. A potential cycling procedure with lower potential levels could possibly be applied to minimize carbon corrosion, but would also result in a slow Pt catalyst degradation rate at low temperatures.

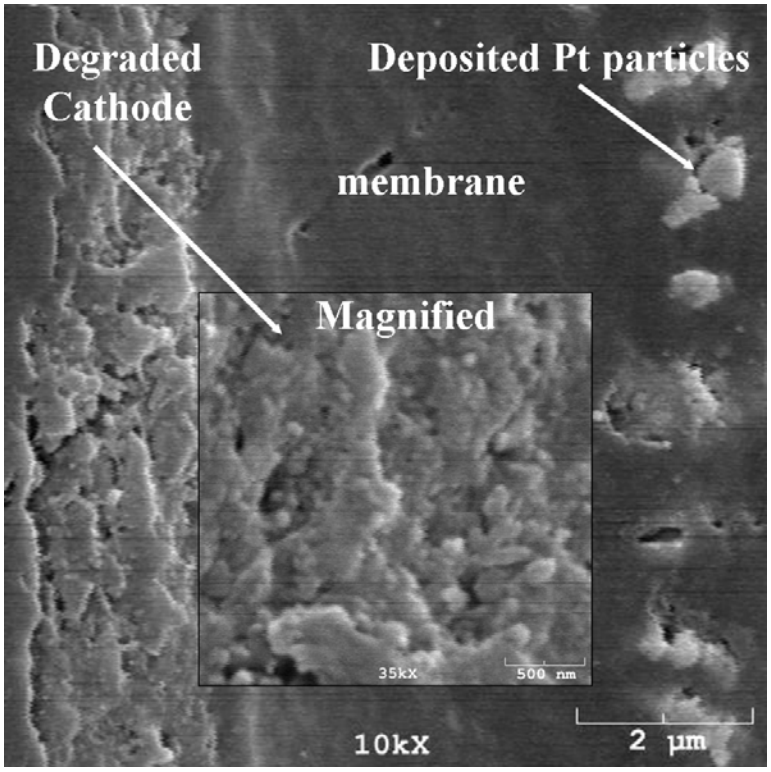

Figure 5.9: SEM images of the degraded cathode in CCM #9

Pt distributions at the degraded CCM cross-sections colleted by SEM-EDS in Figure 5.10 show a Pt "band" near each cathode. Pt deposition in the membrane has been discussed previously. The brighter Pt bands in CCM #8 and CCM #9 indicated higher Pt atom density in bands and more Pt loss from the cathodes. With the SEM-EDS elemental analysis applying the surface coated gold as a constant reference composition, Pt atom percentages in the anode, the cathode and Pt band regions were calculated with the data listed in Table 5.3. The anodes had similar Pt percentages of 38-41 %, close to the measure value of 40 % in a fresh anode, which suggested no significant anode Pt loss during potential cycling as expected. Higher degradation temperatures resulted in greater Pt loss from the cathodes through dissolution. For CCM #9, almost half of the Pt originally in the cathode was found in the membrane after cycling. Typical Pt ion

concentrations in effluent water were around 1-10 pg/g measured by a Inductively Coupled Plasma Mass Spectroscopy with a detection limit of 1 pg/g. Compared the amount Pt transported into the membrane electrolyte, the amount of Pt dissolved in water effluents is negligible.

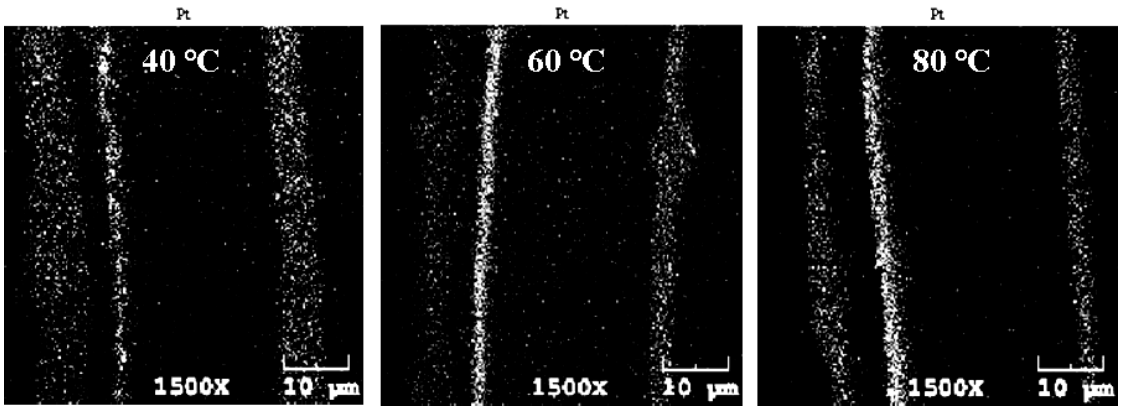

Figure 5.10: Pt distribution SEM-EDS cross-section images of the degraded CCMs: CCM #7 (40 °C), CCM #8 (60 °C) and CCM #9 (80 °C)

Table 5.3: Average Pt/Au ratios and widths of the anode, the cathode and the Pt "bands" and the calculated overall Pt% in the degraded CCMs

CCMs/Regions		Pt/Au ratio	Width (μm)	Estimated CCM Pt%
CCM #7	Cathode	0.7±0.1	7.0±1.0	43
	Pt band	1.1±0.2	1.6±0.2	16
	Anode	1.0±0.2	4.7±1.0	41
CCM #8	Cathode	0.9±0.1	7.5±1.1	36
	Pt band	2.5±0.6	1.7±0.3	23
	Anode	1.5±0.3	5.2±1.6	41
CCM #9	Cathode	1.9±0.4	5.7±0.8	32
	Pt band	4.0±1.0	2.6±0.6	30
	Anode	2.4±0.4	5.4±1.6	38

Accounting for the Pt lost from the cathode into the ionomer and accounting for the increase in particle size after cycling, the catalyst surface area in the degraded cathode can be estimated as a fraction of the original area.

$$\frac{\mathrm{ECA}_{\mathrm{estimated}}}{\mathrm{ECA}_{\mathrm{original}}} = \frac{m_c^f}{m_c^o} \times \frac{D_o}{D_f}. \qquad \text{(Equation 5.5)}$$

These data are shown in last column on the right of Table 5.2. The estimated values are close to the measured ECA, indicting a good consistency of our measured data by XRD, SEM-EDS and electrochemical methods.

To calculate Pt catalyst dissolution rates ($g/cm^2Pt/cycle$ or $g/cm^2Pt/min$) during potential cycles, we assume that the dissolution rates depends only on the degradation temperature and Pt particle size, but not surface area *S(N)*. It was generally believed smaller Pt particles are less stable with larger surface energies. Based on the Darling and Meyers's calculations [16], the Pt dissolution thermodynamic equilibrium potential adjusted by the Kelvin equation with a surface tension of 2.37 J/mol had down shifts of 75 mV and 28 mV for Pt particles with 3 nm and 8 nm diameters, respectively. This small difference of potential shifts magnified by an exponential term in Butler-Volmer equation would result in about five times of Pt dissolution rate difference based on the Darling and Meyers's dissolution rate model [16]. So taking account of such a particle size effect on Pt dissolution rate, we can write the following differential equation for the cathode Pt mass loss rate (g/cycle or g/min):

$$\frac{dm_{\mathrm{Pt}}}{dN} = k_D^0 e^{\frac{-E_a}{RT}} e^{\frac{1}{RT}\frac{\sigma M}{\rho}\frac{1}{D}} \times S(N) \times CL\,, \qquad \text{(Equation 5.6)}$$

where, k_D^0 is the apparent dissolution rate constant with an activation energy of *Ea*, σ is the surface tension (2.37 J/mol) [16], *M* is the Pt molecular weight (0.1951 kg/mol), ρ is the Pt metal density (21450 kg/m^3), *D* is the Pt particle diameter, and *CL* is the cathode Pt loading (12.5 mg per CCM). If we further assume linear increases of Pt particle sizes and locally linear profiles of surface areas *S(N)* between two nearest measurements during potential cycling, the activation energy E_a was calculated to be 37.8 (kJ/mol) with a value of 2.15×10^{-5} (g/cm^2 Pt/cycle) for k_D^0 constant. Comparing the activation energy of 25.4 (kJ/mol) for surface area loss applying a first order rate model discussed previously in section 5.2.2, this larger activation energy of Pt dissolution rate was due to the inclusion of the particle size (*D*) term in the calculation and such calculation resulted the activation energy was more meaningful. The Pt dissolution rates ($k_D^0 e^{\frac{-E_a}{RT}} e^{\frac{1}{RT}\frac{\sigma M}{\rho}\frac{1}{D}}$) shown in Figure 5.11 were quite close to those observed in Johnson [32], Rand [31] and Kinoshita's [27] dissolution studies in acid solutions. The dissolution rates decreased with potential cycling due to the increase Pt particle sizes.

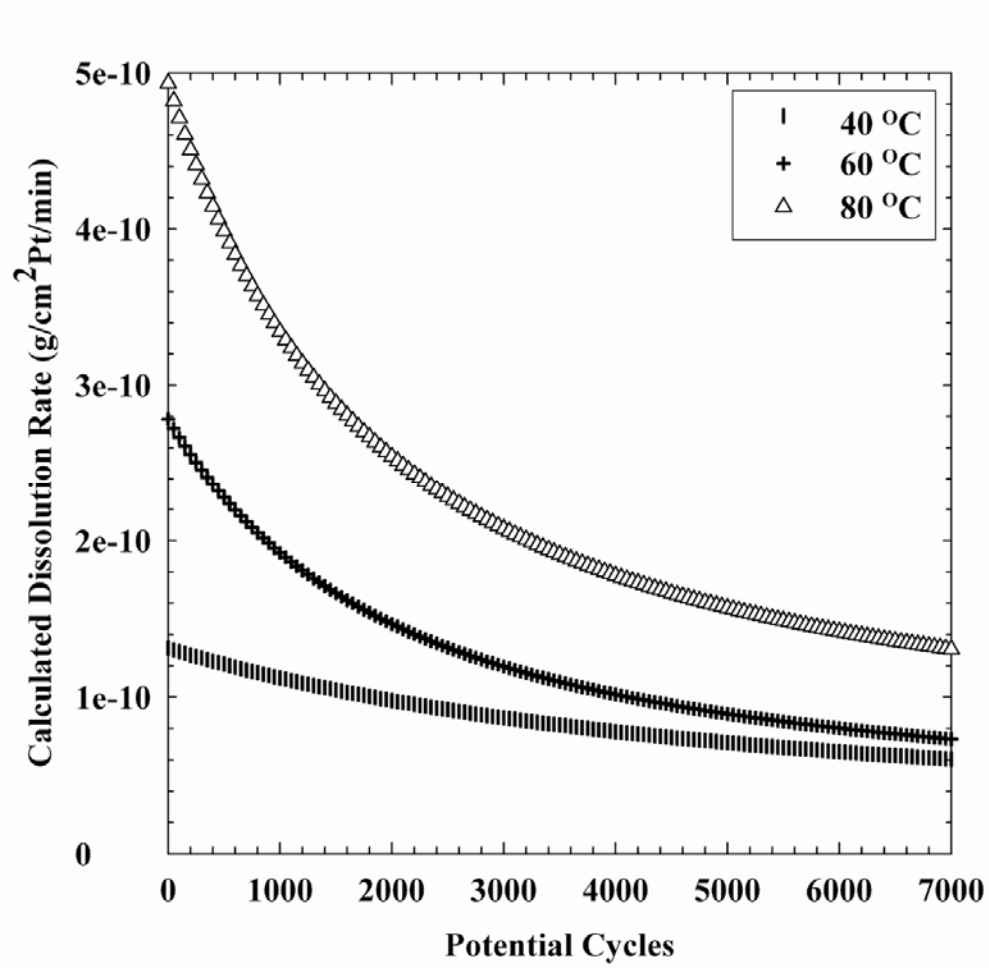

Figure 5.11: Calculated Pt dissolution rates during potential cycling for CCM #7 (40 °C), CCM #8 (60 °C) and CCM #9 (80 °C)

5.3 Summary

In summary, carbon supported Pt catalyst durability was studied at three degradation temperatures of 40, 60 and 80 °C under square-wave potential cycling. Membrane degradation was found to be minimal during the overall 160 hours in each degradation test. With potential cycling, cell performances and cathode electrochemically active surface areas decreased. The loss rates of the cell voltages and ECAs were

accelerated at the higher degradation temperatures. A Pt band was formed in the membrane after degradation test due to the dissolved Pt ions diffusion and deposition by hydrogen reduction in membranes. Increased amount of Pt atoms were lost into membrane at higher degradation temperatures. The remained Pt catalysts in the degraded cathodes had the increased average particle sizes compared to 3.3 nm in the fresh cathode, and it increased with the degradation temperatures. The cathode in CCM #9 degraded at 80 °C suffered significant carbon corrosion due to the high degradation temperature and applied high voltage during the potential cycling. So there is a large tradeoff the benefits running PEM fuel cell at relatively high temperatures due to the limited lifetimes of catalyst and its support. New catalysts with the improved durability are needed for future commercial applications at relatively high temperatures.

CHAPTER 6

RELATIVE HUMIDITY AND OXYGEN PARTIAL PRESSURE EFFECTS ON PT/C DEGRADATION

Membrane allowing for high temperature and low humidity fuel cell operations provide many advantages such as better heat transfer. In general, we were interested in the study of environmental variable's effects on cathode catalyst degradation, including temperature, humidity, and gas partial pressures. We know that the location of Pt deposition in the membrane, forming a Pt band, depends on the oxygen partial (chapter 4). Both water activity and oxygen partial pressure affect Pt surface oxidation [49, 63] with the details further discussed in chapter 7. Also, transport of Pt ions in the membrane may be affected by the water content in the ionomer, although the details of cation transport in Nafion® are still under investigation. So in this chapter, we further explored the effects of relative humidity (or water activity) and oxygen partial pressure on carbon supported platinum catalyst degradation under the accelerated cathode degradation conditions.

6.1: Potential Cycling Degradation Test

As previously described, commercial CCMs (#10-15): 5×5 cm constructed from Nafion® 117 membrane and Pt/C catalyst layers with Pt loadings of 0.3 mg_{Pt} cm^{-2} in both the anode and cathode were used. All CCMs were wet-up and conditioned as described in Appendix B. Following conditioning, the potential of the cell was cycled at a cell temperature of 60 °C with a square-wave between 0.87 and 1.2 V vs. reference hydrogen

electrode (RHE) and a time step of 30 s at each potential, using a Potentiostat/Galvanostat (EG&G Princeton Applied Research 273A). Pure hydrogen (0.38 dm^3/min) was supplied to the anode, which served as both the reference and the counter electrodes. Either pure N_2 (CCM #10-11), air (CCM #12-13), or pure oxygen (CCM #14-15) was supplied to the cathode, working electrode, at a flow rate of 0.91 dm^3/min. The temperatures of both anode and cathode saturators were set to be 45.8 °C (50 %RH for tests of CCM #11, #13, and #15) or 60 °C (100 %RH for tests of CCM #10, #12, and #14). During the 3600 total potential cycles, the cathode active surface areas (ECAs) were measured periodically. The degraded CCMs were all observed by SEM/EDS to study the distribution of Pt catalyst in the CCM cross-sections. The Pt particle sizes and size spatial distributions in the degraded CCMs were studied by X-Ray diffraction with a fixed incidence angle of 0.5-20 degrees. The RHE potential under the two humidity levels at 60 °C changed very slightly due to the different hydrogen partial pressures at the anode. So at fully humidified condition, cycled potentials of the cathode were 1.6 mV higher than those at the 50 %RH condition based on Nernst equation. This potential difference was believed to have less than 1 % differences of catalyst mass, surface, or radius initial change rate, calculated by our cathode degradation model presented in chapter 9. Hence this difference was neglected during the further discussions in this chapter.

6.2: Results and Discussions

6.2.1 Catalyst ECAs

During the cathode degradation tests, the active surface areas decreased due to both Pt particle growth and Pt mass loss. All CCMs (#10-15) had the quite high initial active surface areas of 105-135 m^2/gPt with an average Pt particle size of 2.2 nm diameter. The ECAs plotted in Figure 6.1 shows a similar 1st order loss rate with number of potential cycles as we previously discussed in section 5.2.2. The relative humidity effect on the catalyst active surface area loss was quite clear. All three tests conducted at 100 % RH had the almost twice higher rates of active surface area loss than their lower humidity counterparts. It was found that high relative humidity (or water activity) increases the rate of Pt surface oxidation [49]. Since the dissolution of Pt which is generally considered as an important reaction for catalyst degradation, faster Pt oxidation or higher oxide surface coverage should reduce the rate of Pt dissolution. Hence, it is speculated that high humidity or water content accelerates Pt ions transport in the ionomer, located in either the cathode or membrane, resulting in a faster Pt nanoparticle growth and a greater rate of Pt mass loss through Pt deposition by hydrogen reduction. On the other hand, oxygen partial pressure only had a minor effect, with a very slightly lower ECA loss rate at a higher oxygen partial pressure, possibly due to the beneficial high Pt oxide surface coverage.

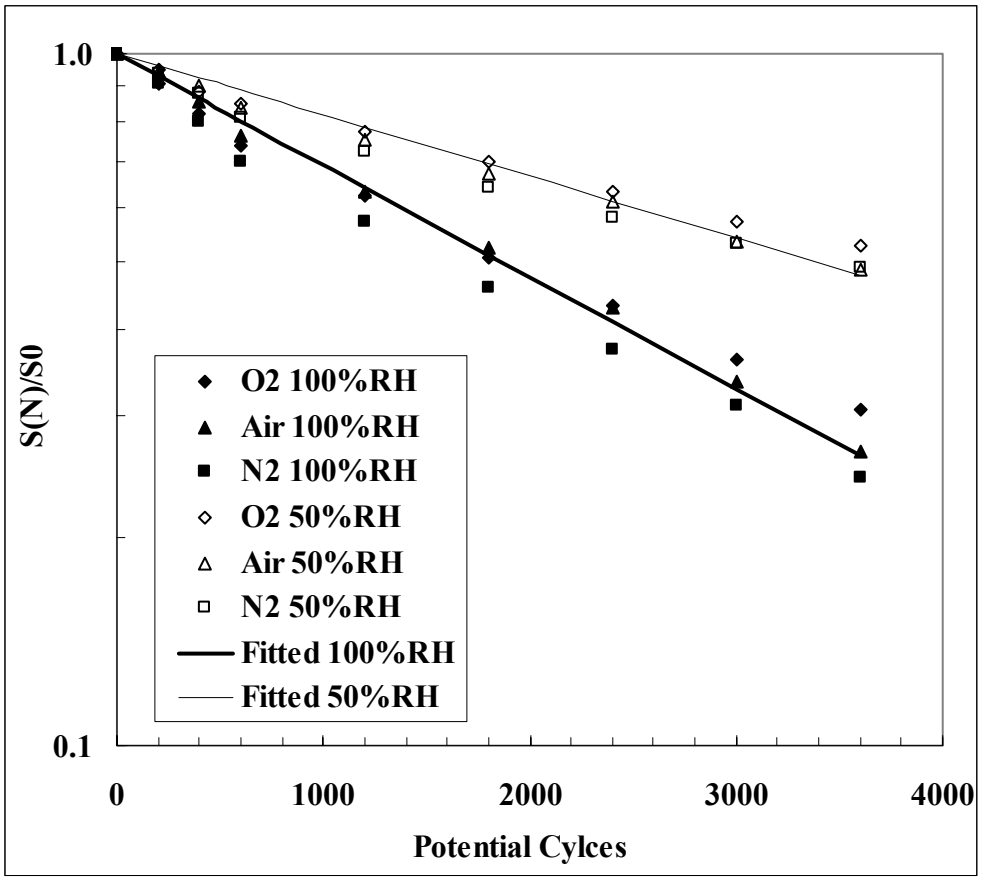

Figure 6.1: Cathode active surface area losses during the potential cycling

6.2.2 Pt Distribution at CCM Cross-Sections

The cross-sections of all degraded CCMs were observed by SEM, and the images are shown in Figure 6.2. Flowing air (CCM #12-13) or pure oxygen (CCM #14-15) at the cathode resulted in Pt band formations in the membrane with the locations (listed in Table 4.3) depending on gas crossover rates previously studied. As expected, there was no Pt band in CCM #10-11 with nitrogen flowing at the cathode.

Pt element SEM/EDS line scans around the degraded cathode cross-sections, shown in Figure 6.3, confirmed the Pt deposition at the cathode-membrane interface with nitrogen at the cathode. And it's very clear that there was significantly greater deposition of Pt under fully humidified condition (CCM #10) compared to the low humidity case (CCM #11). When oxygen flowed at the cathode (CCM #14-15), the distribution of Pt was relatively uniform, which is also expected for CCM #12-13. The amount of Pt deposited in the Pt bands was estimated and is listed in Table 6.1. Similar to the loss rate of catalyst active surface, the Pt mass losses were more than double at the high humidity than the low humidity condition. Again, no significant difference of cathode Pt loss was observed between air and pure oxygen tests for both high and low humidity conditions.

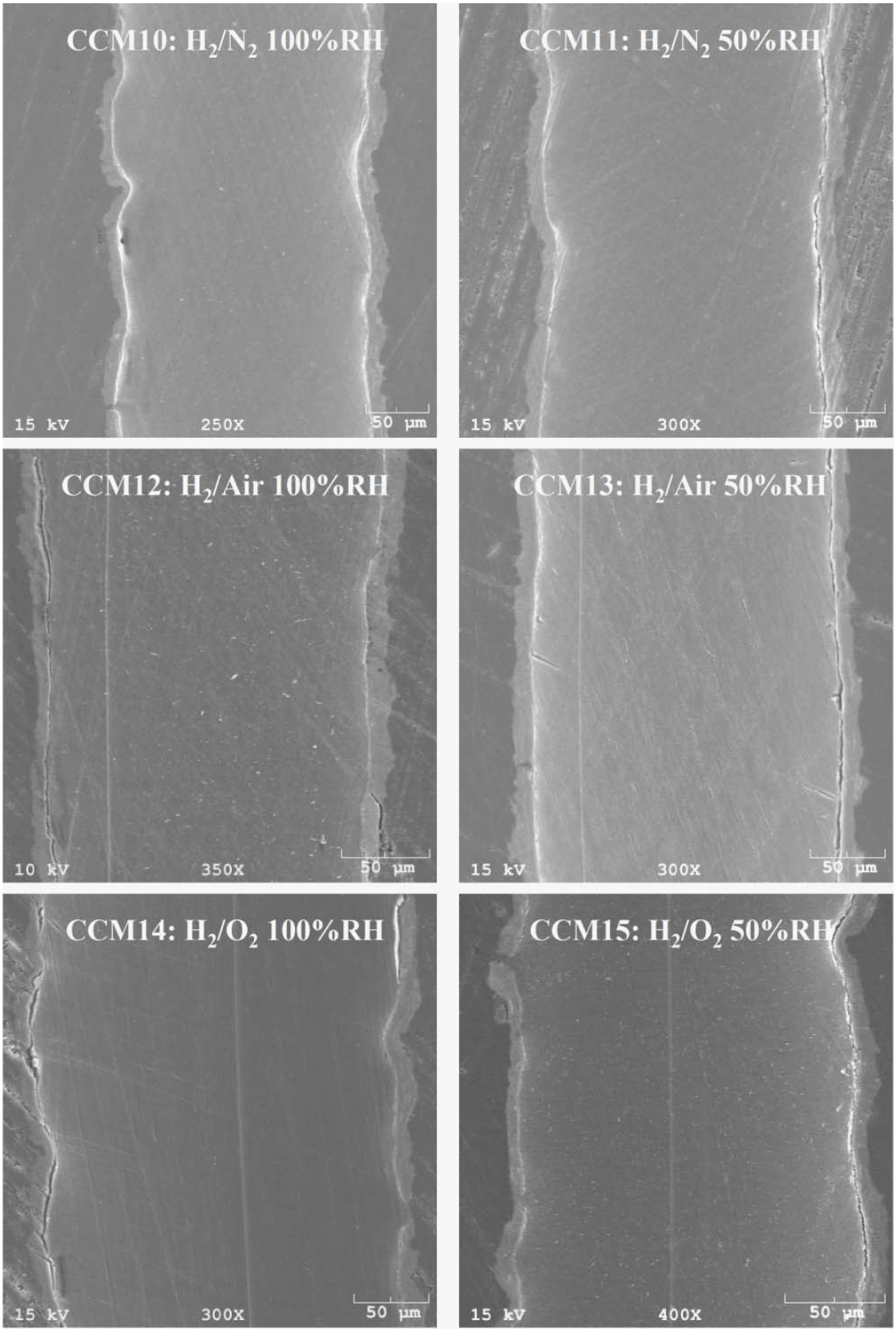

Figure 6.2: SEM images of the degraded CCMs cross-sections (all cathodes on the left)

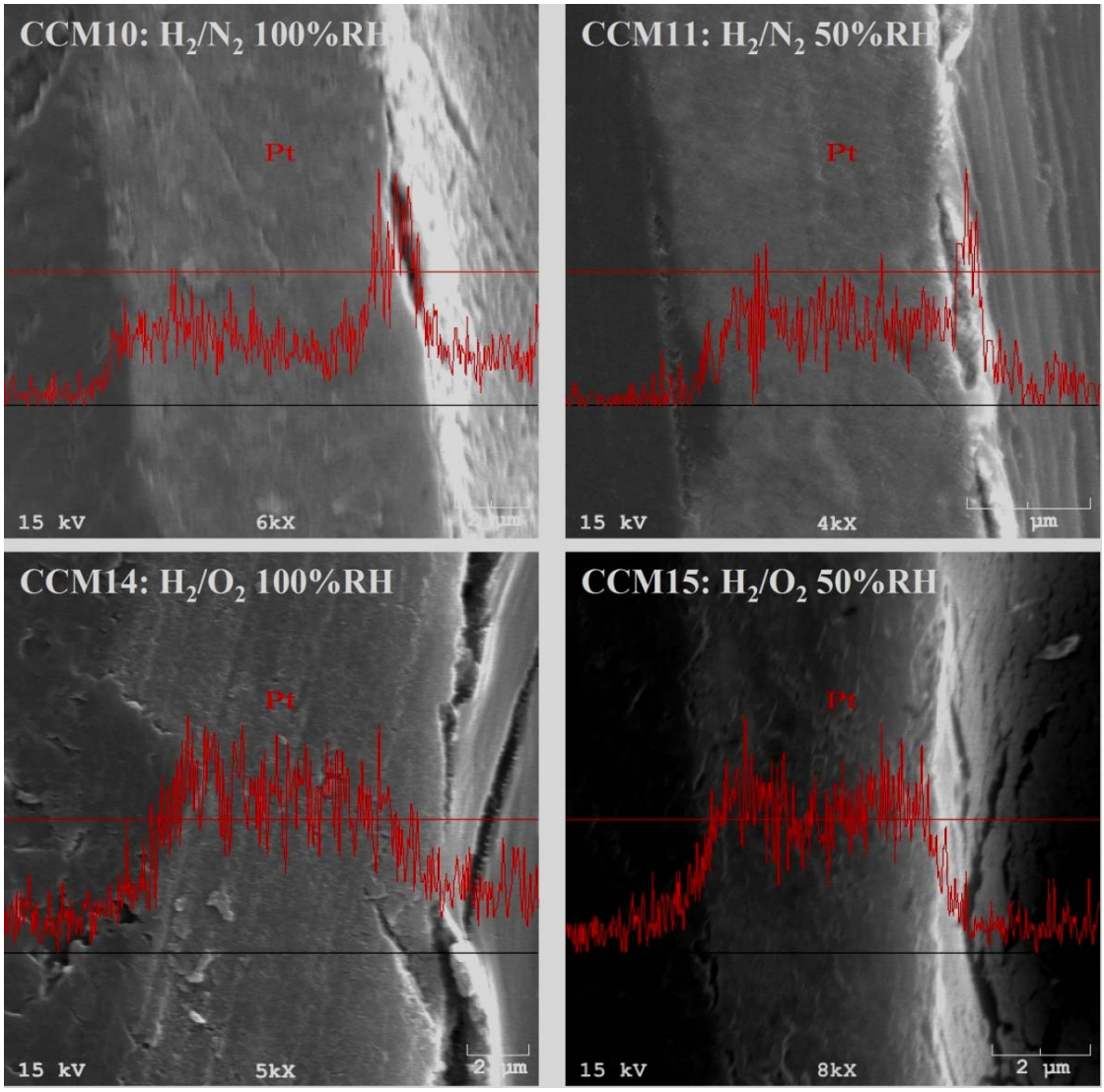

Figure 6.3: SEM line scans of Pt element content in the degraded CCMs cathodes

Table 6.1: Platinum distributions in a fresh and the degraded CCMs

CCMs/Regions		Pt/Au ratio	Width (μm)	Estimated CCM Pt %	Cathode Pt mass loss %
Fresh CCM	Cathode	1.10±0.07	10.7±1.6	50.7	
	Anode	1.09±0.03	11.1±1.0	49.3	
CCM #12 (H_2/Air 100 %RH)	Cathode	0.9±0.1	11.3±0.5	33.7	30
	Pt band	5.2±0.5	0.8±0.1	14.5	
	Anode	1.3±0.3	11.5±0.5	51.8	
CCM #13 (H_2/Air 50 %RH)	Cathode	1.1±0.3	12.5±0.4	44.5	11
	Pt band	2.6±0.5	0.66±0.04	5.9	
	Anode	1.2±0.2	12.8±0.6	49.7	
CCM #14 (H_2/O_2 100 %RH)	Cathode	0.57±0.05	10.3±0.6	33.9	29
	Pt band	1.85±0.29	1.3±0.2	13.9	
	Anode	0.88±0.04	10.5±1.6	52.3	
CCM #15 (H_2/O_2 50 %RH)	Cathode	1.3±0.4	9.6±0.6	44.3	12
	Pt band	1.7±0.4	1.0±0.1	6.0	
	Anode	1.4±0.3	10.0±1.0	49.7	

6.2.3 Pt Particle Sizes

The Pt particle sizes in the degraded CCMs were measured by X-ray diffraction with the copper anode Kα radiation. To probe the Pt particle sizes in the cathodes, the cathode/membrane interfaces, and the Pt bands in the membrane, the X-ray incidence angle was varied from 0.5 to 20 degrees. To estimate the X-ray penetration depth in a fresh CCM, relative intensities of the incidence X-ray were calculated (Equation 6.1) at the varied vertical penetration distances (x) from the cathode surface. The electrode and membrane (Nafion® 1100) mass attenuation coefficients (μ/ρ) and density (ρ) were calculated (Table 6.2) based on elemental mass attenuation coefficients [64] weighted by element percentages in the electrode and the membrane. The electrode contained 30 wt.% Nafion® 1100 polymer and Pt supported on Vulcan carbon (20 wt.% of Pt in Pt/C). The Nafion® polymer was simply assumed to have a composition of CF_2 neglecting elements

of sulfur and oxygen. The Pt catalyst loading in the electrode was 0.3 mgPt/cm^2 (14 wt.% Pt in electrode), and the total electrode mass (0.3/14% mg/cm^2) divided by the electrode thickness of 10 microns gave the estimated overall electrode density about 2.14 g/cm^3. The density of air-dried Nafion® 1100 is about 1.95 g/cm^3 [65].

$$\frac{I(x)}{I_0} = \exp\left[-\left(\frac{\mu}{\rho}\right)\rho x\right] \qquad \text{(Equation 6.1)}$$

Table 6.2: Calculated cathode and membrane mass attenuation coefficients in a fresh Nafion® 117 CCM under the Cu Kα line (8.0478 kV) radiation

Regions	Elements	Element mass attenuation coefficients [64] (cm^2/g)	Element weight percentages (%)	Products	Weighted mass attenuation coefficients (cm^2/g)
Cathode	C	4.505	60	2.703	34.24
	F	15.77	26	4.100	
	Pt	196.0	14	37.44	
Membrane	C	4.505	14	0.631	14.19
	F	15.77	86	13.562	

The calculated X-ray relative intensities with a vertical penetration distance from a fresh cathode surface are plotted in Figure 6.4. It is clear that with an incidence angle less than 2 degrees only the cathode region is subjected X-ray detection. With an increased incidence angle, Pt particles deposited in membrane (30 μm or 90 μm beneath the cathode/membrane interface for the H_2/air or H_2/O_2 cycled CCMs) can be detected depending on the particle abundance and particle sizes (or Pt element content).

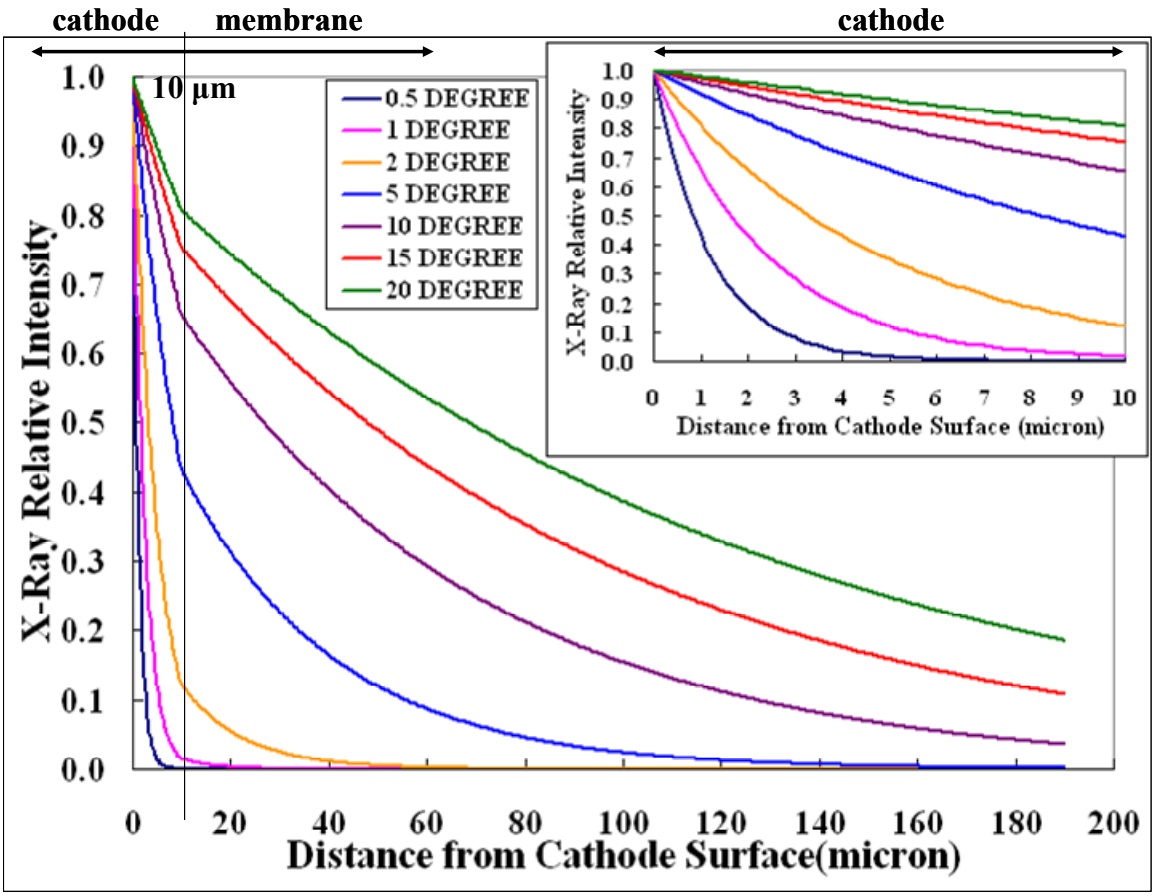

Figure 6.4: Calculated X-ray relative intensities with vertical distances from cathode surface into a fresh Nafion® 117 CCM at the varied incident angles

Platinum X-ray {111} peak were collected (plotted in Appendix C) and fitted by Jade 7.5 (Material Data, Inc.) with the fitted average Pt particle sizes plotted in Figure 6.5. For the H_2/N_2 cycled CCMs (#10-11), platinum amounts were not uniformly distributed in the cathode region. A significant amount of Pt is deposited at the interface as shown in Figure 6.3. Pt particles sizes (CCMs #10-11) determined from the X-ray measurements generally increased with increasing the X-ray incidence angle. Although the measured Pt particles size is the averaged value depending on Pt content, particle sizes and X-ray

intensities in the whole detection region, it was evident that Pt particles deposited at the interface were much larger than those in the cathode. Large Pt particles (about 30 nm) deposited in the ionomer were observed by TEM images in a H_2/N_2 degraded CCM cathode/membrane interface [66]. For the H_2/Air (or pure oxygen) cycled CCMs, the measured Pt particle sizes were relatively uniform with an incidence angle of 0.5-2 degrees. With a further increased X-ray incidence angle, Pt particles in the Pt band were detected as shown by the significant increase of measured Pt particle size. Since the Pt contents in these degraded CCM cathodes were relatively uniform, it suggested that the particle size across the cathode was also relative constant under the H_2/air (or O_2) cycling.

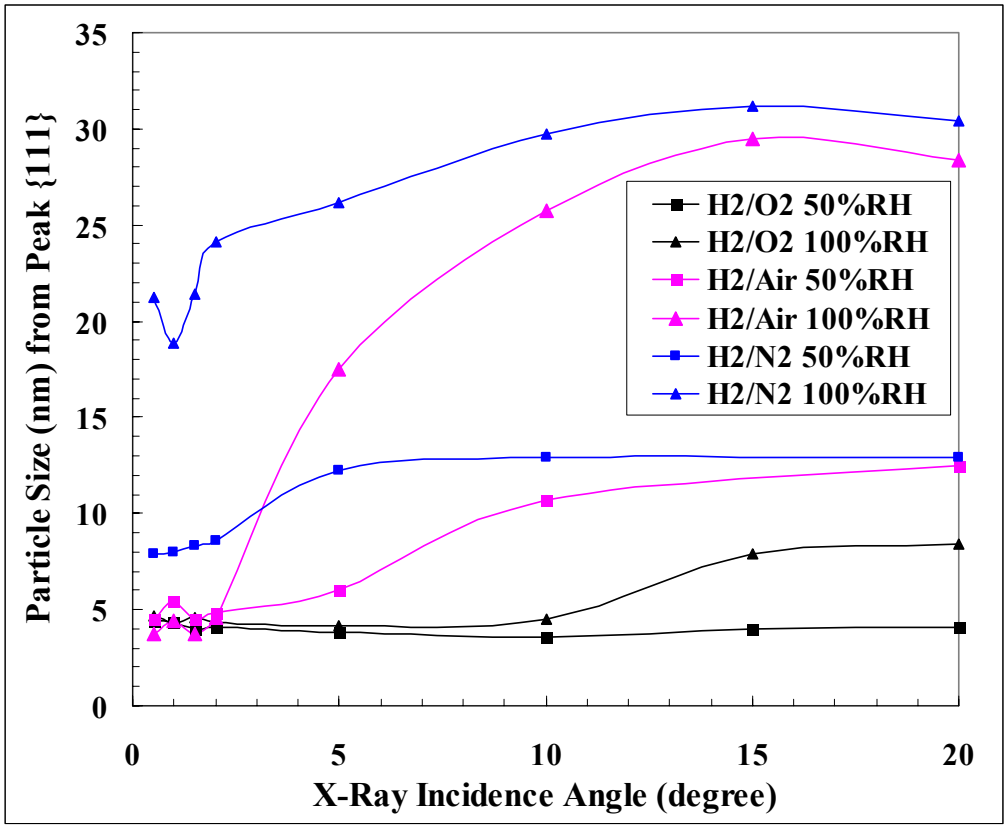

Figure 6.5: Pt particle sizes in the degraded CCMs at varied X-ray incident angles

6.2.4 Cathode Platinum Dissolution Rate

To study the effects of humidity on Pt dissolution rates, cathode Pt mass losses, Pt particle sizes, and catalyst active surface areas were averaged from the tests with air and oxygen at each relative humidity level. Linear profiles of particle size *D(N)* and active surface area *S(N)* were assumed between two experimental measurements. The loss rate of Pt mass from the cathode with the number of potential cycles *N* was simply written to be proportional to active surface area *S(N)* and catalyst loading *CL* (7.5 mgPt/cathode). The exponential term of the inverse of particle size [67] was included due to the concern of particle size effects on Pt dissolution rate in a form of Butler-Volmer equation. σ is the surface tension (2.37 J/mol) [16], *M* is the Pt molecular weight (195.1 g/mol), ρ_{Pt} is the Pt metal density (21.45 g/m^3), and *k'* (g/cm^{2}Pt/min or g/cm^{2}Pt/cycle) is the fitted rate constant. The calculated Pt dissolution rate ($k'e^{\frac{1}{RT}\frac{\sigma M}{\rho_{Pt}}\frac{1}{D(N)}}$: g/cm^{2}Pt/min or g/cm^{2}Pt/cycle) was plotted in Figure 6.6 with the fitted *k'* value of 2.87×10^{-12} and 7.84×10^{-12} (g/cm^{2}Pt/min) at 50 % RH and 100 % RH respectively. Figure 6.6 shows that high humidity accelerated cathode Pt mass loss with the initial Pt dissolution rate close to three times of the rate at the low humidity condition. The dissolution rates decreased with potential cycling due to the particle growth.

$$\frac{dm_{Pt}}{dN} = k'e^{\frac{1}{RT}\frac{\sigma M}{\rho_{Pt}}\frac{1}{D(N)}} \times S(N) \times CL \qquad \text{(Equation 6.2)}$$

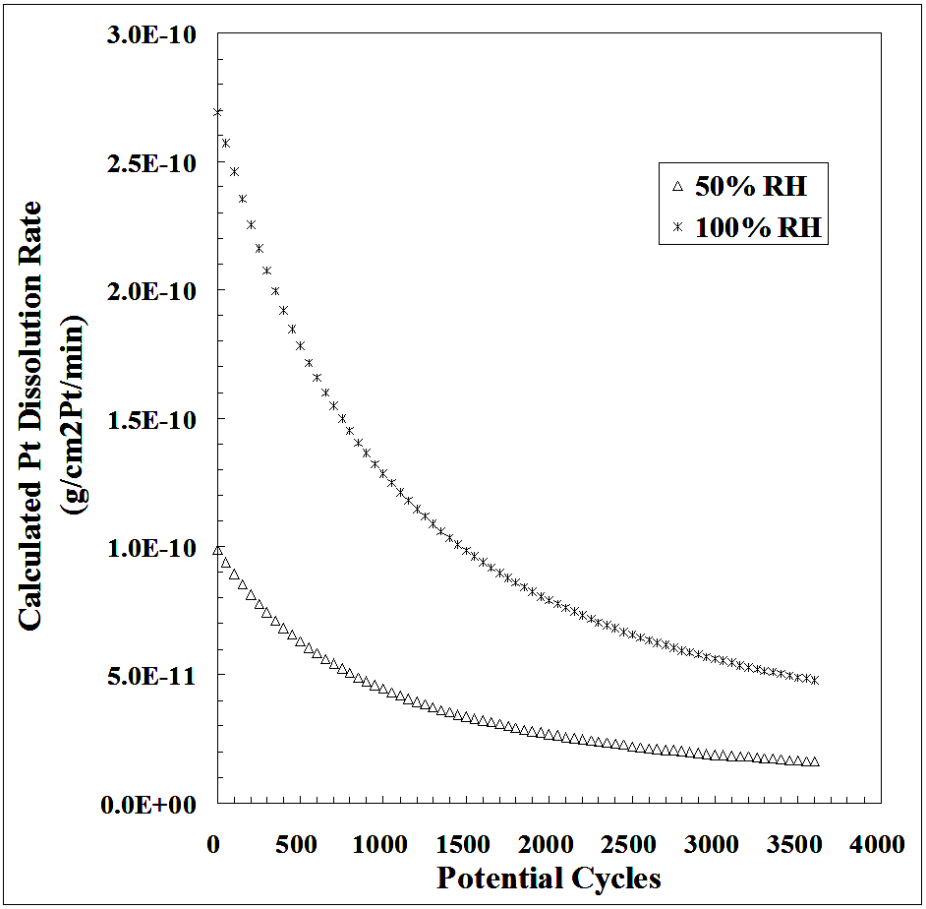

Figure 6.6: Calculated Pt dissolution rate with number of potential cycles

Comparing pairs of high and low humidity conditions, it's clear that with increasing humidity more Pt mass was lost from the cathodes and deposited at the interfaces or in the membranes. High humidity or water activity enhances the Pt electrochemical oxidation process, which is expected to slow down the rate of catalyst degradation. However, this contradicts the observed behavior—increasing rates of degradation at higher humidity. To quantify the effects of humidity on platinum electrochemical oxidation by water, cyclic voltammetry curves were measured as described in chapter 7 in details, and the normalized Pt oxidation charges are listed in Table 7.1. At 60 °C a humidity increase from 50 % RH to 100 % RH only resulted in

about a 20 % increase of normalized oxidation charge. Also, at a fixed total pressure, an increase of relative humidity decreased the oxygen partial pressure by about 10 %, which should slow down Pt oxidation by gaseous oxygen. Hence, we believed that Pt surface oxide coverage under these two humidity levels at 60 °C was only slightly different.

It was concluded in Okada's study that low Nafion® water content resulted in low cationic mobility, depending on relative size of the moving cation and the ionic channel [68]. So it was mostly likely that the high humidity or increased polymer electrolyte water content results in larger and more abundant water (and ionic) channel networks facilitating the soluble platinum species transport, hence the faster Pt mass loss from the cathode. Based on the parametric study results from the cathode degradation model in Chapter 9, a three fold increase of Pt ion transport (or diffusivity) was estimated to account for the accelerated loss of Pt mass or active surface area when increasing humidity from 50 % RH to 100 % RH. This increase of the apparent Pt ion diffusivity seems pretty reasonable considering other research results: a two-four fold increase of membrane water content between 30 °C and 80 °C [69], a three fold increase of water diffusivity at 30 °C [70], and a five fold increase of proton conductivity at 60 °C [71].

6.3: Summary

It is summarized that the increased relative humidity accelerated the catalyst degradation including the faster active surface area loss and more cathode Pt mass loss. This was mostly due to the accelerated transport of dissolved platinum species in possible expanded water (or ionic) channel networks insides the polymer electrolytes. Also no

significant differences of catalyst degradation rates were found at varied oxygen partial pressures suggesting that Pt oxidation by oxygen gas may not be an important factor under the potential cycling degradation tests.

CHAPTER 7

PT ELECTROCHEMICAL OXIDATION AND REDUCTION

Platinum oxidation is an important process affecting oxygen reduction activity and durability of fuel cell Pt based catalyst. Oxygen molecules can not react on Pt surface covered by oxide species, and hence ORR activity is reduced. With regard to catalyst stability, coverage by surface oxides will slow down Pt dissolution, which is a dominant degradation process for Pt catalyst subjected to dynamic potential conditions. It was found in Paik's study [63] that about 80 % of oxide was formed through Pt oxidation by oxygen gas at the cathode potential of 0.85 V vs. RHE at 25 °C and 100 %RH. However, in a more recent study by Xu *et al.* [49], a series of reactions was proposed for the oxidation of Pt by gaseous oxygen as shown in reactions 7.1-7.4. It was also found that at 0.85 V vs. RHE and 100 °C, 50 % of the oxide was from electrochemical oxidation by water at 20 %RH, and the percentage increased to 70 % at 100 %RH.

$$Pt + O_2 \rightarrow Pt\text{-}O_2 \qquad \text{(Reaction 7.1)}$$

$$Pt\text{-}O_2 + H^+ + e^- \rightarrow Pt\text{-}HO_2 \qquad \text{(Reaction 7.2)}$$

$$Pt\text{-}HO_2 + Pt \rightarrow Pt\text{-}OH + Pt\text{-}O \qquad \text{(Reaction 7.3)}$$

$$Pt\text{-}OH \rightarrow Pt\text{-}O + H^+ + e^- \qquad \text{(Reaction 7.4)}$$

Since our fuel cell tests are mainly conducted at temperatures near 60 °C under fully humidified conditions, we are more interested in the study of electrochemical oxidation of Pt by water under a nitrogen protected environment. In this chapter, cyclic

voltammetry (CV) experiments conducted under various temperature and relative humidity conditions are reported. Platinum oxidation and oxide reduction kinetics were simulated and compared to experimental data.

7.1 Platinum Oxidation by Cyclic Voltammetry

Cyclic voltammetry curves were measured in the potential range of 20-1000 mV (vs. RHE) with a typical scan rate of 50 mV/s under the varied cell temperatures (25-80 °C) and humidity conditions (15 %RH-100 %RH). Pure hydrogen and nitrogen at atmospheric pressures were provided to the anode and the cathode, respectively. The measured CV curves are plotted in Figures 7.1-7.2, showing the effects of humidity and temperature respectively. At a given cell temperature, the areas of hydrogen adsorption/desorption and Pt oxidation/oxide reduction peaks increased with humidity as shown in Figure 7.1. The electrochemical oxidation of Platinum was delayed at the low humidity condition. Similar effects of humidity on CV curves were observed and discussed in the work [49] by Xu *et al*. On the other hand, temperature only slightly affected the shapes of the CV curves especially at a low humidity condition as shown in Figure 7.2(a). At the fully humidified condition (Figure 7.2(c)), an increase of cell temperature resulted in faster platinum redox reaction rates and slower hydrogen adsorption/desorption rates. In the study by Radovic-Hrapovic and Jerkiewicz [72], it was observed that hydrogen/anion adsorption/desorption peaks of a Pt(110) single-crystal electrode shifted to slightly less positive potentials in 0.5 M H_2SO_4 when the temperature was increased from 273 K to 333 K. In contrast to our observations, the total adsorption charge density was unchanged. This difference could result from either different Pt

electrodes, such that Nafion® polymer morphological change with temperature resulted in the catalyst/electrolyte interface (electrochemically active) area change in our tests, or the opposite temperature effect on hydrogen and anion adsorption in Radovic-Hrapovic and Jerkiewicz's work.

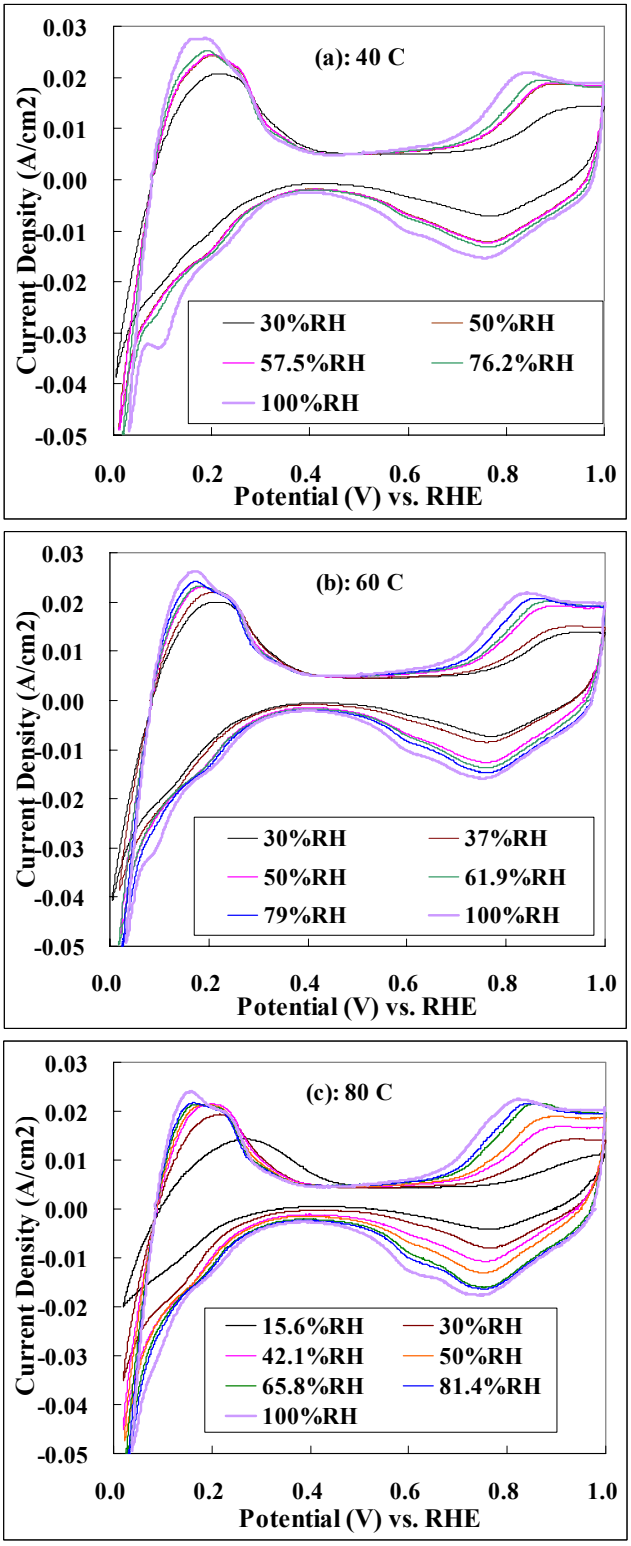

Figure 7.1: CV curves at the varied humidity and temperature (a) 40 °C, (b) 60 °C, and (c) 80 °C

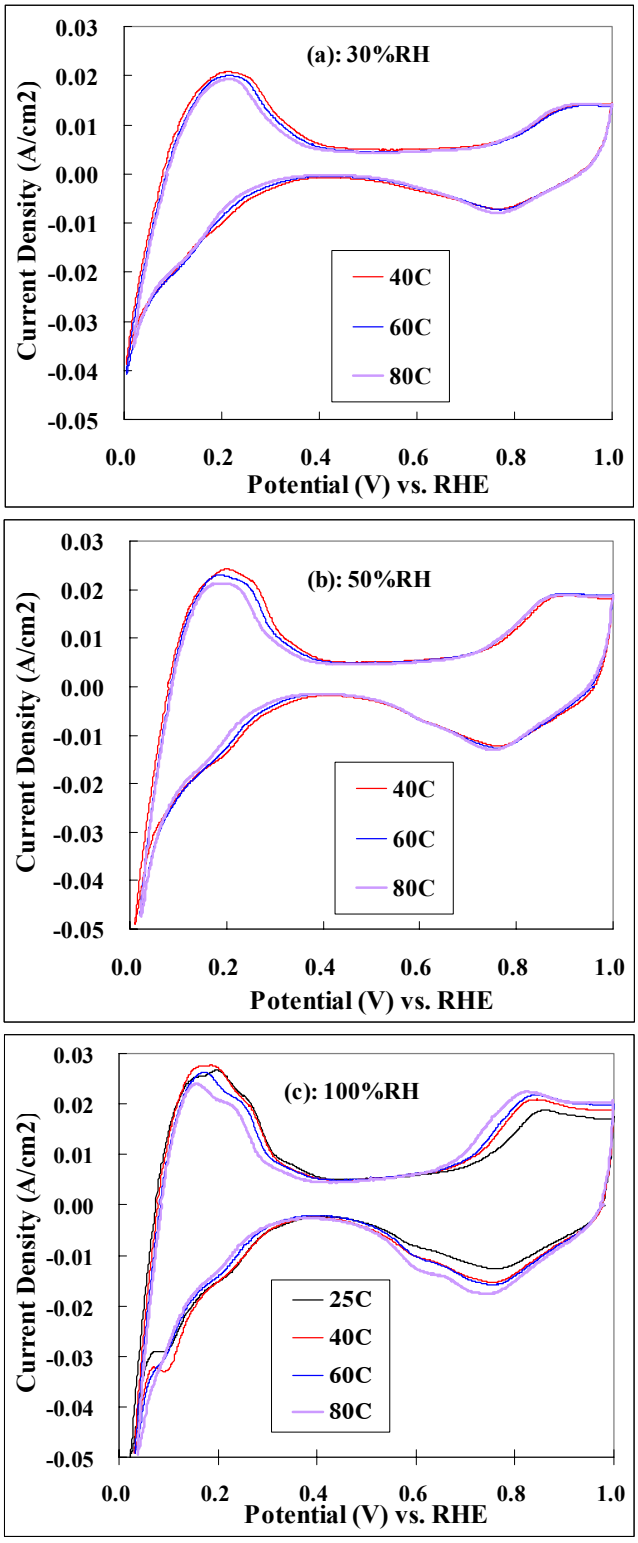

Figure 7.2: CV curves at the varied humidity and temperature (a) 30 %RH, (b) 50 %RH, and (c) 100 %RH

The charges in Coulombs associated with Pt oxidation of the total electrode (25 cm^2) were calculated by integrating oxidation peak areas with the charging/de-charging current and hydrogen crossover current removed. Due to the some overlapping hydrogen adsorption and hydrogen evolution peaks utilizing nitrogen at the working electrode as we discussed in chapter 3, the electrochemically active surface areas were reported as the average value from hydrogen adsorption (ECA_{AD}: integration down to 60 mV vs. RHE) and hydrogen desorption (ECA_{DE}) peak areas with a catalyst loading of 0.3 $mgPt/cm^2$. Then the Pt oxidation charges were normalized with the active surface area with the data all listed in Table 7.1.

Table 7.1: Normalized Pt oxidation charge at varied temperature and humidity conditions

Cell T (°C)	Humidifier T (°C)	RH%	Total Charge (Coul.)	ECA_{AD} (m^2/gPt)	ECA_{DE} (m^2/gPt)	Avg. ECA (m^2/gPt)	Norm. Charge ($Coul./m^2Pt$)
25	25	100.0	1.530	117.5	122.6	120.1	1.69
40	19	30.0	0.828	87.1	93.3	90.2	1.22
40	27.6	50.0	1.459	99.8	106.2	103.0	1.89
40	30	57.5	1.488	100.8	107.5	104.2	1.91
40	35	76.2	1.612	105.8	108.6	107.2	2.00
40	40	100.0	2.048	123.5	122.6	123.1	2.22
60	36	30.0	0.848	85.4	86.1	85.8	1.32
60	40	37.0	1.014	91.8	93.7	92.8	1.46
60	45.8	50.0	1.573	98.6	95.6	97.1	2.16
60	50	61.9	1.679	95.8	94.6	95.2	2.35
60	55	79.0	1.832	100.4	96.1	98.3	2.49
60	60	100.0	2.139	112.1	106.0	109.1	2.62
80	40	15.6	0.461	56.5	64.8	60.7	1.01
80	53	30.0	0.936	80.3	76.6	78.5	1.59
80	60	42.1	1.316	88.6	87.2	87.9	2.00
80	63.8	50.0	1.598	87.7	85.1	86.4	2.47
80	70	65.8	1.998	90.8	84.4	87.6	3.04
80	75	81.4	2.091	92.4	85.1	88.8	3.14
80	80	100.0	2.422	102.1	94.7	98.4	3.28

The normalized oxidation charges are plotted against relative humidity and water vapor partial pressure as shown in Figure 7.3 and Figure 7.4, respectively. Figure 7.3 shows the significantly positive effects of temperature on platinum electrochemical oxidation. Comparing the cases between 25 °C and 80 °C, both at fully humidified conditions, the normalized oxidation charge (Table 7.1) almost doubled at the higher temperature. Although the extent of oxidation increased with an increase of either relative humidity (or water activity in membrane electrolyte) or water partial pressure at the same cell temperature, relative humidity is a more meaningful parameter. As can be seen in Figure 7.4, the oxidation charge decreased with a temperature increase at the same water partial pressure. This decrease is ascribed to the relative humidity decrease. So the positive effects of temperature and relative humidity may explain the observations by Paik [63] and Xu [49] that high temperature and high humidity results that Pt oxidation is dominated by the electrochemical Pt oxidation by water instead of gaseous oxygen.

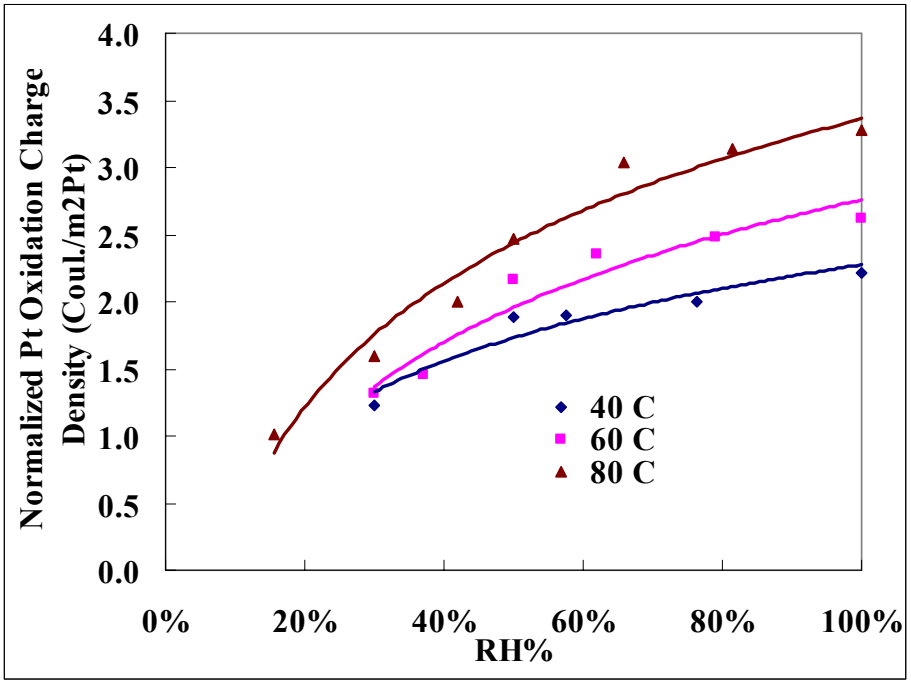

Figure 7.3: Plot of the normalized Pt oxidation charge density vs. relative humidity

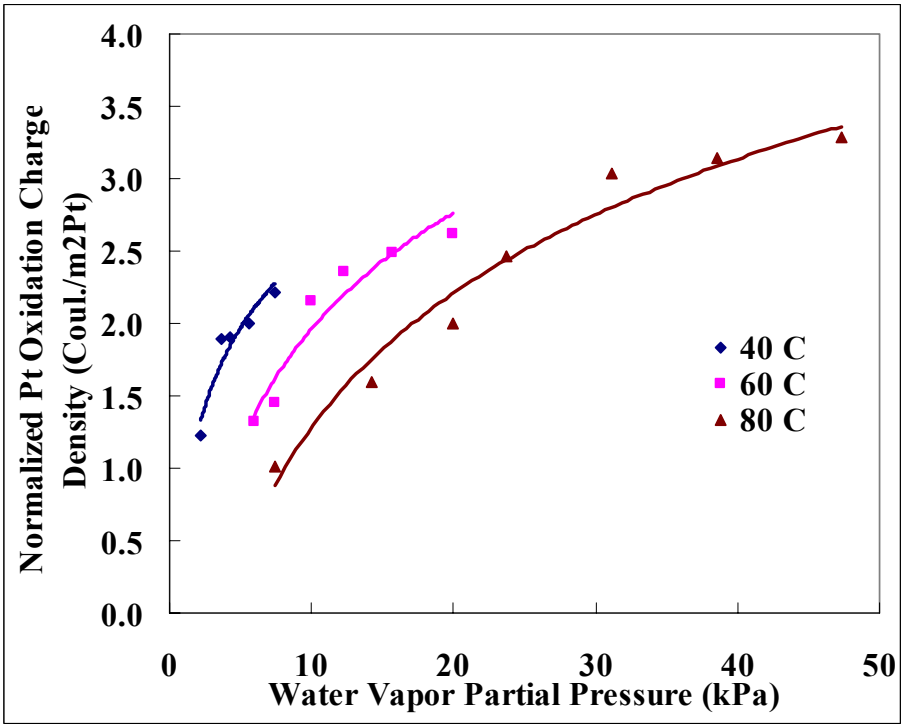

Figure 7.4: Plot of the normalized Pt oxidation charge density vs. water vapor pressure

7.2 Pt Oxidation Kinetic Simulation

Direct logarithmic growth of Pt oxide by water electrochemical oxidation at constant potential holds has been previously studied and simulated by Conway [73] and Heyd [37]. More recently, Darling and Meyers [16] incorporated a Pt oxide electrochemical reduction term in a modified Butler-Volmer equation (in the form of Equation 7.1) to simulate both oxidation and reduction behaviors in a cyclic voltammetry scan. The thermodynamic Pt oxidation potential (U^o) was adjusted (Equation 7.2) considering the high chemical potential (surface energy) of Pt and PtO at the nano-scale. Darling and Meyers's model also resulted in a thermodynamic equilibrium Pt oxide surface coverage at steady state during a potential hold. The continuous oxide production at a long potential holds is due to the oxygen atom penetration into Pt lattice or the so called Pt-O dipole-dipole "place exchange" in the electric field [74-76] leaving the oxide protection of the metal surface incomplete. The Pt-O dipole-dipole interaction coefficient (ω) represents the dipole place exchange mechanism, which also limits the Pt oxidation rate as shown a plateau current in CV curves at high oxidizing potential in Figure 7.1 and 7.2. In the combined kinetic expression of Pt oxidation (equation 7.1), only total oxides were counted and oxygen atoms in the different depth of Pt particle surface were not distinguished in Darling and Meyers's model. And this place-exchange process was not reflected in the Pt oxide reduction term. Under dynamic potential conditions, such as a cyclic voltammetry scan or high-low potential cycles, Darling and Meyers's model performed well due to the slow oxidation kinetics. The lag between the potential change and oxidation resulted in the hysteresis loop of Pt oxide coverage [16].

$$r = k\left\{\exp\left\{\frac{-\omega\theta}{RT}\right\}\exp\left\{\frac{\alpha_a n\ F(E-U)}{RT}\right\} - c_H^2\theta\exp\left\{\frac{-\alpha_c n\ F(E-U\ )}{RT}\right\}\right\} \quad \text{(Equation 7.1)}$$

$$U = U^0 + \frac{1}{2F}\left[\Delta\mu_{\mathrm{PtO}}^0 + \frac{\sigma_{\mathrm{Pt\,O}} M_{\mathrm{PtO}}}{\rho_{\mathrm{PtO}}}\frac{1}{RR} - \frac{\sigma_{\mathrm{Pt}} M_{\mathrm{Pt}}}{\rho_{\mathrm{Pt}}}\frac{1}{RR}\right] \quad \text{(Equation 7.2)}$$

Since we are more interested in the catalyst degradation under dynamic potential conditions, in our work we simply modified Darling and Meyers's model with added additional parameters reflecting temperature (activation energies: E_A *and* E_C) and humidity effects (*RH%* or water activity) on Pt oxidation and PtO reduction rates (Equation 7.3). A further improved platinum oxidation model including separate reaction/physical steps of top surface Pt oxidation and Pt-O dipole-dipole place exchange is recommended for the future work. Since the Pt electrochemical dissolution current is insignificant compared to Pt oxidation current [16], the cyclic voltammetry currents at high potentials (above 0.4 V vs. RHE) are solely ascribed to platinum electrochemical oxidation and PtO reduction. Similarly, Pt and PtO species mass balances were applied in terms of oxide surface coverage (θ) and Pt metal core radius (*RR*) as shown in Equation 7.4 and 7.5 respectively, where Γ_{max} represents the maximum Pt oxide coverage per surface area with a value of 2.18e-5 mol/m^2 calculated by dividing a specific charge of 210 μC/cm^2 for hydrogen adsorption/de-sorption at Pt surface by the Faraday's constant.

$$r = k_A(RH\%)\exp\left\{\frac{-E_A}{RT}\right\}\exp\left\{\frac{-\omega\theta}{RT}\right\}\exp\left\{\frac{\alpha_a n\ F(E-U)}{RT}\right\} - k_C c_H^2 \theta \exp\left\{\frac{-E_C}{RT}\right\}\exp\left\{\frac{-\alpha_c n\ F(E-U\ )}{RT}\right\} \quad \text{(Equation 7.3)}$$

$$\frac{d\theta}{dt} = \frac{r}{\Gamma_{\max}} - \left(\frac{2\theta}{RR}\right)\frac{dRR}{dt} \quad \text{(Equation 7.4)}$$

$$\frac{dRR}{dt} = -\frac{M_{\mathrm{Pt}}}{\rho_{\mathrm{Pt}}} r \quad \text{(Equation 7.5)}$$

The normalized CV curves with a scan rate of 50 mV/s at the varied temperature and humidity were simulated. The initial Pt particles had an average diameter of 3 nm. The concentration of protons was assumed to be 1 M as in Darling and Meyers's work [16]. One example of simulated CV at 60 °C and 100 %RH was compared to the normalized lab curve in Figure 7.5. The fitted parameter values were listed in Table 7.2, together with the other three cases at different temperatures and all fully humidified conditions. The locations of red-ox peaks matched the measured ones, and both the oxidation plateau current and oxide reduction peak current were comparable to the tested values, although there were slight differences of the curve shapes locally applying this simple model. The oxide coverage during the CV scan plotted in Figure 7.6 shows the similar hysteretic loop as observed by Darling and Meyers [16], due to the slow kinetics of Pt oxidation and PtO reduction resulted in the non-equilibrium conditions at the finite rate of potential sweeps. Our fitted oxidation reaction rate constants (k_A, k_C) were higher

than the other reference values as shown in Table 7.2, mostly due to the different nature of Pt electrode (either Pt wire or Pt/C nanoparticles with different particle sizes) and the different simulated experimental conditions (cell temperature and scan rate). All other parameters had the similar fitted values as literature data.

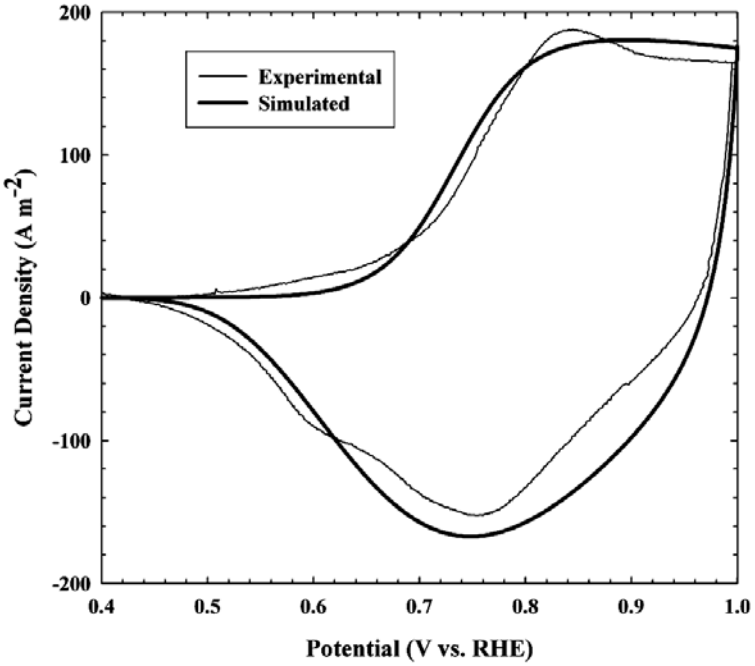

Figure 7.5: Simulated and measured normalized CV curves at 60 °C and 100% RH with a scan rate of 50 mV/s

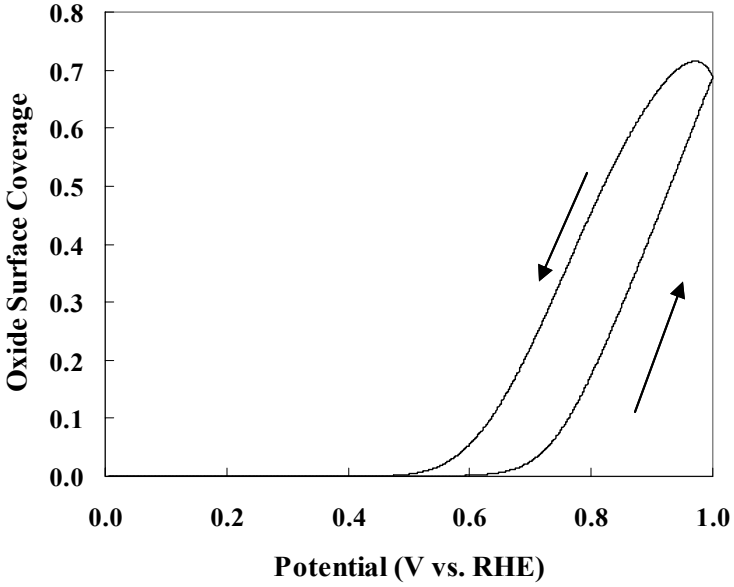

Figure 7.6: Simulated Pt oxide surface coverage during a CV scan at 60 °C and 100% RH with a scan rate of 50 mV/s

Table 7.2: Fitted parameter values for Pt electrochemical oxidation at 100 %RH condition

T (°C)	25	40	60	80	Adopted Values	Reference Values
U^0 (V)					0.98 V [25]	
α_a	0.3	0.35	0.4	0.4		0.25 ~ 0.45 [37]; 0.35 [16]
α_c	0.1	0.1	0.1	0.1		0.15 [16]
$\Delta\mu_{PtO}{}^0$ (kJ mol^{-1})	-30.4	-34.2	-38.0	-43.7		-42.3 [16]
σ_{Pt} (J m^{-2})					2.37 J m^{-2} [16]	
σ_{PtO} (J m^{-2})					1.00 J m^{-2} [16]	
ω (kJ mol^{-1})	30	30	30	30		24 ~ 35 [37]; 30 [16]
$k_A = k_C$ (mol m^{-2} s^{-1})	1.0×10^{-4}	1.0×10^{-4}	1.0×10^{-4}	1.0×10^{-4}		
$E_A = E_C$ (kJ mol^{-1})	7.37	7.37	7.37	7.37		
$k_A\times e^{(-E_A/RT)}$; $k_C\times e^{(-E_C/RT)}$ (mol m^{-2} s^{-1})	5.0×10^{-6}	6.0×10^{-6}	7.0×10^{-6}	8.0×10^{-6}		1.0×10^{-9} ~ 1.0×10^{-14} [37]; 1.36×10^{-7} [16]

A universal set of parameter values was unable to fit all of the CV curves. Instead, the ranges of the fitted parameter values are listed in the Table 7.3. All simulated CVs and oxide overages at the varied temperature and humidity are listed in the Appendix D. As we see in Figure 7.1 and 7.2, humidity had a large effect on the shapes of CV curves. Decreasing relative humidity results in a lower slope of the oxidation peak and a lower plateau current; hence, the increase of fitted values of E_A and ω. Proton concentration or activity may also vary with water content in the polymer electrolyte. At fully humidified conditions, increasing temperature shifts the Pt/PtO red-ox peaks to a less positive

potential and also increases both the slope of the oxidation peak and the plateau current, although with smaller effects compared to relative humidity. Hence, both the fitted chemical potential shift $\Delta\mu_{PtO}^{0}$ and anodic exchange coefficient (α_a) increased at higher temperatures for all fitted parameters listed in Table 7.2 with four different temperatures. The failure of a set of universal parameters to fit all CV curves may also arise from the complexity of Pt surface re-construction during oxidation and reduction including oxygen atoms penetration into Pt metal lattice through Pt oxide dipole place exchange.

Table 7.3: Values of the fitted parameters for Pt electrochemical oxidation

Parameter	Fitted Values	Adopted Values	Other Values in Literature
U^0(V)		0.98 [25]	
α_a	0.30 ~ 0.50		0.25 ~ 0.45 [37]; 0.35 [16]
α_c	0.10 ~ 0.15		0.15 [16]
$\Delta\mu_{PtO}^{0}$ (kJ mol^{-1})	-30 ~ -50		-42.3 [16]
σ_{Pt} (J m^{-2})		2.37 [16]	
σ_{PtO} (J m^{-2})		1.00 [16]	
ω (kJ mol^{-1})	30 ~ 36		24 ~ 35 [37]; 30 [16]
k_A (mol m^{-2} s^{-1})	1.0×10^{-4}~ 1.0×10^{2}		
k_C (mol m^{-2} s^{-1})	1.0×10^{-5} ~1.0×10^{-4}		
E_A (kJ mol^{-1})	10 ~ 40		
E_C (kJ mol^{-1})	1 ~ 10		
$k_A\times e^{(-E_A/RT)}$; $k_C\times e^{(-E_C/RT)}$ (mol m^{-2} s^{-1})	3×10^{-6} ~ 5×10^{-5}		1.0×10^{-9} ~ 1.0×10^{-14} [37]; 1.36×10^{-7} [16]

CHAPTER 8

PT DISSOLUTION MECHANISMS

Platinum dissolution processes that generate soluble Pt species are important causes of cathode catalyst degradation. But the involved Pt species and the detailed reactions haven't been clearly elucidated. In a study by Ota [77], the solubility of Pt black powder (~10 nm nanoparticles) in dilute H_2SO_4 solution was measured while exposed to air using the Dithizone-Benzene Method (shown as reactions 8.1 and 8.2). Pt(IV) species were reduced to Pt(II), which then formed complexes with dithizone/benzene. To measure the concentration of Pt(II), the first reduction step was neglected. It was found that no Pt(II) species were detected with the detection limit of 1.5×10^{-6} M of this method. The Pt nanoparticle powder had a solubility of 2.9×10^{-6} M at 23 °C in 0.5 M H_2SO_4, and solubility of Pt increased with increasing temperature and decreasing pH. A dependence of the logarithm of Pt solubility on pH was close to a value of -1. Hence, it was proposed that Pt was first oxidized by oxygen gas (reaction 8.3) and subsequently oxidized to form soluble $Pt(OH)_3^+$ (reaction 8.4).

$$Pt^{4+}, Pt^{2+} \xrightarrow{16\%\ SnCl_2/HCl} Pt^{2+} \qquad \text{(Reaction 8.1)}$$

$$Pt^{2+} \xrightarrow{0.1\%\ \text{dithizone}-\text{benzene/phase separation}} \text{benzene phase} \xrightarrow{0.5M\ H_2SO_4} \xrightarrow{0.5M\ Na_2CO_3} \xrightarrow{0.1\%\ NH_4OH} Pt^{2+} - \text{dithizone/benzene} \qquad \text{(Reaction 8.2)}$$

$$Pt + \frac{1}{2}O_2 \rightarrow PtO \qquad \text{(Reaction 8.3)}$$

$$PtO + \frac{1}{2}O_2 + H_2O + H^+ \Leftrightarrow Pt(OH)_3^+ \qquad \text{(Reaction 8.4)}$$

To study electrochemical dissolution of Pt under a potential cycling condition in an inert nitrogen environment, the rotating ring-disk electrode (RRDE) method was applied in Kawahara's work [78]. The electrode potential of Pt disk was cycled between 0.05 to 1.5V (vs. RHE), and the mass loss rate of Pt disk electrode was determined by weighing the electrode before and after potential cycling. Due to the incomplete recovery (replating) of the dissolved Pt ions that diffused away from the disk electrode, the measured oxidation charge was higher than the reduction charge. The number of electrons transferred in the Pt dissolution reaction was derived by plotting the charge difference of oxidation and reduction against the Pt mass loss. However, at the very high potential of 1.5V (vs.RHE), both PtO (reaction 8.5) and PtO_2 (reaction 8.6) occurred, which complicated the dissolution processes. In addition, the oxygen evolution current could also obscure the elucidation of the Pt dissolution mechanism.

$$Pt + H_2O = PtO + 2H^+ + 2e^- \qquad \text{(Reaction 8.5)}$$

$$PtO + H_2O = PtO_2 + 2H^+ + 2e^- \qquad \text{(Reaction 8.6)}$$

In other recent work, Dam [79] *et al.* monitored the Pt electrode weight with a highly sensitive quartz crystal microbalance during Pt dissolution tests at a constant electrode potential. The electrode weight increased at the beginning of the potential hold due to surface oxidation of Pt (gaining weight of oxygen atoms), then started to decrease as the oxidation of Pt slowed and the weight loss from Pt dissolution increased. Several possible dissolution reactions (reactions 8.7-8.9) could be involved in the author's opinion depending on the potential level. In the case of 1.4 V (vs. RHE) potential

holding, the calculated charge passing the electrode was found to be much higher than the value corresponding to the net mass change in all possible dissolution steps. Dam *et al.* believed that it was caused by the continuous Pt oxidation with a small oxidation current observed. But this could partially be the oxygen evolution current at the very high potentials. Unfortunately, no study of charge-mass relation was presented in this work at the relatively low potentials.

$$Pt = Pt^{2+} + 2e^{-} \qquad \text{(Reaction 8.7)}$$

$$PtO + 2H^{+} = Pt^{2+} + H_2O \qquad \text{(Reaction 8.8)}$$

$$PtO_2 + 4H^{+} + 2e^{-} = Pt^{2+} + 2H_2O \qquad \text{(Reaction 8.9)}$$

As discussed above, the platinum dissolution processes were quite complex and difficult to study without effective analytical tools to identify the Pt species and reactions. Both platinum oxidation and Pt dissolution can occur through chemical reactions with oxygen gas molecules or through electrochemical (electron transfer) reactions. However, no investigation of both possible routes was conducted within the same experimental frame work. To understand further the dissolution processes of Pt, we studied Pt dissolution at constant potentials and monitored the soluble Pt concentration in a perchloric acid solution under the either nitrogen or oxygen environment.

8.1 Electrochemical Dissolution Tests in Acid Aqueous Media

The details of the electrochemical H-cell and dissolution procedures have been described in Chapter 3.4. In brief, the working electrode was Pt gauze purchased from

Sigma-Aldrich (100 mesh, 99.9 % pure). A mercury-mercurous sulfate (Hg/Hg_2SO_4 with saturated K_2SO_4) electrode (from Radiometer Analytical) was used as the reference electrode with a gold wire (Sigma-Aldrich, 99.99 % pure) counter electrode. Before dissolution experiments, the Pt mesh electrode was electrochemically cleaned, soaked and rinsed in high purity 18 Mohm de-ionized (D.I.) water. About 10 ml of 0.5 M $HClO_4$ electrolyte solution was contained in the working chamber and was stirred with a Teflon stir bar and either nitrogen or air bubbled through to solution. Under the nitrogen environment, the working electrode was held at 0.8 V, 1.0 V, 1.2 V (vs. RHE) or electrically disconnected. For the tests with air, the working electrode potential was 0.8 V (vs. RHE) or there was no electric connection. With Pt oxidation and dissolution, oxygen reduction also took place at Pt electrode with the potential holding at 0.8 V (vs. RHE) in air, which was a similar situation as that on a fuel-cell cathode at a power-providing condition. Samples before and during the dissolution tests (either electrochemical dissolution or chemical dissolution) were collected and subjected to ICP/MS measurement of the total Pt concentration. The acid solution was replenished by adding fresh solution during dissolution tests.

8.2 Results and Discussions

Time profiles of the total concentration of soluble Pt are plotted in Figure 8.1 with the average value in the middle and a standard deviation as the bar range. Platinum had a pseudo-steady state solubility as low as about 2 ng/g (ppb) in 0.5 M $HClO_4$ under the nitrogen environment at 23 °C. When saturated with air, the solubility was much high at about 170 ng/g (8.7×10^{-7} M). This was close to, but lower than, the solubility (2.9×10^{-6}

M) of Pt black nanoparticle powder (10 nm) in 0.5 M H_2SO_4 at room temperature, due to the different pH values of the solutions and also Pt electrode particle sizes. Increasing the holding potential in nitrogen, the measured solubility dramatically increased, which was also close to the values measured by Wang (Figure 2.1) [30].

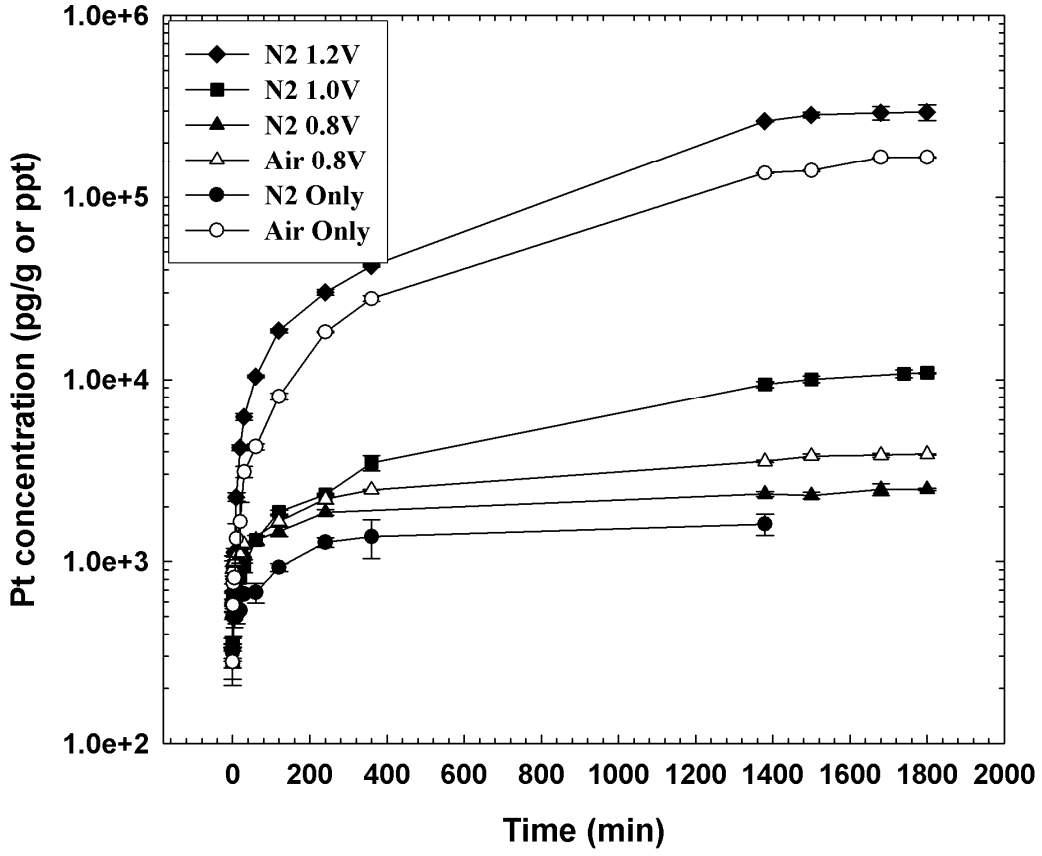

Figure 8.1: Total soluble Pt concentrations with dissolution time

More interesting, at a potential of 0.8 V (vs. RHE) in air, the Pt solubility was much lower than that in air without an electrical connection, but slightly higher than at the same potential in nitrogen. Considering some differences of the measured active

surface areas of Pt electrode and the solution volumes in the working chamber for each test, the Pt concentrations were normalized in a unit of mass per active surface area (ng/cm^2) as shown in Figure 8.2. The initial rates of dissolution (Figure 8.2) were almost the same at 0.8 V in air and nitrogen, and then the difference of Pt concentrations became significant with prolonged potential holding in the two tests. It's possible that at the initial stage there was small Pt oxide coverage due to slow Pt oxidation rate at 0.8 V as shown in the CV curve (Figure 8.3) of the electrode in the same electrolyte solution at room temperature. So the dissolution kinetics followed the Pt electrochemical process (reaction 8.7) in both tests. With long potential holds, platinum surface oxide could be continuously built up. The oxides could be further oxidized and dissolved in the acid through the reaction 8.4.

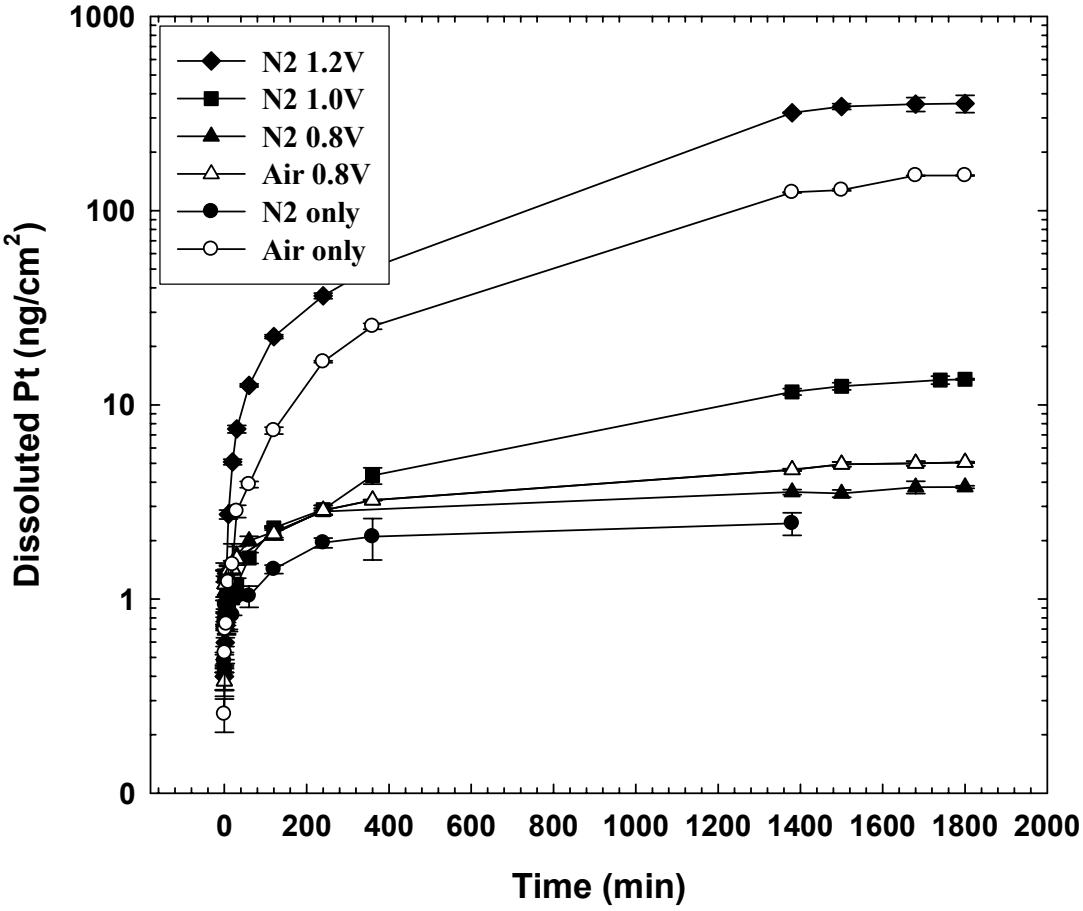

Figure 8.2: Total dissolved Pt (ng/cm^2) with dissolution time

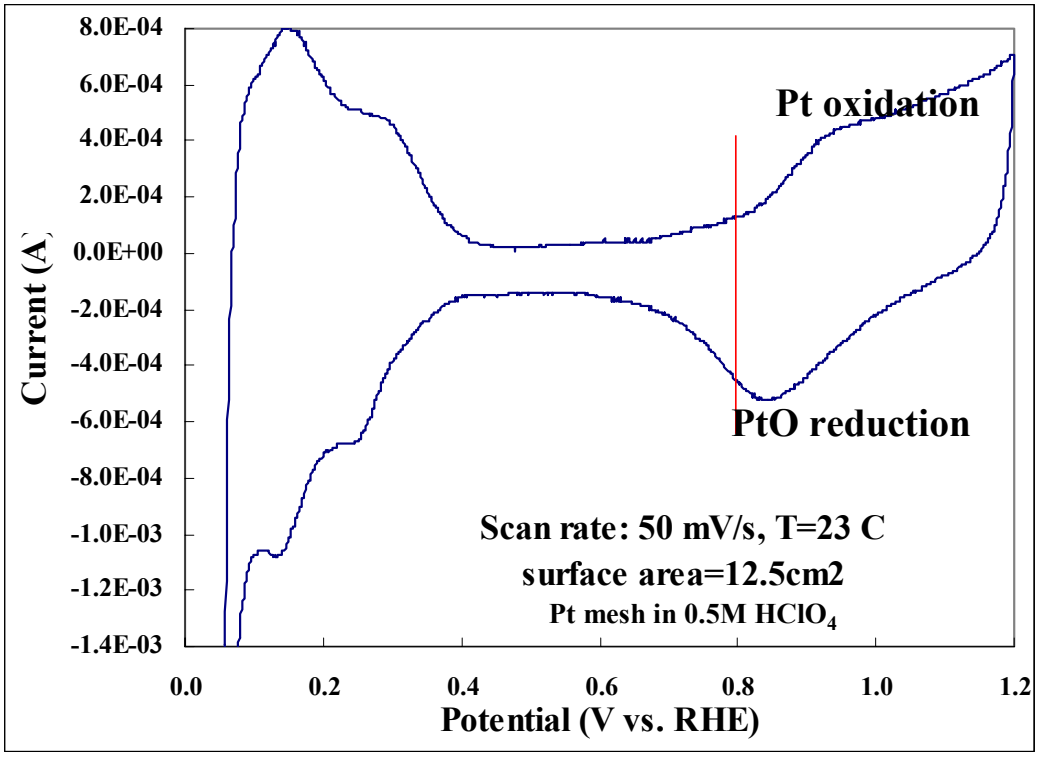

Figure 8.3: Pt gauze electrode CV curve in 0.5 M $HClO_4$ at room temperature

Considering the above discussions, two distinct mechanisms of Pt dissolution for a hydrogen-air PEM fuel cell cathode under open circuit (no load) and load conditions are proposed. At an open-circuit condition, platinum will be oxidized by oxygen molecules reaction 8.3) and further oxidized and dissolved in acidic electrolyte (reaction 8.4). At a closed-circuit condition, it is probably a much more complex process. Platinum can be oxidized by both oxygen chemically (reaction 8.3) and by water electrochemically (reactions 8.5-8.6), with their relative strength depending on humidity and temperature [49, 63]. Both electrochemical dissolution (reactions 8.7 and 8.9) and chemical dissolution (reactions 8.4 and 8.8) can contribute to the generation of soluble Pt species.

The different behaviors of Pt oxidation at open-circuit and closed-circuit conditions were also supported by the different cell potential loss rates as shown in Figure 8.4 at 60 °C and 100 %RH. The potential loss was caused mainly by the buildup of the oxide coverage that blocked Pt active sites for ORR, and pulsing to a low potential was able to reduce the oxide, renew the clean surface, and recover the potential [80, 81]. Although the potential was higher at the small constant-current holds than at open-circuit conditions (Figure 8.4), the loss rate of the cell potential was significantly lower in the former cases than the latter one. This can be explained by the faster rate of Pt oxide formation at the catalyst surface under the open-circuit condition with the chemical oxidization by oxygen as we proposed previously, which was different from the mixed process of electrochemical and chemical reactions at closed-circuit conditions.

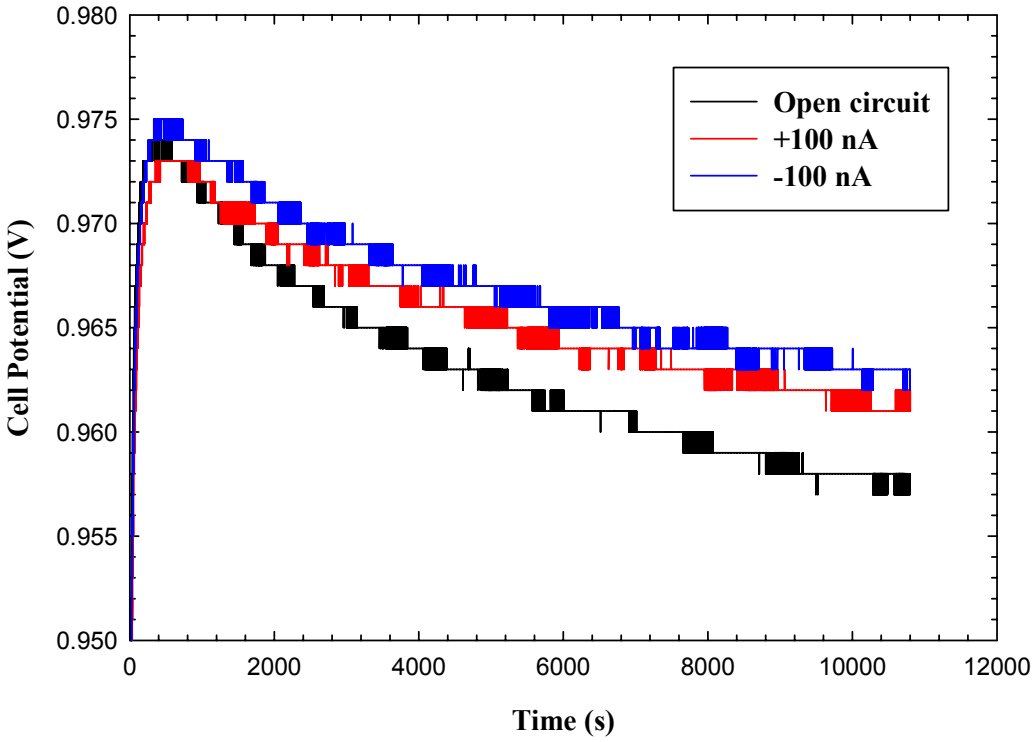

Figure 8.4: Comparison of PEM fuel cell voltage decrease at open circuit and small constant currents at 60 °C and 100% RH

CHAPTER 9

MODELING PT CATALYST DEGRADATION UNDER FUEL CELL CONDITIONS

Carbon-supported platinum or its alloys have the best kinetics for oxygen reduction and the best electrode performance for low temperature acid fuel cells. At the same time, platinum has a small but finite solubility [25, 29, 30] under the highly acidic and oxidizing cathodic environment of PEM fuel cells. Carbon-supported platinum catalyst degrades through dissolution [27, 31, 32], which is a process accelerated by potential cycling. Platinum surface atoms on nanoparticles can be oxidized by both water and oxygen at cathode [37, 49, 73, 76, 82]. At relative high temperature and high humidity fuel cell conditions, platinum oxidation by water is dominant [49]. With techniques of electrochemical quartz-crystal nanobalance, cyclic-voltammetry and Auger electron spectroscopy, Jerkiewicz's work [75] confirmed that anhydrous PtO instead of Pt(OH)x is the only oxidized form of Pt in the potential range of 0.85-1.4 V (vs. NHE) and that a surface PtO lattice formed by an interfacial place-exchange process at potentials of 1.1-1.2 V (vs. NHE).

From the PEM fuel cell cathode, dissolved Pt ions can be transported to other regions of the fuel cell. These dissolved Pt ions can be reduced electrochemically and deposited on existing Pt particles [66] within the cathode. These Pt ions can also diffuse away from the cathode into the membrane. Subsequently, hydrogen that permeates through the membrane from the anode can reduce the cations, forming a Pt "band" in the membrane. The Pt "band" position is determined by the rates of permeation of hydrogen

and oxygen [29, 34, 47, 48]. It is also possible that some dissolved platinum leaves the cell with the product water. However, the concentration of soluble Pt species in fuel cell product water has been determined at ppt levels in our tests by Inductively Coupled Plasma Mass Spectroscopy (ICP/MS). These low amounts indicate that relative to the other mechanisms for platinum loss from the cathode a negligible amount of platinum leaves the fuel-cell system.

Pt dissolution and re-deposition causes Pt catalyst structure morphological changes with a concomitant decrease in electrochemically active surface area and reduced activity for oxygen reduction. Processes of Pt dissolution from small particles, and Pt ion deposition on large particles result in increased mean particle size and widened Gaussian size distribution. However, the detailed mechanisms of Pt catalyst degradation haven't been completely understood. Ferreira *et al.* [29] observed with TEM that the size distributions of carbon-supported Pt particles changed from a Gaussian distribution at the cathode surface region to a uniform distribution at the cathode/membrane interface. Also, the average particle size increased in the direction towards the interface. Other X-Ray diffraction work by More and Reeves [83] showed that the Pt particle size distribution becomes "bi-modal," but with a large portion of the smallest particles still present after degradation tests. The authors believed that new small Pt particles were produced during the degradation processes. Also, coarsening of neighboring Pt clusters and/or nanoparticles is speculated even though PEM fuel cells operate at relatively low temperatures. Electrochemical reactions of Pt oxidation [16, 37, 73] and Pt dissolution [16] have been simulated with various forms of the Butler-Volmer equation.

The thrust of our research is to develop detailed physics-based models for degradation phenomena. From these models two objectives are pursued. First, through a better understanding of the mechanisms and physical processes, propose system-level approaches to mitigate degradation. The second objective is to predict life performance of catalyst systems under conditions appropriate for transportation applications, *i.e.*, hundreds of thousands of potential cycles over several thousands of hours of operation. More specifically, from a given cell potential and temperature as a function of time we seek to predict these observed phenomena: 1) the rate of platinum dissolution and diffusion in the membrane, 2) changes in electrochemical area (ECA), 3) the growth of particle size, and 4) the coverage of oxides. Furthermore, the general characteristics of these macroscopic models are 1) physics based, 2) well-defined and measurable quantities, 3) consistent with thermodynamics, and 4) a limited number empirical or fitted parameters.

Darling and Meyers [17] proposed the first Pt/C catalyst degradation model for PEM fuel cells. This model used a two particle size profile to simulate cathode surface area loss through Pt dissolution/deposition and Pt ion transport in membrane electrode assembly (MEA). Their model [17] predicted a decrease in size for both small and large particles after degradation. Also the model allowed the dissolved Pt ions from the cathode to be transported through membrane and further electrochemically deposited at the anode, which is more appropriate in phosphoric acid fuel cells, but is not typically observed in PEM fuel cell systems [34, 47, 48].

In this work, a Pt catalyst degradation model is proposed that builds on the earlier work of Darling and Meyers [17]. This new model includes some different features such as cathode Pt mass loss into membrane forming a Pt "band," as discussed earlier. Under the defined cathode potential temporal profiles, cathode platinum mass, catalyst particle size, and platinum surface area are predicted and compared to the experimental data, assisting further understanding catalyst degradation mechanisms.

9.1 Pt/C Cathode Catalyst Degradation Model Details

Only Pt (II) species were considered in this initial work since we were not interested in the extremely high cathode potential conditions where water oxidation and carbon oxidation are also involved. Platinum oxidation was assumed solely by water due to the dominated electrochemical oxidation at high humidity fuel-cell conditions [49]. In this simplified model, catalyst degradation caused by Pt dissolution and deposition was modeled with three reactions: Pt electrochemical dissolution (Reaction 9.1) and Pt oxidation (Reaction 9.2), and diffusion of Pt ions and subsequent precipitation by hydrogen reduction (Reaction 9.3). This last reaction, precipitation of Pt ions in the membrane, was assumed to be irreversible and contributes to Pt mass loss from cathode. Only electrochemical Pt dissolution was considered under a dynamic potential (closed-circuit) condition. As discussed in chapter 8, the pseudo-steady state of Pt concentrations under air environment was higher than, but close to, that in the nitrogen environment during a potential holding. The initial dissolution rates were almost the same under both cases. So dissolution involved with oxygen was neglected. Also chemical dissolution of Pt oxide (Reaction 9.4) was not considered due to the unclear kinetics. What's more,

inclusion of this reaction did not affect the results measurably due to its most likely slow kinetics [16].

$$\mathrm{Pt} = \mathrm{Pt}^{2+} + 2\mathrm{e}^{-} \quad (U_1^0 = 1.188\ \mathrm{V}) \qquad \text{(Reaction 9.1)}$$

$$\mathrm{Pt} + \mathrm{H_2O} = \mathrm{PtO} + 2\mathrm{H}^{+} + 2\mathrm{e}^{-} \quad (U_2^0 = 0.98\ \mathrm{V}) \qquad \text{(Reaction 9.2)}$$

$$\mathrm{Pt}^{2+} + \mathrm{H_2} = \mathrm{Pt} + 2\mathrm{H}^{+} \qquad \text{(Reaction 9.3)}$$

$$\mathrm{PtO} + 2\mathrm{H}^{+} = \mathrm{Pt}^{2+} + \mathrm{H_2O} \qquad \text{(Reaction 9.4)}$$

The model details and assumptions are described below, and model variables and constants are listed in Table 9.1.

1) It's a one-dimensional model since the thickness (order of 10 μm) of MEA is much thinner than MEA in-plane dimensions (order of cm). And in-plane uniformity was assumed.

2) The cathode included Pt/C solid phase uniformly mixed with Nafion® electrolyte and gas pore phase. The polymer (and/or ionomer) volume fractions were assumed to be 30 % (ε_C) in the cathode and 100 % (ε_M) in Nafion® membrane.

3) Pt particles were uniformly distributed across the cathode. In principle, any Pt particle size distribution can be simulated. For this degradation mechanism focused study, we adopted a simple bi-modal particle size distribution: small particles with the particle size R_S and large particles with the size of $R_{L,}$ which also allowed us to observe the

particle size effects on degradation behaviors. All Pt particles were assumed to be spherical. The radius of particle represented the Pt metal core, excluding the surface Pt oxide. Pt dissolution (equation 9.1-9.2) and oxidation (equation 9.3-9.4) rates were expressed by the modified Butler-Volmer equations with electrochemical potentials adjusted based on particle radius by the Kelvin equation assuming constant surface properties (equation 9.2 and 9.4) [16].

$$r_{1i} = k_1 \theta_i^V \left[\begin{array}{l} \exp\left\{ \dfrac{\alpha_{1a} n_1 F (E - U_{1i})}{RT} \right\} \\ -\dfrac{c}{c_{ref}} \exp\left\{ \dfrac{-\alpha_{1c} n_1 F (E - U_{1i})}{RT} \right\} \end{array} \right] \qquad \text{[Equation 9.1]}$$

$$U_{1i} = U_1^0 - \frac{1}{2F} \frac{\sigma_{\mathrm{Pt}} M_{\mathrm{Pt}}}{\rho_{\mathrm{Pt}}} \frac{1}{RR_i} \qquad \text{[Equation 9.2]}$$

$$r_{2i} = k_2 \left[\begin{array}{l} \exp\left\{ \dfrac{-\omega \theta_i}{RT} \right\} \exp\left\{ \dfrac{\alpha_{2a} n_2 F (E - U_{2i})}{RT} \right\} \\ -c_H^2 \theta_i \exp\left\{ \dfrac{-\alpha_{2c} n_2 F (E - U_{2i})}{RT} \right\} \end{array} \right] \qquad \text{[Equation 9.3]}$$

$$U_{2i} = U_2^0 + \frac{1}{2F} \left[\Delta\mu_{\mathrm{PtO}}^0 + \frac{\sigma_{\mathrm{PtO}} M_{\mathrm{PtO}}}{\rho_{\mathrm{PtO}}} \frac{1}{RR_i} - \frac{\sigma_{\mathrm{Pt}} M_{\mathrm{Pt}}}{\rho_{\mathrm{Pt}}} \frac{1}{RR_i} \right] \qquad \text{[Equation 9.4]}$$

4) Pt ions were dissolved in the Nafion or its ionomer phase in the cathode and in the membrane separator. Both large and small Pt particles “saw” a mixed (average) Pt ion concentration at the same location in cathode.

5) Pt ions from the cathode were transported by diffusion into membrane. Under the simulated potential cycling conditions [67, 84], the potential field (Φ) in the electrolyte phase was relatively weak due to the small current density (I: less than 20 mA cm^{-2}), the high electrolyte concentration and the low cell resistance (R_{FC}). The contribution of Pt ion transport by migration was estimated to be at least one order of magnitude smaller than transport by diffusion. The ratio of diffusion to migration flux is estimated to be:

$$\frac{N_{diff}}{N_{migr}} = \frac{D\nabla C}{zuFC\nabla\Phi} \approx \frac{D\nabla C}{z\frac{D}{RT}FC\nabla\Phi} \approx \frac{RT}{zF(I*R_{FC})} \approx \frac{8.314*333}{2*96485*(0.02*0.06)} \approx 12,$$

assuming Pt ion mobility (u) as diffusivity (D)/RT. Hence, migration was neglected in these simulations. At the interface between the cathode and the gas diffusion layer (GDL), the concentration gradient of Pt ions was set to be zero, *i.e.*, zero flux. Loss of platinum into the effluent product water was determined to be insignificant in our fuel cell tests, so it was neglected in the model. A mass balance on platinum ions gives

$$\varepsilon_j \frac{\partial c}{\partial t} = D\varepsilon_j^{1.5}\frac{\partial^2 c}{\partial x^2} + \sum_{i=S,L} A_i r_{1i}\,, \qquad \text{[Equation 9.5]}$$

where $A_i = \frac{4\pi R_i^2}{V}N_i$ is the specific interfacial surface area for the platinum particles. The diffusion coefficient was adjusted by electrolyte volume fraction ε_j within region j, and assuming a tortuosity ($\tau=\varepsilon^{-0.5}$). In the region of membrane, there was no reaction term in equation 9.5.

6) Pt ions transported into the membrane can be chemically reduced by hydrogen that permeates through the membrane from the anode, forming a Pt "band". The deposited platinum atoms were located at the position predicted by the rates of permeation of hydrogen and oxygen [48]. The width of the Pt band was neglected and the concentration of Pt ion at the "band" location was set to be zero.

7) Pt atoms on a nanoparticle surface can be electrochemically oxidized allowing more than monolayer oxide coverage, and the formed PtO can be partially or completely reduced at the reduction conditions. In the case of beyond one monolayer surface oxide coverage, platinum oxide prevented the metal underneath from continuously dissolving. Although PtO has a certain small solubility, chemical dissolution of PtO is not treated due to its possible slow kinetics [16].

8) The number of each type of Pt particles is held constant (50% each type), but the sizes of these particles are allowed to change during degradation. When small Pt particles shrink into platinum clusters, for example, a 7-atom Pt cluster with an estimated radius of 0.3 nm, no special treatment was introduced due to the limited understanding so far. The volume-average overall (RR_O), small (RR_S), and large (RR_L) Pt particle radii in cathode were calculated by equations 9.6 and 9.7. The definition of volume-average overall particle radius (RR_O), different from the defined average particle size consistent to uniform particle size distribution in Darling and Meyers's model [17], allowed direct comparison to average particle size measured by X-ray diffraction.

$$RR_O = \frac{\sum_x \sum_{i=S,L} N_{x,i} RR_{x,i}^4}{\sum_x \sum_{i=S,L} N_{x,i} RR_{x,i}^3} (x : \text{location in cathode}) . \qquad \text{[Equation 9.6]}$$

$$RR_i = \frac{\sum_x \left(N_{x,i} RR_{x,i}^4 \right)}{\sum_x \left(N_{x,i} RR_{x,i}^3 \right)} (i = S, L) . \qquad \text{[Equation 9.7]}$$

The total platinum particle surface area was given by

$$S = \sum_x \sum_{i=S,L} 4\pi N_{x,i} RR_{x,i}^2 , \qquad \text{[Equation 9.8]}$$

but this area neglected the surface oxide layer. The loss of measured electrochemical surface area (in the unit of m^2 instead of typical m^2/gPt, due to unknown Pt mass in cathode with degradation) can be compared with the simulated results. The total mass of Pt was simply the initial mass minus that which diffused away over the course of the simulation;

$$M(t) = M(t=0) + A \int_0^t \varepsilon_M D \left. \frac{\partial c}{\partial x} \right|_{x=L} dt . \qquad \text{[Equation 9.9]}$$

Table 9.1: Model variables and constants

Variables constants	Units	Physical meaning
A	m^2	MEA in-plane area (25 cm^2=2.5E-3 m^2)
A_S, A_L	m^2/m^3	Specific surface areas of small and large Pt particles
C	mol/m^3	Pt ion concentration
CH	unitless	Relative proton activity (1M/1M=1)
C_{Ref}	mol/m^3	Concentration reference value (1M=1000 mol/m^3)
D	m^2/s	Pt ions diffusion coefficient in cathode or membrane
E	V	Externally applied potential at cathode during durability test
F	C/equiv	Faraday's constant (96485 C/equiv)
k_1	$mol/m^2/s$	Pt dissolution reaction rate constant
k_2	$mol/m^2/s$	Pt oxidation reaction rate constant
M	kg	Total Pt mass in cathode
M_{Pt}	kg/mol	Pt molecular weight (0.1951 kg/mol)
M_{PtO}	kg/mol	PtO molecular weight (0.2110 kg/mol)
n_1	equiv/mol	Number of equivalent electrons transferred per mole of Pt dissoluted (2 equiv/mol)
n_2	equiv/mol	Number of equivalent electrons transferred per mole of Pt oxidized (2 equiv/mol)
N_S, N_L	unitless	Number of small and large Pt particles in each cathode mesh
N_{OUT}	$mol/m^2/s$	Pt ion diffusion flux at the cathode/membrane interface
R	m	Pt particle radius for Pt oxidation simulation
R	J/mol/K	Universal gas constant (8.314 J/mol/K)
r_{1S}, r_{1L}	$mol/m^2/s$	Pt dissolution rate on small and large particles
r_{2S}, r_{2L}	$mol/m^2/s$	Pt oxidation rate on small and large particles
RH	Unitless	Relative water activity or relative humidity
R_S, R_L	m	Radius of small and large Pt particles (exclude oxide layers) at a specific location in cathode
RR_O	m	Volume-average Pt particle radius in cathode
RR_S, RR_L	m	Volume-average small and large Pt particle radius in cathode
S	m^2	Total Pt surface area in cathode
t	s	Time
T	K	Fuel cell temperature
U_1^0	V	Standard thermodynamic potential of Pt dissolution (1.188V)
U_2^0	V	Standard thermodynamic potential of Pt oxidation (0.980V)
U_{1S}, U_{1L}	V	Adjusted thermodynamic dissolution potential for small and large Pt particles
U_{2S}, U_{2L}	V	Adjusted thermodynamic oxidation potential for small and large Pt particles
V	m^3	Volume of each cathode mesh
x	m	Distance away from the GDL/cathode interface in the direction across the MEA

Table 9.1: Model variables and constants (continued)

Variables constants	Units	Physical meaning
α_{1a}	unitless	Anodic transfer coefficient of Pt dissolution reaction
α_{1c}	unitless	Cathodic transfer coefficient of Pt dissolution reaction
α_{2a}	unitless	Anodic transfer coefficient of Pt oxidation reaction
α_{2c}	unitless	Cathodic transfer coefficient of Pt oxidation reaction
ε_C	unitless	Nafion polymer or ionomer volume fraction in cathode
ε_M	unitless	Nafion polymer or ionomer volume fraction in membrane
Γ_{max}	mol/m^2	Maximum oxide at Pt surface 2.18e-5 (atom ratio of Pt:O=1:1)
$\Delta\mu_{PtO}{}^0$	J/mol	Fitted chemical potential shift for PtO
θ_S, θ_L	unitless	Total surface oxide coverage at small and large Pt particles
θ_{max}	Unitless	Maximum surface oxide coverage at the top monolayer
$\theta_S{}^V$, $\theta_L{}^V$	Unitless	Pt oxide vacancy at the top surface monolayer of small and large Pt particles
ρ_{Pt}	kg/m^3	Pt metal density (21090 kg/m^3)
ρ_{PtO}	kg/m^3	PtO density (14100 kg/m^3)
σ_{Pt}	J/m^2	Surface tension of Pt nanoparticles (2.37 J/m^2) [16]
σ_{PtO}	J/m^2	Surface tension of PtO nanoparticles (1.00 J/m^2) [16]
ω	J/mol	PtO-PtO interaction coefficient

The set of partial differential equations with boundary conditions are linearlized (Appendix F), cast in finite difference form, and solved numerically. The Crank-Nicolson implicit method was used to evaluate the derivatives with time. Due to the different electrolyte volume faction in the cathode and the membrane, Pt ion mass balance in the interface was dealt with the control volume method.

9.2 Model and Lab Results under Square-Wave Potential Cycling

Platinum (catalyst in fuel cell cathode) electrochemical oxidation kinetics has been studied in chapter 7 and the fitted Pt oxidation parameters (Table 7.2) were then adopted for use in the cathode catalyst degradation model. Accelerated catalyst

degradation testing under square-wave potential cycling was simulated and compared with experiment. The cathode potential was cycled between 0.87 V and 1.20 V (vs. RHE) with a step time 30 s (1 min per cycle) at 60 °C and fully humidified conditions. The cathode electrochemically active surface area (ECA) was measured periodically during degradation. After the completion of potential cycling, the Pt particle size in the cathode was measured by X-Ray diffraction, and the mass distributions determined through SEM-EDS analysis of MEA cross-sections [48]. The experimental details and results were presented in chapter 5 and elsewhere [67, 84]. In this simulation, we used a simplified bi-modal particle size distribution with equal numbers of the small and large Pt particles. The assumed representative initial particle radii were 1.50 nm and 1.75 nm for the small and large particles respectively, which matches the volume-average value of 1.65 nm in a fresh cathode measured by X-ray diffraction. The sensitivity of catalyst degradation rates on the initial Pt particles radii and the number percentage for each type particle was not investigated.

Previous modeling results [17] showed decreasing particle radii, which might be caused by an overemphasis on Pt cation transport in MEA. Therefore, we first simulated catalyst degradation without the Pt ion diffusion and subsequent hydrogen reduction processes. Under these conditions, both the small and large Pt particle radii remained uniform across the cathode during the simulation. The volume average overall Pt particle radius (RR_O) increased with potential cycling as shown in Figure 9.1. Since the driving force for electrochemical dissolution of Pt increases with decreasing Pt particle size [85], the smaller Pt particle has a higher Pt dissolution rate during the anodic sweep, and a

lower Pt ion deposition rate during the cathodic sweep. Hence, small Pt particles shrank during potential cycling due to a net Pt mass loss through Pt dissolution, and large particles grew with a net gain by Pt ion deposition. An increase of the dissolution rate constant (k_1) resulted in the faster Pt dissolution and Pt ion deposition rates; thus, faster Pt mass exchange between small and large particles, and a faster overall Pt particle size growth rate. These simulations confirmed that in the absence of platinum diffusion the expected changes in particle size occur.

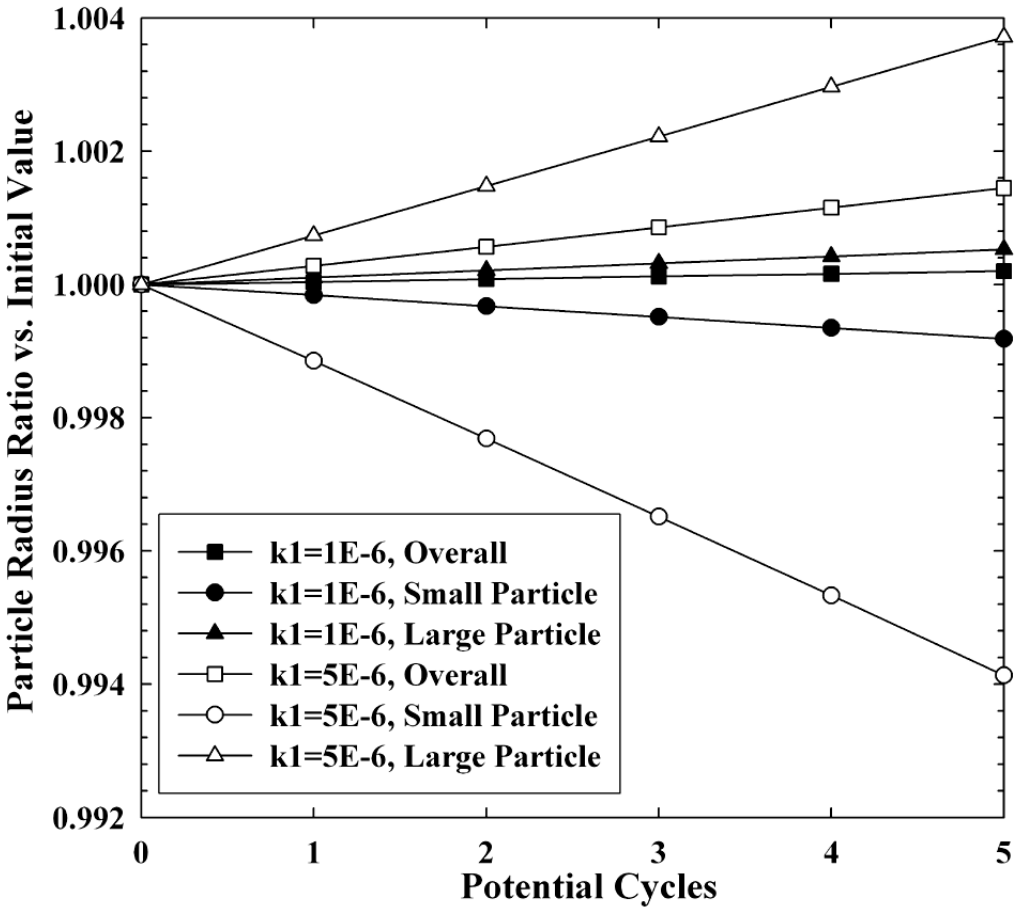

Figure 9.1: Simulated overall, small and large Pt particle size changes in cathode during potential cycling under no Pt ion diffusion conditions

In fact, significant loss of cathode Pt mass was observed [67, 84] experimentally under potential cycling. Since negligible platinum was found in the water, the loss of platinum from the catalyst layer was presumably due to Pt ion transport and its deposition by hydrogen reduction in membrane. It was reported that Pt ion had a fairly small diffusivity of 5.0×10^{-12} m^2 s^{-1} in Nafion® electrolyte [86]. During the potential cycling, fluoride ion concentrations in waste water from both the anode and cathode were measured by ICS-2000 Ion Chromatography System (Dionex Corporation). The levels typically measured, 10-200 ng/g (ppb), were much higher than the detected Pt concentrations (<10 ppt). Small amount of chloride ions might also be present in MEA from de-ionized water, although it was not significantly detected by ion chromatography. A concentration of 10 ppm Cl^- resulted the delay of Pt electrode oxidation due to Cl^- ion electrode adsorption in the CV curve, and both $PtCl_6^{2-}$ and $PtCl_4^{2-}$ complexes were detected in the UV spectrum during a potential holding at 1.1 V (vs. SHE) in 1 M HCl solution [87]. Although there could be some concentration differences between in the liquid phase (waste water) and in the solid phase (Nafion® electrolyte) for both fluoride ions, chloride ions and soluble Pt species, it was very likely that $(PtF_x)^{n-}$ and/or $(PtCl_x)^{n-}$ complexes can be formed. The negatively charged complexes could further slow down the Pt ion diffusion. The effective diffusivity of Pt^{4+} ion complex $(PtCl_6)^{2-}$ in Nafion® 117 membrane was measured about 1.4×10^{-12} m^2 s^{-1} [88], which is much smaller than the assumed value of 10^{-10} m^2 s^{-1} (already one order of magnitude smaller than that of Pt ions in water) in Darling and Meyers's simulation work [16].

With a Pt ion diffusivity of 10^{-10} m^2 s^{-1} and an assumed Pt dissolution rate constant (k_I=5×10^{-9} mol m^{-2} s^{-1}) close to Darling and Meyers's fitted value, the simulated cathode Pt surface area had a negligible loss under the potential cycling conditions. The measured ECAs for the fresh and the degraded (after 300 and 1000 potential cycles) cathodes are plotted in Figure 9.2 with a linear interpolation between experimental data points. These data, in fact, show significant loss of surface area with potential cycling. Similarly, the assumed Pt ion diffusivity and Pt dissolution rate constant yielded no significant Pt mass loss in the cathode as shown in Figure 9.3. The estimated Pt mass in the cathode was presented in our previous work based on the SEM-EDS measurements before and after potential cycling [67, 84]. Compared to Darling and Meyers's simulation results [17], these much lower surface area and mass loss rates were caused by the smaller Pt ion concentration due to the faster Pt oxidation rate with higher oxide coverage. With potential cycling, the simulated overall Pt particle radius actually decreased slightly as shown in Figure 9.4, similar to Darling and Meyers's simulation results [17]. Such particle shrinking behaviors were due to the relatively faster Pt ion transport than Pt dissolution and deposition processes, which could even result in both small and large Pt particle size decrease.

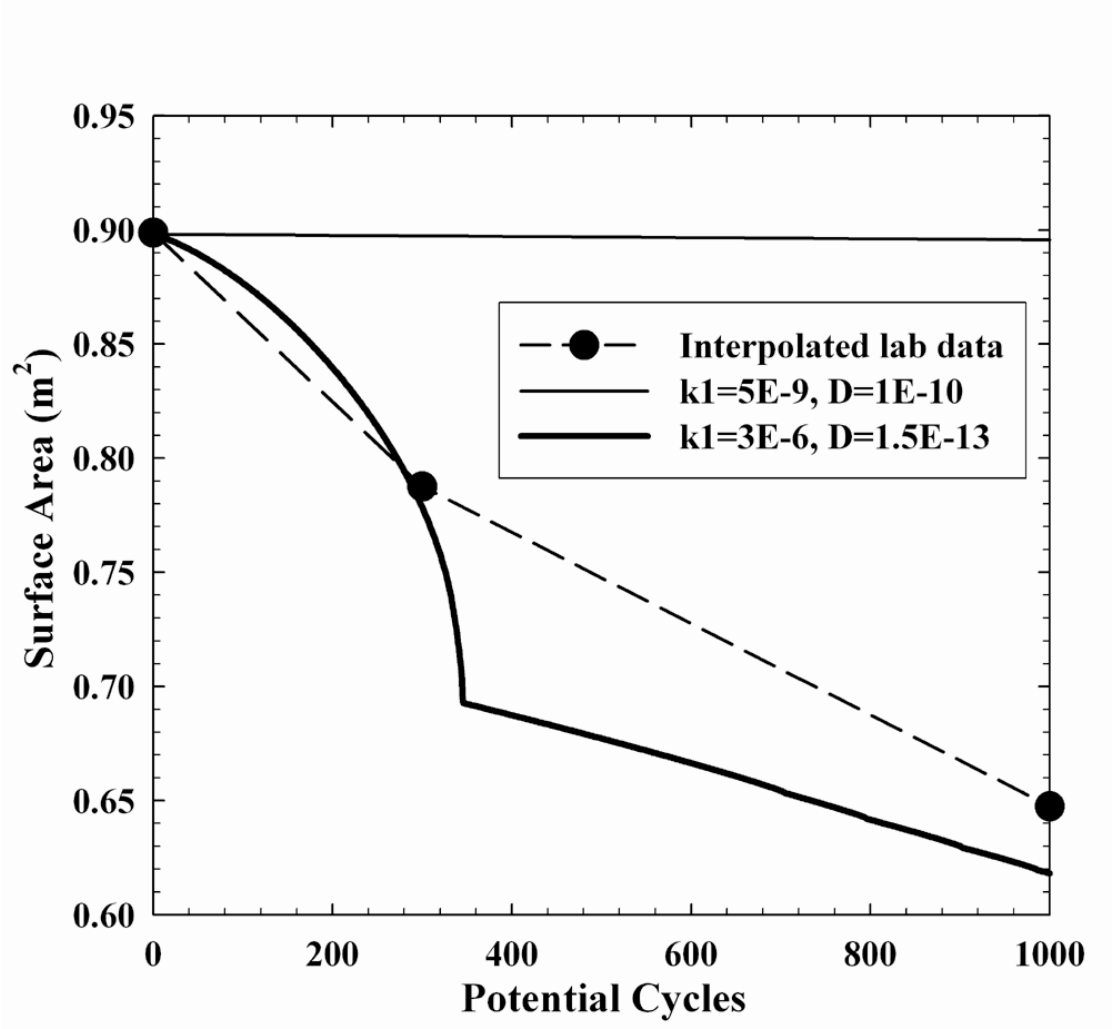

Figure 9.2: Simulated cathode Pt surface areas under potential cycling with linearly interpolated measured electrochemically active surface area

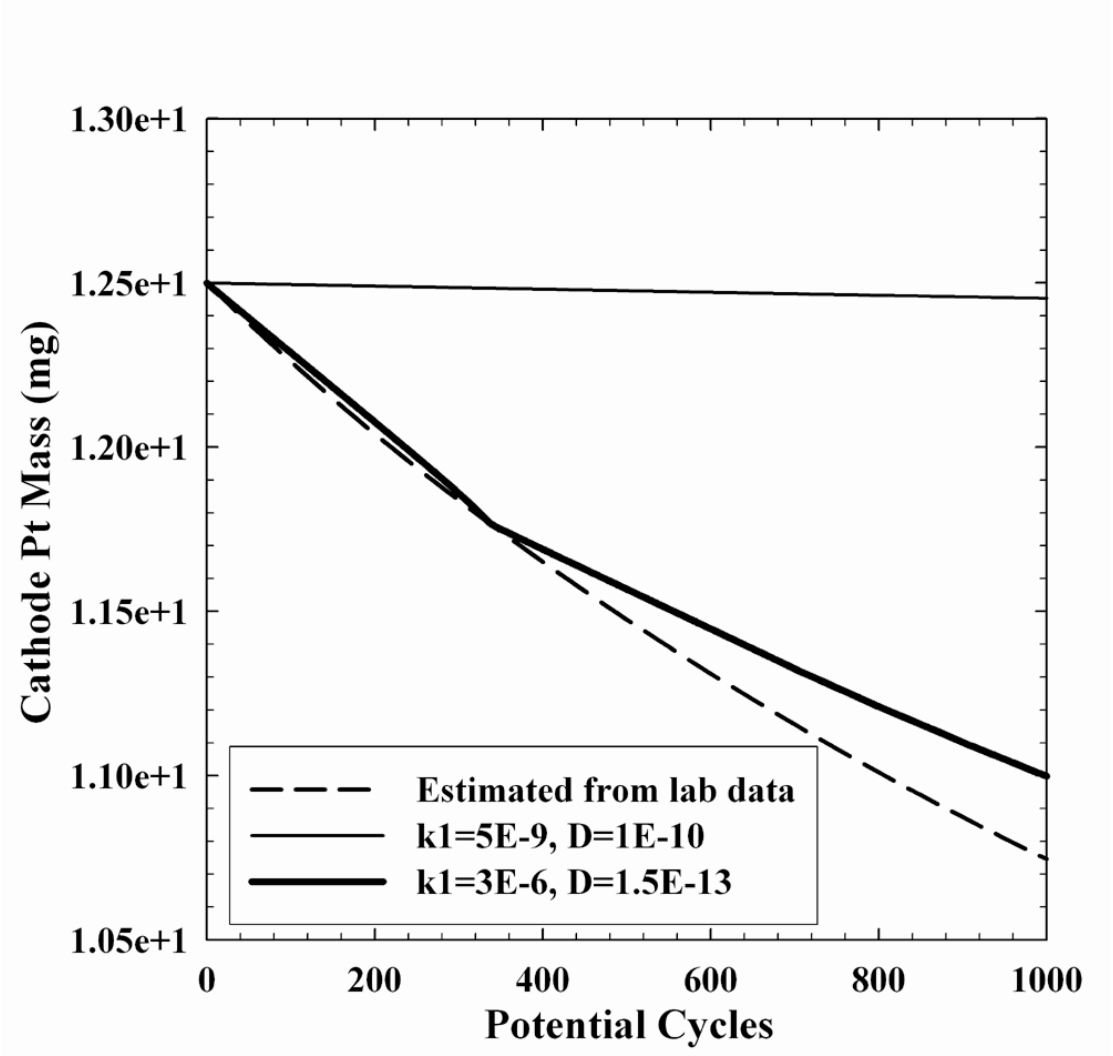

Figure 9.3: Simulated cathode Pt mass loss during potential cycling with calculated values based on lab data [67, 84]

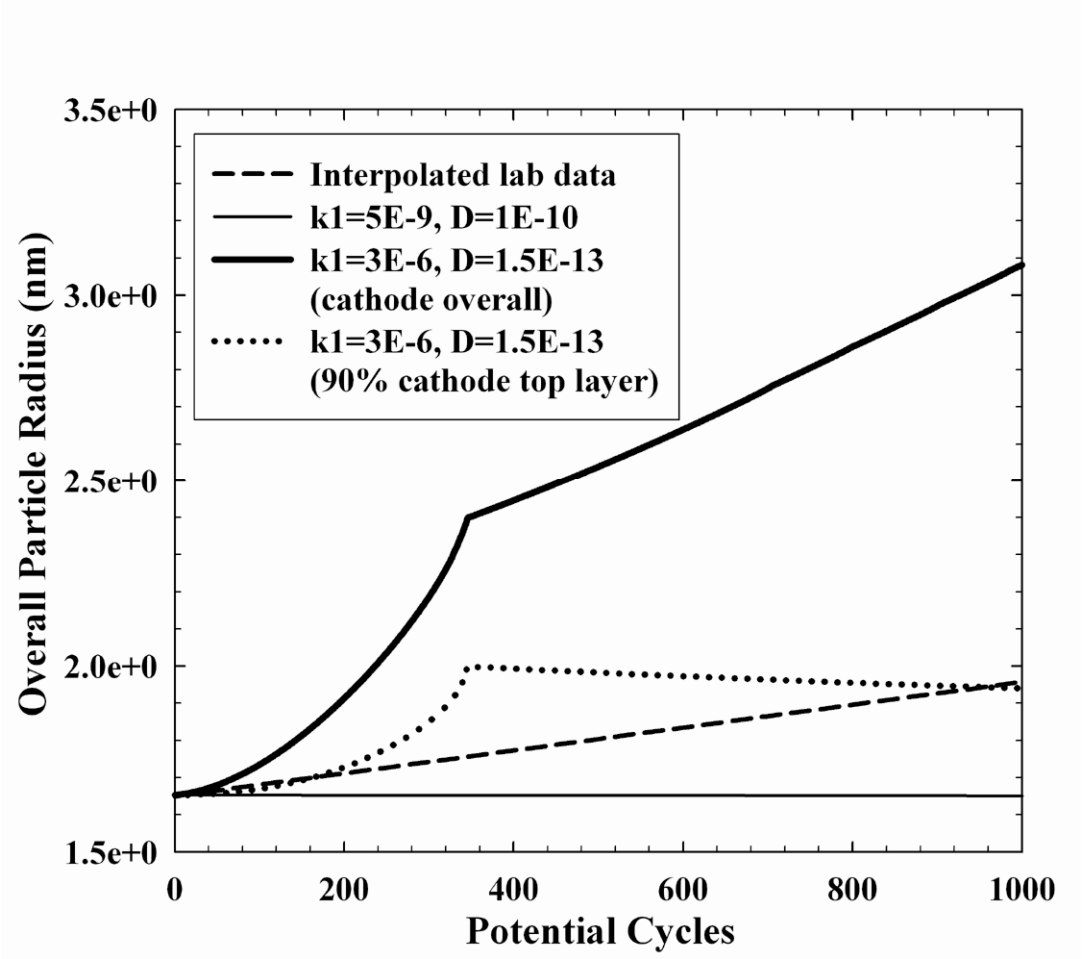

Figure 9.4: Simulated overall cathode Pt particle radius during potential cycling with linearly interpolated data of fresh and degraded cathode measured by X-Ray diffraction

Since the cathode Pt mass loss rate depends on both Pt ion diffusivity and ion concentration, the Pt dissolution rate constant was increased and Pt ion diffusivity was decreased to match Pt mass loss and particle growth behaviors. With the adjusted Pt ion diffusivity (1.5×10^{-13} m^2 s^{-1}) and Pt dissolution rate constant (3×10^{-6} mol m^{-2} s^{-1}), the cathode surface area loss rate had a similar magnitude as the measured data as shown in Figure 9.2. However, the simulated surface area profile had an initial concave-down shape with the dramatic surface loss after 300 potential cycles. This was caused by the

accelerated dissolution rate for the small Pt particle with decreasing size. Figure 5(a) shows the small Pt particles at the cathode center shrank at an increasing rate until reaching a size of 0.15 nm, at about 350 potential cycles. During the further potential cycling, the small Pt clusters (except those close to the cathode/membrane interface) will be fully covered with oxide even after 30 seconds of reduction phase at 0.87 V, which is still much higher than the adjusted dissolution thermodynamic potential (lower than 0.5 V for such a small cluster). So these small Pt clusters only experienced oxidation and oxide reduction without mass losses by dissolution, thus the size remained as constant. Presumably, these small particles can diffuse, but coarsening of these Pt clusters was not treated in this work.

The Pt mass loss in the cathode matched the estimated values from measured data as shown in Figure 9.3. However, the overall Pt particle growth rate was much faster than the estimated rate by linearly interpolating the measured particle determined from X-ray diffraction before and after degradation by (Figure 9.4). Since a small X-ray incident angle (1 degree) was applied on the cathode layer in MEA to avoid collecting the diffracted signals from Pt particles in Pt "band" (only about 5.5 μm away from the cathode/membrane interface), Pt particles in the cathode close to the cathode/membrane interface might not be well detected by X-ray. To account for this possible effect, Pt particles in the 90% of the cathode top layer were used to calculate the volume-average particle size, which showed a better matching. The volume average particle size quickly approached the large particle size as shown in Figure 5(b). This is attributed to the fact that small Pt particles are less weighted in the calculation of volume-average particle size.

The larger particles produced at the cathode/membrane interface as shown in Figure 9.5(a) and 9.5(b) were caused by the Pt ion diffusion back from the membrane and deposition at the interface region during the reduction period of the potential cycling. The Pt ion concentration spatial profiles during the 100^{th} potential cycle are plotted in Figure 9.6. The cathode thickness was 7 μm and the Pt band located in the membrane 5.5 μm away from the cathode-membrane interface. Due to the high dissolution rate and low Pt ion diffusivity, Pt ion concentration in membrane was much higher than that in the cathode during the reduction period (the second 30 seconds of the one-minute potential cycle) resulting in Pt ion in the membrane diffusing towards both the cathode and the Pt band location to be reduced electrochemically or chemically by hydrogen, respectively. Figure 9.7 shows the Pt particle spatial profiles with the decreased sizes of large Pt particles towards the cathode/membrane interface. This was caused by the rapid particle growth at the interface which drove the surrounding particles shrinkage. Since small particle shrank with degradation, its size distribution across the cathode was more uniform with only a small dip close to interface region.

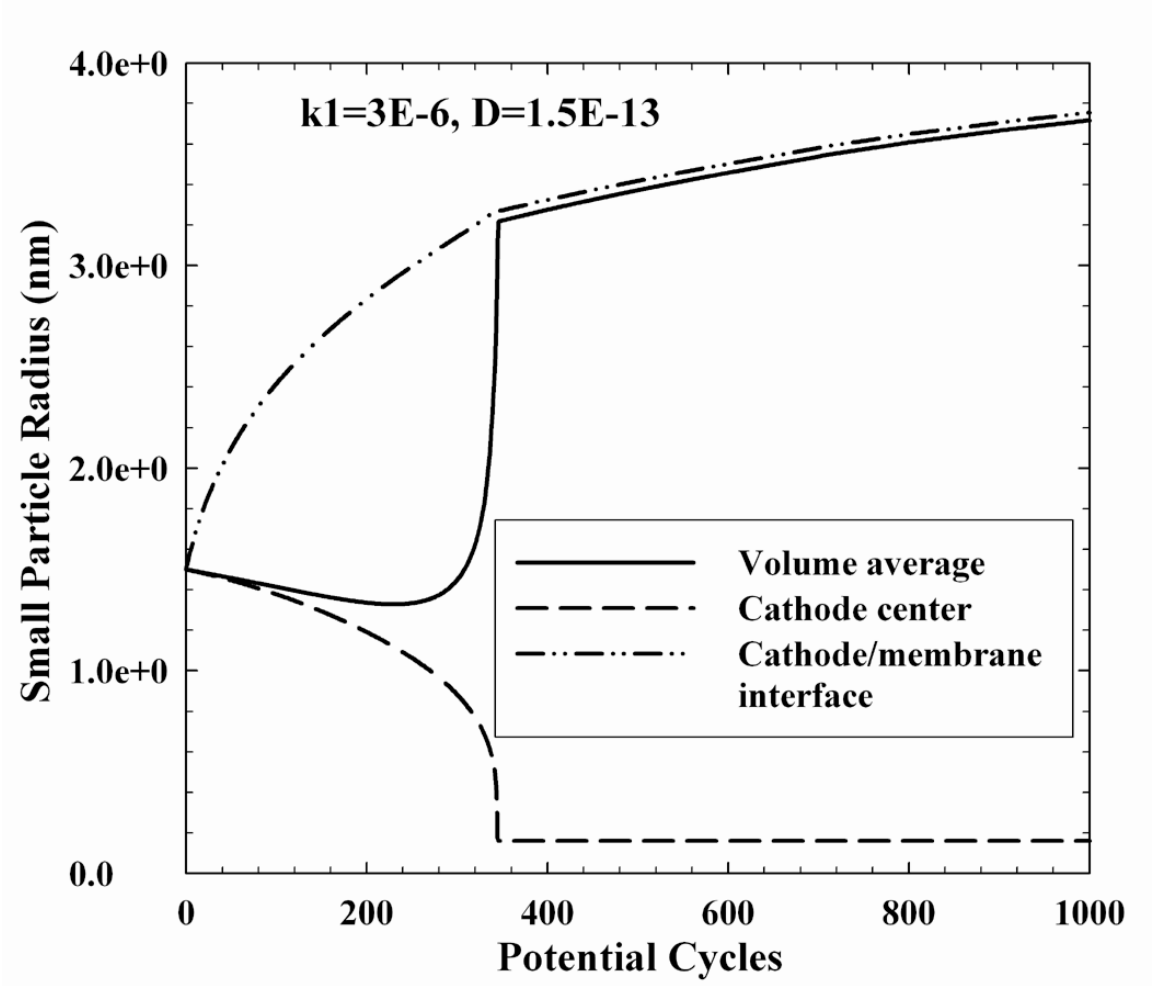

Figure 9.5(a): Simulated volume average radius of small Pt particle in cathode and Pt radius at cathode center and cathode-membrane interface

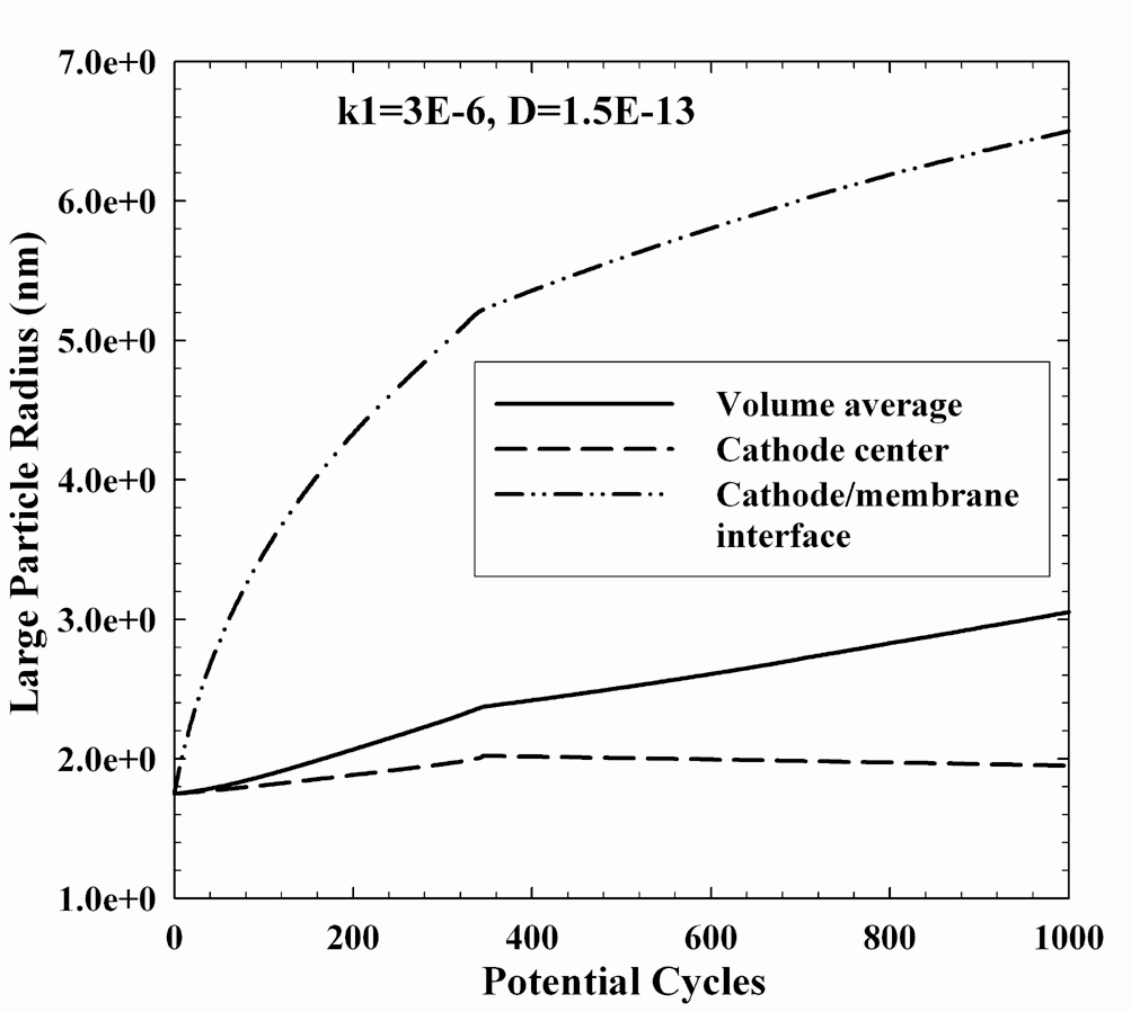

Figure 9.5(b): Simulated volume average radius of large Pt particle in cathode and Pt radius at cathode center and cathode-membrane interface

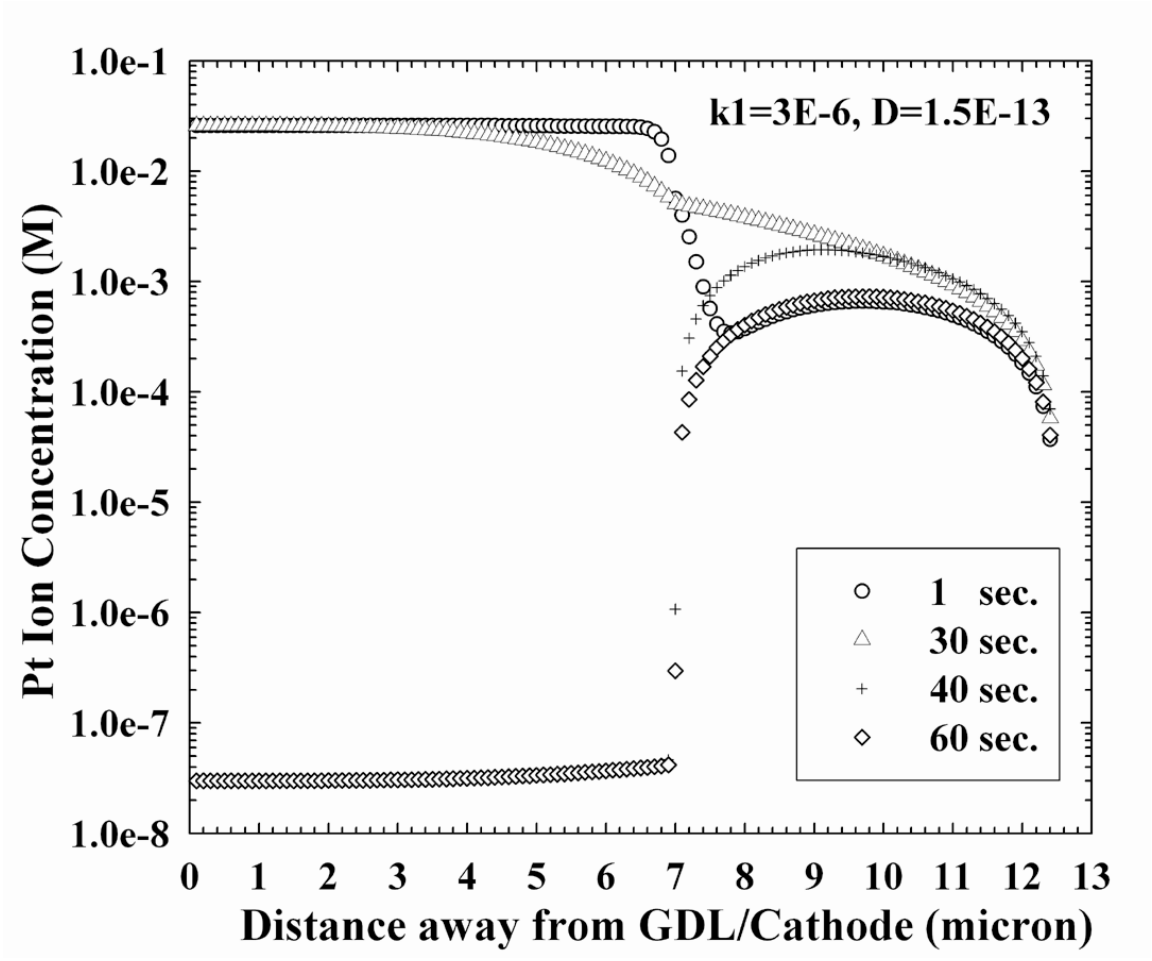

Figure 9.6: Simulated Pt ion concentration spatial profiles during the 100th potential cycle (cathode thickness: 7 microns)

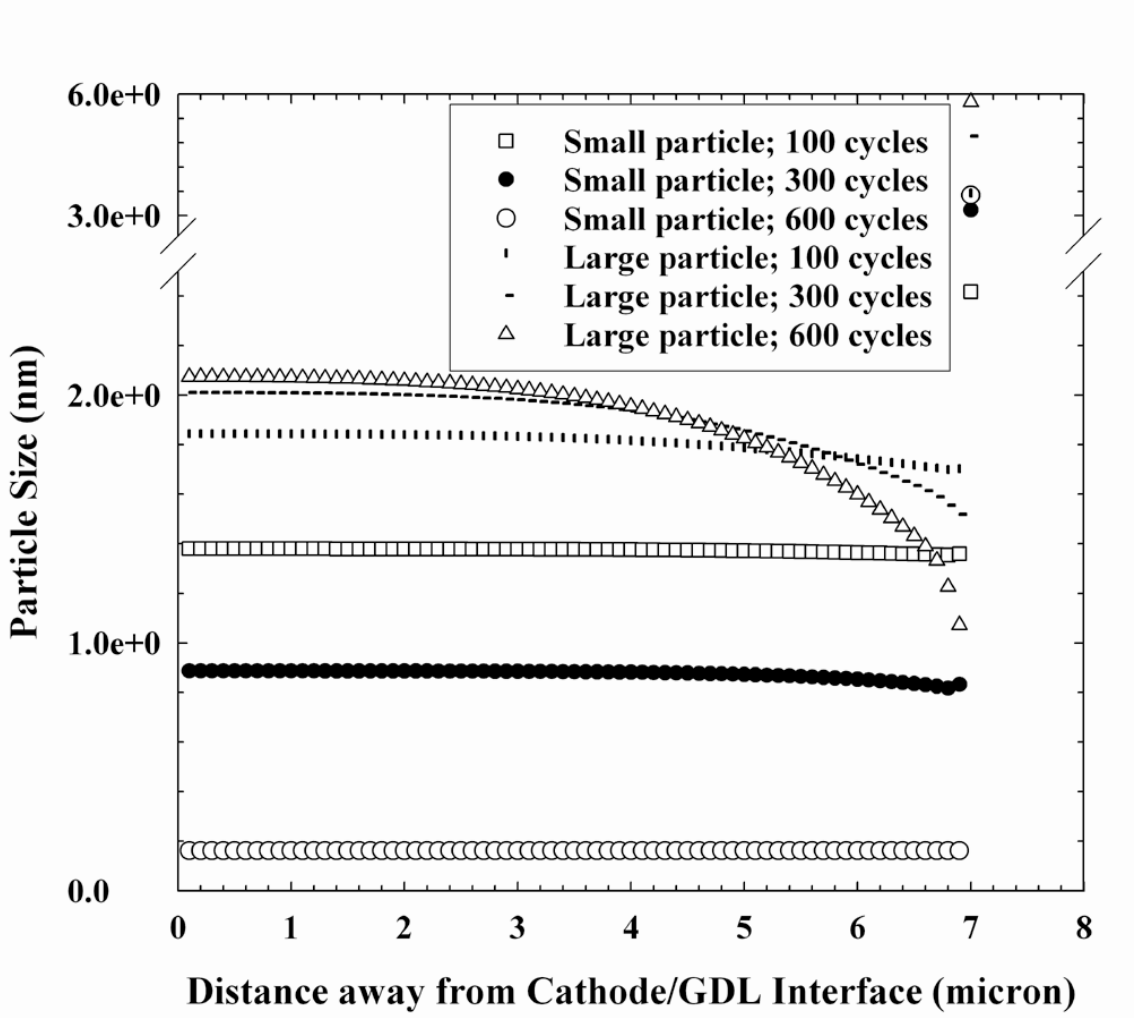

Figure 9.7: Simulated cathode Pt particle size spatial profiles during potential cycling (cathode thickness 7 microns)

Pt particle growth at the cathode/membrane interface was not investigated in our experiments; however, the simulated particle size spatial profiles contradict Ferreira's observations [29]. So it seemed that the Pt ion concentration shown in Figure 9.7 was unlikely high during the anodic period of the potential cycling. The assumed effective Pt ion diffusivity with porosity and tortuosity correction was two orders of magnitude lower

than the measured diffusivity of $(PtCl_6)^{2-}$ complex in Nafion® electrolyte [88]. Even with the further parameter adjustment, this proposed Pt/C catalyst degradation model will lead to the small Pt particle quickly decreasing in size decrease. This resulted in a dramatic surface area loss and a sharp increase in the overall particle size after the small particles reach the sub-nanoparticle region. This was also partly due to the untreated neighboring Pt clusters or sub-nanoparticles coarsening in the model. So our simulation results suggested that degradation processes besides Pt dissolution and Pt ion deposition are important in catalyst degradation. Also, the model assumption of Pt ion electrochemical deposition solely on Pt metals excludes the nucleation of fresh Pt particles or clusters on carbon support. In fact, More's experimental work also suggests that new Pt nanoparticle formation during catalyst degradation [83]. With the added features of new Pt cluster formation and its coarsening in a recommended future model, small Pt particles will not diminish with catalyst degradation. It is likely that with reasonable Pt ion concentration and Pt ion diffusion rate that Pt particle growth and losses of catalyst surface area and cathode Pt mass could be well predicted.

A parametric study of cathode degradation rates under the initial 200 same square-wave potential cycles of a fresh 25 cm^2 CCM [67] was conducted with the varied Pt ion diffusivity and electrochemical dissolution rate constant. Both Pt mass and surface area loss rates increased with dissolution rate and ion diffusion rate increase as shown in Figure 9.8 and Figure 9.9, respectively. For the overall particle growth, it was more complex as shown in Figure 9.10 depending on the magnitudes of both the dissolution rate and the ion diffusion rate. The particle size change (increase or decrease) rate

increased with the Pt dissolution rate increase or Pt ion concentration increase. Increase Pt ion diffusion rate initially increased the particle size growth rate due to the enhanced mass exchange rate between small and large type particles. But at the very high diffusion rate of the soluble Pt ions, the overall particle size decreased due to the dominated Pt mass loss into membrane resulted in the both type particle shrinkage discussed previously.

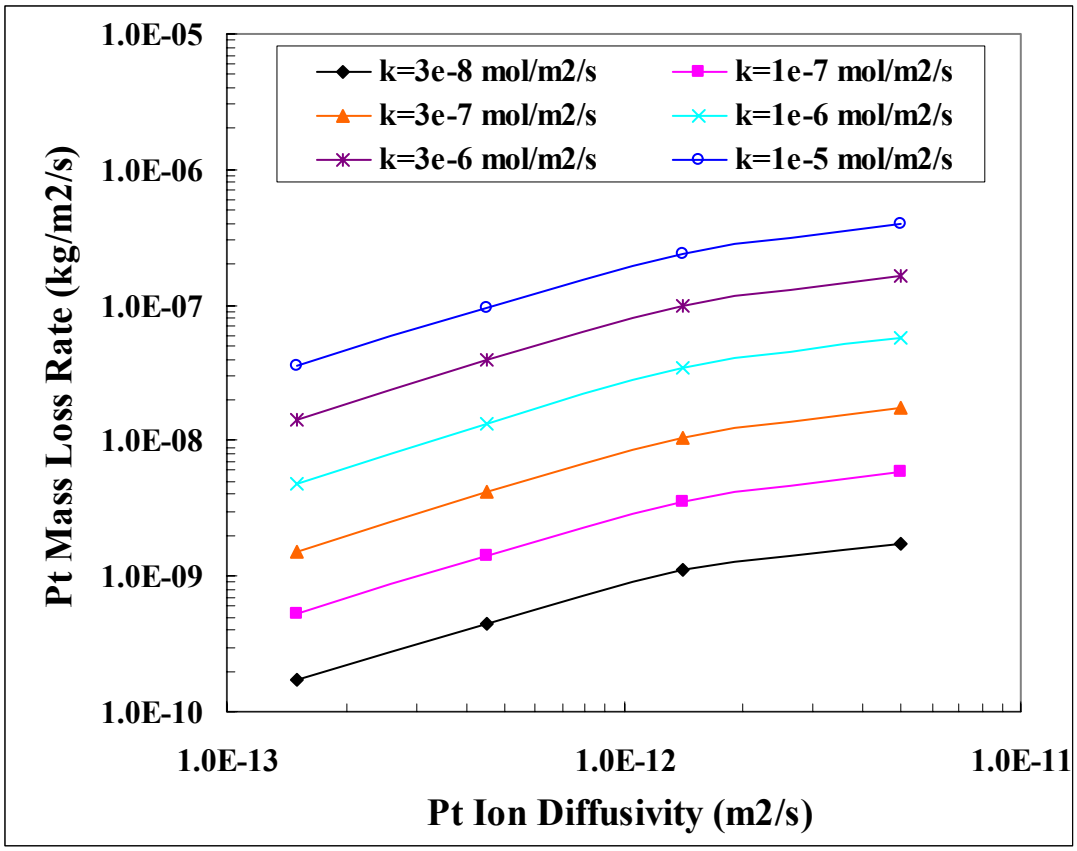

Figure 9.8: Parametric study of initial cathode Pt mass loss rate during the square-wave potential cycling

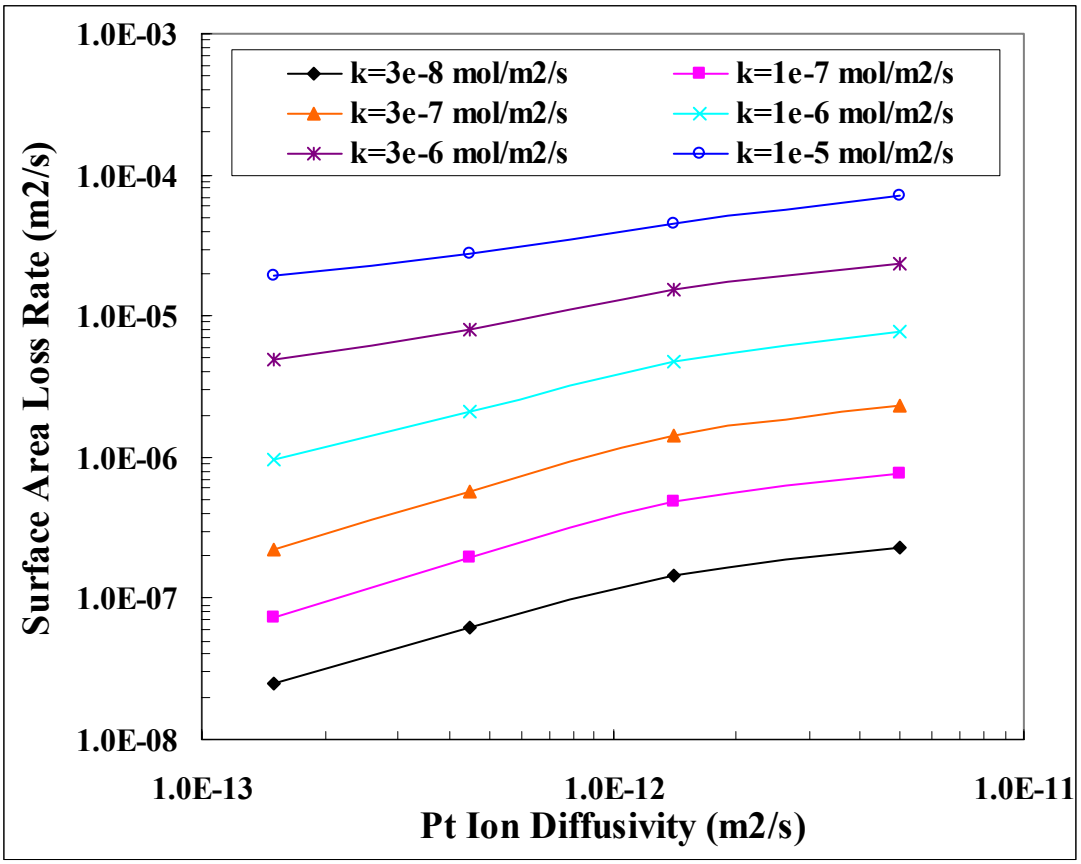

Figure 9.9: Parametric study of initial cathode surface area loss rate during the square-wave potential cycling

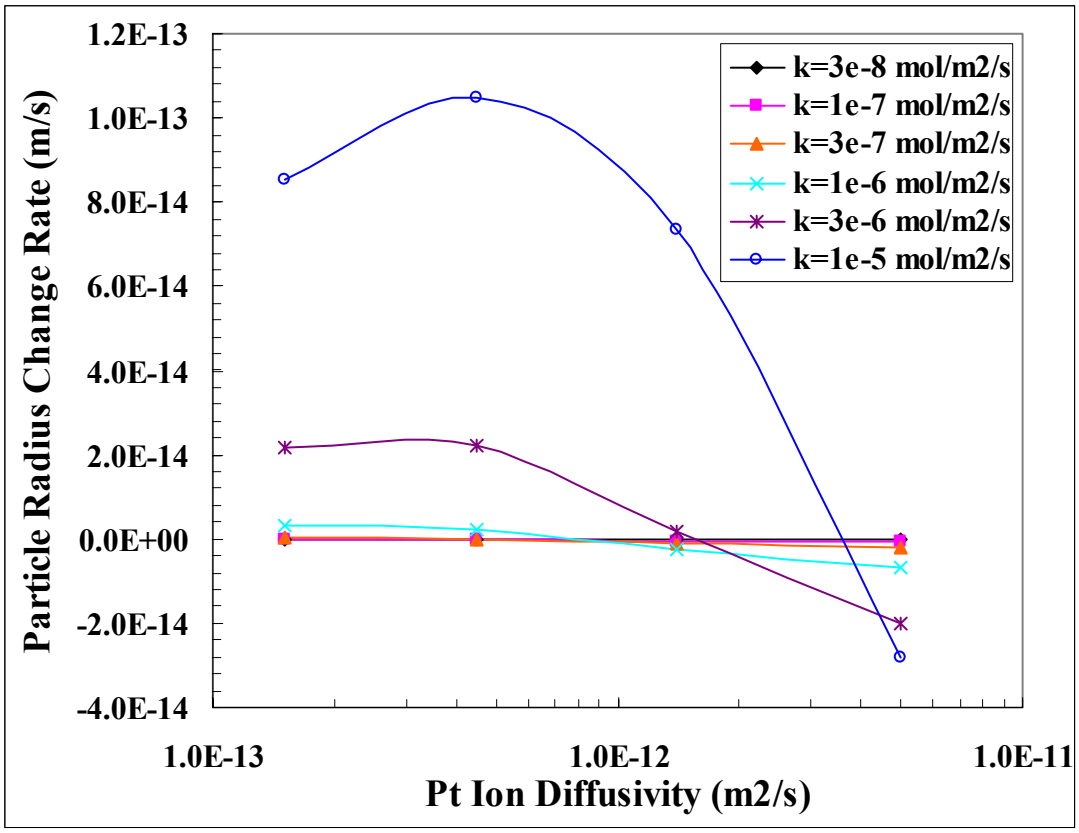

Figure 9.10: Parametric study of initial cathode particle growth rate during the square-wave potential cycling

Based on the parametric study results of initial cathode degradation rates, the total simulation error (E_{SIMU}) plotted in figure 9.11 was calculated by equation 9.10 based on the simulated values (X_i^{simu}: mass, surface area, and radius), mean of measured lab data (X_i^{lab}), and lab data variance (V_i^{lab}). The variance of experimental surface areas was calculated from two lab measurements. For particle size, the variance was estimated from the particle size data of four Pt X-ray peaks which was further scaled by a factor of 200/7000 based on the number of cycles since the particle size was only measured after 7000 potential cycles. For Pt mass in cathode, a 10 % relative error was assumed for the estimated value calculated from equation 5.6. A low error region is clearly shown in

figure 9.11 with the good fitting parameters of diffusivity (D) and dissolution rate constant (k *or* $k1$) in the range of 2×10^{-13} - 2×10^{-12} m^2/s and 5×10^{-7} - 3×10^{-6} $mol/m^2/s$, respectively.

$$E_{\mathrm{SIMU}} = \sum_i \frac{(X_i^{simu} - X_i^{\mathrm{lab,mean}})^2}{V_i^{lab}} \quad (i: \text{mass, area, \& radius}) \quad \text{(Equation 9.10)}$$

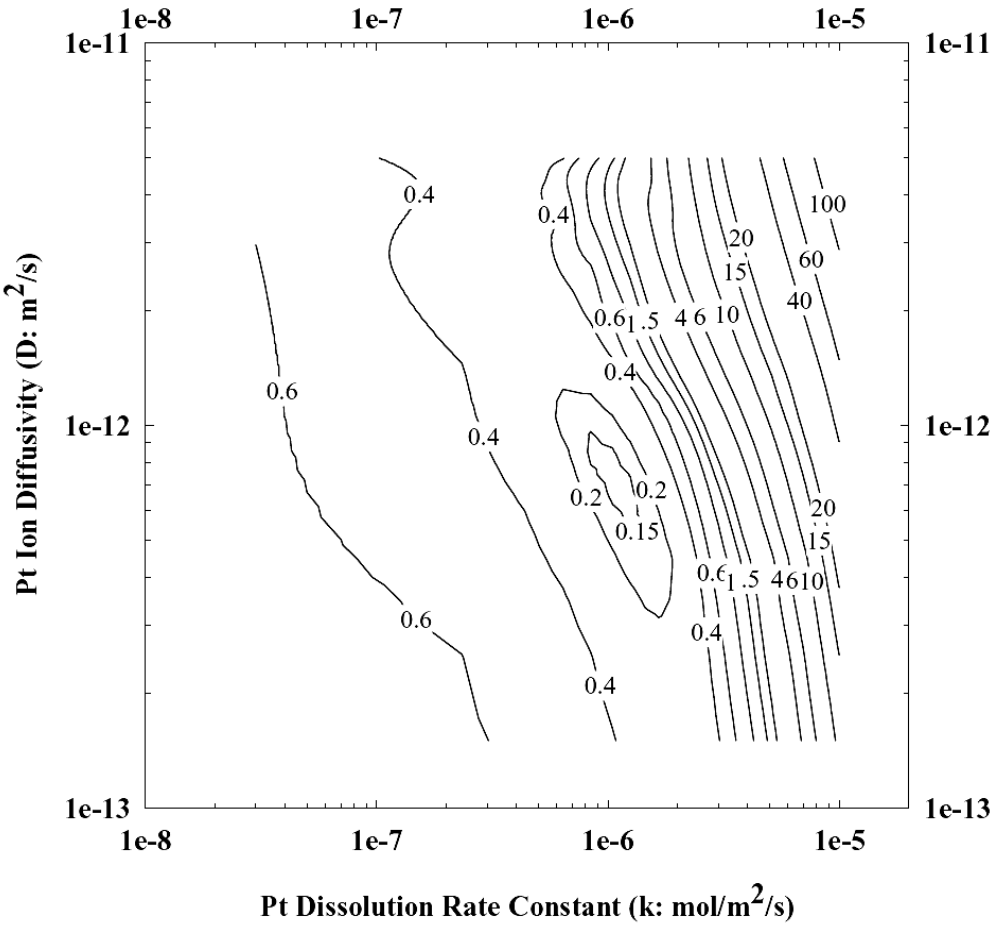

Figure 9.11: Contour plot of relative simulation error

9.3 Catalyst Degradations under Varied Potential Dynamic Conditions

Under varied dynamic cathode potentials conditions, we were interested in applying the catalyst degradation model to identify the factors affecting cathode degradation rates in a fresh 25 cm^2 CCM [67]. In this work, we varied the potential wave shapes (symmetric square-wave and triangle-wave with different symmetries), the highest (upper) and lowest (lower) potential levels, and the potential cycle frequency. A more detailed study of these variables with experimental designs and statistical analyses were done in collaboration with Ms. Rajeswari Chandrasekaran and published elsewhere [89].

For the potential levels in the square-wave potential cycling (10 s/cycle), the upper potential level of the cycle was the major factor with the expected orders of magnitude increase of the catalyst degradation rates with upper potential level increase as shown in Table 9.2. In contrast, the change of lower potential level between 0.5 and 0.6 V (vs. RHE) only resulted less than 2 % change of cathode degradation rates. For a medium high upper potential, increase of lower potential increased the degradation rate due to the overall high potential level. With the increased upper potential level, the degradation rate difference decreased between two different lower potential level cases. At the upper potential level of 1.1 V, the surface area loss rate and particle growth rate were even become lower at the lower potential level of 0.6 V than at 0.5 V. This can be caused by the increased Pt oxide coverage with a high upper potential and incomplete oxide reduction at an increased lower potential level.

Table 9.2: Cathode degradation rates under varied high and low potential levels of square-wave potential cycles with a time step of 5 s (10 s/cycle)

Upper potential (V)	0.8		0.9		1.0		1.1	
Lower potential (V)	0.5	0.6	0.5	0.6	0.5	0.6	0.5	0.6
Mass loss ($kg/m^2/s$)	5.64×10^{-16}	5.76×10^{-16}	6.80×10^{-13}	6.85×10^{-13}	4.70×10^{-10}	4.75×10^{-10}	1.36×10^{-8}	1.37×10^{-8}
Surface area loss (m^2/s)	5.62×10^{-9}	5.74×10^{-9}	1.35×10^{-7}	1.36×10^{-7}	3.20×10^{-6}	3.22×10^{-6}	3.17×10^{-5}	3.11×10^{-5}
Particle growth rate (m/s)	1.66×10^{-17}	1.70×10^{-17}	3.97×10^{-16}	4.01×10^{-16}	9.52×10^{-15}	9.58×10^{-15}	1.05×10^{-13}	1.04×10^{-13}

Also, we compared four kinds of potential cycles: (symmetric) square-wave, symmetric, slow anodic and fast anodic triangle waves with the cathode degradation rates shown in Table 9.3. The square-wave potential cycling resulted in the much higher degradation rates due to the overall high potential levels, which were observed in Paik's recent experimental study on fuel cell cathode [60]. But Kinoshita *et al.* observed the opposite experimental phenomena of the Pt electrode dissolution in acid solution [27], which was mostly due to the batch reactor system different from open fuel cell system. In fuel cells, dissolved Pt ions from the cathode can be transported into the membrane and be reduced by the permeated hydrogen, thus some Pt permanently was lost into the polymer electrolyte. In a dissolution cell, Pt can be dissolved into solution, but the ions still can be replated back to the electrode during the reduction period. So the higher upper potential in potential cycling might be more important for catalyst degradation rate such as mass loss in fuel cell systems, while the lower reduction potential might be dominated factor for dissolution in a closed electrochemical cell. Certainly, the different potential levels in Kinoshita's work may also cause the different observation.

For the triangle-wave potential cycling, the relatively faster anodic scan resulted in the faster cathode degradation. This can be explained by the lower oxide coverage during the faster anodic scan which resulted in higher catalyst dissolution rate. Such the same behaviors were also observed in Kawahara's experimental work [78].

Table 9.3: Cathode degradation rates under square-wave and triangle wave potential cycling between 1.0 V and 0.5 V (10 s/cycle)

Potential wave shape	Symmetric square wave	Symmetric triangle wave	Slow anodic (8 s ox. & 2 s red.) triangle wave	Fast anodic (2 s ox. & 8 s red.) triangle wave
Mass loss ($kg/m^2/s$)	4.70×10^{-10}	2.97×10^{-11}	2.65×10^{-11}	3.16×10^{-11}
Surface area loss (m^2/s)	3.20×10^{-6}	4.84×10^{-7}	4.80×10^{-7}	4.94×10^{-7}
Particle growth rate (m/s)	9.52×10^{-15}	1.44×10^{-15}	1.44×10^{-15}	1.47×10^{-15}

For the potential cycle frequency, the model predicted higher catalyst degradation rates with increasing cycling frequency on a time basis as shown in Table 9.4. It can be explained by the lower platinum oxide coverage during a fast oxidation and reduction cycle. The similar behaviors of fast loss rate of cathode active surface area and fuel cell performance at a high frequency potential cycling were observed in Paik's experimental work [60].

Table 9.4: Cathode degradation rates under different frequencies of symmetric triangle wave potential cycling between 1.2 V and 0.5 V

Potential cycle frequency	10 s/cycle	40 s/cycle
Mass loss ($kg/m^2/s$)	8.68×10^{-9}	5.54×10^{-9}
Surface area loss (m^2/s)	2.50×10^{-5}	2.19×10^{-6}
Particle growth rate (m/s)	8.26×10^{-14}	6.80×10^{-15}

9.4 Conclusions

A physics-based model of catalyst degradation was proposed for platinum supported on carbon for a PEM fuel cell. The following processes have been treated in the model: 1) electrochemical dissolution and re-deposition in the cathode; 2) Pt ion transport by diffusion in MEA; and 3) Pt ion chemical reduction in membrane by hydrogen that permeates from the anode. A simplified bi-modal particle size distribution was adopted to simulate the overall cathode Pt particle growth, surface area loss and Pt mass loss. Overall Pt particle growth by Pt mass exchange between small and large particles was clearly demonstrated through Pt dissolution and Pt ion deposition. In this initial study, a simplified model was developed to elucidate cathode catalyst degradation. Further refinements are needed to describe more accurately cathode degradation behavior in order to predict degradation over typical lifetimes of PEM fuel cells. The degradation model did not well predict Pt catalyst degradation rate with the reasonable parameters. It seemed that the assumed Pt ion diffusion rate was too low and Pt ion concentration was too high. We concluded that additional mechanism besides Pt dissolution and Pt ion deposition involve in the catalyst degradation process. Catalyst degradation processes of Pt cluster formation on carbon support and neighboring Pt clusters and/or nanoparticles coarsening were proposed for further experimental and numerical investigations.

Consistent with experimental results, the model also showed that cathode cycling upper potential and cycle frequency had major significantly positive effects on catalyst degradation rate. In a potential cycle with fast anodic and slow cathodic scans was predicted to result in a fast degradation rate due to the low surface coverage.

CHAPTER 10

CONCLUSIONS

10.1 Summary of Work

Durability of carbon-supported platinum oxygen reduction electrocatalysts is one of the limiting factors for their commercial applications in PEM fuel cells. In this dissertation, we applied both experimental and numerical tools to study the mechanisms of platinum degradation. During the typical driving conditions of a fuel cell (or hybrid) vehicle, cathode potentials are frequently oscillated with the changes of power demands. We established an accelerated cathode degradation protocol through cycling the cathode potential in a square-wave profile, which resulted in insignificant polymer electrolyte degradation. During the degradation procedures, fuel cell performances, Pt/C catalyst ORR activity, and active surface areas were periodically monitored by non-destructive electrochemical methods. Post-mortem analyses of cathode catalyst particle sizes were conducted by grazing incidence X-ray diffraction and varied incidence angle X-ray diffraction. Changes of Pt elemental distributions in CCMs were studied by SEM/EDS analyses with the surface coated Au as the reference element [48].

The mechanisms of Platinum deposition in PEM were investigated and the formed Pt band location in the membrane was predicted and experimental confirmed based on the gas permeation rates in the membrane [48]. The effects of fuel cell operating variables (including cell temperature [67, 84], relative humidity, and oxygen partial pressure) on cathode degradation rates were studied.

To further understand the detailed reactions involved during the catalyst degradation, experimental studies of two major processes (platinum oxidation and dissolution) were conducted. Surface electrochemical oxidation of platinum by water was generally believed to provide the beneficial effect of slowing down Pt dissolution. The kinetics of Pt electrochemical oxidation was studied by Pt/C cathode cyclic voltammetry and further mathematical simulation. As for the detailed Pt dissolution process, it's quite complex. A simple system of Pt mesh as the working electrode in an electrochemical H-cell with 0.5 M $HClO_4$ electrolyte solution was utilized to conduct Pt dissolution tests under both non-reacting nitrogen and oxygen gas environments. The total soluble Pt species were quantified by ICP/MS. Based on the dissolution results, multiple chemical and electrochemical reactions were suspected under open-circuit and closed-circuit fuel-cell conditions.

Finally, a simplified cathode Pt/C catalyst model was built to study the catalyst degradation under dynamic potential conditions [90]. The model considered several important catalyst degradation processes: 1) platinum electrochemical oxidation, 2) Pt electrochemical dissolution, 3) Pt ion diffusion in the CCM, and 4) Pt ion chemical reduction and deposition in the membrane. A simplified bi-modal particle size distribution was adopted to simulate the overall cathode Pt particle growth, surface area loss and Pt mass loss. With the degradation model, platinum electrochemical dissolution rate (Pt ion concentration) and Pt ion diffusion rate were discussed in related to catalyst degradation. Parametric study of various potential cycling profiles (potential levels, cycle

symmetry, and cycle frequency) were conducted to further identify the major affecting variables and further develop effective strategies to mitigate catalyst degradation rate.

10.2 Conclusions

One of the interesting phenomena during the cathode degradation was platinum deposition and Pt band formation in the membrane under the H_2/air (or pure O_2 or its mixture with N_2) potential cycling. In contrast, platinum was deposited at the cathode/membrane interface under the H_2/N_2 potential cycling. SEM/EDS Pt distribution analyses of the degraded and fresh CCMs confirmed that the deposited Pt atoms originated from the cathode, through dissolution forming soluble species during the potential cycling. It was hypothesized that Pt ions diffused into the membrane and were reduced by the hydrogen that permeated from the anode. The oxygen and hydrogen gas crossover rates were measured several orders of magnitude higher than the average Pt deposition rate during the whole degradation test. These deposited Pt atoms can catalyze combustion of the permeating oxygen and hydrogen. With the protection of oxygen (dominated near the cathode), Pt ions can diffuse further towards the anode until reaching the location where the crossovered hydrogen and oxygen completely reacted with each other. Then a pseudo-steady state of Pt ion diffusion and Pt deposition at such a location continued and eventually formed a Pt band. So Pt band locations were predicted based on the gas permeation rates and were experimentally verified successfully. It was also found that these deposited Pt atoms will not re-dissolve and re-deposit to another location in the membrane when changing the cathode gas oxygen partial pressure. To all intents and

purposes, it is impossible to recover these lost Pt atoms without recycling the entire CCM.

An active research thrust for PEM fuel cells is the development of high-temperature membranes to allow operation at temperatures above 80 °C under a medium-low humidity condition. Raising PEM fuel cell operating temperature has multiple benefits such as better heat rejection and CO tolerance at anode. So we investigated cathode degradation under different cell temperature, relative humidity and oxygen partial pressure conditions. We concluded that the benefits running PEM fuel cell at relatively high temperatures must be traded against the reduced lifetimes of catalysts and their supports. The cathode degradation rates (cell performances, cathode electrochemically active surface areas, and Pt mass loss into membrane) were dramatically accelerated when the cell temperature was raised from 40 °C to 80 °C.

As for the humidity, cyclic voltammetry studies showed that the electrochemical oxidation rate of Pt by water increased with increasing cell humidity. However, increasing cell humidity from 50 % to 100 % at 60 °C resulted in a 50 % higher rate of active surface area loss and nearly doubled loss of Pt into membrane. We concluded that the accelerated catalyst degradation was due to the fast transport of dissolved platinum species in possibly expanded water (or ionic) channel networks insides the polymer electrolytes under high humidity conditions.

In the literature, oxygen was reported to contribute to surface oxidation of Pt especially under the conditions of low temperature and low humidity. Our study showed no significant differences in degradation rates of Pt at three oxygen partial pressures (nitrogen, air and pure oxygen) and two humidity levels (50% and 100% RH), which suggested that Pt oxidation by oxygen gas may not be an important factor under the potential cycling conditions.

In an effort to elucidate the detailed Pt dissolution processes, dissolution of Pt gauze electrode in 0.5 M $HClO_4$ solution was conducted. Large positive effects of holding potentials on dissolution rates and pseudo-steady state soluble Pt concentrations were observed. Without an external holding potential, the dissolution rate of Pt was much higher under air bubbling condition, with a more than two orders magnitude higher pseudo-steady state Pt concentration than that under the nitrogen environment. However, at a holding potential of 0.8 V (vs. RHE), the Pt concentration in air was less than 100% higher than that in nitrogen, indicating different dissolution processes when electrochemical reactions are involved. Hence, we proposed two distinct mechanisms of Pt dissolution for a hydrogen-air PEM fuel-cell cathode under no load (open circuit) and load conditions. At an open-circuit condition, platinum will be oxidized by oxygen molecule (reaction 8.3) and further oxidized and dissolved in the acidic electrolyte (reaction 8.4). Whereas under closed-circuit conditions, platinum can be oxidized by both oxygen chemically (reaction 8.3) and by water electrochemically (reactions 8.5-8.6) depending on the relative humidity and temperature, and electrochemical (reactions 8.7 and 8.9) and chemical dissolution (reactions 8.4 and 8.8) processes can be both involved.

The kinetics of platinum electrochemical oxidation kinetics was studied and mathematically simulated by cyclic voltammetry. In a simplified cathode degradation model aiming to study catalyst degradation, Pt electrochemical dissolution was assumed to be the dominated reaction forming soluble Pt ions, and diffusion and further reduction of Pt ions into membrane described Pt mass loss into membrane. Overall Pt particle growth by Pt mass exchange between small and large particles was clearly demonstrated through favored Pt dissolution from small Pt particles and Pt ion deposition on large particles due to a particle size effect. Also the model showed that cathode cycling upper potential and cycle frequency had major significantly positive effects on catalyst degradation rate, which agreed our and other experimental observations. A potential cycle with the fast anodic and slow cathodic scans was predicted to result in a fast degradation rate due to the low surface coverage.

Finally, Pt dissolution posts a challenging limit for the cathode durability in a PEM fuel cell. More durable electrode materials will be needed for PEM fuel cell commercial applications. Also an effective management of cell potentials can prolong cathode lifetime.

CHAPTER 11

FUTURE WORK RECOMMENDATIONS

Elucidating platinum catalyst degradation processes in PEM fuel cell cathode are challenging due to the catalyst particle size of a few nanometers, multiple phases and components in catalyst layers, and limited analytical tools to study interfacial chemical and physical events. The following studies are recommended in future studies.

Transmission electron microscopy (TEM) imaging of platinum nanoparticle provides good visual observations of catalyst structural and particle morphological changes during fuel cell cathode lifetime and degradation tests. The difficulty comes from the preparation of good quality 10-100 nm thick TEM samples. This work can be cooperated with Dr. Yulin Deng's research lab and the Center for Nanostructure Characterization and Fabrication at Georgia Tech. Applying cathode TEM imaging techniques, changes of Pt nanoparticle shapes, sizes and size distributions across cathode can be studied after fuel-cell tests. Such results will provide important information to understand catalyst nanoparticle degradation processes.

Platinum electrochemical oxidation processes: surface oxide formation and Pt-O dipole-dipole exchange (or oxygen penetration into Pt lattice) are simulated in a combined kinetic expression with a plateau current representing dipole exchange limited oxidation process at high potential in a CV curve. Total Pt oxide is not distinguished into surface oxide and sub-surface oxide through dipole exchange. Hence Pt dissolution was blocked in the catalyst model with a beyond one monolayer total oxide coverage at long

periods of oxidizing potentials. A more accurate Pt oxidation model with Pt surface electrochemical oxidation by water and multiple physical steps of PtO dipole exchange is recommended for future work.

Investigation of platinum dissolution is not straightforward and the involved species are not completely clear. Multiple processes of chemical and electrochemical reactions may be involved. We suspected that Pt dissolution processes in fuel-cell cathode (with air) are different under open-circuit and closed-circuit conditions. Rotating ring-disk electrode (RRDE) can be used to study soluble Pt species under various potential conditions. More advanced techniques such as in-situ quartz-crystal microbalance coupled with electrochemical measurements can monitor in-situ electrode mass change and current passed through electrode. Total Pt concentration in solution can be tested by ICP/MS. Combining these techniques, platinum dissolution processes and platinum species can be further elucidated. Kinetic study of Pt dissolution can be conducted and further simulated to improve the catalyst degradation model.

As for the cathode degradation model, we suspected that additional mechanism besides Pt dissolution and Pt ion deposition involve in the catalyst degradation process. Pt cluster formation on carbon support and neighboring Pt clusters and/or nanoparticles coarsening were proposed for further simulative investigation.

APPENDIX A

FUEL CELL WET UP AND CONDITIONING PROCEDURES

To wet-up the MEA and hydrate the membrane to its maximum water absorption capacity, the following steps are recommended. First, set the cell temperature at 80 °C. Set fuel and air saturator temperatures at the same temperature as the cell. Both gas line temperatures are set 5 °C above the gas saturator temperatures. Without applying fuel, wait for the system to warm up and reach the temperature set points. Next, continuous purge the system for 30 minutes with N_2. Set the fuel flow rate at 0.3 L/min and the air flow rate at 0.3 L/min. Then apply fuel/air, and leave the cell at open circuit for 1 hour. Hydrogen fuel is flammable and explosive gas. A H_2 detector (TIF 8800A) will be used to check for the existence of hydrogen, especially at the gasket position at the middle of cell assembly.

Hydrogen fuel diffuses through the separator from anode to cathode and will react with the oxidant, which results in cell voltage loss. To check for fuel crossover, simply shut off the air supply while maintaining constant hydrogen flow. Prevent external air entry by sealing the air effluent exit using Teflon tape. Monitor the open circuit voltage (OCV) for 10 minutes. If OCV continues dropping to zero, it indicates a gas crossover. Significant fuel crossover should be eliminated before further tests are done.

Constant current method is used for cell conditioning. For Nafion® 111 CCMs, they are conditioned at the current densities of 50, 200, 500, 800 and 1000 mA/cm^2 (each step five hours) at 80 °C and fully humidified conditions. For Nafion® 117 CCMs with much lower performances, they are conditioned at the current densities of 20, 100 and 200 mA/cm^2 (each step eight hours) at 80 °C and fully humidified conditions. The fuel

and air flow rates are load based as followings: Fuel (pure H_2)=0.3 L/min +0.0385 (L/min/A)*Current (A); Air=0.3 L/min+0.1464 (L/min/A)*Current (A).

APPENDIX B

TABLE LIST OF ALL CCMS TESTS

#	Electro-lyte: Nafion®	Catalyst Loading (A/C)*: mg/cm^2	Wet Up & Conditioning (@100%RH)	Experiments			
				Cell (°C)	% RH	Gas Flows (L/min)	Procedures (SQ: square wave; TS: time step)
1	111	0.3/0.5	65 °C, 25h (a)	65	100	H_2/N_2: 0.1/0.3	3000 SQ 0.87-1.2V TS 15s
2	111	0.3/0.5	65 °C, 25h (a)	65	100	H_2/air: 0.1/0.3	3000 SQ 0.87-1.2V TS 15s
3	117	0.3/0.3	65 °C, 24h (b)	65	100	H_2/50%O_2 in N_2: 0.38/0.91	3000SQ 0.87-1.2V TS 15s
4	111	0.3/0.5	65 °C, 25h (a)	65	100	H_2/O_2: 0.1/0.3 followed by H_2/air: 0.1/0.3	H2/O2 3000SQ 0.87-1.2V TS 15s +H_2/air 3000SQ 0.87-1.2V TS 15s
5	111	0.3/0.5	65 °C, 25h (a)	65	100	H_2/ air: 0.1/0.3 followed by H_2/ O_2: 0.1/0.3	H_2/air 3000SQ 0.87-1.2V TS 15s +H_2/O_2 3000SQ 0.87-1.2V TS 15s
6	111	0.3/0.5	65 °C, 25h (a)	65	100	H_2/ air: 0.1/0.3 followed by H_2/ O_2: 0.1/0.3	H_2/air 3000SQ 0.87-1.2V TS 15s +H_2/O_2 25hours 0.8A/cm^2
7	111	0.3/0.5	80 °C, 25h (a)	40	100	H_2/air: 0.38/0.91	7000 SQ 0.87-1.2V TS 30s
8	111	0.3/0.5	80 °C, 25h (a)	60	100	H_2/air: 0.38/0.91	7000 SQ 0.87-1.2V TS 30s
9	111	0.3/0.5	80 °C, 25h (a)	80	100	H_2/air: 0.38/0.91	7000 SQ 0.87-1.2V TS 30s
10	117	0.3/0.3	80 °C, 24h (b)	60	100	H_2/N_2: 0.38/0.91	3600 SQ 0.87-1.2V TS 30s
11	117	0.3/0.3	80 °C, 24h (b)	60	50	H_2/N_2: 0.38/0.91	3600 SQ 0.87-1.2V TS 30s
12	117	0.3/0.3	80 °C, 24h (b)	60	100	H_2/air: 0.38/0.91	3600 SQ 0.87-1.2V TS 30s
13	117	0.3/0.3	80 °C, 24h (b)	60	50	H_2/air: 0.38/0.91	3600 SQ 0.87-1.2V TS 30s
14	117	0.3/0.3	80 °C, 24h (b)	60	100	H_2/ O_2: 0.38/0.91	3600 SQ 0.87-1.2V TS 30s
15	117	0.3/0.3	80 °C, 24h (b)	60	50	H_2/ O_2: 0.38/0.91	3600 SQ 0.87-1.2V TS 30s

Notes

*: A/C: Anode/Cathode.

(a): Conditioning currents: 50, 200, 500, 800 and 1000 mA/cm^2, each stage 5 hours.

(b): Conditioning currents: 20, 100 and 200 mA/cm^2, each stage 8 hours.

APPENDIX C

CCM #10-15 PT{111} X-RAY DIFFRACTION PATTERNS

This appendix includes CCM #10-15 of Pt{111} X-ray diffraction patterns at the varied X-ray beam incidence angles.

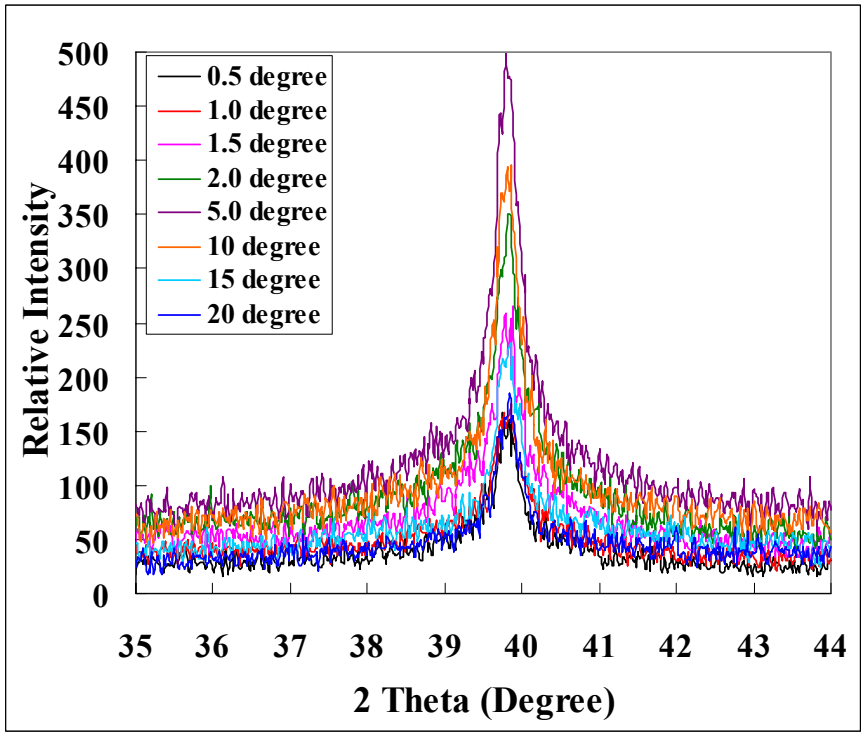

Figure C.1: CCM #10 Pt{111} peak at the varied X-ray incidence angles

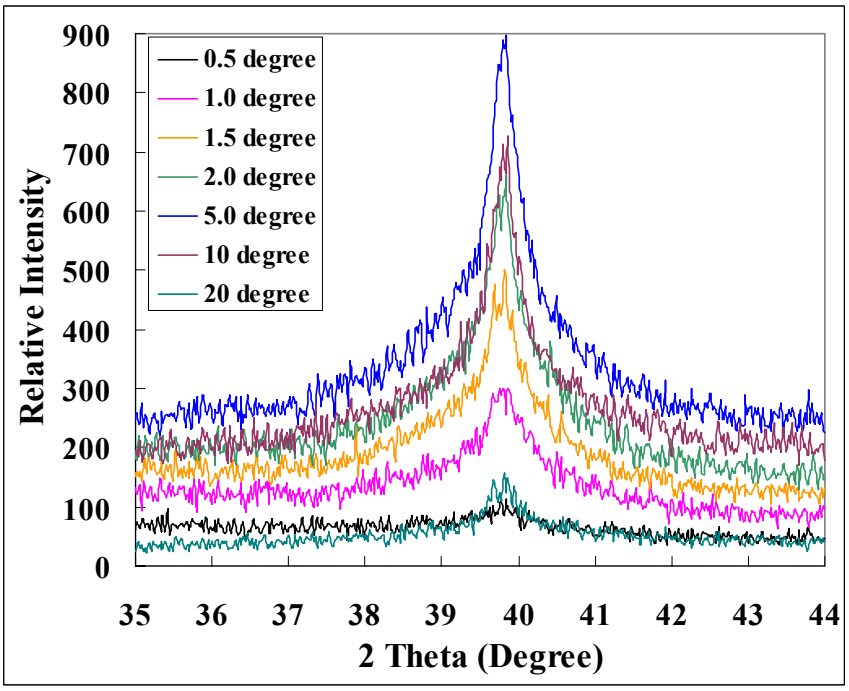

Figure C.2: CCM #11 Pt{111} peak at the varied X-ray incidence angles

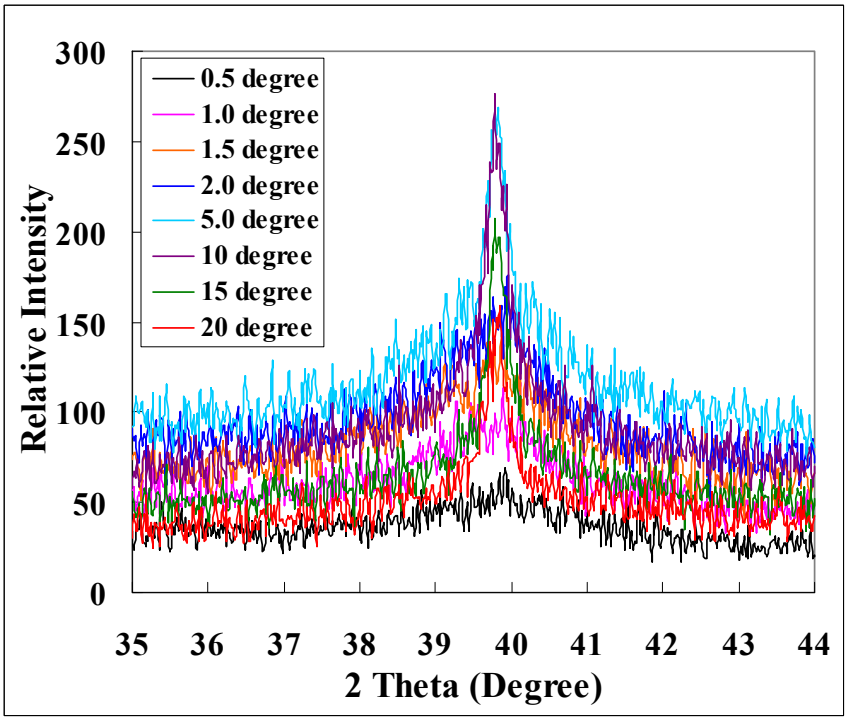

Figure C.3: CCM #12 Pt{111} peak at the varied X-ray incidence angles

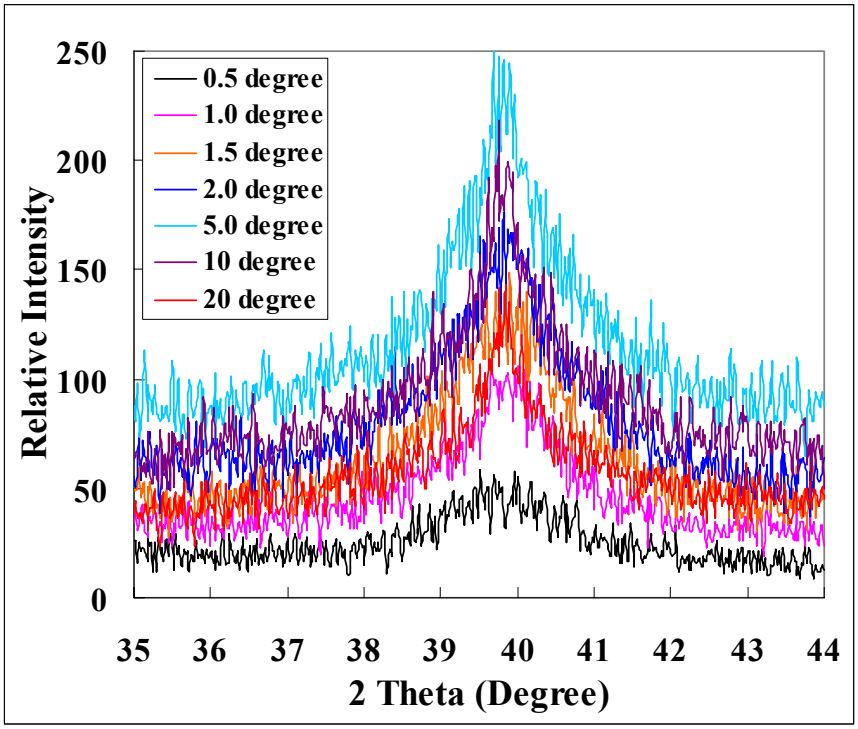

Figure C.4: CCM #13 Pt{111} peak at the varied X-ray incidence angles

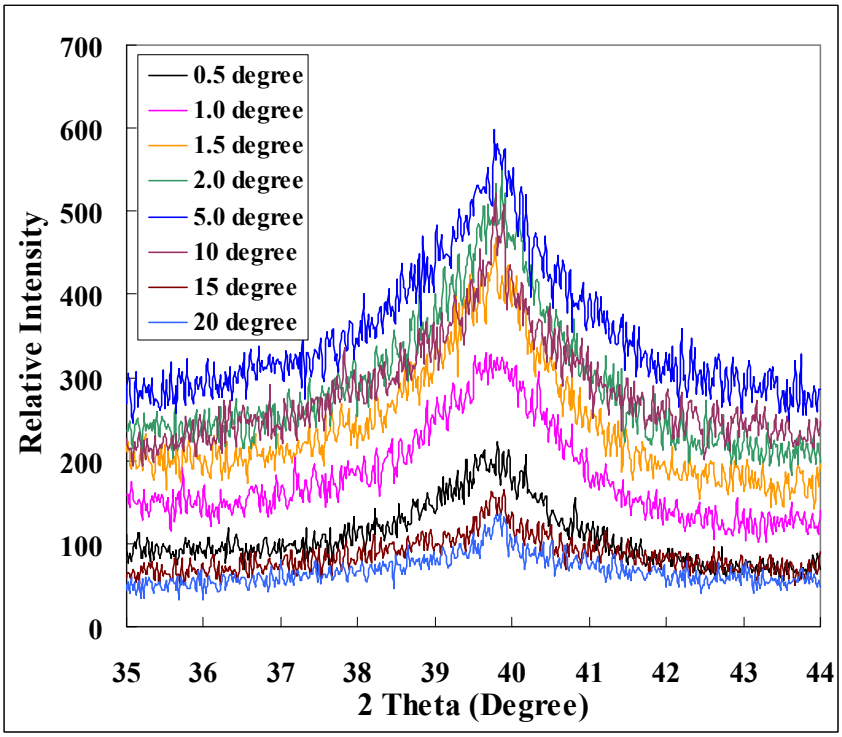

Figure C.5: CCM #14 Pt{111} peak at the varied X-ray incidence angles

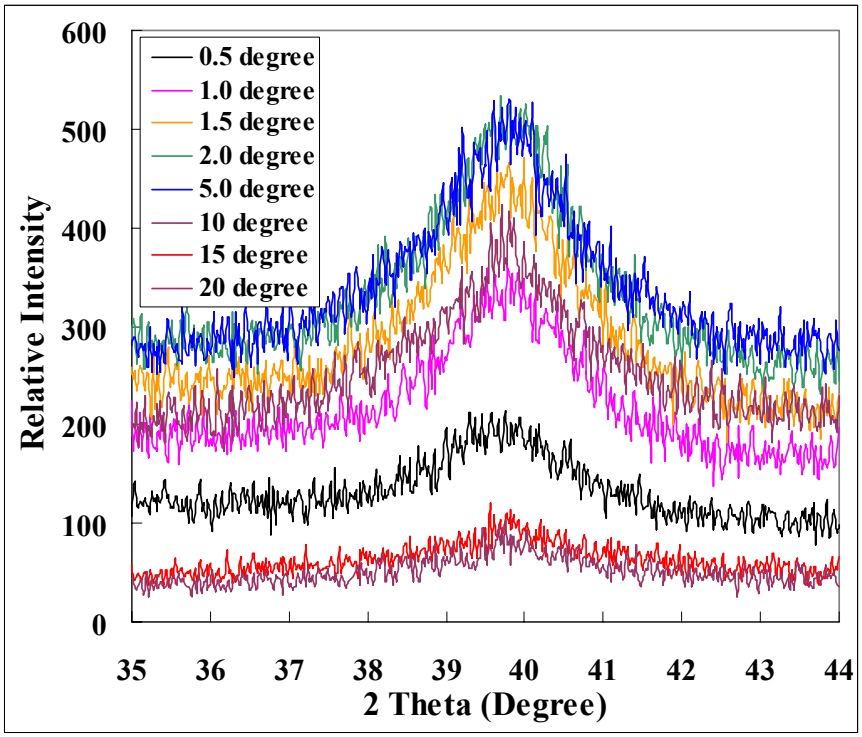

Figure C.6: CCM #15 Pt{111} peak at the varied X-ray incidence angles

APPENDIX D

MEASURED AND SIMULATED NORMALIZED CYCLIC VOLTAMMETRY CURVES

This appendix includes all the measured and simulated normalized CV curves at a potential scan rate of 50 mV/s, and the corresponding simulated surface oxide coverage.

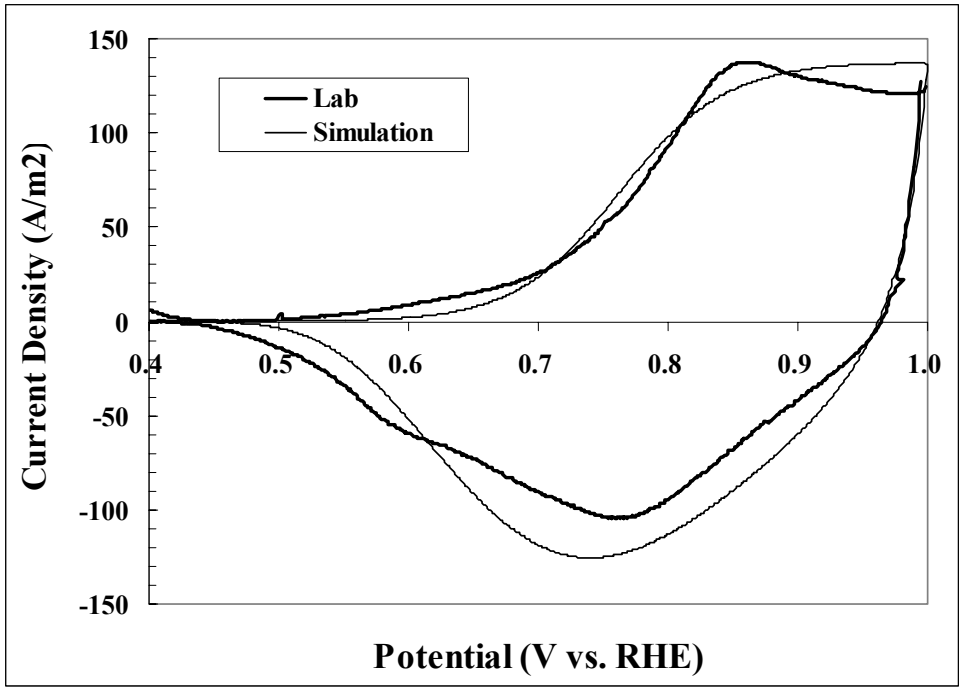

Figure D.1: Measured and simulated normalized CV curves at 25 °C and 100 %RH

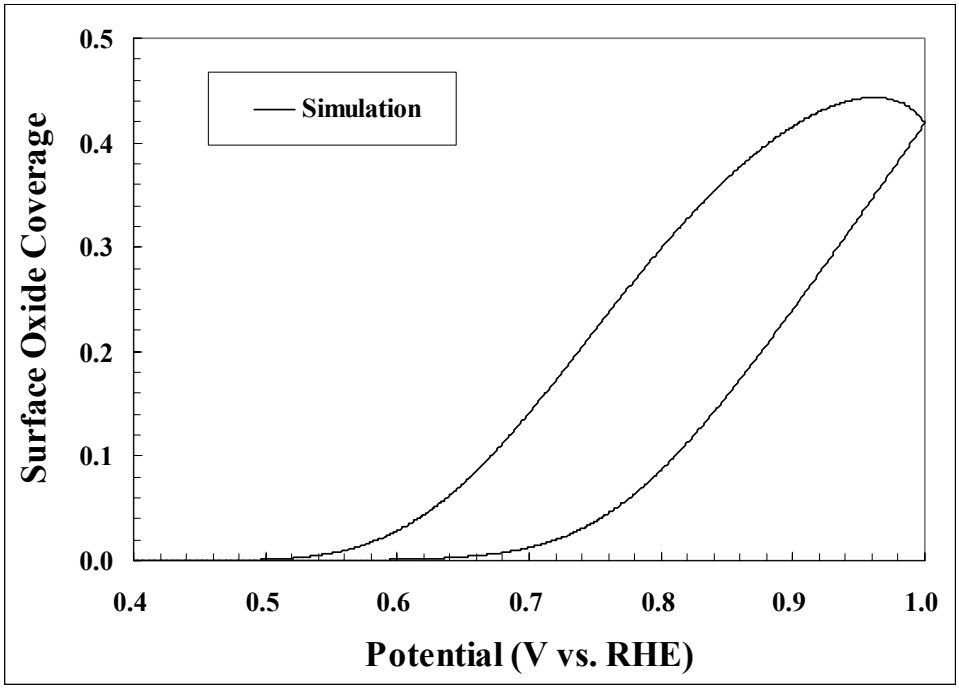

Figure D.2: Simulated surface oxide coverage during the CV scan at 25 °C and 100 %RH

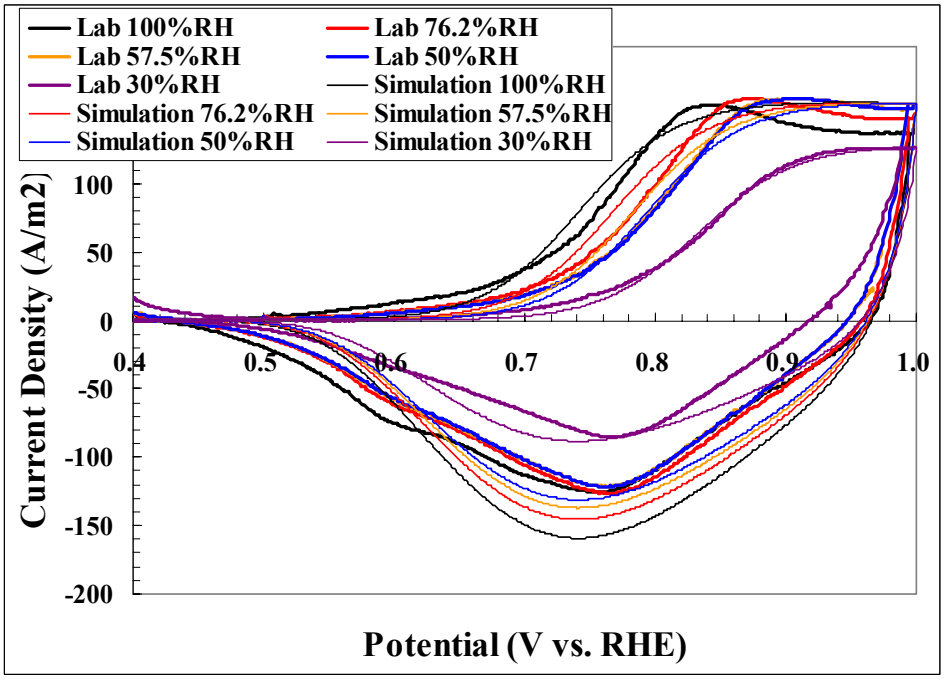

Figure D.3: Measured and simulated normalized CV curves at 40 °C

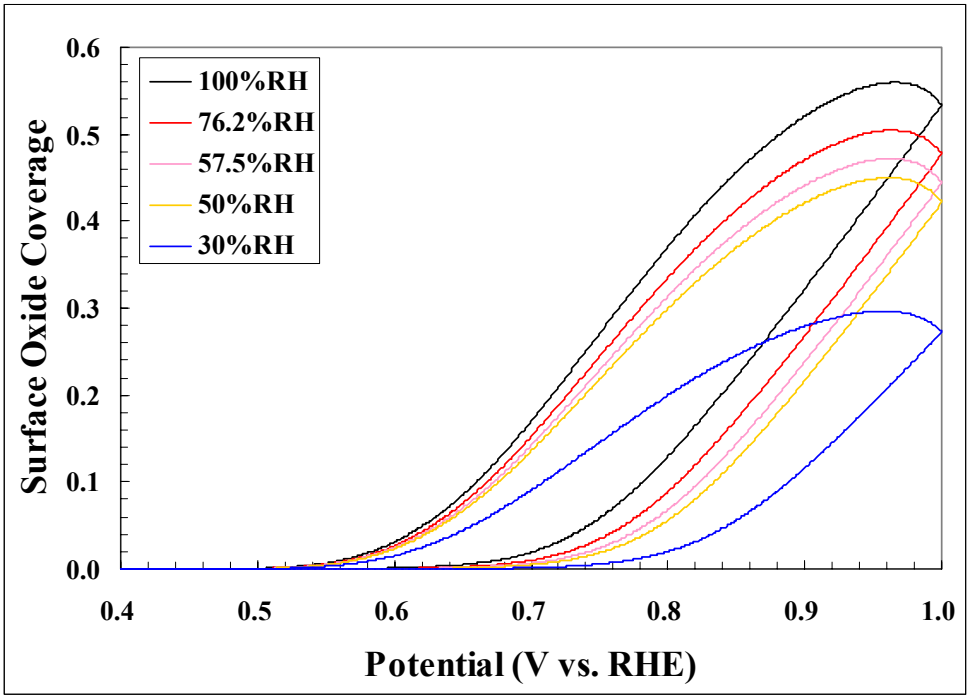

Figure D.4: Simulated surface oxide coverage during CV scans at 40 °C

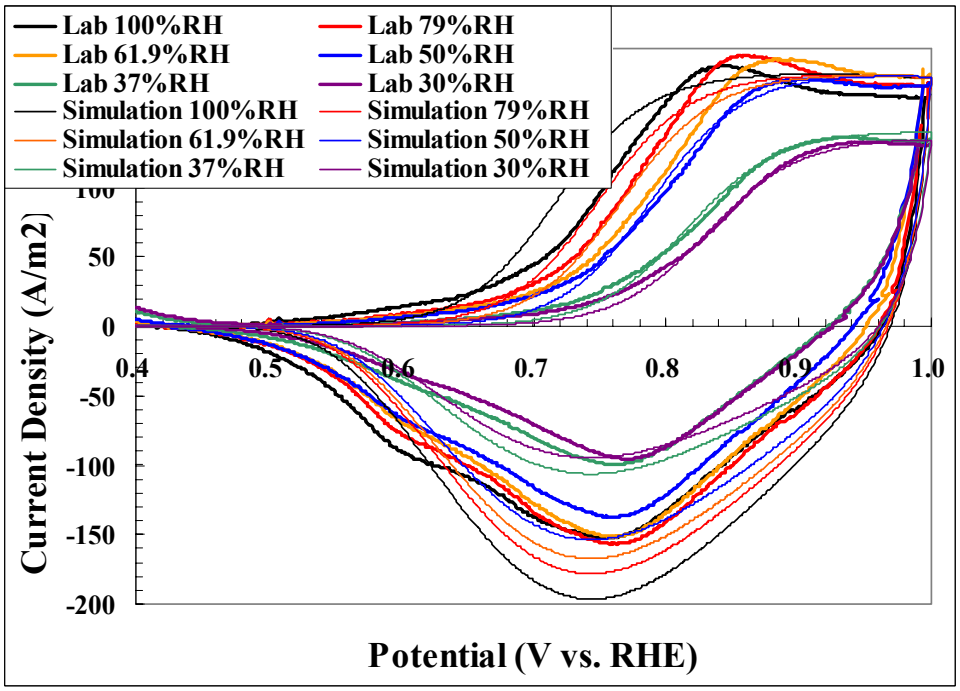

Figure D.5: Measured and simulated normalized CV curves at 60 °C

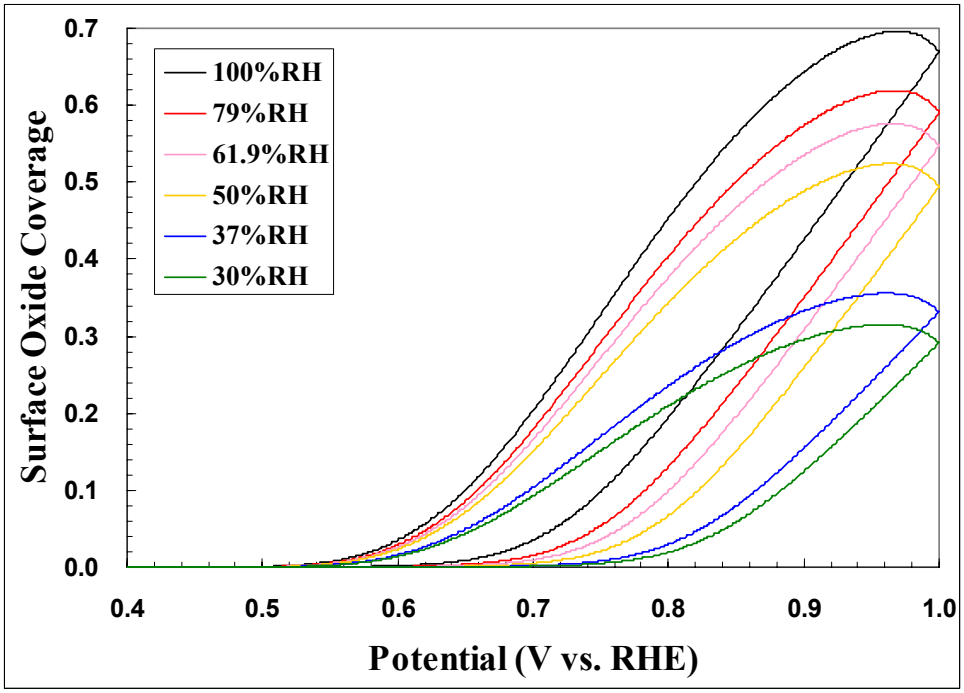

Figure D.6: Simulated surface oxide coverage during CV scans at 60 °C

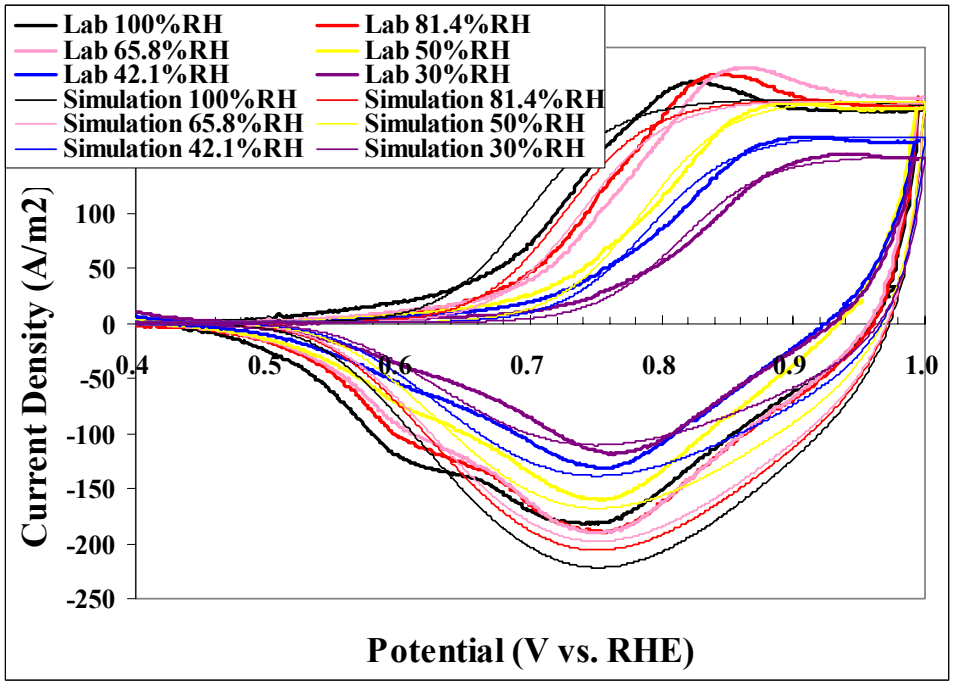

Figure D.7: Measured and simulated normalized CV curves at 80 °C

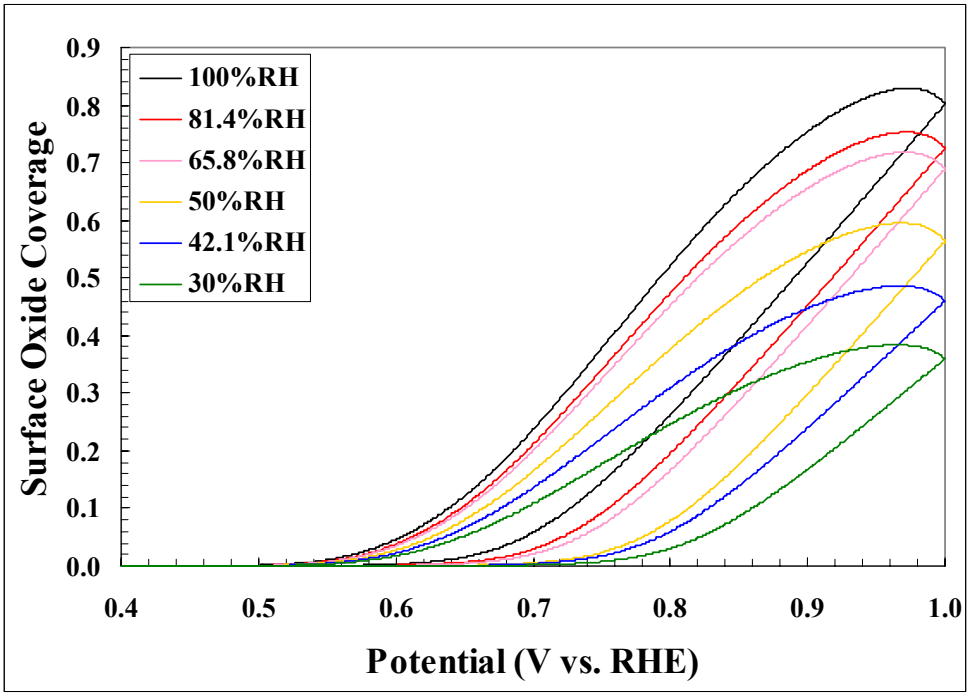

Figure D.8: Simulated surface oxide coverage during CV scans at 80 °C

APPENDIX E

EXAMPLE FORTRAN CODES FOR CYCLIC VOLTAMMETRY SIMULATION

```
Program Platinum
Implicit None
! Define constants with all standard SI units
Real, Parameter:: u20=0.98d0
! Thermodynamic potential
Real, Parameter:: m_p=0.1951d0, rou_p=21000d0, m_o=0.211d0, rou_o=14100d0
! Molecular weight and density of Pt(p) and PtO(o)
Real, Parameter:: n2=2.0d0
! Reaction 1 and 2 electron number
Real, Parameter:: CH=1.0d0, Cpref=1000.0d0
! concentration of proton: 1M
Real, Parameter:: sigma_p=2.37d0, sigma_o=1.0d0
! Surface energy coefficient of Pt and PtO

! Define other general constants
Real, Parameter:: F=96485.0d0, R=8.314d0, TM=333.0d0, pi=3.1415926d0
Real, parameter:: RH=1.0d0
! Relative humidity
Real, Parameter:: FMAX=2.18d-5, poros=0.2d0, a=1.94d7, L=1.875d-5
! a=2.75d7, for 55m2/gPt in catalyst loading of 0.5mg/cm2

Real, Parameter:: mu=-38000d0
! Standard chemical potential of PtO
Real, Parameter:: v=0.05d0, Emax=1.0d0, phi_max=1.0d0
! Constant of CV scan and maximum surface oxide coverage
Real, parameter:: delt=0.02d0
! Time step

! Define variables
Integer, parameter:: size=2*Emax/v/delt
Real, dimension(0:size):: rr, phi
! Particle radius, and surface coverage
Real, dimension(0:size):: r2, r2a, r2c
! Reaction 2 (oxidation) rate, r2a: anodic rate, r2c: cathodic rate
Real, dimension(0:size):: u2
! Thermodynamic potential of Pt oxidation
Real, dimension(0:size):: E
! External potential
Real, dimension(0:size):: CU
```

```
! Current
Real, dimension(0:size):: tt
! Time
Real, dimension(0:size):: phi_v
! Surface oxide vacancy
Real:: delt1_phi, delt2_phi, delt1_rr, delt2_rr
Real:: omiga=30000, k2a=7.0d-6, k2c=7.0d-6, alphi_a2=0.4d0, alphi_c2=0.1d0
! Oxidation kinetic rate constant and transfer coefficients
Integer:: i=0

! Define initial values
rr(0)=1.65e-9
! Radius of nanoparticles initially to be 3.3nm for Dupont® MEA
phi(0)=0.0
E(0)=0.0
tt(0)=0.0
u2(0)=u20+(0.50/F)*(mu+sigma_o*m_o/rou_o/rr(0)-sigma_p*m_p/rou_p/rr(0))
phi_v(0)=1.0-phi(0)
r2(0)=k2a*RH*exp(-omiga*phi(0)/R/TM)*exp(alphi_a2*n2*F*(E(0)-u2(0))/(R*TM))-
k2c*phi(0)*CH*CH*exp(-alphi_c2*n2*F*(E(0)-u2(0))/(R*TM))
CU(0)=2.0*a*F*L*r2(0)

Open (unit=112, file="CV OXIDATION 60C RH.txt")
Write (112, 03) "scan rate", v*1000, "RH=", RH, "T(K)=", TM,  "Emax=", Emax,
"mu=", mu
03 Format (1X, A16, F16.8, A16, F16.8, A16, F16.8, A16, F16.8, a16, f16.8)
WRITE (112, 04)  "OMIGA=",omiga
WRITE (112, 04)  "ALPHI_A2=",alphi_a2, "ALPHI_C2=", alphi_c2, "K2A=", k2a,
"K2C=",k2c
04 FORMAT (1X, A16, F16.8, A16, F16.8, A16, F16.8, A16, F16.8, A16, F16.8, a16,
f16.8)

Do i=1, size

 if (i<=Emax/v/delt) then
 E(i)=E(i-1)+v*delt
 Else
 E(i)=E(i-1)-v*delt
 end if
 tt(i)=i*delt

 rr(i)=rr(i-1)+delt*(-m_p/rou_p)*r2(i-1)
 delt1_rr=rr(i)-rr(i-1)
 phi(i)=phi(i-1)+delt*(r2(i-1)/FMAX-(2*phi(i-1)/rr(i-1))*(rr(i)-rr(i-1))/delt)
 delt1_phi=phi(i)-phi(i-1)
 u2(i)=u20+(0.50/F)*(mu+sigma_o*m_o/rou_o/rr(i)-sigma_p*m_p/rou_p/rr(i))
```

```
 If (phi(i)>phi_max) then
 phi_v(i)=1.0d0-phi_max
 else if (phi(i)<=phi_max.and.phi(i)>=1.0d-31) then
 phi_v(i)=1.0-phi(i)
 else if (phi(i)<1.0d-31) then
 Phi_v(i)=1.0
 phi(i)=1.0d-31
 end if

 r2(i)=k2a*RH*exp(-omiga*phi(i)/R/TM)*exp(alphi_a2*n2*F*(E(i)-u2(i))/(R*TM))&
 &-k2c*Phi(i)*CH*CH*exp(-alphi_c2*n2*F*(E(i)-u2(i))/(R*TM))
 delt2_rr=delt*(-m_p/rou_p)*r2(i)
 delt2_phi=delt*(r2(i)/FMAX-(2*phi(i)/rr(i))*(delt2_rr/delt))

 phi(i)=phi(i-1)+(delt1_phi+delt2_phi)/2.0d0
 rr(i)=rr(i-1)+(delt1_rr+delt2_rr)/2.0d0
 u2(i)=u20+(0.50/F)*(mu+sigma_o*m_o/rou_o/rr(i)-sigma_p*m_p/rou_p/rr(i))

 if (phi(i)>phi_max) then
 phi_v(i)=1.0d0-phi_max
 else if (phi(i)<=phi_max.and.phi(i)>=1.0d-31) then
 phi_v(i)=1.0-phi(i)
 else if (phi(i)<1.0d-31) then
 Phi_v(i)=1.0
 phi(i)=1.0d-31
 end if

  r2(i)=k2a*RH*exp(-omiga*phi(i)/R/TM)*exp(alphi_a2*n2*F*(E(i)-u2(i))/(R*TM))&
  &-k2c*Phi(i)*CH*CH*exp(-alphi_c2*n2*F*(E(i)-u2(i))/(R*TM))
 r2a(i)=k2a*RH*exp(-omiga*phi(i)/R/TM)*exp(alphi_a2*n2*F*(E(i)-u2(i))/(R*TM))
 r2c(i)=-k2c*phi(i)*CH*CH*exp(-alphi_c2*n2*F*(E(i)-u2(i))/(R*TM))
 CU(i)=2.0*a*F*L*r2(i)

End Do

Write (unit=112,9) "i", "tt(i)", "E(i)", "phi(i)", "rr(i)", "r2(i)", "CU(i)", "r2a(i)", "r2c(i)",
"u2(i)"
9 FORMAT (1X, 11A16)

Do i=0, size
Write (unit=112,10) i, tt(i), E(i), phi(i), rr(i), r2(i), CU(i), r2a(i), r2c(i), u2(i)
10 Format(1X, I16, 10ES16.8)
End DO
End Program Platinum
```

APPENDIX F

CATALYST DEGRADATION MODEL MATHEMATICAL DESCRIPTION AND EQUATIONS LINEARIZATION

1. Model Variables and Equations in Cathode:

1): 13 core variables

K=1, Pt ion concentration, C (mol/m^3).
K=2, total surface oxide coverage at small Pt particles, θ_S (unitless).
K=3, total surface oxide coverage at large Pt particles, θ_L (unitless).
K=4, radius of small Pt particles (exclude oxide layers), R_S (m).
K=5, radius of large Pt particles (exclude oxide layers), R_L (m).
K=6, small Pt particles dissolution rate, r_{1S} ($mol/m^2/s$).
K=7, large Pt particles dissolution rate, r_{1L} ($mol/m^2/s$).
K=8, small Pt particles oxidation rate, r_{2S} ($mol/m^2/s$).
K=9, small Pt particles dissolution rate, r_{2L} ($mol/m^2/s$).
K=10, adjusted thermodynamic dissolution potential for small Pt particles, U_{1S} (V).
K=11, adjusted thermodynamic dissolution potential for large Pt particles, U_{1L} (V).
K=12, adjusted thermodynamic oxidation potential for small Pt particles, U_{2S} (V).
K=13, adjusted thermodynamic oxidation potential for large Pt particles, U_{2L} (V).

Note the program calculate the solutions at the current time step for several iterations until the solutions converged, or up to the preset maximum times of iterations. When the program is executed, each variable has several forms of values stored in memory, including the values at the old time step(s), and the current time steps including both the last iteration and the current iteration.

2): 13 core equations

I=1, $$\frac{\partial C}{\partial t} = D\frac{\partial^2 C}{\partial x^2} + \frac{A_S}{\varepsilon_C} r_{1S} + \frac{A_L}{\varepsilon_C} r_{1L}$$

I=2, $$\frac{d\theta_S}{dt} = \frac{r_{2S}}{\Gamma_{\max}} + \frac{2\theta_S}{R_S}\frac{M_{Pt}}{\rho_{Pt}}(r_{1S} + r_{2S})$$

I=3, $$\frac{d\theta_L}{dt} = \frac{r_{2L}}{\Gamma_{\max}} + \frac{2\theta_L}{R_L}\frac{M_{Pt}}{\rho_{Pt}}(r_{1L} + r_{2L})$$

I=4, $$\frac{dR_S}{dt} = -\frac{M_{Pt}}{\rho_{Pt}}(r_{1S} + r_{2S})$$

I=5, $$\frac{dR_L}{dt} = -\frac{M_{Pt}}{\rho_{Pt}}(r_{1L} + r_{2L})$$

I=6,

$$r_{1S} = k_1 \theta_S^V \left[\exp(\alpha_{1a} n_1 F(E - U_{1S})/RT) - \frac{C}{C_{ref}} \exp(-\alpha_{1C} n_1 F(E - U_{1S})/RT) \right]$$

I=7,

$$r_{1L} = k_1 \theta_L^V \left[\exp(\alpha_{1a} n_1 F(E - U_{1L})/RT) - \frac{C}{C_{ref}} \exp(-\alpha_{1C} n_1 F(E - U_{1L})/RT) \right]$$

I=8,

$$r_{2S} = k_2 \left[\exp(-\omega\theta_S / RT) \exp(\alpha_{2a} n_2 F(E - U_{2S})/RT) - CH^2 \theta_S \exp(-\alpha_{2C} n_2 F(E - U_{2S})/RT) \right]$$

I=9,

$$r_{2L} = k_2 \left[\exp(-\omega\theta_L / RT) \exp(\alpha_{2a} n_2 F(E - U_{2L})/RT) - CH^2 \theta_L \exp(-\alpha_{2C} n_2 F(E - U_{2L})/RT) \right]$$

I=10, $$U_{1S} = U_1^0 - \frac{1}{2F} \frac{\sigma_{Pt} M_{Pt}}{\rho_{Pt}} \frac{1}{R_S}$$

I=11, $$U_{1L} = U_1^0 - \frac{1}{2F} \frac{\sigma_{Pt} M_{Pt}}{\rho_{Pt}} \frac{1}{R_L}$$

I=12, $$U_{2S} = U_2^0 + \frac{1}{2F} (\Delta\mu_{Pt}^0 + \frac{\sigma_{PtO} M_{PtO}}{\rho_{PtO}} \frac{1}{R_S} - \frac{\sigma_{Pt} M_{Pt}}{\rho_{Pt}} \frac{1}{R_S})$$

I=13, $$U_{2L} = U_2^0 + \frac{1}{2F} (\Delta\mu_{Pt}^0 + \frac{\sigma_{PtO} M_{PtO}}{\rho_{PtO}} \frac{1}{R_L} - \frac{\sigma_{Pt} M_{Pt}}{\rho_{Pt}} \frac{1}{R_L})$$

3): other equations

$$A_S = \frac{4\pi R_S^2}{V} N_S$$

$$A_L = \frac{4\pi R_L^2}{V} N_L$$

$$\theta_S^V = 1.0 - \theta_S (\theta_S < \theta_{\max}) \quad \text{or} \quad \theta_S^V = 1.0 - \theta_{\max} (\theta_S \geq \theta_{\max})$$

$$\theta_L^V = 1.0 - \theta_L (\theta_L < \theta_{\max}) \quad \text{or} \quad \theta_L^V = 1.0 - \theta_{\max} (\theta_L \geq \theta_{\max})$$

$$m(t) = m(0) - \int_0^t NA dt$$

$$m = \sum_x \left(\begin{array}{l} \frac{4\pi}{3} \rho_{Pt} (N_S R_S^3 + N_L R_L^3) + \\ \frac{4\pi}{3} \rho_{PtO} \frac{M_{Pt}}{M_{PtO}} [N_S \theta_S ((R_S + d_O)^3 - R_S^3) + N_L \theta_L ((R_L + d_O)^3 - R_L^3)] \end{array} \right)$$

The second method of mass calculation is summation all Pt species masses in cathode, but PtO monolayer thickness (d_O) is not accurately known. So the first

method calculating Pt mass loss through Pt ions diffusion into membrane is more convenient.

$$S = \sum_x 4\pi\left(N_S R_S^2 + N_L R_L^2\right)$$

$$RR = \frac{\sum_x \left(N_S R_S^4 + N_L R_L^4\right)}{\sum_x \left(N_S R_S^3 + N_L R_L^3\right)}$$

$$RS = \frac{\sum_x \left(N_S R_S^4\right)}{\sum_x \left(N_S R_S^3\right)}$$

$$RL = \frac{\sum_x \left(N_L R_L^4\right)}{\sum_x \left(N_L R_L^3\right)}$$

2. Model Variables and Equations in membrane:

Only one variable Pt ion concentration, C (mol/m^3)

One diffusion equation: $$\frac{\partial C}{\partial t} = D\frac{\partial^2 C}{\partial x^2}$$

3. Model Variables and Equations cathode/membrane interface and boundaries:

The cathode and membrane mesh was set up as the followings. Note that both the first and the last meshes only have the half volume of the other ones. Both the number 1 and number N represent the edge of the ends and all other numbers represent the center (points) of each mesh, so that the distances between all neighboring points (or number) are equal, defined as Δx.

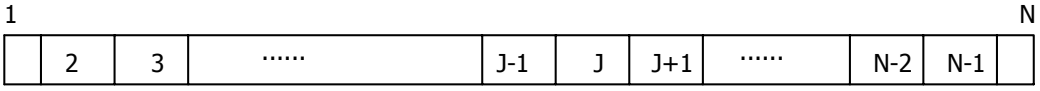

1): J=1, the boundary at GDL/Cathode, Pt ions diffusion flux is set to be zero.

$$\left.\frac{\partial C}{\partial x}\right|_{J=1} = \frac{-3C(1) + 4C(2) - C(3)}{2\Delta x} = 0$$

2): J=N, the Pt band location in membrane where Pt ions concentration is set to be zero.

$$C(N) = 0$$

3): The interface of cathode and membrane is located in the center of mesh number J. Due to the different polymer or ionomer volume faction in cathode and membrane, Pt ions mass balance by control volume methods is applied in this interface. So Pt ions

mass change includes the calculations of Pt ions mass in and out the volume and the produced or consumed Pt ions in the left half volume belonging to the cathode.

$$\frac{\varepsilon_C + \varepsilon_M}{2} V \times \Delta C(J) = (N_{IN} - N_{OUT}) A \times \Delta t + \frac{4\pi}{2} \times \Delta t \times (N_S R_S^2 r_{1S} + N_L R_L^2 r_{1L})$$

$$N_{IN} = -\varepsilon_C D \frac{C(J) - C(J-1)}{\Delta x}$$

$$N_{OUT} = -\varepsilon_M D \frac{C(J+1) - C(J)}{\Delta x}$$

4. Numerical Methods

All core equations including boundary and interface equations are linearlized to the following forms to use Dr. Newman's codes: "Band(J)" subroutine solving the linearlized equations. The ith equation and the kth variable C_k are previously defined. Only coefficients $A_{i,k}$, $B_{i,k}$, $D_{i,k}$, $X_{i,k}$, $Y_{i,k}$ and G_i are needed to supply to Band(J) subroutine.

In the region of the cathode, the membrane or the cathode/membrane interface, the ith equation (i=1 to n) is linearlized to the following form:

$$\sum_{k=1}^{n} A_{i,k}(J) C_k(J-1) + B_{i,k}(J) C_k(J) + D_{i,k}(J) C_k(J+1) = G_i(J)$$, for J=2, 3, …, N-1.

At boundary of GDL/cathode (J=1), there is no J=0 point, so the equations are linearlized to be:

$$\sum_{k=1}^{n} B_{i,k}(1) C_k(1) + D_{i,k}(1) C_k(2) + X_{i,k} C_k(3) = G_i(1)$$, for J=1.

At the boundary of Pt band in the membrane, there is no J=N+1, so a different form of linearization is used:

$$\sum_{k=1}^{n} Y_{i,k} C_k(N-2) + A_{i,k}(N) C_k(N-1) + B_{i,k}(N) C_k(N) = G_i(N)$$, for J=N.

The details of each equation linearization are shown as the followings.

1) Linearization equations in cathode regions

I=1, $$\frac{\partial C}{\partial t} = D \frac{\partial^2 C}{\partial x^2} + \frac{A_S}{\varepsilon_C} r_{1S} + \frac{A_L}{\varepsilon_C} r_{1L}$$

$$\frac{\partial C}{\partial t} = \frac{C(J, t+\Delta t) - C(J,t)}{\Delta t}$$

Apply central difference method and Crank-Nicolson technique to express the 2nd order derivatives.

$$\frac{\partial^2 C}{\partial x^2} = \frac{1}{2\Delta x^2}(C(J+1,t+\Delta t) + C(J-1,t+\Delta t) - 2C(J,t+\Delta t) + C(J+1,t) + C(J-1,t) - 2C(J,t))$$

Since $A_S = \frac{4\pi R_S^2}{V} N_S$ and $A_L = \frac{4\pi R_L^2}{V} N_L$, $R_S{}^2 r_{1S}$ and $R_L{}^2 r_{1L}$ must be linearlized.

$$R_S^2(J,t+\Delta t) r_{1S}(J,t+\Delta t) \approx (R_S(J,t) + \Delta R_S)^2 (r_{1S}(J,t) + \Delta r_{1S})$$

$$\approx R_S^2(J,t) r_{1S}(J,t) + R_S^2(J,t)\Delta r_{1S} + 2R_S(J,t) r_{1S}(J,t)\Delta R_S$$

$$= R_S^2(J,t) r_{1S}(J,t+\Delta t) + 2R_S(J,t) r_{1S}(J,t) R_S(J,t+\Delta t) - 2R_S^2(J,t) r_{1S}(J,t)$$

We also apply the Crank-Nicolson technique to the term, so

$$\frac{1}{2}(R_S^2(J,t+\Delta t) r_{1S}(J,t+\Delta t) + R_S^2(J,t) r_{1S}(J,t))$$

$$\approx \frac{1}{2}(R_S^2(J,t) r_{1S}(J,t+\Delta t) + 2R_S(J,t) r_{1S}(J,t) R_S(J,t+\Delta t) - R_S^2(J,t) r_{1S}(J,t))$$

The similar results for $R_L{}^2 r_{1L}$:

$$\frac{1}{2}(R_L^2(J,t+\Delta t) r_{1L}(J,t+\Delta t) + R_L^2(J,t) r_{1L}(J,t))$$

$$\approx \frac{1}{2}(R_L^2(J,t) r_{1L}(J,t+\Delta t) + 2R_L(J,t) r_{1L}(J,t) R_L(J,t+\Delta t) - R_L^2(J,t) r_{1L}(J,t))$$

So, the first equation could be finalized as:

$$\frac{D}{2\Delta x^2} C(J+1,t+\Delta t) - (\frac{D}{\Delta x^2} + \frac{1}{\Delta t}) C(J,t+\Delta t) + \frac{D}{2\Delta x^2} C(J-1,t+\Delta t)$$

$$+ \frac{2\pi}{V\varepsilon_C}(N_S R_S^2(J,t) r_{1S}(J,t+\Delta t) + 2N_S R_S(J,t) r_{1S}(J,t) R_S(J,t+\Delta t)$$

$$+ N_L R_L^2(J,t) r_{1L}(J,t+\Delta t) + 2N_L R_L(J,t) r_{1L}(J,t) R_L(J,t+\Delta t))$$

$$= -\frac{D}{2\Delta x^2} C(J+1,t) - (-\frac{D}{\Delta x^2} + \frac{1}{\Delta t}) C(J,t) - \frac{D}{2\Delta x^2} C(J-1,t)$$

$$+ \frac{2\pi}{V\varepsilon_C}(N_S R_S^2(J,t) r_{1S}(J,t)) + N_L R_L^2(J,t) r_{1L}(J,t))$$

So coefficients A(i,k), B(i,k), D(i,k) and G(i) can be determined and supplied to subroutine Band(J).

$$A(1,1) = D(1,1) = \frac{D}{2\Delta x^2}$$

$$B(1,1) = -(\frac{D}{\Delta x^2} + \frac{1}{\Delta t})$$

$$B(1,4) = \frac{4\pi}{V\varepsilon_C} N_S R_S(J,t) r_{1S}(J,t)$$

$$B(1,5) = \frac{4\pi}{V\varepsilon_C} N_L R_L(J,t) r_{1L}(J,t)$$

$$B(1,6) = \frac{2\pi}{V\varepsilon_C} N_S R_S^2(J,t)$$

$$B(1,7) = \frac{2\pi}{V\varepsilon_C} N_L R_L^2(J,t)$$

$$G(1) = -\frac{D}{2\Delta x^2} C(J+1,t) - (-\frac{D}{\Delta x^2} + \frac{1}{\Delta t}) C(J,t) - \frac{D}{2\Delta x^2} C(J-1,t)$$

$$+ \frac{2\pi}{V\varepsilon_C} [N_S R_S^2(J,t) r_{1S}(J,t)) + N_L R_L^2(J,t) r_{1L}(J,t)]$$

All other coefficients for equation I=1 are zero.

I=2, $\qquad \frac{d\theta_S}{dt} = \frac{r_{2S}}{\Gamma_{\max}} + \frac{2\theta_S}{R_S} \frac{M_{Pt}}{\rho_{Pt}} (r_{1S} + r_{2S})$

$$\frac{d\theta_S}{dt} = \frac{\theta_S(J,t+\Delta t) - \theta_S(J,t)}{\Delta t}$$

Apply Crank-Nicolson technique to two terms on the right side of equation 2.

$$r_{2S} = \frac{1}{2}(r_{2S}(J,t+\Delta t) + r_{2S}(J,t))$$

$$\frac{\theta_S}{R_S} r_{1S} = \frac{1}{2}\left(\frac{\theta_S(J,t)}{R_S(J,t)} r_{1S}(J,t) + \frac{\theta_S(J,t+\Delta t)}{R_S(J,t+\Delta t)} r_{1S}(J,t+\Delta t)\right)$$

$$\because \frac{\theta_S(J,t+\Delta t)}{R_S(J,t+\Delta t)} r_{1S}(J,t+\Delta t) = (\theta_S(J,t)+\Delta\theta_S)(r_{1S}(J,t)+\Delta r_{1S})(R_S(J,t)+\Delta R_S)^{-1}$$

$$\approx (\theta_S(J,t) r_{1S}(J,t) + \theta_S(J,t)\Delta r_{1S} + r_{1S}(J,t)\Delta\theta_S)\left(\frac{1}{R_S(J,t)} - \frac{\Delta R_S}{R_S^2(J,t)}\right)$$

$$\approx \frac{\theta_S(J,t) r_{1S}(J,t) + \theta_S(J,t)\Delta r_{1S} + r_{1S}(J,t)\Delta\theta_S}{R_S(J,t)} - \frac{\theta_S(J,t) r_{1S}(J,t)\Delta R_S}{R_S^2(J,t)}$$

$$= \frac{\theta_S(J,t) r_{1S}(J,t+\Delta t)}{R_S(J,t)} + \frac{r_{1S}(J,t)(\theta_S(J,t+\Delta t) - \theta_S(J,t))}{R_S(J,t)}$$

$$- \frac{\theta_S(J,t) r_{1S}(J,t)(R_S(J,t+\Delta t) - R_S(J,t))}{R_S^2(J,t)}$$

$$= \frac{\theta_S(J,t) r_{1S}(J,t+\Delta t)}{R_S(J,t)} + \frac{r_{1S}(J,t)\theta_S(J,t+\Delta t)}{R_S(J,t)} - \frac{\theta_S(J,t) r_{1S}(J,t) R_S(J,t+\Delta t)}{R_S^2(J,t)}$$

$$\therefore \frac{\theta_S}{R_S} r_{1S} \approx \frac{1}{2}\left(\frac{\theta_S(J,t)}{R_S(J,t)} r_{1S}(J,t) + \frac{\theta_S(J,t) r_{1S}(J,t+\Delta t)}{R_S(J,t)} + \frac{r_{1S}(J,t)\theta_S(J,t+\Delta t)}{R_S(J,t)}\right.$$

$$\left. - \frac{\theta_S(J,t) r_{1S}(J,t) R_S(J,t+\Delta t)}{R_S^2(J,t)}\right)$$

Similarly, we have:

$$\frac{\theta_S}{R_S} r_{2S} \approx \frac{1}{2}\left(\frac{\theta_S(J,t)}{R_S(J,t)} r_{2S}(J,t) + \frac{\theta_S(J,t) r_{2S}(J,t+\Delta t)}{R_S(J,t)} + \frac{r_{2S}(J,t)\theta_S(J,t+\Delta t)}{R_S(J,t)}\right.$$

$$\left. - \frac{\theta_S(J,t) r_{2S}(J,t) R_S(J,t+\Delta t)}{R_S^2(J,t)}\right)$$

So equation 2 is finalized to be:

$$\left(\frac{1}{\Delta t} - \frac{M_{Pt}}{\rho_{Pt}} \frac{r_{1S}(J,t) + r_{2S}(J,t)}{R_S(J,t)}\right)\theta_S(J,t+\Delta t) - \left(\frac{1}{2\Gamma_{\max}} + \frac{M_{Pt}}{\rho_{Pt}} \frac{\theta_S(J,t)}{R_S(J,t)}\right) r_{2S}(J,t+\Delta t)$$

$$- \frac{M_{Pt}}{\rho_{Pt}} \frac{\theta_S(J,t)}{R_S(J,t)} r_{1S}(J,t+\Delta t) + \frac{M_{Pt}}{\rho_{Pt}} \frac{\theta_S(J,t)(r_{1S}(J,t) + r_{2S}(J,t))}{R_S^2(J,t)} R_S(J,t+\Delta t)$$

$$= \frac{\theta_S(J,t)}{\Delta t} + \frac{r_{2S}(J,t)}{2\Gamma_{\max}} + \frac{M_{Pt}}{\rho_{Pt}} \frac{\theta_S(J,t)(r_{1S}(J,t) + r_{2S}(J,t))}{R_S(J,t)}$$

So,

$$B(2,2) = \frac{1}{\Delta t} - \frac{M_{Pt}}{\rho_{Pt}} \frac{r_{1S}(J,t) + r_{2S}(J,t)}{R_S(J,t)}$$

$$B(2,4) = \frac{M_{Pt}}{\rho_{Pt}} \frac{\theta_S(J,t)(r_{1S}(J,t) + r_{2S}(J,t))}{R_S^2(J,t)}$$

$$B(2,6) = -\frac{M_{Pt}}{\rho_{Pt}} \frac{\theta_S(J,t)}{R_S(J,t)}$$

$$B(2,8) = -\frac{1}{2\Gamma_{\max}} - \frac{M_{Pt}}{\rho_{Pt}} \frac{\theta_S(J,t)}{R_S(J,t)}$$

$$G(2) = \frac{\theta_S(J,t)}{\Delta t} + \frac{r_{2S}(J,t)}{2\Gamma_{\max}} + \frac{M_{Pt}}{\rho_{Pt}} \frac{\theta_S(J,t)(r_{1S}(J,t) + r_{2S}(J,t))}{R_S(J,t)}$$

All other coefficients for equation I=2 are zero.

I=3, $\frac{d\theta_L}{dt} = \frac{r_{2L}}{\Gamma_{\max}} + \frac{2\theta_L}{R_L} \frac{M_{Pt}}{\rho_{Pt}} (r_{1L} + r_{2L})$

Similarly as equation 2, we can write:

$$(\frac{1}{\Delta t} - \frac{M_{Pt}}{\rho_{Pt}} \frac{r_{1L}(J,t) + r_{2L}(J,t)}{R_L(J,t)})\theta_L(J,t+\Delta t) - (\frac{1}{2\Gamma_{\max}} + \frac{M_{Pt}}{\rho_{Pt}} \frac{\theta_L(J,t)}{R_L(J,t)})r_{2L}(J,t+\Delta t)$$

$$-\frac{M_{Pt}}{\rho_{Pt}} \frac{\theta_L(J,t)}{R_L(J,t)} r_{1L}(J,t+\Delta t) + \frac{M_{Pt}}{\rho_{Pt}} \frac{\theta_L(J,t)(r_{1L}(J,t) + r_{2L}(J,t))}{R_L^2(J,t)} R_L(J,t+\Delta t)$$

$$= \frac{\theta_L(J,t)}{\Delta t} + \frac{r_{2L}(J,t)}{2\Gamma_{\max}} + \frac{M_{Pt}}{\rho_{Pt}} \frac{\theta_L(J,t)(r_{1L}(J,t) + r_{2L}(J,t))}{R_L(J,t)}$$

So

$$B(3,3) = \frac{1}{\Delta t} - \frac{M_{Pt}}{\rho_{Pt}} \frac{r_{1L}(J,t) + r_{2L}(J,t)}{R_L(J,t)}$$

$$B(3,5) = \frac{M_{Pt}}{\rho_{Pt}} \frac{\theta_L(J,t)(r_{1L}(J,t) + r_{2L}(J,t))}{R_L^2(J,t)}$$

$$B(3,7) = -\frac{M_{Pt}}{\rho_{Pt}} \frac{\theta_L(J,t)}{R_L(J,t)}$$

$$B(3,9) = -\frac{1}{2\Gamma_{\max}} - \frac{M_{Pt}}{\rho_{Pt}} \frac{\theta_L(J,t)}{R_L(J,t)}$$

$$G(3) = \frac{\theta_L(J,t)}{\Delta t} + \frac{r_{2L}(J,t)}{2\Gamma_{\max}} + \frac{M_{Pt}}{\rho_{Pt}} \frac{\theta_L(J,t)(r_{1L}(J,t) + r_{2L}(J,t))}{R_L(J,t)}$$

All other coefficients for equation I=3 are zero.

I=4, $\frac{dR_S}{dt} = -\frac{M_{Pt}}{\rho_{Pt}}(r_{1S} + r_{2S})$

$$\frac{dR_S}{dt} = \frac{R_S(J,t+\Delta t) - R_S(J,t)}{\Delta t}$$

$$r_{1S} = \frac{1}{2}(r_{1S}(J,t+\Delta t) + r_{1S}(J,t))$$

$$r_{2S} = \frac{1}{2}(r_{2S}(J,t+\Delta t) + r_{2S}(J,t))$$

So, equation 4 can be written as:

$$\frac{R_S(J,t+\Delta t)}{\Delta t} + \frac{M_{Pt}}{2\rho_{Pt}}(r_{1S}(J,t+\Delta t) + r_{2S}(J,t+\Delta t))$$

$$= \frac{R_S(J,t)}{\Delta t} - \frac{M_{Pt}}{2\rho_{Pt}}(r_{1S}(J,t) + r_{2S}(J,t))$$

So, we have:

$$B(4,4) = \frac{1}{\Delta t}$$

$$B(4,6) = B(4,8) = \frac{M_{Pt}}{2\rho_{Pt}}$$

$$G(4) = \frac{R_S(J,t)}{\Delta t} - \frac{M_{Pt}}{2\rho_{Pt}}(r_{1S}(J,t) + r_{2S}(J,t))$$

All other coefficients for equation I=4 are zero.

I=5, $\frac{dR_L}{dt} = -\frac{M_{Pt}}{\rho_{Pt}}(r_{1L} + r_{2L})$

Similarly as equation 4, we can write:

$$\frac{R_L(J,t+\Delta t)}{\Delta t} + \frac{M_{Pt}}{2\rho_{Pt}}(r_{1L}(J,t+\Delta t) + r_{2L}(J,t+\Delta t))$$

$$= \frac{R_L(J,t)}{\Delta t} - \frac{M_{Pt}}{2\rho_{Pt}}(r_{1L}(J,t) + r_{2L}(J,t))$$

So, we have:

$$B(5,5) = \frac{1}{\Delta t}$$

$$B(5,7) = B(5,9) = \frac{M_{Pt}}{2\rho_{Pt}}$$

$$G(5) = \frac{R_L(J,t)}{\Delta t} - \frac{M_{Pt}}{2\rho_{Pt}}(r_{1L}(J,t) + r_{2L}(J,t))$$

All other coefficients for equation I=4 are zero.

Equation 6 to equation 13 is not a partial differential equation without time or space derivative terms. So all variables in these equation are $C_{i,k}(J, t+\Delta t)$ at location J and the new time step $t+\Delta t$. To be simple, J and $t+\Delta t$ is neglected. All variables are calculated based on values at the previous iteration at the new time step (until current iteration results converge with respect to the previous iteration data), instead of the values at the previous time step t. In the following linearization of equation 6-13, the previous iteration values are marked with a superscript zero sign. So previous and current iteration values are represented by $C_{i,k}^{0}$ and $C_{i,k}$, respectively.

$$\text{I=6, } r_{1S} = k_1 \theta_S^V \left[\exp(\alpha_{1a} n_1 F(E - U_{1S})/RT) - \frac{C}{C_{ref}} \exp(-\alpha_{1C} n_1 F(E - U_{1S})/RT) \right]$$

Case I: $\theta_S^V = 1.0 - \theta_S (\theta_S < \theta_{\max})$

$$r_{1S} = k_1 (1 - \theta_S) \left[\exp(\alpha_{1a} n_1 F(E - U_{1S})/RT) - \frac{C}{C_{ref}} \exp(-\alpha_{1C} n_1 F(E - U_{1S})/RT) \right]$$

$$= k_1 \exp(\alpha_{1a} n_1 F(E - U_{1S})/RT) - k_1 \frac{C}{C_{ref}} \exp(-\alpha_{1C} n_1 F(E - U_{1S})/RT)$$

$$- k_1 \theta_S \exp(\alpha_{1a} n_1 F(E - U_{1S})/RT) + k_1 \theta_S \frac{C}{C_{ref}} \exp(-\alpha_{1C} n_1 F(E - U_{1S})/RT)$$

The four terms were linearlized to be:

1st term:

$$k_1 \exp(\alpha_{1a} n_1 F(E - U_{1S})/RT) = k_1 \exp(\alpha_{1a} n_1 F(E - U_{1S}^0)/RT) \exp(-\alpha_{1a} n_1 F \Delta U_{1S}/RT)$$

$$\approx k_1 \exp(\alpha_{1a} n_1 F(E - U_{1S}^0)/RT)(1 - \alpha_{1a} n_1 F \Delta U_{1S}/RT)$$

$$= k_1 \exp(\alpha_{1a} n_1 F(E - U_{1S}^0)/RT) - \frac{k_1 \alpha_{1a} n_1 F \Delta U_{1S}}{RT} \exp(\alpha_{1a} n_1 F(E - U_{1S}^0)/RT)$$

$$= -\frac{k_1 \alpha_{1a} n_1 F}{RT} \exp(\alpha_{1a} n_1 F(E - U_{1S}^0)/RT) U_{1S} + k_1 \exp(\alpha_{1a} n_1 F(E - U_{1S}^0)/RT)(1 + \frac{\alpha_{1a} n_1 F U_{1S}^0}{RT})$$

2nd term:

$$- k_1 \frac{C}{C_{ref}} \exp(-\alpha_{1C} n_1 F(E - U_{1S})/RT)$$

$$= -k_1 \frac{C}{C_{ref}} \exp(-\alpha_{1C} n_1 F(E - U_{1S}^0)/RT) \exp(\alpha_{1C} n_1 F \Delta U_{1S}/RT)$$

$$\approx -k_1 \frac{C}{C_{ref}} \exp(-\alpha_{1C} n_1 F(E - U_{1S}^0)/RT)(1 + \alpha_{1C} n_1 F \Delta U_{1S}/RT)$$

$$= -\frac{k_1}{C_{ref}} \exp(-\alpha_{1C} n_1 F(E - U_{1S}^0)/RT)(1 + \frac{\alpha_{1C} n_1 F}{RT} \Delta U_{1S})(C^0 + \Delta C)$$

$$\approx -\frac{k_1}{C_{ref}} \exp(-\alpha_{1C} n_1 F(E - U_{1S}^0)/RT)(C + \frac{\alpha_{1C} n_1 F}{RT} C^0 U_{1S} - \frac{\alpha_{1C} n_1 F}{RT} C^0 U_{1S}^0)$$

3rd term:

$$-k_1\theta_S \exp(\alpha_{1a} n_1 F(E-U_{1S})/RT)$$

$$= -k_1(\theta_S^0 + \Delta\theta_S)\exp(\alpha_{1a} n_1 F(E-U_{1S}^0)/RT)\exp(-\alpha_{1a} n_1 F\Delta U_{1S}/RT)$$

$$\approx -k_1(\theta_S^0 + \Delta\theta_S)\exp(\alpha_{1a} n_1 F(E-U_{1S}^0)/RT)(1-\alpha_{1a} n_1 F\Delta U_{1S}/RT) \qquad 4^{th} \text{ term:}$$

$$\approx -k_1 \exp(\alpha_{1a} n_1 F(E-U_{1S}^0)/RT)(\theta_S - \frac{\alpha_{1a} n_1 F}{RT}\theta_S^0 U_{1S} + \frac{\alpha_{1a} n_1 F}{RT}\theta_S^0 U_{1S}^0)$$

$$k_1\theta_S \frac{C}{C_{ref}} \exp(-\alpha_{1C} n_1 F(E-U_{1S})/RT)$$

$$= k_1(\theta_S^0 + \Delta\theta_S)\frac{(C^0 + \Delta C)}{C_{ref}}\exp(-\alpha_{1C} n_1 F(E-U_{1S}^0)/RT)\exp(\alpha_{1C} n_1 F\Delta U_{1S}/RT)$$

$$\approx \frac{k_1}{C_{ref}}\exp(-\alpha_{1C} n_1 F(E-U_{1S}^0)/RT)(\theta_S^0 C^0 + \theta_S^0\Delta C + C^0\Delta\theta_S)(1+\frac{\alpha_{1C} n_1 F}{RT}\Delta U_{1S})$$

$$\approx \frac{k_1}{C_{ref}}\exp(-\alpha_{1C} n_1 F(E-U_{1S}^0)/RT)(\theta_S^0 C^0 + \theta_S^0\Delta C + C^0\Delta\theta_S + \frac{\alpha_{1C} n_1 F}{RT}\theta_S^0 C^0\Delta U_{1S})$$

$$= \frac{k_1}{C_{ref}}\exp(-\alpha_{1C} n_1 F(E-U_{1S}^0)/RT) *$$

$$(\theta_S^0 C + C^0\theta_S - C^0\theta_S^0 + \frac{\alpha_{1C} n_1 F}{RT}\theta_S^0 C^0 U_{1S} - \frac{\alpha_{1C} n_1 F}{RT}\theta_S^0 C^0 U_{1S}^0)$$

So, the equation becomes:

$$r_{1S} = -\frac{k_1\alpha_{1a} n_1 F}{RT}\exp(\alpha_{1a} n_1 F(E-U_{1S}^0)/RT)U_{1S} + k_1\exp(\alpha_{1a} n_1 F(E-U_{1S}^0)/RT) * (1+\frac{\alpha_{1a} n_1 F U_{1S}^0}{RT})$$

$$-\frac{k_1}{C_{ref}}\exp(-\alpha_{1C} n_1 F(E-U_{1S}^0)/RT)(C + \frac{\alpha_{1C} n_1 F}{RT}C^0 U_{1S} - \frac{\alpha_{1C} n_1 F}{RT}C^0 U_{1S}^0)$$

$$-k_1\exp(\alpha_{1a} n_1 F(E-U_{1S}^0)/RT)(\theta_S - \frac{\alpha_{1a} n_1 F}{RT}\theta_S^0 U_{1S} + \frac{\alpha_{1a} n_1 F}{RT}\theta_S^0 U_{1S}^0)$$

$$+\frac{k_1}{C_{ref}}\exp(-\alpha_{1C} n_1 F(E-U_{1S}^0)/RT)(\theta_S^0 C + C^0\theta_S - C^0\theta_S^0$$

$$+\frac{\alpha_{1C} n_1 F}{RT}\theta_S^0 C^0 U_{1S} - \frac{\alpha_{1C} n_1 F}{RT}\theta_S^0 C^0 U_{1S}^0)$$

It can be finalized to be:

$$r_{1S} + k_1 \frac{n_1 F}{RT}[\alpha_{1a} \exp(\alpha_{1a} n_1 F(E - U_{1S}^0)/RT) + \frac{C^0}{C_{ref}} \alpha_{1C} \exp(-\alpha_{1C} n_1 F(E - U_{1S}^0)/RT)](1 - \theta_S^0) U_{1S}$$

$$+ \frac{k_1}{C_{ref}} \exp(-\alpha_{1C} n_1 F(E - U_{1S}^0)/RT)(1 - \theta_S^0) C$$

$$+ k_1[\exp(\alpha_{1a} n_1 F(E - U_{1S}^0)/RT) - \frac{C^0}{C_{ref}} \exp(-\alpha_{1C} n_1 F(E - U_{1S}^0)/RT)]\theta_S$$

$$= k_1 \exp(\alpha_{1a} n_1 F(E - U_{1S}^0)/RT)(1 + \frac{\alpha_{1a} n_1 F U_{1S}^0}{RT}(1 - \theta_S^0))$$

$$+ k_1 \frac{C^0}{C_{ref}} \exp(-\alpha_{1C} n_1 F(E - U_{1S}^0)/RT)(\frac{\alpha_{1C} n_1 F}{RT} U_{1S}^0 (1 - \theta_S^0) - \theta_S^0)$$

So, we have:

$$B(6,1) = \frac{k_1}{C_{ref}}(1 - \theta_S^0) \exp(-\alpha_{1C} n_1 F(E - U_{1S}^0)/RT)$$

$$B(6,2) = k_1[\exp(\alpha_{1a} n_1 F(E - U_{1S}^0)/RT) - \frac{C^0}{C_{ref}} \exp(-\alpha_{1C} n_1 F(E - U_{1S}^0)/RT)]$$

$$B(6,6) = 1$$

$$B(6,10) = k_1 \frac{n_1 F}{RT}[\alpha_{1a} \exp(\alpha_{1a} n_1 F(E - U_{1S}^0)/RT) + \frac{C^0}{C_{ref}} \alpha_{1C} \exp(-\alpha_{1C} n_1 F(E - U_{1S}^0)/RT)](1 - \theta_S^0)$$

$$G(6) = k_1(1 + \frac{\alpha_{1a} n_1 F U_{1S}^0}{RT}(1 - \theta_S^0)) \exp(\alpha_{1a} n_1 F(E - U_{1S}^0)/RT)$$

$$+ k_1 \frac{C^0}{C_{ref}}(\frac{\alpha_{1C} n_1 F}{RT} U_{1S}^0 (1 - \theta_S^0) - \theta_S^0) \exp(-\alpha_{1C} n_1 F(E - U_{1S}^0)/RT)$$

All other coefficients for equation I=6 (case I) are zero.

Case II: $\theta_S^V = 1.0 - \theta_{\max}(\theta_S \geq \theta_{\max})$

$$r_{1S} = k_1(1 - \theta_{\max})\left[\exp(\alpha_{1a} n_1 F(E - U_{1S})/RT) - \frac{C}{C_{ref}} \exp(-\alpha_{1C} n_1 F(E - U_{1S})/RT)\right]$$

$$\because \exp(\alpha_{1a} n_1 F(E - U_{1S})/RT) = \exp(\alpha_{1a} n_1 F(E - U_{1S}^0)/RT)\exp(-\alpha_{1a} n_1 F \Delta U_{1S}/RT)$$

$$\approx \exp(\alpha_{1a} n_1 F(E - U_{1S}^0)/RT)(1 - \alpha_{1a} n_1 F \Delta U_{1S}/RT)$$

$$= \exp(\alpha_{1a} n_1 F(E - U_{1S}^0)/RT)(1 + \alpha_{1a} n_1 F U_{1S}^0/RT - \alpha_{1a} n_1 F U_{1S}/RT)$$

and

$$-\frac{C}{C_{ref}}\exp(-\alpha_{1C} n_1 F(E - U_{1S})/RT)$$

$$= -\frac{(C^0 + \Delta C)}{C_{ref}}\exp(-\alpha_{1C} n_1 F(E - U_{1S}^0)/RT)\exp(\alpha_{1C} n_1 F \Delta U_{1S}/RT)$$

$$\approx -\frac{(C^0 + \Delta C)}{C_{ref}}\exp(-\alpha_{1C} n_1 F(E - U_{1S}^0)/RT)(1 + \alpha_{1C} n_1 F \Delta U_{1S}/RT)$$

$$\approx -\frac{1}{C_{ref}}\exp(-\alpha_{1C} n_1 F(E - U_{1S}^0)/RT)(C + \alpha_{1C} n_1 F C^0 \Delta U_{1S}/RT)$$

$$= -\frac{1}{C_{ref}}\exp(-\alpha_{1C} n_1 F(E - U_{1S}^0)/RT)(C + \alpha_{1C} n_1 F C^0 U_{1S}/RT - \alpha_{1C} n_1 F C^0 U_{1S}^0/RT)$$

So, the equation can be finalized to be:

$$r_{1S} + k_1(1 - \theta_{\max})[\frac{\alpha_{1a} n_1 F}{RT}\exp(\alpha_{1a} n_1 F(E - U_{1S}^0)/RT)$$

$$+ \frac{C^0}{C_{ref}}\frac{\alpha_{1C} n_1 F}{RT}\exp(-\alpha_{1C} n_1 F(E - U_{1S}^0)/RT)]U_{1S}$$

$$+ [\frac{k_1(1 - \theta_{\max})}{C_{ref}}\exp(-\alpha_{1C} n_1 F(E - U_{1S}^0)/RT)]C$$

$$= k_1(1 - \theta_{\max})[(1 + \alpha_{1a} n_1 F U_{1S}^0/RT)\exp(\alpha_{1a} n_1 F(E - U_{1S}^0)/RT$$

$$+ \frac{C^0}{C_{ref}}\frac{\alpha_{1C} n_1 F}{RT}U_{1S}^0\exp(-\alpha_{1C} n_1 F(E - U_{1S}^0)/RT)]$$

So, we have:

$$B(6,1) = \frac{k_1(1 - \theta_{\max})}{C_{ref}}\exp(-\alpha_{1C} n_1 F(E - U_{1S}^0)/RT)$$

$$B(6,6) = 1$$

$$B(6,10) = k_1(1 - \theta_{\max})[\frac{\alpha_{1a} n_1 F}{RT}\exp(\alpha_{1a} n_1 F(E - U_{1S}^0)/RT)$$

$$+ \frac{C^0}{C_{ref}}\frac{\alpha_{1C} n_1 F}{RT}\exp(-\alpha_{1C} n_1 F(E - U_{1S}^0)/RT)]$$

$$G(6) = k_1(1 - \theta_{\max})[(1 + \alpha_{1a} n_1 F U_{1S}^0/RT)\exp(\alpha_{1a} n_1 F(E - U_{1S}^0)/RT$$

$$+ \frac{C^0}{C_{ref}}\frac{\alpha_{1C} n_1 F}{RT}U_{1S}^0\exp(-\alpha_{1C} n_1 F(E - U_{1S}^0)/RT)]$$

All other coefficients for equation I=6 (case II) are zero.

I=7,

$$r_{1L} = k_1\theta_L^V\left[\exp(\alpha_{1a}n_1F(E-U_{1L})/RT) - \frac{C}{C_{ref}}\exp(-\alpha_{1C}n_1F(E-U_{1L})/RT)\right]$$

Similarly as equation 6, we can find:

Case I: $\theta_L^V = 1.0-\theta_L(\theta_L < \theta_{\max})$

$$r_{1L} + k_1\frac{n_1F}{RT}[\alpha_{1a}\exp(\alpha_{1a}n_1F(E-U_{1L}^0)/RT) + \frac{C^0}{C_{ref}}\alpha_{1C}\exp(-\alpha_{1C}n_1F(E-U_{1L}^0)/RT)](1-\theta_L^0)U_{1L}$$

$$+\frac{k_1}{C_{ref}}\exp(-\alpha_{1C}n_1F(E-U_{1L}^0)/RT)(1-\theta_L^0)C$$

$$+k_1[\exp(\alpha_{1a}n_1F(E-U_{1L}^0)/RT) - \frac{C^0}{C_{ref}}\exp(-\alpha_{1C}n_1F(E-U_{1L}^0)/RT)]\theta_L$$

$$= k_1\exp(\alpha_{1a}n_1F(E-U_{1L}^0)/RT)(1+\frac{\alpha_{1a}n_1FU_{1L}^0}{RT}(1-\theta_L^0))$$

$$+k_1\frac{C^0}{C_{ref}}\exp(-\alpha_{1C}n_1F(E-U_{1L}^0)/RT)(\frac{\alpha_{1C}n_1F}{RT}U_{1L}^0(1-\theta_L^0)-\theta_L^0)$$

So, we have:

$$B(7,1) = \frac{k_1}{C_{ref}}(1-\theta_L^0)\exp(-\alpha_{1C}n_1F(E-U_{1L}^0)/RT)$$

$$B(7,3) = k_1[\exp(\alpha_{1a}n_1F(E-U_{1L}^0)/RT) - \frac{C^0}{C_{ref}}\exp(-\alpha_{1C}n_1F(E-U_{1L}^0)/RT)]$$

$$B(7,7) = 1$$

$$B(7,11) = k_1\frac{n_1F}{RT}[\alpha_{1a}\exp(\alpha_{1a}n_1F(E-U_{1L}^0)/RT) + \frac{C^0}{C_{ref}}\alpha_{1C}\exp(-\alpha_{1C}n_1F(E-U_{1L}^0)/RT)](1-\theta_L^0)$$

$$G(7) = k_1(1+\frac{\alpha_{1a}n_1FU_{1L}^0}{RT}(1-\theta_L^0))\exp(\alpha_{1a}n_1F(E-U_{1L}^0)/RT)$$

$$+k_1\frac{C^0}{C_{ref}}(\frac{\alpha_{1C}n_1FU_{1L}^0}{RT}(1-\theta_L^0)-\theta_L^0)\exp(-\alpha_{1C}n_1F(E-U_{1L}^0)/RT)$$

All other coefficients for equation I=7 (case I) are zero.

Case II: $\theta_L^V = 1.0-\theta_{\max}(\theta_L \geq \theta_{\max})$

$$r_{1L} + k_1(1-\theta_{\max})[\frac{\alpha_{1a}n_1F}{RT}\exp(\alpha_{1a}n_1F(E-U_{1L}^0)/RT) + \frac{C^0}{C_{ref}}\frac{\alpha_{1C}n_1F}{RT}\exp(-\alpha_{1C}n_1F(E-U_{1L}^0)/RT)]U_{1L}$$

$$+[\frac{k_1(1-\theta_{\max})}{C_{ref}}\exp(-\alpha_{1C}n_1F(E-U_{1L}^0)/RT)]C$$

$$= k_1(1-\theta_{\max})[(1+\alpha_{1a}n_1FU_{1L}^0/RT)\exp(\alpha_{1a}n_1F(E-U_{1L}^0)/RT$$

$$+\frac{C^0}{C_{ref}}\frac{\alpha_{1C}n_1F}{RT}U_{1L}^0\exp(-\alpha_{1C}n_1F(E-U_{1L}^0)/RT)]$$

So, we have:

$$B(7,1) = \frac{k_1(1-\theta_{\max})}{C_{ref}} \exp(-\alpha_{1C} n_1 F(E - U_{1L}^0)/RT)$$

$$B(7,7) = 1$$

$$B(7,11) = k_1(1-\theta_{\max})[\frac{\alpha_{1a} n_1 F}{RT} \exp(\alpha_{1a} n_1 F(E - U_{1L}^0)/RT) + \frac{C^0}{C_{ref}} \frac{\alpha_{1C} n_1 F}{RT} \exp(-\alpha_{1C} n_1 F(E - U_{1L}^0)/RT)]$$

$$G(7) = k_1(1-\theta_{\max})[(1 + \alpha_{1a} n_1 F U_{1L}^0/RT) \exp(\alpha_{1a} n_1 F(E - U_{1L}^0)/RT$$

$$+ \frac{C^0}{C_{ref}} \frac{\alpha_{1C} n_1 F}{RT} U_{1L}^0 \exp(-\alpha_{1C} n_1 F(E - U_{1L}^0)/RT)]$$

All other coefficients for equation I=7 (case II) are zero.

I=8,

$$r_{2S} = k_2 \begin{bmatrix} \exp(-\omega\theta_S/RT) \exp(\alpha_{2a} n_2 F(E - U_{2S})/RT) \\ -CH^2 \theta_S \exp(-\alpha_{2C} n_2 F(E - U_{2S})/RT) \end{bmatrix}$$

Two terms can be linearlized to be:

1st term:

$$\exp(-\omega\theta_S/RT) \exp(\alpha_{2a} n_2 F(E - U_{2S})/RT)$$

$$\approx \exp(-\omega\theta_S^0/RT) \exp(\alpha_{2a} n_2 F(E - U_{2S}^0)/RT)(1 - \omega\Delta\theta_S/RT)(1 - \alpha_{2a} n_2 F\Delta U_{2S}/RT)$$

$$\approx \exp(-\omega\theta_S^0/RT) \exp(\alpha_{2a} n_2 F(E - U_{2S}^0)/RT)(1 - \omega\Delta\theta_S/RT - \alpha_{2a} n_2 F\Delta U_{2S}/RT)$$

$$= \exp(-\omega\theta_S^0/RT) \exp(\alpha_{2a} n_2 F(E - U_{2S}^0)/RT)$$

$$\times (1 - \omega\theta_S/RT - \alpha_{2a} n_2 F U_{2S}/RT + \omega\theta_S^0/RT + \alpha_{2a} n_2 F U_{2S}^0/RT)$$

2nd term:

$$-CH^2 \theta_S \exp(-\alpha_{2C} n_2 F(E - U_{2S})/RT)$$

$$= -CH^2(\theta_S^0 + \Delta\theta_S) \exp(-\alpha_{2C} n_2 F(E - U_{2S}^0)/RT) \exp(\alpha_{2C} n_2 F\Delta U_{2S}/RT)$$

$$\approx -CH^2(\theta_S^0 + \Delta\theta_S) \exp(-\alpha_{2C} n_2 F(E - U_{2S}^0)/RT)(1 + \alpha_{2C} n_2 F\Delta U_{2S}/RT)$$

$$\approx -CH^2 \exp(-\alpha_{2C} n_2 F(E - U_{2S}^0)/RT)(\theta_S + \alpha_{2C} n_2 F\theta_S^0 U_{2S}/RT - \alpha_{2C} n_2 F\theta_S^0 U_{2S}^0/RT)$$

So, the equation can be finalized to be:

$$r_{2S} + k_2[\exp(-\omega\theta_S^0/RT) \exp(\alpha_{2a} n_2 F(E - U_{2S}^0)/RT) \frac{\alpha_{2a} n_2 F}{RT}$$

$$+ CH^2 \exp(-\alpha_{2C} n_2 F(E - U_{2S}^0)/RT) \frac{\alpha_{2C} n_2 F\theta_S^0}{RT}] U_{2S}$$

$$+ k_2[\frac{\omega}{RT} \exp(-\omega\theta_S^0/RT) \exp(\alpha_{2a} n_2 F(E - U_{2S}^0)/RT) + CH^2 \exp(-\alpha_{2C} n_2 F(E - U_{2S}^0)/RT)]\theta_S$$

$$= k_2 \exp(-\omega\theta_S^0/RT) \exp(\alpha_{2a} n_2 F(E - U_{2S}^0)/RT)(1 + \omega\theta_S^0/RT + \alpha_{2a} n_2 F U_{2S}^0/RT)$$

$$+ k_2 CH^2(\alpha_{2C} n_2 F\theta_S^0 U_{2S}^0/RT) \exp(-\alpha_{2C} n_2 F(E - U_{2S}^0)/RT)$$

So, we have:

$$B(8,2) = k_2[\frac{\omega}{RT}\exp(-\omega\theta_S^0 / RT)\exp(\alpha_{2a}n_2F(E-U_{2S}^0)/RT) + CH^2\exp(-\alpha_{2C}n_2F(E-U_{2S}^0)/RT)]$$

$$B(8,8) = 1$$

$$B(8,12) = k_2[\exp(-\omega\theta_S^0 / RT)\frac{\alpha_{2a}n_2F}{RT}\exp(\alpha_{2a}n_2F(E-U_{2S}^0)/RT)$$

$$+ CH^2\frac{\alpha_{2C}n_2F\theta_S^0}{RT}\exp(-\alpha_{2C}n_2F(E-U_{2S}^0)/RT)]$$

$$G(8) = k_2\exp(-\omega\theta_S^0 / RT)(1+\omega\theta_S^0 / RT + \alpha_{2a}n_2FU_{2S}^0 / RT)\exp(\alpha_{2a}n_2F(E-U_{2S}^0)/RT)$$

$$+ k_2CH^2(\alpha_{2C}n_2F\theta_S^0U_{2S}^0 / RT)\exp(-\alpha_{2C}n_2F(E-U_{2S}^0)/RT)$$

All other coefficients for equation I=8 are zero.

I=9,

$$r_{2L} = k_2\begin{bmatrix}\exp(-\omega\theta_L / RT)\exp(\alpha_{2a}n_2F(E-U_{2L})/RT)\\ -CH^2\theta_L\exp(-\alpha_{2C}n_2F(E-U_{2L})/RT)\end{bmatrix}$$

Similarly as the equation 8, we have:

$$r_{2L} + k_2[\exp(-\omega\theta_L^0 / RT)\exp(\alpha_{2a}n_2F(E-U_{2L}^0)/RT)\frac{\alpha_{2a}n_2F}{RT}$$

$$+ CH^2\exp(-\alpha_{2C}n_2F(E-U_{2L}^0)/RT)\frac{\alpha_{2C}n_2F\theta_L^0}{RT}]U_{2L}$$

$$+ k_2[\frac{\omega}{RT}\exp(-\omega\theta_L^0 / RT)\exp(\alpha_{2a}n_2F(E-U_{2L}^0)/RT) + CH^2\exp(-\alpha_{2C}n_2F(E-U_{2L}^0)/RT)]\theta_L$$

$$= k_2\exp(-\omega\theta_L^0 / RT)\exp(\alpha_{2a}n_2F(E-U_{2L}^0)/RT)(1+\omega\theta_L^0 / RT + \alpha_{2a}n_2FU_{2L}^0 / RT)$$

$$+ k_2CH^2(\alpha_{2C}n_2F\theta_L^0U_{2L}^0 / RT)\exp(-\alpha_{2C}n_2F(E-U_{2L}^0)/RT)$$

So, we have:

$$B(9,3) = k_2[\frac{\omega}{RT}\exp(-\omega\theta_L^0 / RT)\exp(\alpha_{2a}n_2F(E-U_{2L}^0)/RT) + CH^2\exp(-\alpha_{2C}n_2F(E-U_{2L}^0)/RT)]$$

$$B(9,9) = 1$$

$$B(9,13) = k_2[\exp(-\omega\theta_L^0 / RT)\frac{\alpha_{2a}n_2F}{RT}\exp(\alpha_{2a}n_2F(E-U_{2L}^0)/RT)$$

$$+ CH^2\frac{\alpha_{2C}n_2F\theta_L^0}{RT}\exp(-\alpha_{2C}n_2F(E-U_{2L}^0)/RT)]$$

$$G(9) = k_2\exp(-\omega\theta_L^0 / RT)(1+\omega\theta_L^0 / RT + \alpha_{2a}n_2FU_{2L}^0 / RT)\exp(\alpha_{2a}n_2F(E-U_{2L}^0)/RT)$$

$$+ k_2CH^2(\alpha_{2C}n_2F\theta_L^0U_{2L}^0 / RT)\exp(-\alpha_{2C}n_2F(E-U_{2L}^0)/RT)$$

All other coefficients for equation I=9 are zero.

I=10, $\quad U_{1S} = U_1^0 - \frac{1}{2F}\frac{\sigma_{Pt}M_{Pt}}{\rho_{Pt}}\frac{1}{R_S}$

$$\frac{1}{R_S} = \frac{1}{R_S^0}(1+\frac{\Delta R_S}{R_S^0})^{-1} \approx \frac{1}{R_S^0}(1-\frac{\Delta R_S}{R_S^0}) = \frac{1}{(R_S^0)^2}(2R_S^0 - R_S)$$

So the equation can be finalized to be:

$$U_{1S} = U_1^0 - \frac{1}{2F}\frac{\sigma_{Pt}M_{Pt}}{\rho_{Pt}}\frac{1}{(R_S^0)^2}(2R_S^0 - R_S)$$

$$U_{1S} - \frac{1}{2F}\frac{\sigma_{Pt}M_{Pt}}{\rho_{Pt}}\frac{1}{(R_S^0)^2}R_S = U_1^0 - \frac{1}{F}\frac{\sigma_{Pt}M_{Pt}}{\rho_{Pt}}\frac{1}{R_S^0}$$

So, we have:

$$B(10,4) = -\frac{1}{2F}\frac{\sigma_{Pt}M_{Pt}}{\rho_{Pt}}\frac{1}{(R_S^0)^2}$$

$$B(10,10) = 1$$

$$G(10) = U_1^0 - \frac{1}{F}\frac{\sigma_{Pt}M_{Pt}}{\rho_{Pt}}\frac{1}{R_S^0}$$

All other coefficients for equation I=10 are zero.

I=11, $$U_{1L} = U_1^0 - \frac{1}{2F}\frac{\sigma_{Pt}M_{Pt}}{\rho_{Pt}}\frac{1}{R_L}$$

Similarly as equation 10, we can write:

$$U_{1L} - \frac{1}{2F}\frac{\sigma_{Pt}M_{Pt}}{\rho_{Pt}}\frac{1}{(R_L^0)^2}R_L = U_1^0 - \frac{1}{F}\frac{\sigma_{Pt}M_{Pt}}{\rho_{Pt}}\frac{1}{R_L^0}$$

So, we have:

$$B(11,5) = -\frac{1}{2F}\frac{\sigma_{Pt}M_{Pt}}{\rho_{Pt}}\frac{1}{(R_L^0)^2}$$

$$B(11,11) = 1$$

$$G(11) = U_1^0 - \frac{1}{F}\frac{\sigma_{Pt}M_{Pt}}{\rho_{Pt}}\frac{1}{R_L^0}$$

All other coefficients for equation I=11 are zero.

I=12, $$U_{2S} = U_2^0 + \frac{1}{2F}(\Delta\mu_{Pt}^0 + \frac{\sigma_{PtO}M_{PtO}}{\rho_{PtO}}\frac{1}{R_S} - \frac{\sigma_{Pt}M_{Pt}}{\rho_{Pt}}\frac{1}{R_S})$$

Equation 12 can be written as: $U_{2S} = (U_2^0 + \frac{\Delta\mu_{Pt}^0}{2F}) + \frac{1}{2F}(\frac{\sigma_{PtO}M_{PtO}}{\rho_{PtO}} - \frac{\sigma_{Pt}M_{Pt}}{\rho_{Pt}})\frac{1}{R_S}$

$$\frac{1}{R_S} = \frac{1}{R_S^0}(1 + \frac{\Delta R_S}{R_S^0})^{-1} \approx \frac{1}{R_S^0}(1 - \frac{\Delta R_S}{R_S^0}) = \frac{1}{(R_S^0)^2}(2R_S^0 - R_S)$$

So equation 12 can be linearlized to be:

$$U_{2S} = (U_2^0 + \frac{\Delta\mu_{Pt}^0}{2F}) + \frac{1}{2F}(\frac{\sigma_{PtO}M_{PtO}}{\rho_{PtO}} - \frac{\sigma_{Pt}M_{Pt}}{\rho_{Pt}})\frac{1}{(R_S^0)^2}(2R_S^0 - R_S)$$

$$U_{2S} + \frac{1}{2F}(\frac{\sigma_{PtO}M_{PtO}}{\rho_{PtO}} - \frac{\sigma_{Pt}M_{Pt}}{\rho_{Pt}})\frac{1}{(R_S^0)^2}R_S = U_2^0 + \frac{\Delta\mu_{Pt}^0}{2F} + \frac{1}{F}(\frac{\sigma_{PtO}M_{PtO}}{\rho_{PtO}} - \frac{\sigma_{Pt}M_{Pt}}{\rho_{Pt}})\frac{1}{R_S^0}$$

So, we have:

$$B(12,4) = \frac{1}{2F}\left(\frac{\sigma_{PtO} M_{PtO}}{\rho_{PtO}} - \frac{\sigma_{Pt} M_{Pt}}{\rho_{Pt}}\right)\frac{1}{(R_S^0)^2}$$

$$B(12,12) = 1$$

$$G(12) = U_2^0 + \frac{\Delta\mu_{Pt}^0}{2F} + \frac{1}{F}\left(\frac{\sigma_{PtO} M_{PtO}}{\rho_{PtO}} - \frac{\sigma_{Pt} M_{Pt}}{\rho_{Pt}}\right)\frac{1}{R_S^0}$$

All other coefficients for equation I=12 are zero.

I=13, $\quad U_{2L} = U_2^0 + \frac{1}{2F}\left(\Delta\mu_{Pt}^0 + \frac{\sigma_{PtO} M_{PtO}}{\rho_{PtO}}\frac{1}{R_L} - \frac{\sigma_{Pt} M_{Pt}}{\rho_{Pt}}\frac{1}{R_L}\right)$

Similarly as equation12, we can write equation 13 as:

$$U_{2L} + \frac{1}{2F}\left(\frac{\sigma_{PtO} M_{PtO}}{\rho_{PtO}} - \frac{\sigma_{Pt} M_{Pt}}{\rho_{Pt}}\right)\frac{1}{(R_L^0)^2} R_L = U_2^0 + \frac{\Delta\mu_{Pt}^0}{2F} + \frac{1}{F}\left(\frac{\sigma_{PtO} M_{PtO}}{\rho_{PtO}} - \frac{\sigma_{Pt} M_{Pt}}{\rho_{Pt}}\right)\frac{1}{R_L^0}$$

So, we have:

$$B(13,5) = \frac{1}{2F}\left(\frac{\sigma_{PtO} M_{PtO}}{\rho_{PtO}} - \frac{\sigma_{Pt} M_{Pt}}{\rho_{Pt}}\right)\frac{1}{(R_L^0)^2}$$

$$B(13,13) = 1$$

$$G(13) = U_2^0 + \frac{\Delta\mu_{Pt}^0}{2F} + \frac{1}{F}\left(\frac{\sigma_{PtO} M_{PtO}}{\rho_{PtO}} - \frac{\sigma_{Pt} M_{Pt}}{\rho_{Pt}}\right)\frac{1}{R_L^0}$$

All other coefficients for equation I=13 are zero.

2) Linearization equations in membrane regions

I=1, $\frac{\partial C}{\partial t} = D\frac{\partial^2 C}{\partial x^2}$ (only one variable k=1, Pt ions concentration C)

The Pt ion diffusion coefficient D in membrane might be different from the value in cathode, although Pt ion diffusion is assumed in polymer and/or ionomer phase.

$$\frac{\partial C}{\partial t} = \frac{C(J,t+\Delta t) - C(J,t)}{\Delta t}$$

Apply central difference method and Crank-Nicolson technique to express the 2nd order derivatives.

$$\frac{\partial^2 C}{\partial x^2} = \frac{1}{2\Delta x^2}(C(J+1,t+\Delta t) + C(J-1,t+\Delta t) - 2C(J,t+\Delta t)$$
$$+ C(J+1,t) + C(J-1,t) - 2C(J,t))$$

So, the equation can be finalized to be:

$$\frac{D}{2\Delta x^2}C(J+1,t+\Delta t) - \left(\frac{D}{\Delta x^2} + \frac{1}{\Delta t}\right)C(J,t+\Delta t) + \frac{D}{2\Delta x^2}C(J-1,t+\Delta t)$$
$$= -\frac{D}{2\Delta x^2}C(J+1,t) - \left(-\frac{D}{\Delta x^2} + \frac{1}{\Delta t}\right)C(J,t) - \frac{D}{2\Delta x^2}C(J-1,t)$$

So, we have:

$$A(1,1) = D(1,1) = \frac{D}{2\Delta x^2}$$

$$B(1,1) = -(\frac{D}{\Delta x^2} + \frac{1}{\Delta t})$$

$$G(1) = -\frac{D}{2\Delta x^2} C(J+1,t) - (-\frac{D}{\Delta x^2} + \frac{1}{\Delta t}) C(J,t) - \frac{D}{2\Delta x^2} C(J-1,t)$$

All other coefficients for equation I=1 are zero.

3) J=1 at GDL/cathode interface

I=1, $\left.\frac{\partial C}{\partial x}\right|_{J=1} = \frac{-3C(1) + 4C(2) - C(3)}{2\Delta x} = 0$ linearlized.

So, we have:

$$B(1,1) = -\frac{3}{2\Delta x}; D(1,1) = \frac{2}{\Delta x}; X(1,1) = -\frac{1}{2\Delta x}$$

All other coefficients for equation I=1 are zero.

Equations from I=2 to I=13 do not involve the mesh volume, so these 12 equations have the same linearlized forms in the cathode.

4) J=N at the Pt band location in membrane

I=1, $C(N) = 0$ already linearlized.

We have:

B(1,1)=1

All other coefficients are zero.

5) Cathode/membrane interface

I=1,

$$\frac{\varepsilon_C + \varepsilon_M}{2} V \times \Delta C(J) = (N_{IN} - N_{OUT}) A \times \Delta t + \frac{4\pi}{2} \times \Delta t \times (N_S R_S^2 r_{1S} + N_L R_L^2 r_{1L})$$

$$N_{IN} = -\varepsilon_C D \frac{C(J) - C(J-1)}{\Delta x}$$

$$N_{OUT} = -\varepsilon_M D \frac{C(J+1) - C(J)}{\Delta x}$$

$$\Delta C(J) = C(J, t+\Delta t) - C(J,t)$$

$$\Delta x = \frac{V}{A}$$

The equation can be rewritten as:

$$\frac{C(J,t+\Delta t) - C(J,t)}{\Delta t} = \frac{2}{\varepsilon_C + \varepsilon_M} \frac{1}{\Delta x} (N_{IN} - N_{OUT}) + \frac{4\pi}{V(\varepsilon_C + \varepsilon_M)} \times (N_S R_S^2 r_{1S} + N_L R_L^2 r_{1L})$$

$$N_{IN} - N_{OUT} = -\varepsilon_C D \frac{C(J) - C(J-1)}{\Delta x} + \varepsilon_M D \frac{C(J+1) - C(J)}{\Delta x}$$

$$= \frac{D}{\Delta x}[\varepsilon_M C(J+1) - (\varepsilon_C + \varepsilon_M)C(J) + \varepsilon_C C(J-1)]$$

Apply Crank-Nicolson method to the term, we have:

$$N_{IN} - N_{OUT} = \frac{D}{2\Delta x}[\varepsilon_M C(J+1,t+\Delta t) - (\varepsilon_C + \varepsilon_M)C(J,t+\Delta t) + \varepsilon_C C(J-1,t+\Delta t)$$
$$+ \varepsilon_M C(J+1,t) - (\varepsilon_C + \varepsilon_M)C(J,t) + \varepsilon_C C(J-1,t)]$$

Previously we have derived the followings:

$$\frac{1}{2}(R_S^2(J,t+\Delta t)r_{1S}(J,t+\Delta t) + R_S^2(J,t)r_{1S}(J,t))$$

$$\approx \frac{1}{2}(R_S^2(J,t)r_{1S}(J,t+\Delta t) + 2R_S(J,t)r_{1S}(J,t)R_S(J,t+\Delta t) - R_S^2(J,t)r_{1S}(J,t))$$

$$\frac{1}{2}(R_L^2(J,t+\Delta t)r_{1L}(J,t+\Delta t) + R_L^2(J,t)r_{1L}(J,t))$$

$$\approx \frac{1}{2}(R_L^2(J,t)r_{1L}(J,t+\Delta t) + 2R_L(J,t)r_{1L}(J,t)R_L(J,t+\Delta t) - R_L^2(J,t)r_{1L}(J,t))$$

Since the dissolution reaction rate at the location of J does not truly represent the center of reaction zone (left half of the mesh J), it would be better estimated by the rates at location of J-1 and J with a fraction of ¼ and ¾, respectively.

So, we have:

$$N_S R_S^2 r_{1S}$$

$$\approx \frac{N_S(J-1)}{8}[R_S^2(J-1,t)r_{1S}(J-1,t+\Delta t) + 2R_S(J-1,t)r_{1S}(J-1,t)R_S(J-1,t+\Delta t)$$

$$- R_S^2(J-1,t)r_{1S}(J-1,t)]$$

$$+ \frac{3N_S(J)}{8}[R_S^2(J,t)r_{1S}(J,t+\Delta t) + 2R_S(J,t)r_{1S}(J,t)R_S(J,t+\Delta t) - R_S^2(J,t)r_{1S}(J,t)]$$

and

$$N_L R_L^2 r_{1L}$$

$$\approx \frac{N_L(J-1)}{8}[R_L^2(J-1,t)r_{1L}(J-1,t+\Delta t)$$

$$+ 2R_L(J-1,t)r_{1L}(J-1,t)R_L(J-1,t+\Delta t) - R_L^2(J-1,t)r_{1L}(J-1,t)]$$

$$+ \frac{3N_L(J)}{8}[R_L^2(J,t)r_{1L}(J,t+\Delta t) + 2R_L(J,t)r_{1L}(J,t)R_L(J,t+\Delta t) - R_L^2(J,t)r_{1L}(J,t)]$$

So, the interface equation can be written as:

$$\frac{C(J,t+\Delta t)-C(J,t)}{\Delta t}$$
$$=\frac{2}{\varepsilon_C+\varepsilon_M}\frac{1}{\Delta x}\frac{D}{2\Delta x}[\varepsilon_M C(J+1,t+\Delta t)-(\varepsilon_C+\varepsilon_M)C(J,t+\Delta t)+\varepsilon_C C(J-1,t+\Delta t)$$
$$+\varepsilon_M C(J+1,t)-(\varepsilon_C+\varepsilon_M)C(J,t)+\varepsilon_C C(J-1,t)]$$
$$+\frac{4\pi}{V(\varepsilon_C+\varepsilon_M)}$$
$$\times\{\frac{N_S(J-1)}{8}[R_S^2(J-1,t)r_{1S}(J-1,t+\Delta t)$$
$$+2R_S(J-1,t)r_{1S}(J-1,t)R_S(J-1,t+\Delta t)-R_S^2(J-1,t)r_{1S}(J-1,t)]$$
$$+\frac{3N_S(J)}{8}[R_S^2(J,t)r_{1S}(J,t+\Delta t)+2R_S(J,t)r_{1S}(J,t)R_S(J,t+\Delta t)-R_S^2(J,t)r_{1S}(J,t)]$$
$$\frac{N_L(J-1)}{8}[R_L^2(J-1,t)r_{1L}(J-1,t+\Delta t)+2R_L(J-1,t)r_{1L}(J-1,t)R_L(J-1,t+\Delta t)-R_L^2(J-1,t)r_{1L}(J-1,t)]$$
$$+\frac{3N_L(J)}{8}[R_L^2(J,t)r_{1L}(J,t+\Delta t)+2R_L(J,t)r_{1L}(J,t)R_L(J,t+\Delta t)-R_L^2(J,t)r_{1L}(J,t)]\}$$

It can be finalized as:

$$\frac{D\varepsilon_M}{(\varepsilon_C+\varepsilon_M)\Delta x^2}C(J+1,t+\Delta t)-(\frac{D}{\Delta x^2}+\frac{1}{\Delta t})C(J,t+\Delta t)+\frac{D\varepsilon_C}{(\varepsilon_C+\varepsilon_M)\Delta x^2}C(J-1,t+\Delta t)$$
$$+\frac{\pi N_S(J-1)}{2V(\varepsilon_C+\varepsilon_M)}R_S^2(J-1,t)r_{1S}(J-1,t+\Delta t)+\frac{\pi N_L(J-1)}{2V(\varepsilon_C+\varepsilon_M)}R_L^2(J-1,t)r_{1L}(J-1,t+\Delta t)$$
$$+\frac{3\pi N_S(J)}{2V(\varepsilon_C+\varepsilon_M)}R_S^2(J,t)r_{1S}(J,t+\Delta t)+\frac{3\pi N_L(J)}{2V(\varepsilon_C+\varepsilon_M)}R_L^2(J,t)r_{1L}(J,t+\Delta t)$$
$$+\frac{\pi N_S(J-1)}{V(\varepsilon_C+\varepsilon_M)}R_S(J-1,t)r_{1S}(J-1,t)R_S(J-1,t+\Delta t)+\frac{\pi N_L(J-1)}{V(\varepsilon_C+\varepsilon_M)}R_L(J-1,t)r_{1L}(J-1,t)R_L(J-1,t+\Delta t)$$
$$+\frac{3\pi N_S(J)}{V(\varepsilon_C+\varepsilon_M)}R_S(J,t)r_{1S}(J,t)R_S(J,t+\Delta t)+\frac{3\pi N_L(J)}{V(\varepsilon_C+\varepsilon_M)}R_L(J,t)r_{1L}(J,t)R_L(J,t+\Delta t)$$
$$=-\frac{D\varepsilon_M}{(\varepsilon_C+\varepsilon_M)\Delta x^2}C(J+1,t)+(\frac{D}{\Delta x^2}-\frac{1}{\Delta t})C(J,t)-\frac{D\varepsilon_C}{(\varepsilon_C+\varepsilon_M)\Delta x^2}C(J-1,t)$$
$$+\frac{\pi N_S(J-1)}{2V(\varepsilon_C+\varepsilon_M)}R_S^2(J-1,t)r_{1S}(J-1,t)+\frac{\pi N_L(J-1)}{2V(\varepsilon_C+\varepsilon_M)}R_L^2(J-1,t)r_{1L}(J-1,t)$$
$$+\frac{3\pi N_S(J)}{2V(\varepsilon_C+\varepsilon_M)}R_S^2(J,t)r_{1S}(J,t)+\frac{3\pi N_L(J)}{2V(\varepsilon_C+\varepsilon_M)}R_L^2(J,t)r_{1L}(J,t)$$

So we have:

$$A(1,1) = \frac{D\varepsilon_C}{(\varepsilon_C + \varepsilon_M)\Delta x^2}$$

$$D(1,1) = \frac{D\varepsilon_M}{(\varepsilon_C + \varepsilon_M)\Delta x^2}$$

$$B(1,1) = -(\frac{D}{\Delta x^2} + \frac{1}{\Delta t})$$

$$A(1,4) = \frac{\pi N_S(J-1)}{V(\varepsilon_C + \varepsilon_M)} R_S(J-1,t) r_{1S}(J-1,t)$$

$$B(1,4) = \frac{3\pi N_S(J)}{V(\varepsilon_C + \varepsilon_M)} R_S(J,t) r_{1S}(J,t)$$

$$A(1,5) = \frac{\pi N_L(J-1)}{V(\varepsilon_C + \varepsilon_M)} R_L(J-1,t) r_{1L}(J-1,t)$$

$$B(1,5) = \frac{3\pi N_L(J)}{V(\varepsilon_C + \varepsilon_M)} R_L(J,t) r_{1L}(J,t)$$

$$A(1,6) = \frac{\pi N_S(J-1)}{2V(\varepsilon_C + \varepsilon_M)} R_S^2(J-1,t)$$

$$B(1,6) = \frac{3\pi N_S(J)}{2V(\varepsilon_C + \varepsilon_M)} R_S^2(J,t)$$

$$A(1,7) = \frac{\pi N_L(J-1)}{2V(\varepsilon_C + \varepsilon_M)} R_L^2(J-1,t)$$

$$B(1,7) = \frac{3\pi N_L(J)}{2V(\varepsilon_C + \varepsilon_M)} R_L^2(J,t)$$

$$G(1) = -\frac{D\varepsilon_M}{(\varepsilon_C + \varepsilon_M)\Delta x^2} C(J+1,t) + (\frac{D}{\Delta x^2} - \frac{1}{\Delta t}) C(J,t) - \frac{D\varepsilon_C}{(\varepsilon_C + \varepsilon_M)\Delta x^2} C(J-1,t)$$
$$+ \frac{\pi N_S(J-1)}{2V(\varepsilon_C + \varepsilon_M)} R_S^2(J-1,t) r_{1S}(J-1,t) + \frac{\pi N_L(J-1)}{2V(\varepsilon_C + \varepsilon_M)} R_L^2(J-1,t) r_{1L}(J-1,t)$$
$$+ \frac{3\pi N_S(J)}{2V(\varepsilon_C + \varepsilon_M)} R_S^2(J,t) r_{1S}(J,t) + \frac{3\pi N_L(J)}{2V(\varepsilon_C + \varepsilon_M)} R_L^2(J,t) r_{1L}(J,t)$$

All other coefficients for equation I=1 are zero.

Equations from I=2 to I=13 do not involve the mesh volume, so these 12 equations have the same linearlized forms in the cathode

APPENDIX G

EXAMPLE FORTRAN CODES FOR CATALYST DEGRADATION SIMULATION

```
Program Platinum_degradation
 ! file name: 31_1.0_a, All SI units
 ! Pt mass calculation must include Pt oxide layer
 ! Initial oxide coverage is set as the equilibrium at 0.87v
 ! Diffusion coefficient tortuosity corrected.
 ! s: small particle, b: large particle

 Implicit real*8(a-h,k-m, o-z)                    !only I, J, N started variable as integers
 Common /bnd/ A(20,20), B(20,20), C(20,301), D(20,41)
 Common /mat/ G(20), X(20,20), Y(20,20)
 Common /n/ n, nj

 Dimension cpt_old(200), cpt_itr(200)
 Dimension phi_s_old(200), phi_s_itr(200)
 Dimension phi_b_old(200), phi_b_itr(200)
 Dimension rs_old(200), rs_itr(200)
 Dimension rb_old(200), rb_itr(200)
 Dimension r1s_old(200), r1s_itr(200)          !dissolution rate for small particle
 Dimension r1b_old(200), r1b_itr(200)          !dissolution rate for large particle
 Dimension r2s_old(200), r2s_itr(200)         !oxidation rate for small particle
 Dimension r2b_old(200), r2b_itr(200)         !oxidation rate for large particle

 Dimension u1s_itr(200), u1b_itr(200)         !dissolution potential
 Dimension u2s_itr(200), u2b_itr(200)         !oxidation potential
 Dimension Ps(200), Pb(200)                   !number of particle in each mesh

 DATA  U10/1.188D0/, U20/0.98D0/
 DATA  alphi_a1/0.5D0/, alphi_c1/0.5D0/, alphi_a2/0.4D0/, alphi_c2/0.1D0/
 DATA  k1/3.0d-6/,  k2a/7d-6/, k2c/7d-6/, DIFF/1.5D-13/
 DATA  m_p/0.1951d0/, rou_p/21090d0/, m_o/0.211d0/, rou_o/14100d0/
 DATA  FMAX/2.18d-5/,fract_c/0.3d0/, fract_m/0.99d0/
 DATA  n1/2/, n2/2/
 DATA  CH/1.0d0/, Cptref/1000.0d0/
 DATA  sigma_p/2.37d0/, sigma_o/1.0d0/
 DATA  omiga/30000.00d0/,  mu/-38000.0d0/
 DATA  Phi_max/1.0d0/
 DATA  F/96485.0d0/, R/8.314d0/, TM/333.0d0/, pi/3.1415926d0/
 !DATA  dd/3.444d-10/ !oxide monolayer thickness 0.3444nm
```

```
delt=0.01d0                          ! time step
delx=0.1d-6                          !mesh zie 0.1 micron
V=DELX*25.0D0/10000.0D0              !VOLUME OF MESH
rr_min=2d-10                         !mininum particle size 0.2nm radius
Nmax=1000                            !total cycle number

size_t=NINT(Nmax*60/delt)
size_x1=NINT(7D-6/delx)
size_x2=NINT(12.5D-6/delx)

n=13
nj=size_x2
n_itr=20                             !max iteration number


 Open (unit=111, file="31_1.0_a.out")                !only major data OUTPUT
 Write (111,05) "cycle#", "mass(fluxright)", "area", "Radius", "R_small", "R_large",
"CPT(35)", "PHI_S(35)", "PHI_B(35)", "RS_OLD(35)", "RB_OLD(35)",
"RS_OLD(70)", "RB_OLD(70)", "Radius_1", "R_small_1", "R_large_1"
 05 Format(1X, 16A23)

 Open (unit=115, file="31_1.0_a_raw1.out")      !detailed data at 100, 200, …cycles
 WRITE (115, 06) "DISTANCE(UM)", "CPT", "PHI_S", "PHI_B", "RS", "RB","R1S",
"R1B", "R2S", "R2B","U1S","U1B","U2S", "U2B"
 06 FORMAT (1X, 14A23)

 OPEN (UNIT=116, FILE="31_1.0_a_raw2.out") !Data at cathode/membrane interface
 WRITE (116, 06) "CPT", "PHI_S", "PHI_B", "RS", "RB","R1S", "R1B", "R2S",
"R2B","U1S","U1B","U2S", "U2B"

Do I=1, NJ
do J=1,N
C(J,I)=0.0D0
END DO
cpt_old(I)=0.0D0; cpt_itr(I)=0.0D0; phi_s_old(I)=0.0D0;
phi_s_itr(I)=0.0D0;phi_b_old(I)=0.0D0; phi_b_itr(I)=0.0D0
rs_old(I)=0.0D0; rs_itr(I)=0.0D0;rb_old(I)=0.0D0; rb_itr(I)=0.0D0;r1s_old(I)=0.0D0;
r1s_itr(I)=0.0D0
r1b_old(I)=0.0D0; r1b_itr(I)=0.0D0; r2s_old(I)=0.0D0;
r2s_itr(I)=0.0D0;r2b_old(I)=0.0D0; r2b_itr(I)=0.0D0
u1s_itr(I)=0.0D0; u1b_itr(I)=0.0D0;u2s_itr(I)=0.0D0; u2b_itr(I)=0.0D0;Ps(I)=0.0D0;
Pb(I)=0.0D0
END DO

!set initial conditions and output the data
S=0.0d0!compared to ECA
```

```
 RRR=0.0D0!compared to the XRD measured size/2.0
 R_U=0.0d0;  R_D=0.0d0
 RS_U=0.0D0; RS_D=0.0D0
 RB_U=0.0D0; RB_D=0.0D0

 RRR1=0.0D0; RS1=0.0D0;RB1=0.0D0
!CALCUALTE SIZE EXCLUDING THE INTERFACE 90%TOP LAYER OF cathode
R_U1=0.0d0;  R_D1=0.0d0
 RS_U1=0.0D0; RS_D1=0.0D0
 RB_U1=0.0D0; RB_D1=0.0D0

 E=0.87D0                !INITIAL POTENTIAL 1V

 Do i=1, size_x1 !initial values

 PS(I)=1.9497896d14
 PB(I)=1.9497896d14

 RS_OLD(I)=1.5D-9;            RB_OLD(I)=1.75D-9
 C(4, I)=RS_OLD(I);  C(5, I)=RB_OLD(I)

phi_s_old(I)=0.4339335D0;  PHI_B_OLD(I)=0.42484033D0
!equilibrium oxide coverage initially at 0.87v
 C(2, I)=phi_s_old(i); C(3, I)=phi_b_old(i)

 CPT_OLD(I)=3.0D-5
 C(1, I)=CPT_OLD(I)


 U1S_ITR(i)=u10-(0.50d0/F)*(sigma_p*m_p/rou_p/RS_old(i)); C(10, I)=U1S_ITR(i)
 U1B_ITR(i)=u10-(0.50d0/F)*(sigma_p*m_p/rou_p/RB_old(i)); C(11, I)=U1B_ITR(i)
 U2S_ITR(i)=u20+(0.50d0/F)*(mu+sigma_o*m_o/rou_o/RS_old(i)-
sigma_p*m_p/rou_p/RS_old(i))
 C(12, I)=U2S_ITR(i)
 U2B_ITR(i)=u20+(0.50d0/F)*(mu+sigma_o*m_o/rou_o/RB_old(i)-
sigma_p*m_p/rou_p/RB_old(i))
 C(13, I)=U2B_ITR(i)

 R1S_OLD(i)=k1*(1.0d0-phi_s_old(i))*(exp(alphi_a1*N1*F*(E-U1S_ITR(i))/(R*TM))-
(CPT_old(i)/Cptref)*&
  &exp(-alphi_c1*n1*F*(E-u1s_itr(i))/(R*TM)))
 C(6, I)=R1S_OLD(i)
 R1B_OLD(i)=k1*(1.0d0-phi_b_old(i))*(exp(alphi_a1*n1*F*(E-U1B_ITR(i))/(R*TM))-
(CPT_old(i)/Cptref)*&
  &exp(-alphi_c1*n1*F*(E-U1B_itr(i))/(R*TM)))
 C(7, I)=R1B_OLD(i)
```

```
 R2S_OLD(i)=k2a*exp(-omiga*phi_S_old(i)/R/TM)*exp(alphi_a2*n2*F*(E-
u2s_itr(i))/(R*TM))&
  &-k2c*phi_s_old(i)*CH*CH*exp(-alphi_c2*n2*F*(E-u2s_itr(i))/(R*TM))
 C(8, I)=R2S_OLD(i)
 R2B_OLD(i)=k2a*exp(-omiga*phi_B_old(i)/R/TM)*exp(alphi_a2*n2*F*(E-
u2B_itr(i))/(R*TM))&
  &-k2c*phi_B_old(i)*CH*CH*exp(-alphi_c2*n2*F*(E-u2B_itr(i))/(R*TM))
 C(9, I)=R2B_OLD(i)


 If (I==1.or.i==size_x1) then
 S=S+(4.0d0*pi)*(PS(I)*RS_old(I)**2.0d0+PB(I)*RB_old(I)**2.0d0)/2.0D0
 RS_U=RS_U+PS(I)*RS_old(I)**4.0d0/2.0D0
 RS_D=RS_D+PS(I)*RS_old(I)**3.0d0/2.0D0
 RB_U=RB_U+PB(I)*RB_old(I)**4.0d0/2.0D0
 RB_D=RB_D+PB(I)*RB_old(I)**3.0d0/2.0D0
 R_U=R_U+PS(I)*RS_old(I)**4.0d0/2.0D0+PB(I)*RB_old(I)**4.0d0/2.0D0
 R_D=R_D+PS(I)*RS_old(I)**3.0d0/2.0D0+PB(I)*RB_old(I)**3.0d0/2.0D0

 else
 S=S+(4.0d0*pi)*(PS(I)*RS_old(I)**2.0d0+PB(I)*RB_old(I)**2.0d0)
 RS_U=RS_U+PS(I)*RS_old(I)**4.0d0
 RS_D=RS_D+PS(I)*RS_old(I)**3.0d0
 RB_U=RB_U+PB(I)*RB_old(I)**4.0d0
 RB_D=RB_D+PB(I)*RB_old(I)**3.0d0
 R_U=R_U+PS(I)*RS_old(I)**4.0d0+PB(I)*RB_old(I)**4.0d0
 R_D=R_D+PS(I)*RS_old(I)**3.0d0+PB(I)*RB_old(I)**3.0d0

If (I<=NINT(0.9*SIZE_X1)) then
   RS_U1=RS_U; RS_D1=RS_D; RB_U1=RB_U; RB_D1=RB_D; R_U1=R_U;
R_D1=R_D
   END IF
 end if

 END DO
RRR=R_U/R_D
 RS=RS_U/RS_D
 RB=RB_U/RB_D
 RRR1=R_U1/R_D1
 RS1=RS_U1/RS_D1
 RB1=RB_U1/RB_D1

 mass_b=1.25d-5                !12.5mg


 DO I=SIZE_X1+1, SIZE_X2                  !MEMBRANE PHASE
```

```
CPT_OLD(I)=0.0D0; C(1, I)=CPT_OLD(I)
END DO

Write (unit=111,20) 0, mass_b, S, RRR, RS, RB, CPT_OLD(35), PHI_S_OLD(35),
PHI_B_OLD(35), RS_OLD(35), RB_OLD(35), RS_OLD(70), RB_OLD(70), RRR1,
RS1, RB1
20 FORMAT (1X, I23, 15E23.15)


!time step loop starts
Do i=1, SIZE_T

!FOR 0.01 SECOND AS TIME STEP
if (mod(i, 6000)<100 .And.mod(i, 6000)>0 ) then
E=0.87d0+0.0033d0*mod(i, 6000)
ELSE IF (mod(i, 6000)<=3000 .and. mod(i, 6000)>=100) then
E=1.2d0
else if (mod(i, 6000)<=3100 .and. mod(i, 6000)>3000) then
E=1.2d0-0.0033d0*(mod(i, 6000)-3000)
else if (mod(i, 6000)>3100 .and.mod(i, 6000)<6000) then
E=0.87d0
else if (mod(i, 6000)==0)THEN
E=0.87d0
end if
PRINT *,E

 !Guess the values for the new time step for c(k,j)
 !SMPLY USE THE LAST UPDATED VALUES
Do II=1, size_x1                        !cathode
C(1,II)=CPT_OLD(II)
C(2,II)=phi_s_old(iI);          C(3, II)=phi_b_old(iI)
C(4,II)=RS_OLD(II);             C(5, II)=RB_OLD(II)
C(6, II)=R1S_OLD(iI);           C(7, II)=R1B_OLD(iI)
C(8, II)=R2S_OLD(iI);           C(9, II)=R2B_OLD(iI)
C(10,iI)=C(10,II)*0.99d0;
C(11,II)=C(11,II)*0.99d0
C(12,II)=C(12,II)*0.99d0
C(13,II)=C(13,II)*0.99d0
end do

DO II=SIZE_X1+1, SIZE_X2          !MEMBRANE PHASE
IF (II==SIZE_X2) THEN
C(1,II)=0.0D0
ELSE
C(1,II)=CPT_OLD(II)
END IF
```

```
 END DO

 ! Start the Iteration for convergence for each time step

 IT=0
 1000 IT=IT+1

!INITIATE THE X, Y VALUES, ONLY 1 EQUATION AND 1 VARIBALE
 DO II=1, N
 DO iii=1, N
 X(II,iii)=0.0D0
 Y(II,iii)=0.0D0
 END DO
 END DO

 !STORE PREVIOUS ITERATION RESULTS OF c_new TO c_ITE
 Do II=1, size_x1                    !cathode
 CPT_ITR(II)=C(1,II)
 phi_s_ITR(iI)=C(2,II);          phi_b_ITR(iI)=C(3, II)
 RS_ITR(II)=C(4,II);  RB_ITR(II)=C(5, II)
 R1S_ITR(iI)=C(6, II);           R1B_ITR(iI)=C(7, II)
 R2S_ITR(iI)=C(8, II);           R2B_ITR(iI)=C(9, II)
 U1S_ITR(II)=C(10, II); U1B_ITR(II)=C(11, II)
 U2S_ITR(II)=C(12, II);          U2B_ITR(II)=C(13, II)
 end do

 DO II=SIZE_X1+1, SIZE_X2          !MEMBRANE PHASE
 CPT_ITR(II)=C(1,II)
 END DO

! start x dimension loop calling band

 DO J=1, NJ

 ! INITIATE A, B,D, G
 DO ii=1, n
 G(ii)=0.0D0
 do iii=1, n
 A(ii,iii)=0.0D0
 B(ii,iii)=0.0D0
 D(ii,iii)=0.0D0
 end do
 end do

 !CALL BAND TO CALCULATE C(K,J)
 IF (J>=1.AND.J<=SIZE_X1) THEN
```

```
    If (J==1) then
!BOUNDARY AT GDL/CATHODE ASSUME NO CATALYST REACTION
          B(1,1)=-1.5D0/DELX
          D(1,1)=2.0D0/DELX
          X(1,1)=-0.5D0/DELX
    ELSE IF (J>1.AND.J<SIZE_X1) THEN!CATHODE PHASE
          !1ST EQUATION
          A(1,1)=DIFF/2.0D0/DELX/DELX*fract_c**0.5d0
          D(1,1)=DIFF/2.0D0/DELX/DELX*fract_c**0.5d0
          B(1,1)=-DIFF/DELX/DELX*fract_c**0.5d0-1.0D0/DELT
          B(1,4)=4.0*PI*PS(J)*RS_OLD(J)*R1S_OLD(J)/V/fract_c
          B(1,5)=4.0*PI*PB(J)*RB_OLD(J)*R1B_OLD(J)/V/fract_c
          B(1,6)=2.0D0*PI*PS(J)*RS_OLD(J)*RS_OLD(J)/V/fract_c
          B(1,7)=2.0D0*PI*PB(J)*RB_OLD(J)*RB_OLD(J)/V/fract_c
          G(1)=-DIFF*fract_c**0.5d0/2.0D0/DELX/DELX*CPT_OLD(J+1)-
(1.0D0/DELT-DIFF*fract_c**0.5d0/DELX/DELX)*CPT_OLD(J)
          -DIFF*fract_c**0.5d0/2.0D0/DELX/DELX*CPT_OLD(J-
1)+(2.0D0*PI/V/fract_c)*(PS(J)*RS_OLD(J)*RS_OLD(J)*R1S_OLD(J)+PB(J)*RB_OL
D(J)*RB_OLD(J)*R1B_OLD(J))
     Else if (j==size_x1) then
    !interface of cathode and membrane by control volume
     !due to the different effective diffusion coefficient (ionomer volume fraction
different)
     A(1,1)=FRACT_C**1.5d0*DIFF/(FRACT_M+FRACT_C)/DELX**2.0D0
     D(1,1)=FRACT_M**1.5d0*DIFF/(FRACT_M+FRACT_C)/DELX**2.0D0
B(1,1)=-1.0D0/DELT-
DIFF/DELX**2.0D0*(FRACT_C**1.5d0+FRACT_m**1.5d0)/(Fract_m+Fract_c)
     A(1,4)=PI*PS(J-1)*RS_OLD(J-1)*R1S_OLD(J-1)/V/(FRACT_M+FRACT_C)
     B(1,4)=3.0d0*PI*PS(J)*RS_OLD(J)*R1S_OLD(J)/V/(FRACT_M+FRACT_C)
     A(1,5)=PI*PB(J-1)*RB_OLD(J-1)*R1B_OLD(J-1)/V/(FRACT_M+FRACT_C)
     B(1,5)=3.0d0*PI*PB(J)*RB_OLD(J)*R1B_OLD(J)/V/(FRACT_M+FRACT_C)
     A(1,6)=0.5d0*PI*PS(J-1)*RS_OLD(J-1)**2.0D0/V/(FRACT_M+FRACT_C)
     B(1,6)=1.50d0*PI*PS(J)*RS_OLD(J)**2.0D0/V/(FRACT_M+FRACT_C)
     A(1,7)=0.5d0*PI*PB(J-1)*RB_OLD(J-1)**2.0D0/V/(FRACT_M+FRACT_C)
     B(1,7)=1.5d0*PI*PB(J)*RB_OLD(J)**2.0D0/V/(FRACT_M+FRACT_C)


G(1)=((FRACT_C**1.5d0+FRACT_m**1.5d0)/(FRACT_M+FRACT_C)*Diff/delx**2.
0d0-1.0D0/DELT)*CPT_OLD(J)-
FRACT_M**1.5d0*DIFF/(FRACT_M+FRACT_C)/DELX**2.0D0*CPT_OLD(J+1)
     -FRACT_C**1.5d0*DIFF/(FRACT_M+FRACT_C)/DELX**2.0D0*CPT_OLD(J-1)
     +PI*0.5D0/V/(FRACT_M+FRACT_C)*(PS(J-1)*RS_OLD(J-
1)**2.0D0*R1S_OLD(J-1)+PB(J-1)*RB_OLD(J-1)**2.0D0*R1B_OLD(J-1))
+PI*1.5D0/V/(FRACT_M+FRACT_C)*(PS(J)*RS_OLD(J)**2.0D0*R1S_OLD(J)+PB(
J)*RB_OLD(J)**2.0D0*R1B_OLD(J))
```

```
    End if

 !2ND EQUATION modified included r1s and two terms of r2s
 B(2,2)=1.0D0/DELT-M_P/ROU_P/RS_OLD(J)*(R1S_OLD(J)+R2S_OLD(J))
B(2,4)=M_P/ROU_P*PHI_S_OLD(J)/RS_OLD(J)/RS_OLD(J)*(R1S_OLD(J)+R2S_OL
D(J))
 B(2,6)=-M_P/ROU_P*PHI_S_OLD(J)/RS_OLD(J)
 B(2,8)=-0.5D0/FMAX-M_P/ROU_P*PHI_S_OLD(J)/RS_OLD(J)

G(2)=PHI_S_OLD(J)/DELT+R2S_OLD(J)/2.0D0/FMAX+M_P/ROU_P*PHI_S_OLD(J
)/RS_OLD(J)*(R1S_OLD(J)+R2S_OLD(J))
 !3RD EQUATION modified included r1b and two terms of r2b
 B(3,3)=1.0D0/DELT-M_P/ROU_P/RB_OLD(J)*(R1B_OLD(J)+R2B_OLD(J))
B(3,5)=M_P/ROU_P*PHI_B_OLD(J)/RB_OLD(J)/RB_OLD(J)*(R1B_OLD(J)+R2B_O
LD(J))
 B(3,7)=-M_P/ROU_P*PHI_B_OLD(J)/RB_OLD(J)
 B(3,9)=-0.5D0/FMAX-M_P/ROU_P*PHI_B_OLD(J)/RB_OLD(J)
G(3)=PHI_B_OLD(J)/DELT+R2B_OLD(J)/2.0D0/FMAX+M_P/ROU_P*PHI_B_OLD(
J)/RB_OLD(J)*(R1B_OLD(J)+R2B_OLD(J))
 !4TH EQUATION
 B(4,4)=1.0D0/DELT
 B(4,6)=M_P/ROU_P/2.0D0
 B(4,8)=M_P/ROU_P/2.0D0
 G(4)=RS_OLD(J)/DELT-M_P/ROU_P/2.0D0*(R1S_OLD(J)+R2S_OLD(J))!RADIUS
CHANGE BY DISSOLTUION AND OXIDATION
 !5TH EQUATION
 B(5,5)=1.0D0/DELT
 B(5,7)=M_P/ROU_P/2.0D0
 B(5,9)=M_P/ROU_P/2.0D0
 G(5)=RB_OLD(J)/DELT-M_P/ROU_P/2.0D0*(R1B_OLD(J)+R2B_OLD(J))

 If (phi_s_itr(j)<phi_max) then
 !6TH EQUATION !ALLOW COMPLETE OXIDE COVERAGE AND BLOCKING
DISSOLUTION if phi_max=1.0
 B(6,1)=K1/CPTREF*(1.0D0-PHI_S_ITR(J))*EXP(-ALPHI_C1*N1*F*(E-
U1S_ITR(J))/R/TM)
 B(6,2)=K1*EXP(ALPHI_A1*N1*F*(E-U1S_ITR(J))/R/TM)-
K1*CPT_ITR(J)/CPTREF*EXP(-ALPHI_C1*N1*F*(E-U1S_ITR(J))/R/TM)
 B(6,6)=1.0D0
 B(6,10)=K1*(1.0D0-
PHI_S_ITR(J))*(ALPHI_A1*N1*F/R/TM)*EXP(ALPHI_A1*N1*F*(E-
U1S_ITR(J))/R/TM)&
          &+K1*CPT_ITR(J)/CPTREF*(1.0D0-
PHI_S_ITR(J))*(ALPHI_C1*N1*F/R/TM)*EXP(-ALPHI_C1*N1*F*(E-
U1S_ITR(J))/R/TM)
```

```
 G(6)=K1*EXP(ALPHI_A1*N1*F*(E-
U1S_ITR(J))/R/TM)*(1.0D0+(ALPHI_A1*N1*F/R/TM)*U1S_ITR(J)*(1.0D0-
PHI_S_ITR(J)))&
       &+K1*CPT_ITR(J)/CPTREF*EXP(-ALPHI_C1*N1*F*(E-U1S_ITR(J))/R/TM)&
       &*((ALPHI_C1*N1*F/R/TM)*U1S_ITR(J)*(1.0D0-PHI_S_ITR(J))-
PHI_S_ITR(J))
 else
 B(6,1)=k1*(1.0D0-phi_max)/cptref*exp(-alphi_c1*n1*F*(E-U1S_ITR(J))/R/TM)
 B(6,6)=1.0D0
 B(6,10)=K1*(1.0D0-
PHI_MAX)*(ALPHI_A1*N1*F/R/TM*EXP(ALPHI_A1*N1*F/R/TM*(E-
U1S_ITR(J)))+&
         &CPT_ITR(J)/CPTREF*(ALPHI_C1*N1*F/R/TM)*EXP(-
ALPHI_C1*N1*F/R/TM*(E-U1S_ITR(J))))
 G(6)=K1*(1.0D0-
PHI_MAX)*((1.0D0+ALPHI_A1*N1*F*U1S_ITR(J)/R/TM)*EXP(ALPHI_A1*N1*F/
R/TM*(E-U1S_ITR(J)))+&
         &CPT_ITR(J)/CPTREF*(ALPHI_C1*N1*F/R/TM)*U1S_ITR(J)*EXP(-
ALPHI_C1*N1*F/R/TM*(E-U1S_ITR(J))))
 end if


 IF (phi_B_itr(j)<phi_max) then
 !7TH EQUATION !ALLOW COMPLETE OXIDE COVERAGE AND BLOCKING
DISSOLUTION if phi_max=1.0
 B(7,1)=K1/CPTREF*(1.0D0-PHI_B_ITR(J))*EXP(-ALPHI_C1*N1*F*(E-
U1B_ITR(J))/R/TM)
 B(7,3)=K1*EXP(ALPHI_A1*N1*F*(E-U1B_ITR(J))/R/TM)-
K1*CPT_ITR(J)/CPTREF*EXP(-ALPHI_C1*N1*F*(E-U1B_ITR(J))/R/TM)
 B(7,7)=1.0D0
 B(7,11)=K1*(1.0D0-
PHI_B_ITR(J))*(ALPHI_A1*N1*F/R/TM)*EXP(ALPHI_A1*N1*F*(E-
U1B_ITR(J))/R/TM)&
          &+K1*CPT_ITR(J)/CPTREF*(1.0D0-
PHI_B_ITR(J))*(ALPHI_C1*N1*F/R/TM)*EXP(-ALPHI_C1*N1*F*(E-
U1B_ITR(J))/R/TM)
 G(7)=K1*EXP(ALPHI_A1*N1*F*(E-
U1B_ITR(J))/R/TM)*(1.0D0+(ALPHI_A1*N1*F/R/TM)*U1B_ITR(J)*(1.0D0-
PHI_B_ITR(J)))&
       &+K1*CPT_ITR(J)/CPTREF*EXP(-ALPHI_C1*N1*F*(E-U1B_ITR(J))/R/TM)&
       &*((ALPHI_C1*N1*F/R/TM)*U1B_ITR(J)*(1.0D0-PHI_B_ITR(J))-
PHI_B_ITR(J))
 ELSE
 B(7,1)=k1*(1.0D0-phi_max)/cptref*exp(-alphi_c1*n1*F*(E-U1B_ITR(J))/R/TM)
 B(7,7)=1.0D0
```

```
 B(7,11)=K1*(1.0D0-
PHI_MAX)*(ALPHI_A1*N1*F/R/TM*EXP(ALPHI_A1*N1*F/R/TM*(E-
U1B_ITR(J)))+&
         &CPT_ITR(J)/CPTREF*(ALPHI_C1*N1*F/R/TM)*EXP(-
ALPHI_C1*N1*F/R/TM*(E-U1B_ITR(J))))
 G(7)=K1*(1.0D0-
PHI_MAX)*((1.0D0+ALPHI_A1*N1*F*U1B_ITR(J)/R/TM)*EXP(ALPHI_A1*N1*F/
R/TM*(E-U1B_ITR(J)))+&
         &CPT_ITR(J)/CPTREF*(ALPHI_C1*N1*F/R/TM)*U1B_ITR(J)*EXP(-
ALPHI_C1*N1*F/R/TM*(E-U1B_ITR(J))))
 END IF

 !8TH EQUATION
 B(8,2)=K2A*OMIGA/R/TM*EXP(-
OMIGA*PHI_S_ITR(J)/R/TM)*EXP(ALPHI_A2*N2*F/R/TM*(E-U2S_ITR(J)))&
      &+K2C*EXP(-ALPHI_C2*N2*F/R/TM*(E-U2S_ITR(J)))
 B(8,8)=1.0D0
 B(8,12)=K2A*(ALPHI_A2*N2*F/R/TM)*EXP(-
OMIGA*PHI_S_ITR(J)/R/TM)*EXP(ALPHI_A2*N2*F/R/TM*(E-U2S_ITR(J)))&
         &+K2C*(ALPHI_C2*N2*F/R/TM)*PHI_S_ITR(J)*EXP(-
ALPHI_C2*N2*F/R/TM*(E-U2S_ITR(J)))
 G(8)=K2A*EXP(-OMIGA*PHI_S_ITR(J)/R/TM)*EXP(ALPHI_A2*N2*F/R/TM*(E-
U2S_ITR(J)))*(1.0D0+OMIGA*PHI_S_ITR(J)/R/TM+&
         &ALPHI_A2*N2*F/R/TM*U2S_ITR(J))+K2C*(ALPHI_C2*N2*F/R/TM)*PHI
_S_ITR(J)*U2S_ITR(J)*EXP(-ALPHI_C2*N2*F/R/TM*(E-U2S_ITR(J)))
 !9TH EQUATION
 B(9,3)=K2A*OMIGA/R/TM*EXP(-
OMIGA*PHI_B_ITR(J)/R/TM)*EXP(ALPHI_A2*N2*F/R/TM*(E-U2B_ITR(J)))&
         &+K2C*EXP(-ALPHI_C2*N2*F/R/TM*(E-U2B_ITR(J)))
 B(9,9)=1.0D0
 B(9,13)=K2A*(ALPHI_A2*N2*F/R/TM)*EXP(-
OMIGA*PHI_B_ITR(J)/R/TM)*EXP(ALPHI_A2*N2*F/R/TM*(E-U2B_ITR(J)))&
         &+K2C*(ALPHI_C2*N2*F/R/TM)*PHI_B_ITR(J)*EXP(-
ALPHI_C2*N2*F/R/TM*(E-U2B_ITR(J)))
 G(9)=K2A*EXP(-OMIGA*PHI_B_ITR(J)/R/TM)*EXP(ALPHI_A2*N2*F/R/TM*(E-
U2B_ITR(J)))*(1.0D0+OMIGA*PHI_B_ITR(J)/R/TM+&
         &ALPHI_A2*N2*F/R/TM*U2B_ITR(J))+K2C*(ALPHI_C2*N2*F/R/TM)*PHI
_B_ITR(J)*U2B_ITR(J)*EXP(-ALPHI_C2*N2*F/R/TM*(E-U2B_ITR(J)))
 !10TH EQUATION
 B(10,4)=-0.5D0/F*SIGMA_P*M_P/ROU_P/RS_ITR(J)/RS_ITR(J)
 B(10,10)=1.0D0
 G(10)=U10-SIGMA_P*M_P/ROU_P/RS_ITR(J)/F
 !11TH EQUATION
 B(11,5)=-0.5D0/F*SIGMA_P*M_P/ROU_P/RB_ITR(J)/RB_ITR(J)
 B(11,11)=1.0D0
 G(11)=U10-SIGMA_P*M_P/ROU_P/RB_ITR(J)/F
```

```
 !12TH EQUATION
 B(12,4)=0.5D0/F/RS_ITR(J)/RS_ITR(J)*(SIGMA_O*M_O/ROU_O-
SIGMA_P*M_P/ROU_P)
 B(12,12)=1.0D0
 G(12)=U20+MU/2.0D0/F+1.0D0/F/RS_ITR(J)*(SIGMA_O*M_O/ROU_O-
SIGMA_P*M_P/ROU_P)
 !13TH EQUATION
 B(13,5)=0.5D0/F/RB_ITR(J)/RB_ITR(J)*(SIGMA_O*M_O/ROU_O-
SIGMA_P*M_P/ROU_P)
 B(13,13)=1.0D0
 G(13)=U20+MU/2.0D0/F+1.0D0/F/RB_ITR(J)*(SIGMA_O*M_O/ROU_O-
SIGMA_P*M_P/ROU_P)

 CALL BAND(J)


 ELSE IF (J>SIZE_X1.AND.J<SIZE_X2) THEN!MEMBRANE PHASE
 A(1,1)=DIFF/2.0D0/DELX/DELX*fract_m**0.5d0
 D(1,1)=DIFF/2.0D0/DELX/DELX*fract_m**0.5d0
 B(1,1)=-DIFF*fract_m**0.5d0/DELX/DELX-1.0D0/DELT
 G(1)=-DIFF*fract_m**0.5d0/2.0D0/DELX/DELX*CPT_OLD(J+1)-(1.0D0/DELT-
DIFF*fract_m**0.5d0/DELX/DELX)*CPT_OLD(J)&
 &-DIFF*fract_m**0.5d0/2.0D0/DELX/DELX*CPT_OLD(J-1)
 !2-13 VARIBLE NO PHYSICAL MEANINGS IN MEMBRNAE PHASE, BUT SET
TO ZERO TO AVOID ZERO DETERMINANTS
 B(2,2)=1.0D0; B(3,3)=1.0D0; B(4,4)=1.0D0; B(5,5)=1.0D0; B(6,6)=1.0D0;
B(7,7)=1.0D0
 B(8,8)=1.0D0; B(9,9)=1.0D0; B(10,10)=1.0D0; B(11,11)=1.0D0; B(12,12)=1.0D0;
B(13,13)=1.0D0
 CALL BAND(J)

 ELSE IF (J==SIZE_X2) THEN!PT BAND LOCATION CPT=0
 B(1,1)=1.0D0
 B(2,2)=1.0D0; B(3,3)=1.0D0; B(4,4)=1.0D0; B(5,5)=1.0D0; B(6,6)=1.0D0;
B(7,7)=1.0D0
 B(8,8)=1.0D0; B(9,9)=1.0D0; B(10,10)=1.0D0; B(11,11)=1.0D0; B(12,12)=1.0D0;
B(13,13)=1.0D0
 CALL BAND(J)

 END IF


END DO                                  !X DIMENSION LOOP

 !FORCED THE ADJUSTEMENT IF Pt concentration  becomes negative
 Do jj=1, nj
```

```
if (C(1,jj)<0.0d0) then
C(1,jj)=0.0d0
Print *,"negative concentration"
go to 5000 !stop the calculation
End if
End do


!CHECK FOR CONVERGENCE (PICK PT CONCENTRATION VARIABLE)
If (it>=N_ITR) THEN
PRINT *, "MAX ITERATION REACHED"
GO TO 2000
ELSE
  DO JJ=2, NJ-1

  DEL_C=DABS(C(1,JJ)-CPT_ITR(JJ))
 del_rb=dabs(C(5, JJ)-RB_ITR(JJ))
  DEL_RS=DABS(C(4,JJ)-RS_ITR(JJ))

  IF (DEL_C>1.0D-8*CPT_ITR(JJ).OR. DEL_RB>1.0D-8*RB_ITR(JJ).or.del_rs>1.0d-
8*RS_ITR(JJ)) THEN
  GO TO 1000
  END IF

  END DO
  GO TO 2000
END IF


2000  mass_b=mass_b+m_p*2.5d-3*Diff/2.0d0/delx*delt*(fract_m*(C(1,71)-
      C(1,70)+CPT_OLD(71)-CPT_OLD(70)))
!central 2-point flux out

!renew the old values from the previous band results c(k, j)
Do II=1, size_x1                    !cathode
CPT_OLD(II)=C(1,II)
phi_s_old(II)=C(2,II);        phi_b_old(II)=C(3, II)
RS_OLD(II)=C(4,II);           RB_OLD(II)=C(5, II)
R1S_OLD(II)=C(6, II);         R1B_OLD(II)=C(7, II)
R2S_OLD(II)=C(8, II);         R2B_OLD(II)=C(9, II)
end do

DO II=SIZE_X1+1, SIZE_X2      !MEMBRANE PHASE
CPT_OLD(II)=C(1, II)
END DO
```

```
!OUTPUT DATA at the end of EACH 1 CyCLES (I=1*60/DELT=600, 1200 or 3000 OR
6000)
 IF(MOD(I, 6000)==0) THEN
 S=0.0d0
 RRR=0.0d0
 R_U=0.0d0;  R_D=0.0d0
 RS_U=0.0D0; RS_D=0.0D0
 RB_U=0.0D0; RB_D=0.0D0

 RRR1=0.0D0; RS1=0.0D0;RB1=0.0D0
! CALCUALTE SIZE EXCLUDING THE INTERFACE 90%TOP LAYER OF cathode
 R_U1=0.0d0;  R_D1=0.0d0
 RS_U1=0.0D0; RS_D1=0.0D0
 RB_U1=0.0D0; RB_D1=0.0D0

 DO II=1, SIZE_X1
 If (II==1.or.II==size_x1) then

 S=S+(4.0d0*pi)*(PS(II)*RS_old(II)**2.0d0+PB(II)*RB_old(II)**2.0d0)/2.0D0
 RS_U=RS_U+PS(II)*RS_old(II)**4.0d0/2.0D0
 RS_D=RS_D+PS(II)*RS_old(II)**3.0d0/2.0D0
 RB_U=RB_U+PB(II)*RB_old(II)**4.0d0/2.0D0
 RB_D=RB_D+PB(II)*RB_old(II)**3.0d0/2.0D0
 R_U=R_U+PS(II)*RS_old(II)**4.0d0/2.0D0+PB(II)*RB_old(II)**4.0d0/2.0D0
 R_D=R_D+PS(II)*RS_old(II)**3.0d0/2.0D0+PB(II)*RB_old(II)**3.0d0/2.0D0
 else

 S=S+(4.0d0*pi)*(PS(II)*RS_old(II)**2.0d0+PB(II)*RB_old(II)**2.0d0)
 RS_U=RS_U+PS(II)*RS_old(II)**4.0d0
 RS_D=RS_D+PS(II)*RS_old(II)**3.0d0
 RB_U=RB_U+PB(II)*RB_old(II)**4.0d0
 RB_D=RB_D+PB(II)*RB_old(II)**3.0d0
 R_U=R_U+PS(II)*RS_old(II)**4.0d0+PB(II)*RB_old(II)**4.0d0
 R_D=R_D+PS(II)*RS_old(II)**3.0d0+PB(II)*RB_old(II)**3.0d0

   IF (II<=NINT(0.9*SIZE_X1)) then
   RS_U1=RS_U; RS_D1=RS_D; RB_U1=RB_U; RB_D1=RB_D; R_U1=R_U;
R_D1=R_D
   END IF

 end if

 END DO
RRR=R_U/R_D
 RS=RS_U/RS_D
```

```
 RB=RB_U/RB_D
 RRR1=R_U1/R_D1
 RS1=RS_U1/RS_D1
 RB1=RB_U1/RB_D1

 WRITE (111,55) NINT(I/6000.0), mass_b, S, RRR, RS, RB, CPT_OLD(35),
PHI_S_OLD(35), PHI_B_OLD(35),RS_OLD(35), RB_OLD(35), RS_OLD(70),
RB_OLD(70), RRR1, RS1, RB1
 55 FORMAT (1X, I23, 15E23.15)

60 format (1x, A23, I23)
65 FORMAT (1X, 14E23.15)

END IF

!ouptut 100, 200 300 400 600 800 1000th cycles
IF
(((i>=594000.AND.I<600000).OR.(i>=1194000.AND.I<1200000).OR.(i>=1794000.AN
D.I<1800000)&
&.OR.(i>=2394000.AND.I<2400000).OR.(i>=3594000.AND.I<3600000)&
&.OR.(i>=4794000.AND.I<4800000).OR.(i>=5994000.AND.I<6000000)).AND.MOD(I
, 100)==0) then
Write (115, *) "time(s)=", i/100.0
 WRITE (116,65) C(1,70),C(2,70),C(3,70),C(4,70),C(5,70),C(6,70),
C(7,70),C(8,70),C(9,70), C(10,70),C(11,70),C(12,70),C(13,70)
 Do JJ=1, NJ
 WRITE(115,65) JJ*0.1D0,C(1,JJ),C(2,JJ),C(3,JJ),C(4,JJ),C(5,JJ),C(6,JJ),C(7,JJ),
C(8,JJ),C(9,JJ),C(10,JJ),C(11,JJ),C(12,JJ),C(13,JJ)
 END DO
end if


 END DO                  !I THE TIME STEP LOOP

 5000 Rewind 111
 rewind 115
 REWIND 116
 Close(unit=111)
 close(unit=115)
 CLOSE(UNIT=116)
 Print *, "done!"

End Program Platinum_degradation
```

```
Subroutine band(j)
    implicit real*8(a-h,o-z)
    dimension e(20,21,150)
     common /bnd/ A(20,20), B(20,20), C(20,301), D(20,41)
    COMMON /mat/ G(20), X(20,20), Y(20,20)
     common /n/ n, nj
    save e,np1
101 format (/15h determ=0 at j=,i4)
    if (j-2)  1,6,8
  1 np1= n + 1
    do 2 i=1,n
    d(i,2*n+1)= g(i)
    do 2 l=1,n
    lpn= l + n
  2 d(i,lpn)= x(i,l)
    call matinv (n,2*n+1,determ)
    if (determ)  4,3,4
  3 print 101, j
  4 do 5 k=1,n
    e(k,np1,1)= d(k,2*n+1)
    do 5 l=1,n
    e(k,l,1)= - d(k,l)
    lpn= l + n
  5 x(k,l)= - d(k,lpn)
    return
  6 do 7 i=1,n
    do 7 k=1,n
    do 7 l=1,n
  7 d(i,k)= d(i,k) + a(i,l)*x(l,k)
  8 if (j-nj)  11,9,9
  9 do 10 i=1,n
    do 10 l=1,n
    g(i)= g(i) - y(i,l)*e(l,np1,j-2)
    do 10 m=1,n
 10 a(i,l)= a(i,l) + y(i,m)*e(m,l,j-2)
 11 do 12 i=1,n
    d(i,np1)= - g(i)
    do 12 l=1,n
    d(i,np1)= d(i,np1) + a(i,l)*e(l,np1,j-1)
    do 12 k=1,n
 12 b(i,k)= b(i,k) + a(i,l)*e(l,k,j-1)
    call matinv (n,np1,determ)
    if (determ)  14,13,14
 13 print 101, j
 14 do 15 k=1,n
    do 15 m=1,np1
```

```
15 e(k,m,j)= - d(k,m)
   if (j-nj)  20,16,16
16 do 17 k=1,n
17 c(k,j)= e(k,np1,j)
   do 18 jj=2,nj
   m= nj - jj + 1
   do 18 k=1,n
   c(k,m)= e(k,np1,m)
   do 18 l=1,n
18 c(k,m)= c(k,m) + e(k,l,m)*c(l,m+1)
   do 19 l=1,n
   do 19 k=1,n
19 c(k,1)= c(k,1) + x(k,l)*c(l,3)
20 return
   end


Subroutine matinv (n,m,determ)
   implicit real*8(a-h,o-z)
    common /bnd/ A(20,20), B(20,20), C(20,301), D(20,41)
    dimension id(20)
   determ=1.0
   do 1 i=1,n
 1 id(i)=0
   do 18 nn=1,n
   bmax=1.1
   do 6 i=1,n
   if(id(i).ne.0) go to 6
   bnext=0.0
   btry=0.0
   do 5 j=1,n
   if(id(j).ne.0) go to 5
   if(dabs(b(i,j)).le.bnext) go to 5
   bnext=dabs(b(i,j))
   if(bnext.le.btry) go to 5
   bnext=btry
   btry=dabs(b(i,j))
   jc=j
 5 continue
   if(bnext.ge.bmax*btry) go to 6
   bmax=bnext/btry
   irow=i
   jcol=jc
 6 continue
   if(id(jc).eq.0) go to 8
   determ=0.0
```

```
      return
    8 id(jcol)=1
      if(jcol.eq.irow) go to 12
      do 10 j=1,n
      save=b(irow,j)
      b(irow,j)=b(jcol,j)
   10 b(jcol,j)=save
      do 11 k=1,m
      save=d(irow,k)
      d(irow,k)=d(jcol,k)
   11 d(jcol,k)=save
   12 f=1.0/b(jcol,jcol)
      do 13 j=1,n
   13 b(jcol,j)=b(jcol,j)*f
      do 14 k=1,m
   14 d(jcol,k)=d(jcol,k)*f
      do 18 i=1,n
      if(i.eq.jcol) go to 18
      f=b(i,jcol)
      do 16 j=1,n
   16 b(i,j)=b(i,j)-f*b(jcol,j)
      do 17 k=1,m
   17 d(i,k)=d(i,k)-f*d(jcol,k)
   18 continue
      return
      end
```

REFERENCES

1. Grove, W.R., *On voltaic series and the combination of gases by platinum.* Phil. Mag. Ser. 3, 1839. **14**: p. 127.
2. Perry, M.L. and T.F. Fuller, *A Historical Perspective of Fuel Cell Technology in the 20th Century.* Journal of the Electrochemical Society, 2002. **149**(7): p. S59.
3. Wilson, M.S. and S. Gottesfeld, *High Performance Catalyzed Membranes of Ultra-Low Platinum Loadings for Polymer Electrolyte Fuel Cells.* Journal of The Electrochemical Society, 1992. **139**: p. 128.
4. Fuller, T.F., *Research Challenges for Low-Temperature Fuel Cells (NSF Workshop Report)*. 2005: Washington, D.C. p. 21.
5. He, C., et al., *PEM fuel cell catalysts: Cost, performance, and durability.* Electrochemical Society Interface, 2005. **14**(3): p. 41.
6. Wilson, M.S., et al., *Surface area loss of supported platinum in polymer electrolyte fuel cells.* Journal of the Electrochemical Society, 1993. **140**(10): p. 2872.
7. Sishtla, C., et al., *Performance and endurance of a PEMFC operated with synthetic reformate fuel feed.* Journal of Power Sources, 1998. **71**: p. 249.
8. Isono, T., et al., *Development of a high-performance PEFC module operated by reformed gas.* Journal of Power Sources, 2000. **86**: p. 269.
9. Gulzow, E., et al., *Dry layer preparation and characterization of polymer electrolyte fuel cell components.* Journal of Power Sources, 2000. **86**: p. 352-362.

10. Colon-Mercado, H.R., H. Kim, and B.N. Popov, *Durability study of Pt3Ni1 catalysts as cathode in PEM fuel cells.* Electrochemistry Communications, 2004. **6**(8): p. 795.

11. Bonakdarpour, A., et al., *Studies of Transition Metal Dissolution from Combinatorially Sputtered, Nanostructured Pt1-xMx (M = Fe, Ni; 0<x<1) Electrocatalysts for PEM Fuel Cells.* Journal of the Electrochemical Society, 2005. **152**(1): p. A61.

12. Xie, J., et al., *Durability of PEFCs at High Humidity Conditions.* Journal of the Electrochemical Society, 2005. **152**(1): p. A104.

13. Xie, J., et al., *Microstructural changes of membrane electrode assemblies during PEFC durability testing at high humidity conditions.* Journal of the Electrochemical Society, 2005. **152**(5): p. A1011.

14. Yu, J., et al., *Lifetime behavior of a PEM fuel cell with low humidification of feed stream.* Physical Chemistry Chemical Physics, 2005. **7**(2): p. 373.

15. Yu, P., M. Pemberton, and P. Plasse, *PtCo/C cathode catalyst for improved durability in PEMFCs.* Journal of Power Sources, 2005. **144**(1): p. 11.

16. Darling, R.M. and J.P. Meyers, *Kinetic Model of Platinum Dissolution in PEMFCs.* Journal of the Electrochemical Society, 2003. **150**(11): p. A1523.

17. Darling, R.M. and J.P. Meyers, *Mathematical Model of Platinum Movement in PEM Fuel Cells.* Journal of the Electrochemical Society, 2005. **152**(1): p. A242.

18. Stanic, V. and M. Hoberecht. *Mechanism of pin-hole formation in membrane electrode assemblies for PEM fuel cells*. in *2004 Joint International Meeting - 206th Meeting of the Electrochemical Society/2004 Fall Meeting of the*

Electrochemical Society of Japan. 2004. Honolulu, HI, United States: Electrochemical Society Inc.

19. Makharia, R., et al. *Characterization of carbon oxidation: Increased stability of PEM fuel cell electrodes by graphitization of carbon supports*. in *2004 Joint International Meeting - 206th Meeting of the Electrochemical Society/2004 Fall Meeting of the Electrochemical Society of Japan*. 2004. Honolulu, HI, United States Electrochemical Society Inc.

20. Meyers, J.P. and R.M. Darling. *Model of carbon corrosion in PEM fuel cells during regular operation*. in *2004 Joint International Meeting - 206th Meeting of the Electrochemical Society/2004 Fall Meeting of the Electrochemical Society of Japan*. 2004. Honolulu, HI, United States Electrochemical Society Inc.

21. Taniguchi, A., et al., *Analysis of electrocatalyst degradation in PEMFC caused by cell reversal during fuel starvation.* Journal of Power Sources, 2004. **130**(1-2): p. 42.

22. Fuller, T.F. *2-dimensional model of partial hydrogen coverage*. in *2005 AIChE Spring National Meeting, Conference Proceedings*. 2005. Atlanta, GA, United States American Institute of Chemical Engineers.

23. Yu, P.T., et al. *The effects of air purge on the degradation of PEM fuel cells during startup and shutdown procedures*. in *2004 AIChE Spring National Meeting, Conference Proceedings*. 2004. New Orleans, LA, United States: American Institute of Chemical Engineers.

24. McDonald, R.C., C.K. Mittelsteadt, and E.L. Thompson, *Effects of deep temperature cycling on Nafion 112 membranes and membrane electrode assemblies.* Fuel Cells, 2004. **4**(3): p. 208.

25. Pourbaix, M., *Atlas of Electrochemical Equilibria in Aqueous Solution*. 1966, Oxford: Pergamon Press.

26. St-Pierre, J., et al., *Relationships between water management, contamination and lifetime degradation in PEFC.* Journal of New Materials for Electrochemical Systems, 2000. **3**(2): p. 99.

27. Kinoshita, K., J.T. Lunqdist, and P. Stonehart, *Potential Cycling Effects on Platinum Electrocatalyst Surfaces.* Journal of Electroanalytical Chemistry and Interfacial Electrochemistry, 1973. **48**: p. 157.

28. Bindra, P., S.J. Clouser, and E. Yeager, *Platinum dissolution in concentrated phosphoric acid.* Journal of the Electrochemical Society, 1979. **126**(9): p. 1631.

29. Ferreira, P.J., et al., *Instability of Pt/C Electrocatalysts in Proton Exchange Membrane Fuel Cells: A mechanistic Investigation.* Journal of The Electrochemical Society, 2005. **152**(11): p. A2256.

30. Wang, X., R. Kumar, and D.J. Myers, *Effect of Voltage on Platinum Dissolution Relevance to Polymer Electrolyte Fuel Cells.* Electrochemical and Solid-State Letters, 2006. **9**(5): p. A225-A227.

31. Rand, D.A.J. and R. Woods, *A study of The Dissolution of Platinum, Palladium, Rhodium and Gold Electrodes in 1 M Sulphuric Acid by Cyclic Voltammetry.* Journal of Electroanalytical Chemistry, 1972. **35**: p. 209.

32. Johnson, D.C., D.T. Napp, and S. Brunckenstein, *A Ring-Disk Electrode Study of The Current/Potential Behavior of Platinum in 1.0 M Sulphuric Acid and 0.1M Perchloric Acids.* Electrochimica Acta, 1970. **15**: p. 1493.

33. Biegler, T., *Area Change of A Smooth Platinum Electrode.* Journal of the Electrochemical Society, 1967. **114**: p. 1261.

34. Yasuda, K., et al., *Platinum Dissolution and Deposition in the polymer electrolyte membrane of a PEM fuel cell as studied by potential cycling.* Physical Chemistry Chemical Physics, 2006. **8**: p. 746.

35. Harrington, D.A., *Simulation of anodic Pt oxide growth.* Journal of Electroanalytical Chemistry, 1997. **420**(1-2): p. 101.

36. Conway, B.E., et al., *A surface-electrochemical basis for the direct logarithmic growth law for initial stages of extension of anodic oxide films formed at noble metals.* Journal of Chemical Physics, 1990. **93**(11): p. 8361-73.

37. Heyd, D.V. and D.A. Harrington, *Platinum Oxide Growth Kinetics for Cyclic Voltammetry.* Journal of Electroanalytical Chemistry, 1992. **335**: p. 19.

38. Wang, X., R. Kumar, and D.J. Myers, *Effect of Voltage on Platinum Dissolution: Relevance to Polymer Electrolyte Fuel Cells.* Electrochemical and Solid-State Letters, 2006. **9**(5): p. A225-A227.

39. *Protocol on Fuel Cell Component Testing (Primer for Generating Test Plans)*. 2004, US Fuel Cell Council's Joint Hydrogen Quality Task Force.

40. Endoh, E., et al., *Degradation Study of MEA for PEMFCs under Low Humidity Conditions.* Electrochemical and Solid-State Letters, 2004. **7**(7): p. A209.

41. Fisher, G.B., J.L. Gland, and S.J. Schmieg, *The Spectroscopic Observation of Water Formation.* Journal of Vacuum Science and Technology, 1982. **20**(3): p. 518.

42. Fisher, G.B. and J.L. Gland, *The interaction of water with the Pt(111) surface.* Surface Science, 1980. **94**: p. 446.

43. Watanabe, M., et al., *Self-Humidifying Polymer Electrolyte Membranes for Fuel Cells.* Journal of the Electrochemical Society, 1996. **143**(12): p. 3847.

44. Watanabe, M., H. Uchida, and M. Emori, *Analyses of Self-Humidification and Suppression of Gas Crossover in Pt-Dispersed Polymer Electrolyte Membranes for Fuel Cells.* Journal of the Electrochemical Society, 1998. **145**(4): p. 1137.

45. Yang, B., Y.Z. Fu, and A. Manthiram, *Operation of thin Nafion-based self-humidifying membranes in proton exchange membrane fuel cells with dry H_2 and O_2.* Journal of Power Sources, 2005. **139**: p. 170.

46. Patterson, T. *Fuel Cell Technology Topical Conference Proceedings*. in *AIChE Spring National Meeting*. 2002.

47. Ohma, A., et al., *Phenomenon Analysis of PEFC for Automotive Use (1): Membrane Degradation Behavior During OCV Hold Test.* ECS Transactions, 2006. **3**(1): p. 519.

48. Bi, W., G.E. Gray, and T.F. Fuller, *PEM Fuel Cell Pt/C Dissolution and Deposition in Nafion Electrolyte.* Electrochemical and Solid-State Letters, 2007. **10**(5): p. B101.

49. Xu, H., R. Kunz, and J.M. Fenton, *Investigation of Platinum Oxidation in PEM Fuel Cells at Various Relative Humidities.* Electrochemical and Solid-State Letters, 2007 **10**(1): p. B1.

50. Li, J., et al., *Characterization of Catalyst Layer Structure Changes in PEMFC as a Function of Durability Testing.* ECS Transactions, 2006. **3**(1): p. 743.

51. Yasuda, K., et al., *Characteristics of a Platinum Black Catalyst Layer with Regard to Platinum Dissolution Phenomena in a Membrane Electrode Assembly.* Journal of the Electrochemical Society, 2006. **153**(8): p. A1599.

52. Parthasarathy, A., S. Srinivasan, and A.J. Appleby, *Temperature Dependence of the Electrode Kinetics of Oxygen Reduction at the Platinum/Nation Interface--A Microelectrode Investigation.* Journal of the Electrochemical Society, 1992. **139**(9): p. 2530.

53. Santarelli, M.G., M.F. Torchio, and P. Cochis, *Parameters estimation of a PEM fuel cell polarization curve and analysis of their behavior with temperature.* Journal of Power Sources, 2006. **159**: p. 824.

54. Coppo, M., N.P. Siegel, and M.R.v. Spakovsky, *On the influence of temperature on PEM fuel cell operation.* Journal of Power Sources, 2006. **159**: p. 560.

55. Xu, H., et al., *Operation of PEM fuel cells at 120–150 C to improve CO tolerance.* Journal of Power Sources, 2006. **159**: p. 979.

56. Aarhaug, T.A. and M.S. A, *Degradation Rates of PEM Fuel Cells at Open Circuit Voltage.* ECS Transactions, 2006. **3**(1): p. 775.

57. Mittal, V.O., H.R. Kunz, and J.M. Fenton, *Membrane Degradation Mechanisms in PEMFCs.* ECS Transactions, 2006. **3**(1): p. 507.

58. Debe, M.K., et al., *High voltage stability of nanostructured thin film catalysts for PEM fuel cells.* Journal of Power Sources, 2006. **161**: p. 1002.

59. Gasteiger, H.A., et al., *Activity benchmarks and requirements for Pt, Pt-alloy, and non-Pt oxygen reduction catalysts for PEMFCs.* Applied Catalysis B: Environmental, 2005. **56**(1-2): p. 9.

60. Paik, C.H., G.S. Saloka, and G.W. Graham, *Influence of Cyclic Operation on PEM Fuel Cell Catalyst Stability.* Electrochemical and Solid-State Letters, 2007. **10**(2): p. B39.

61. Kinoshita, K., *Electrochemical Oxygen Technology*. 1992, New York: Wiley.

62. Borup, R., et al., *PEM Fuel Cell Durability*, in *DOE Hydrogen Program, FY2005 Progress Report*. 2005. p. 1039.

63. Paik, C.H., T.D. Jarvi, and W.E. O'Grady, *Extent of PEMFC Cathode Surface Oxidation by Oxygen and Water Measured by CV.* Electrochemical and Solid-State Letters, 2004. **7**(4): p. A82.

64. Hubbell, J.H. and S.M. Seltzer, *Tables of X-Ray Mass Attenuation Coefficients and Mass Energy-Absorption Coefficients*. 1996, National Institute of Standards and Technology, http://physics.nist.gov/PhysRefData/XrayMassCoef/tab3.html.

65. Oberbroeckling, K.J., et al., *Density of Nafion Exchanged with Transition Metal Complexes and Tetramethyl Ammonium, Ferrous, and Hydrogen Ions: Commercial and Recast Films.* Analytical Chemistry, 2002. **74**: p. 4794.

66. Ferreira, P.J. and Y. Shao-Horn, *Formation Mechanism of Pt Single-Crystal Nanoparticles in Proton Exchange Membrane Fuel Cells.* Electrochemical and Solid-State Letters, 2007. **10**(3): p. B60.

67. Bi, W. and T.F. Fuller, *Temperature effects on PEM fuel cell Pt/C catalyst degradation.* Journal of the Electrochemical Society, 2008. **155**(2): p. B215.

68. Okada, T., et al., *Ion and Water Transport Characteristics of Perflurosulfonated Ionomer Membranes with H^+ and Alkali Metal Cations.* Journal of Physical Chemistry, B, 2002. **106**: p. 1267.

69. Choi, P., N.H. Jalani, and R. Datta, *Thermodynamics and Proton Transport in Nafion I. Membrane Swelling, Sorption, and Ion-Exchange Equilibrium.* Journal of The Electrochemical Society, 2005. **152**(3): p. e84.

70. Springer, T.E., T.A. Zawodzinski, and S. Gottesfeld, *Polymer Electrolyte Fuel Cell Model.* Journal of Electrochemical Society, 1991. **138**(8).

71. Thampan, T., et al., *Modeling of Conductive Transport in Proton-Exchange Membranes for Fuel Cells.* Journal of The Electrochemical Society, 2000. **147**(9): p. 3242.

72. Radovic-Hrapovic, Z. and G. Jerkiewicz, *The temperature dependence of the cyclic-voltammetry response for the Pt(110) electrode in aqueous H2SO4 solution.* Journal of Electroanalytical Chemistry, 2001. **499**: p. 61.

73. Conway, B.E., et al., *A Surface-electrochemical Basis for the Direct Logarithmic Growth Law for initial stages of Extension of Anodic Oxide films Formed at Noble Metals.* Journal of Chemical Physics, 1990. **93**(11): p. 8361.

74. Wagner, F.T. and P.N. Ross, Jr. , *LEED spot profile analysis of the structure of electrochemically treated Pt(100) and Pt(111) surfaces.* Surface Science, 1985. **160**(1): p. 305.

75. Jerkiewicz, G., et al., *Surface-oxide growth at platinum electrodes in aqueous H2SO 4 Reexamination of its mechanism through combined cyclic-voltammetry, electrochemical quartz-crystal nanobalance, and Auger electron spectroscopy measurements.* Electrochimica Acta, 2004. **49**(9-10): p. 1451.

76. Alsabet, M., M. Grden, and G. Jerkiewicz, *Comprehensive study of the growth of thin oxide layers on Pt electrodes under well-defined temperature, potential, and time conditions.* Journal of Electroanalytical Chemistry, 2006. **589**: p. 120.

77. Ota, K., et al., *Dissolution of Platinum in Acidic Media.* ECS Transactions, 2006. **3**(1): p. 619.

78. Kawahara, S., et al., *Deterioration of Pt Catalyst Under Potential Cycling.* ECS Transactions, 2006. **3**(1): p. 625.

79. Dam, V.A.T. and F.A.d. Bruijn, *The Stability of PEMFC Electrodes Platinum Dissolution vs Potential and Temperature Investigated by Quartz Crystal Microbalance.* Journal of The Electrochemical Society, 2007. **154**(5): p. B494.

80. Uribe, F.A. and J. Thomas A. Zawodzinski, *A study of polymer electrolyte fuel cell performance at high voltages. Dependence on cathode catalyst layer composition and on voltage conditioning.* Electrochimica Acta, 2002. **47**: p. 3799.

81. Eickes, C., et al., *Recoverable Cathode Performance Loss in Direct Methanol Fuel Cells.* Journal of The Electrochemical Society, 2006. **153**(1): p. A171-A178.

82. Paik, C.H., T.D. Jarvi, and W.E. O'Grady, *Extent of PEMFC Cathode Surface Oxidation by Oxygen and Water by CV.* Electrochemical and Solid-State Letters, 2004. **7**(4).

83. More, K.L. and K.S. Reeves, DOE Hydrogen Program Review, 2005.

84. Bi, W. and T.F. Fuller, *Temperature effects on PEM fuel cell Pt/C catalyst degradation.* ECS Transactions, 2007. **11(1, Part 2, Proton Exchange Membrane Fuel Cells 7, Part 2)**: p. 1235-1246.

85. Campbell, C.T., S.C. Parker, and D.E. Starr, *The Effect of Size-Dependent Nanoparticle Energetics on Catalyst Sintering.* Science, 2002. **298**: p. 811.

86. Mitsushima, S., et al. *Dissolution mechanism of platinum in acidic media*. in *212th ECS Meeting* 2007. Washington D. C.

87. Yadav, A.P., A. Nishikata, and T. Tsuru, *Effect of halogen ions on platinum dissolution under potential cycling in 0.5M H2SO4 solution.* Electrochimica Acta, 2007. **52**: p. 7444.

88. Kang, M.S. and Y.I. Joe, *Mathematical modeling for the preparation of platinum–solid-polymer-electrolyte by counter-current diffusion.* Journal of Power Sources, 1999. **77**: p. 49-55.

89. Chandrasekaran, R., W. Bi, and T.F. Fuller, *Robust Design of Battery/Fuel Cell Hybrid Systems-Methodology for Surrogate Models of Pt Stability and Mitigation through System Controls.* Journal of Power Sources, accepted, 2008.

90. Bi, W. and T.F. Fuller, *Modeling of PEM Fuel Cell Pt/C Catalyst Degradation.* Journal of Power Sources, 2008. **178**: p. 188.